Light hadron spectrum, quark masses and meson decay constants from lattice QCD with $O(a)$-improved dynamical Wilson fermions

Derek John Hepburn

Doctor of Philosophy

The University of Edinburgh

2003

Abstract

In this thesis I present results for the light hadron spectrum, light quark masses and meson decay constants from numerical simulations of lattice QCD. The simulations were performed on a $16^3 \times 32$ space-time lattice using the standard Wilson gauge field action and a fully $O(a)$-improved Sheikholeslami-Wohlert fermion action with $N_f = 2$ degenerate flavours of dynamical fermions.

A subset of these simulations were performed at fixed lattice spacing, as determined through the Sommer scale parameter, r_0, in order to investigate the effects associated with a finite sea quark mass whilst keeping cutoff and finite size effects fixed. A quenched simulation was also performed at this lattice spacing for comparative purposes. No clear evidence of unquenching was found in the data presented here although some indications were observed.

Light quark masses were determined from chiral extrapolations of pseudoscalar and vector meson masses for both the standard and PCAC definitions of the quark mass. The bare strange quark mass was fixed through the K, $\mathrm{K}^{\star}$ and ϕ meson masses for comparison. Renormalised quark masses have been determined in the $\overline{\mathrm{MS}}$ scheme at a reference scale of 2GeV with matching performed at two values of the scale parameter, $\mu = 1/a$ and $\mu = \pi/a$, in order to study the systematic effects.

Decay constants have been determined for the light pseudoscalar, vector and axial-vector mesons.

Declaration

This thesis has been composed and written by me and contains my work as part of the UKQCD collaboration. This work has not been submitted for any other degree or professional qualification. The gauge configurations and most of the correlation functions were generated by other members of the collaboration. I generated the correlation functions for the two lightest dynamical datasets using code written by other members of the collaboration. The data analysis presented in Chapter 4 was performed entirely by me, except where otherwise stated, using analysis code written by Edinburgh members of the UKQCD collaboration. I have modified and extended this code for use in this work. Some of the results of my analysis have been published in

- (UKQCD Collaboration) C. Allton *et al.*, Phys. Rev. D65, 054502 (2002), hep-lat/0107021
- (UKQCD Collaboration) D. Hepburn, Nucl. Phys. Proc. Suppl. 106, 278-280 (2002), hep-lat/0110029
- (UKQCD Collaboration) C. Michael *et al.*, Nucl. Phys. Proc. Suppl. 106, 293-295 (2002), hep-lat/0109028
- (UKQCD Collaboration) D. Hepburn, Nucl. Phys. Proc. Suppl. 119, 338-340 (2003), hep-lat/0209036

Acknowledgements

First of all I would like to thank my family for helping and supporting me through all my time at university. Thanks especially to my Mum, Margaret, and my Dad, John. This one's for you.

To all my friends at home I would like to say a big thanks for making the non-working hours so enjoyable and for sharing in the times of random nonsense. The same also goes for all the good friends I've made at university who have made the hours when I should have been working go by so very fast.

In an academic context I would first of all like to thank my supervisors, Prof. Ken Bowler and Dr. Brian J. Pendleton for all their help over the years and for proof reading my thesis. I'd also like to thank Dr Chris Allton, Dr Craig McNeile and Dr Chris Maynard for all the help and advice they have given me over the years.

Finally I gratefully acknowledge the financial support of the Carnegie Trust for the Universities of Scotland for funding this research.

Contents

Chapter 1

INTRODUCTION

The standard model of particle physics, which covers the electromagnetic, weak and strong nuclear forces governing the behaviour of the currently known fundamental particles, has been tremendously successful in predicting many properties of these particles and their interactions from a set of relatively few fundamental parameters such as their masses and the basic couplings of the theory. Part of the main thrust of particle physics today is therefore in exploring the implications of the standard model and comparing its predictions to experiment. This highly non-trivial task is essential in order to test the validity of the standard model and, perhaps more importantly, to find where it disagrees with experiment and therefore indicates the presence of new physics.

The basic mathematical framework of the standard model is that of quantum field theory which allows the essential properties of quantum mechanics, relativity and the dynamics of fields to be combined in order to model the interactions and decays of the fundamental particles and their bound states. The standard model is constructed specifically from the gauge field theory governing the fundamental strong interaction, QCD, and the electro-weak theory of Glashow, Weinberg and Salam which is spontaneously broken down to the theory of the electromagnetic interactions, QED, and the weak interactions through the Higgs mechanism.

To date no analytic method has been found to solve these field theories exactly and it has therefore been necessary to use perturbative approximations to the full theory. Perturbation theory has been extremely successful in standard model calculations, especially in QED where the asymptotic value of the coupling, α, is around $1/137$ and therefore makes a good expansion paramter. Indeed the most celebrated success of any physical theory has been in the prediction of the anomalous magnetic moment of the electron, $g-2$, for which experiment and theory agree to an unprecedented accuracy. Perturbation theory has also been successful in the high energy regime of QCD where, because of the non-abelian nature of the gauge group, the theory exhibits asymptotic freedom and the coupling is small. It is therefore applicable to the theoretical analysis of deep inelastic scattering experiments involving hadrons. Unfortuately perturbation theory is not applicable in the low energy regime of QCD where the coupling can be of order 1. Some non-perurbative means of analysing this strong coupling regime is essential in order to understand the confinement mechanism responsible for the formation of hadrons from constituent quarks and to study their decays.

Perhaps the most important non-perturbative technique known to date is that of lattice field theory, the basis of which is to discretise space-time to the form of a hypercubic lattice. The theory can then be written in terms of discrete 'field' operators at each lattice point which gives a finite number of variables in a finite space-time volume . This has the distinct advantage that numerical techniques such as Monte-Carlo integration can be used to evaluate the field theoretic expressions and therefore determine the properties of the theory we wish to study.

In this thesis I present work on the determination of the spectrum of light hadron masses, light meson decay constants and light quark masses from the lattice discretisation of QCD. This has been done using a particular discretisation of the theory with $N_{\mathrm{f}}=2$ degenerate flavours of dynamical $O(a)$-improved Wilson fermions. I describe this lattice theory in detail in Chapter 2 along with most of the theoretical background required in the work of this thesis. The lattice approach to QCD allows the quark mass dependence of physical observables to be studied in detail by systematically changing their input values. Such freedom actually turns out to be essential because computational difficulties prohibit the simulation of quark masses near those of the up and down quarks. The results must therefore be extrapolated in order to make physical predictions at the light quark masses. I describe the analytic techniques used to determine the lattice observables in Chapter 3 and Section 4.2 and summarise the results in Appendix A. The analysis and results of the quark mass extrapolations are given in Section 4.3 and results summarised in Appendix B.

Prediction of the physical observables from the results of the above analyses needs some experimental input in order to fix the mass scale or equivalently the lattice spacing and to fix the physical points through the quark masses. I have performed this analysis with a range of physical parameters in order to analyse any systematic differences that may arise. The analysis and lattice predictions for the hadron masses, meson decay constants and quark masses are summarised in Section 4.4 and Appendix C respectively.

Finally it is worth pointing out that the particular lattice theory used here treats the quarks in a fully dynamical way which should be contrasted with earlier lattice work in the quenched approximation where the effects of virtual quarks were effectively ignored. One of the main aims of this work has been to determine if any effects associated with the relaxation of the quenched approximation could be seen in the lattice data. Such unquenching effects have been investigated using a set of three dynamical simulations and one quenched simulation with a fixed value of the lattice spacing, a. This has been done to ensure that any systematic effects associated with a finite lattice spacing and finite spatial volume are kept fixed. I present the findings of this investigation in Section 4.5.

Chapter 2

Lattice QCD

In this chapter I set out most of the theory that will be needed in this thesis. I start by introducing some concepts of general field theory in Minkowski and Euclidean space and then specialise to the case of Quantum Chromodynamics. The discussion then turns to the lattice discretisation of this theory including its renormalisation and the continuum limit and how numerical methods can be used to evaluate useful field theoretical quantities. Finally I discuss the particular case of two-point correlation functions which have been central to the work of this thesis. From them the spectrum of light hadron masses and matrix elements associated with the decay of light mesons can be calculated, results which in turn can be used to make lattice predictions for the light quark masses and meson decay constants.

In writing this chapter I have referred to the books by Weinberg [1] and Peskin and Schroeder [2] for general field theory and to the books by Montvay and Munster [3] and Rothe [4] for lattice field theory.

2.1 Quantum field theory

Among the most basic properties of any quantum field theory is that there exists a Hilbert space whose elements represents states of our quantum system.

Furthermore on this Hilbert space there exists a unitary representation of the Poincare group of space-time rotations and translations. The operator representing a space-time rotation, Λ, followed by a translation, a, will be denoted by $U(\Lambda, a)$. The generators of this group of transformations, being hermitean operators, correspond to physical observables which in this case includes the 4-momentum and total angular momentum. There also exist group operators with discrete spectra such as those for parity, time reversal and charge conjugation.

In particular consider the operation of space-time translation by a^μ which is accomplished by the operator

$$U(1, a) = e^{ia^\mu P_\mu}. \tag{2.1}$$

where the Hamiltonian, $H \equiv P_0$. The eigenstates of H form a complete basis for the Hilbert space. These states, also being simultaneous eigenstates of the remaining P_μ operators, can be labelled by their energy, $E_n(\vec{p})$, and momentum, $\vec{p}$, and are denoted here by $|n, \vec{p}\rangle$. The label, n, distinguishes between states with different rest masses or where necessary between states with the same rest mass but different discrete quantum numbers such as spin. An important result, usually referred to as the completeness relation, is that the identity operator on the Hilbert space can be expressed in terms of the energy-momentum eigenbasis by

$$\mathbf{1} = |0\rangle\langle 0| + \sum_n \int \frac{d^3p}{(2\pi)^3} \frac{1}{2E_n(\vec{p})} |n, \vec{p}\rangle\langle n, \vec{p}| \tag{2.2}$$

where the normalisation for the states is taken as

$$\langle m, \vec{q}|n, \vec{p}\rangle = 2E_n(\vec{p})(2\pi)^3 \delta_{mn} \delta^3(\vec{q} - \vec{p}) \tag{2.3}$$

and the vacuum state is represented here by $|0\rangle$ with $\langle 0|0\rangle = 1$.

It should also be noted that the energy-momentum eigenstates of the theory in general include single and multi-particle states as well as bound states composed of a number of interacting particles. These bounds states will be the most important when we come to discuss quantum chromodynamics.

Now for each distinct species of particle in our field theory we define an associated operator acting on the Hilbert space. These operators are constructed to transform under some specific representation of the Poincare group e.g. for the scalar operator, Φ,

$$U(\Lambda,a)\Phi(x)U^{-1}(\Lambda,a) = \Phi(\Lambda x + a). \tag{2.4}$$

Similar expressions can be given for operators transforming in the vector and spinor representations with the general transformation for a set of field operators, $\Phi_i(x)$, being given by

$$U(\Lambda,a)\Phi_i(x)U^{-1}(\Lambda,a) = M_{ij}(\Lambda)\Phi_j(\Lambda x + a) \tag{2.5}$$

where M_{ij} is some general representation matrix depending only on the space-time rotation, Λ. An important consequence of this result which will be useful later is that for a general field operator,

$$\Phi_i(x) = U(1,x)\Phi_i(0)U^{-1}(1,x) = e^{ix^\mu P_\mu}\ \Phi_i(0)\ e^{-ix^\mu P_\mu}. \tag{2.6}$$

Among the most important quantities that can be calculated in a field theory are the vacuum to vacuum matrix elements of operators, $\mathcal{O}$, constructed from time ordered products of fundamental field operators,

$$\langle 0|T(\mathcal{O}(x_1,\ldots,x_n))|0\rangle, \tag{2.7}$$

where T indicates that the fields are time ordered. Such objects are known as the n-point Green's functions of the theory. From them physical quantities such as particle masses (as will be demonstrated later) and S-matrix elements and therefore scattering cross-sections can be calculated. I now go on to discuss their representations in terms of Feynman path integrals.

2.1.1 Path integral representations

The path integral representations for matrix elements and particularly Green's functions of a quantum field theory relate expressions containing quantum operators and Hilbert space states to real-valued integrals. This not only aids computation in some cases but can allow results such as Feynman rules in perturbation theory to be derived in a simple manner.

To start consider the case of a quantum field theory with operators $\Phi_i(x)$. These are Heisenberg operators and can be related to the time independent Schrödinger operators, $\Phi_i(\vec{x})$, through

$$\Phi_i(\vec{x}) \equiv \Phi_i(\vec{x}, 0) = e^{-iHt}\ \Phi_i(x)\ e^{iHt} \tag{2.8}$$

where $x \equiv (\vec{x}, t)$ here and the Heisenberg and Schrödinger operators are equal at reference time, $t = 0$. The simultaneous eigenstates of $\Phi_i(\vec{x})$ can be defined with eigenvalues denoted by $\phi_i(\vec{x})$ through

$$\Phi_i(\vec{x})|\phi\rangle = \phi_i(\vec{x})|\phi\rangle. \tag{2.9}$$

These eigenstates are the equivalent of position eigenstates in non-relativistic quantum mechanics except that now their eigenvalues are indexed by a continuous label, $\vec{x}$. The eigenstates of the Heisenberg operators are defined in such a way that matrix elements are preserved in the two pictures i.e.

$$\Phi_i(x)|\phi, t\rangle = \phi_i(\vec{x})|\phi, t\rangle. \tag{2.10}$$

giving the relation between the two sets of eigenvectors as

$$|\phi, t\rangle = e^{iHt}|\phi\rangle. \tag{2.11}$$

It is through the matrix elements of the states defined above that connection with the path integral representation is made. The Hamiltonian operator for a field theory can generally be written as some function of the fundamental field operators and their conjugates. For a large class of field theories where the Hamiltonian is quadratic in the conjugate operators it can be shown that the following matrix elements have a particularly simple representation in terms of a path integral

$$\langle\phi^{'},t^{'}|T(\mathcal{O}(x_1,\ldots,x_n))|\phi,t\rangle = \int\mathcal{D}\phi\ \mathcal{O}(x_1,\ldots,x_n)\ \exp\left(i\int_t^{t^{'}}dt^{''}L(t^{''})\right). \tag{2.12}$$

where all time variables in $\mathcal{O}$ are between $t^{'}$ and t.

This expression deserves some explanation. Most important of all is that (for bosonic fields) the path integral on the right hand side is written in terms of real or complex valued quantities only. The integration measure, $\mathcal{D}\phi$, is to be read as meaning that for every space-time point and index, i, we have integration over values of the field, $\phi_i(x)$, at that point. Symbolically this can be written as

$$\mathcal{D}\phi = \prod_{x,i} d\phi_i(x). \tag{2.13}$$

The integral can be formally defined through the process of discretising space-time and considering only a finite volume to render the number of integration variables finite. The reduced integral can then in principle be evaluated and the full result recovered in the limit of infinite volume and zero discretisation. This procedure is the basis of lattice field theory and will be described later in the context of QCD.

The function, $L(t)$, is the Lagrangian for the field theory and can be written in terms of a Lagrangian density, $\mathcal{L}$, which is a scalar function depending on the fields, $\phi_i(x)$, and their space-time derivatives, $\partial_\mu\phi_i(x)$, at the point, $x\equiv(\vec{x},t)$,

$$L(t) = \int d^3\vec{x}\ \mathcal{L}(\phi_i(\vec{x},t),\partial_\mu\phi_i(\vec{x},t)). \tag{2.14}$$

I should also mention that although I have used used the same symbol, $\mathcal{O}$, on both sides of Equation (2.12) that on the left it should be thought of as an operator but when inside the path integral it should be interpreted as having all operators replaced by their eigenvalues, $\phi_i(x)$.

One final thing that I will note here is an important difference between bosonic and fermionic operators. In contrast to the bosonic case fermionic field operators obey anti-commutation relations up to contact terms. In order to preserve this property the corresponding integration variables in the path integral will also have to anti-commute with one another. This is not a problem as they can be put on a sound mathematical footing as elements of a Grassmann algebra with clearly defined rules for integration, a subject we will return to in Section 2.3.1.

2.1.2 Euclidean Green's functions

Now that we have path integral representations for general time-ordered operators in the "position" eigenbasis connection to the n-point Green's functions can be made. Inserting complete sets of energy eigenstates, here denoted by $|n\rangle$ for simplicity, gives the following result

$$\langle\phi^{'},t^{'}|T(\mathcal{O}(x_1,\ldots,x_n))|\phi,t\rangle = \langle\phi^{'}|e^{-iHt^{'}}T(\mathcal{O}(x_1,\ldots,x_n))e^{iHt}|\phi\rangle$$

$$= \sum_{m,n}\langle\phi^{'}|n\rangle\langle m|\phi\rangle e^{-iE_n t^{'}}e^{iE_m t}\langle n|T(\mathcal{O}(x_1,\ldots,x_n))|m\rangle. \tag{2.15}$$

The contribution coming from the vacuum to vacuum amplitude (i.e. the Green's function we want) can be projected out using a standard trick of taking $t^{'}$ and t to plus and minus infinity respectively in slightly complex directions. Contributions from higher energy eigenstates then fall off exponentially relative to the vacuum. It should be noted that a necessary condition for this to happen is that there exists a mass gap between the vacuum state and the first excited state.

Now it can be seen that this limiting process projects out the wanted Green's function up to some overlap factors. These factors can be divided out in the following manner giving our final expression as

$$
\begin{aligned}
\langle 0|T(\mathcal{O}(x_1,\ldots,x_n))|0\rangle &= \lim_{t'\to(1-i\epsilon)\infty} \frac{\langle\phi',t'|T(\mathcal{O}(x_1,\ldots,x_n))|\phi,-t'\rangle}{\langle\phi',t'|\phi,-t'\rangle} \\
&= \lim_{t'\to(1-i\epsilon)\infty} \frac{\int \mathcal{D}\phi\ \mathcal{O}(x_1,\ldots,x_n)\ \exp\left(i\int_{-t'}^{t'} dtL(t)\right)}{\int \mathcal{D}\phi\ \exp\left(i\int_{-t'}^{t'} dtL(t)\right)}
\end{aligned} \tag{2.16}
$$

This is one way of defining the path integral representation for n-point Green's functions. However for the purposes of performing numerical lattice calculations another route is required. If instead of remaining in Minkowski space and considering the strange limit in Equation (2.16) we were to analytically continue the expressions in Equation (2.15) to imaginary times i.e. take $x^0 = -ix_4$ then there would be a natural exponential fall off of unwanted contributions. We would then be dealing with a field theory on an Euclidean space-time background but could in principle analytically continue back to real time if necessary. The path integral representations for Euclidean Green's functions are given by

$$
\langle 0|T(\mathcal{O}(x_1,\ldots,x_n))|0\rangle = \frac{\int \mathcal{D}\phi\ \mathcal{O}(x_1,\ldots,x_n)\ e^{-S_{\mathrm{E}}[\phi,\partial_\mu\phi]}}{\int \mathcal{D}\phi\ e^{-S_{\mathrm{E}}[\phi,\partial_\mu\phi]}} \tag{2.17}
$$

where the Euclidean action, $S_{\mathrm{E}}[\phi,\partial_\mu\phi]$, is given by

$$
S_{\mathrm{E}}[\phi,\partial_\mu\phi] = \int_{-\infty}^{\infty} d\tau L_{\mathrm{E}}(\tau) \tag{2.18}
$$

and $L_{\mathrm{E}}(\tau)$ is the Lagrangian for the Euclidean theory. The space-time points, x_i, in this expression are now to be taken as elements of four-dimensional Euclidean space.

In this form Equation (2.17) bears a striking resemblance to expressions for correlation functions in statistical mechanics. The Boltzmann factor is to identified with $\exp(-S_{\mathrm{E}})$ and the partition function, Z, then given by

$$Z = \int \mathcal{D}\phi \; e^{-S_{\mathrm{E}}[\phi,\partial_\mu\phi]} \tag{2.19}$$

It is for this reason that such expressions are also known as n-point correlation functions and are often denoted by $\langle \mathcal{O} \rangle$. More importantly however is that this allows the machinery of statistical mechanics to be used in the evaluation of the functional integrals. The numerical techniques of Monte Carlo integration and importance sampling are of particular use here and will be discussed in more detail in Section 2.3.

2.2 Lattice discretisation of QCD

With the general field theory now in place I would now like to specialise to the particular field theory this thesis is based on, QCD, and its lattice discretisation.

2.2.1 Quantum chromodynamics

The theory of quantum chromodynamics, QCD, is the quantum field theory used to model the fundamental strong force of nature which governs the interactions of quarks and gluons. It is written in term of quark fields, $\overline{\psi}(x)$ and $\psi(x)$, and gauge field, $A_\mu(x)$ and can be thought of as an extension of the quantum theory of the electromagnetic interactions, QED, to the case of a non-abelian gauge group. The quark and gauge fields transform under the spinor and vector representations of the Poincare group respectively. In the case of QCD the gauge field takes values from the Lie algebra of the group $SU(3)$. The field can therefore be expanded in terms of a set of eight generators for the Lie algebra, T_a, giving

$$A_\mu(x) = A_\mu^a(x) T_a. \tag{2.20}$$

where the $A_\mu^a(x)$ can be thought of as fields for the eight gluons in the theory.

The action of QCD, written in terms of quark and gluon fields, is given by

$$S[\overline{\psi}, \psi, A] = \int d^4x \overline{\psi}(x)(i\gamma^\mu D_\mu - m_0)\psi(x) - \frac{1}{2}\mathrm{Tr}(F_{\mu\nu}(x)F^{\mu\nu}(x)) \qquad (2.21)$$

where all colour and spinor indices have been suppressed and m_0 is the bare fermion mass. Only one flavour has been considered here for clarity but the theory is easily extended to multiple flavours. The covariant derivative, D_μ, is defined by

$$D_\mu = \partial_\mu - ig_0 A_\mu(x) \qquad (2.22)$$

where g_0 is the bare gauge coupling which can be thought of as governing the strength of interaction between quarks and gluons.

The trace over the square of the field strength tensor, $F_{\mu\nu}(x)$, is taken over the remaining colour indices after matrix multiplication. The field strength itself is given in terms of the gauge field by

$$F_{\mu\nu}(x) = \partial_\mu A_\nu(x) - \partial_\nu A_\mu(x) - ig_0[A_\mu(x), A_\nu(x)]. \qquad (2.23)$$

The presence of the commutator in $F_{\mu\nu}$, which arises as a result of the non-abelian nature of of the gauge group gives rise to three and four-point self interactions of the gauge field in perturbation theory. These interactions are thought to be responsible for the properties of asymptotic freedom and quark confinement in QCD. As a result the lowest energy eigenstates of the theory do not correspond to the elementary particles but to bound states of colour singlet combinations of them. These include the mesons and baryons and more exotic four-quark states and glueballs.

Before going on to consider the lattice discretisation of QCD we should first continue the theory over to imaginary times and determine the Euclidean action. In this instance the operation not only requires making the substitution $x^0 = -ix_4$ but also requires that we set $A^0(x) = iA_4(x)$ and replace the Dirac gamma matrices by their Euclidean counterparts, γ_μ^{E}, through the relations

$$\gamma^0 = \gamma_4^{\mathrm{E}} \quad \text{and} \quad \gamma^j = i\gamma_j^{\mathrm{E}}, \quad \forall j \in \{1,2,3\}. \tag{2.24}$$

After completing these changes and identifying $S = iS_{\mathrm{E}}$ we get the Euclidean action for QCD

$$S_{\mathrm{E}}[\overline{\psi}, \psi, A] = \int d^4x \overline{\psi}(x)(\gamma_\mu^{\mathrm{E}} D_\mu + m_0)\psi(x) + \frac{1}{2}\mathrm{Tr}(F_{\mu\nu}(x)F_{\mu\nu}(x)). \tag{2.25}$$

The superscript and subscript Es will be dropped from now on since we will be dealing exclusively with Euclidean field theory.

This action can be considered in two parts by defining the fermion action, S_{F}, to be

$$S_{\mathrm{F}}[\overline{\psi}, \psi, A] = \int d^4x \ \overline{\psi}(x)(\gamma_\mu D_\mu + m_0)\psi(x) \tag{2.26}$$

and the gauge field (or Yang-Mills) action, S_{G}, to be

$$S_{\mathrm{G}}[A] = \int d^4x \ \frac{1}{2}\mathrm{Tr}(F_{\mu\nu}(x)F_{\mu\nu}(x)). \tag{2.27}$$

Splitting the action in this natural way will simplify the following analysis.

2.2.2 Discretising QCD

We now move on to consider the discretisation of QCD, an idea first used by Kenneth Wilson in a study of quark confinement [5]. The basis of this procedure is the introduction of a space-time lattice. To be specific the lattice can be defined as consisting of space-time points, x, satisfying $x = an$ where a is the lattice spacing and n is a four-vector having integer valued components in the range $[0, L]$ for spatial directions and $[0, T]$ in the temporal direction. Points with $x_\mu/a = L(\mathrm{or} T)$ are to be identified with points having $x_\mu/a = 0$ to impose boundary conditions. This process not only gives a concrete definition to the functional integrals defined earlier but can also be considered as providing a regulator for the theory. In this context the inverse lattice spacing provides a natural momentum cutoff. I would also like to mention that the above definition of a space-time lattice is by no means unique. It is, however, the form that has been used in the work of this thesis.

The restriction to finite spatial and temporal extent is not necessary in principle but is more of a practical limit, allowing the theory to be simulated on a computer. It also has some important theoretical implications. The first of these is that the eigenvalues of the lattice Hamiltonian and momentum operators are made discrete. The second more problematic effect is that the equality in Equation (2.17) is not exact. It should be remembered that to project out the Euclidean Green's function an infinite time limit was taken. This is now impossible, resulting in contamination from eigenstates of higher energy. The only thing that can be done is to make the temporal extent as large as is practicable and to choose boundary conditions so as to minimise these unwanted contributions. The theoretical implications for lattice two-point correlation functions will be discussed in Section 2.4.1.

2.2.3 Wilson fermion action

With the lattice discretisation in place the fermion fields, $\overline{\psi}(x)$ and $\psi(x)$, are only defined on the lattice points. This therefore raises the question of how to define the derivative in order to discretise the fermion action, S_{F}. It may seems natural to replace the derivative with a finite difference but that would lead to an expression that is not invariant under local gauge transformations on the lattice. In the continuum the comparable problem was solved by replacing ∂_μ with D_μ so that the combination, $\overline{\psi}\gamma_\mu D_\mu \psi$, was gauge invariant. The covariant derivative can be defined symmetrically by

$$n^\mu D_\mu \psi(x) = \lim_{a \to 0} \frac{1}{2a} (U(x, x+an)\psi(x+an) - U(x, x-an)\psi(x-an)) \quad (2.28)$$

where the Schwinger line integral, $U(z, y)$, is defined by

$$U(z,y) = P\exp\left(ig_0\int_y^z dx_\mu A_\mu(x)\right). \tag{2.29}$$

The P in this expression denotes that the path ordering must be maintained when defining the integral. This expression for D_μ has the right gauge transformation properties even before the limit is taken and therefore motivates the following lattice replacement

$$D_\mu\psi(x) = \frac{1}{2a}(U_\mu^\dagger(x)\psi(x+\hat{\mu}) - U_\mu(x-\hat{\mu})\psi(x-\hat{\mu})) \tag{2.30}$$

where $\hat{\mu}$ is a 4-vector of length a in the μ direction and the link variables, $U_\mu(x)$, are defined by

$$U_\mu(x) = U(x+\hat{\mu},x) = \exp\left(ig_0 aA_\mu(x)\right). \tag{2.31}$$

The naive discretisation of S_{F} is then given after replacing the space-time integral by a finite sum over lattice sites by

$$\begin{aligned} S_{\mathrm{F}} &= \sum_x a^4\Big[\ m_0\overline{\psi}(x)\psi(x) \qquad (2.32)\\ &- \frac{1}{2a}\sum_\mu\Big(\ \overline{\psi}(x+\hat{\mu})\gamma_\mu U_\mu(x)\psi(x) - \overline{\psi}(x)\gamma_\mu U_\mu^\dagger(x)\psi(x+\hat{\mu})\ \Big)\Big]. \end{aligned}$$

Unfortunately this naive lattice fermion action suffers from what is known as the fermion doubling problem. The problem is that the contributions to the quark propagator coming from momenta near the Brillouin zone boundaries ($p_\mu = \pi/a$) stay significant even in the limit of zero lattice spacing. This action therefore does not lead to the correct continuum limit.

The problem can however be remedied by adding a particular operator to the naive action to give what is known as the Wilson fermion action

$$S_{\mathrm{F}}^{\mathrm{W}} = S_{\mathrm{F}} - \frac{ar}{2}\sum_x a^4\overline{\psi}(x)\Box\psi(x) \tag{2.33}$$

which depends on an additional parameter, r, that is usually set to 1. Importantly this term vanishes in the continuum limit as necessary to recover the correct theory. It unfortunately also explicitly breaks chiral symmetry on the lattice. Alternatively this can be considered as an additive renormalisation to the fermion mass, effectively changing which value of the mass parameter corresponds to massless fermions. For this reason it is customary to introduce the subtracted bare mass, m_q, given by

$$m_q = m_0 - m_c \tag{2.34}$$

where m_c is the critical value of m_0 yielding massless fermions.

Finally putting a gauge invariant discretisation of the Wilson term into the action gives

$$\begin{aligned} S_{\mathrm{F}}^{\mathrm{W}} &= \sum_x \Big[\overline{\psi}(x)\psi(x) \\ &- \kappa \sum_\mu \Big(\overline{\psi}(x+\hat{\mu})(r+\gamma_\mu)U_\mu(x)\psi(x) + \overline{\psi}(x)(r-\gamma_\mu)U_\mu^\dagger(x)\psi(x+\hat{\mu}) \Big) \Big]. \end{aligned} \tag{2.35}$$

where the fields have been rescaled such that $\psi(x) \to \sqrt{2\kappa}/a^{3/2}\psi(x)$ and the hopping parameter, κ, is defined in terms of the bare fermion mass, m_0, by

$$\kappa = \frac{1}{8r + 2am_0}. \tag{2.36}$$

There will of course be a critical value of the hopping parameter, κ_{crit}, that corresponds to zero quark mass. The bare subtracted mass is then related to κ through

$$am_q = \frac{1}{2}\left(\frac{1}{\kappa} - \frac{1}{\kappa_{\mathrm{crit}}}\right). \tag{2.37}$$

The lattice fermion action is now written only in terms of dimensionless quantities and is therefore suitable for use in numerical simulations. It is important to mention here that any Green's functions calculated using this action will be dimensionless and will need rescaled by appropriate factors of $\sqrt{2\kappa}$ and powers of a to make connection with physical Green's functions.

2.2.4 Wilson gauge field action

It turns out that a lattice discretisation of the gauge field action, S_{G}, can also be written in terms of link variables. The connection is made through ordered products of link variables round the smallest closed loops on the lattice, the so called plaquettes. The plaquette variable, $U_{\mu\nu}(x)$, is defined by

$$\begin{aligned} U_{\mu\nu}(x) &= U(x,x+\hat{\nu})U(x+\hat{\nu},x+\hat{\mu}+\hat{\nu})U(x+\hat{\mu}+\hat{\nu},x+\hat{\mu})U(x+\hat{\mu},x) \\ &= \exp(ig_0a^2G_{\mu\nu}(x)) \end{aligned} \tag{2.38}$$

where $G_{\mu\nu}(x) = F_{\mu\nu}(x) + O(a)$.

The lattice gauge field action can be written directly in terms of these plaquette variables as

$$S_{\mathrm{G}}[U] = \beta \sum_x \sum_{\mu<\nu} \left(1 - \frac{1}{3}\mathrm{ReTr}U_{\mu\nu}(x)\right) \tag{2.39}$$

where the bare gauge coupling, g_0, has been written in terms of the dimensionless constant, $\beta = 6/g_0^2$. This action correctly reduces to the continuum action in the limit of zero lattice spacing with errors only coming in at $O(a^2)$.

2.2.5 $O(a)$-Improvement and Renormalisation

At this point we have a lattice action, parameterised by β and κ, that can be used to calculate Green's functions from numerical simulations. Once properly renormalised these Green's functions and any derived physical quantities would in general have associated $O(a)$ discretisation errors relative to the continuum. A standard procedure would then be to calculate a chosen quantity for a range of lattice spacings and perform an extrapolation to determine the continuum result.

To gain good control over extrapolations where $O(a)$ errors are present requires results for small lattice spacings. This, however, represents a practical challenge because of the computer time needed to perform such simulations. One way to improve the situation would be to eliminate all of the $O(a)$ errors. The leading error would then be reduced to $O(a^2)$ and simulations could be performed at larger lattice spacings whilst still maintaining good control of the extrapolations.

What this requires in general is a way of improving the action and composite operators and a consistent method of renormalising the fundamental parameters and composite operators in the theory.

$O(a)$-Improvement

Early work on the improvement of lattice theories was performed by Symanzik which he successfully applied to ϕ^4 theory [6] and the non-linear sigma model [7]. Applying this program to lattice gauge theories, however, was found to be problematic. It was found [8] that these problems could be circumvented if it was only required that on-shell quantities such as particle energies and matrix elements between on-shell states states be improved.

The improvement program basically consists of adding appropriately weighted higher-dimensional operators to the action and composite operators so as to cancel off discretisation errors of a particular order in the lattice spacing. The situation for $O(a)$-improvement of the lattice gauge action with Wilson fermions is well described in [9].

Improvement of the action is accomplished by adding the so-called Sheikholeslami-Wohlert or clover term [10] to give

$$S_{\mathrm{F}}^{\mathrm{SW}} = S_{\mathrm{F}}^{\mathrm{W}} - c_{\mathrm{SW}}(g_0^2)\frac{i\kappa}{2}\sum_{x,\mu<\nu}\overline{\psi}(x)\sigma_{\mu\nu}P_{\mu\nu}(x)\psi(x) \tag{2.40}$$

where $\sigma_{\mu\nu} = \frac{i}{2}[\gamma_\mu, \gamma_\nu]$ and

$$P_{\mu\nu}(x) = \frac{1}{8}(U_{\mu\nu}(x) + U_{\nu,-\mu}(x) + U_{-\nu,-\mu} + U_{-\nu,\mu}(x) - h.c.) \tag{2.41}$$

is the so-called clover representation of the field strength tensor ($P_{\mu\nu}(x) = ig_0 a^2 F_{\mu\nu}(x) + O(a^4)$).

The coefficient function, $c_{\mathrm{SW}}(g_0^2)$, is not known a priori and has to be tuned to cancel $O(a)$ discretisation errors. This is true generally of improvement coefficients and methods to determine them will be discussed later in this section.

The composite operators that have been used in this thesis are as follows

$$\begin{aligned} P^a(x) &= \overline{\psi}(x)\gamma_5\lambda^a\psi(x) & (2.42)\\ A^a_\mu(x) &= \overline{\psi}(x)\gamma_\mu\gamma_5\lambda^a\psi(x) & (2.43)\\ V^a_\mu(x) &= \overline{\psi}(x)\gamma_\mu\lambda^a\psi(x) & (2.44)\\ T^a_{\mu\nu}(x) &= i\overline{\psi}(x)\sigma_{\mu\nu}\lambda^a\psi(x) & (2.45) \end{aligned}$$

where λ^a are the generators of the flavour group. It turns out that the pseudoscalar operator, $P^a(x)$, is already on-shell improved to $O(a)$. The improvement of the axial vector operator, $A^a_\mu(x)$, and vector operator, $V^a_\mu(x)$, requires the addition of one term to each as follows

$$\begin{aligned} (A_{\mathrm{I}})^a_\mu(x) &= A^a_\mu(x) + c_A(g_0^2)a\partial_\mu P^a(x) & (2.46)\\ (V_{\mathrm{I}})^a_\mu(x) &= V^a_\mu(x) + c_V(g_0^2)a\partial_\nu T^a_{\mu\nu}(x) & (2.47) \end{aligned}$$

where ∂_μ represents some lattice discretisation of the partial derivative. Again coefficient functions, $c_A(g_0^2)$ and $c_V(g_0^2)$, have been introduced and have to be fine tuned to remove $O(a)$ discretisation errors from on-shell matrix elements of the above operators.

Renormalisation

After improving the theory the parameters and composite operators need to be renormalised to make connection with physical observables. The renormalisation must however be done in such a way as to maintain the on-shell $O(a)$-improvement of the theory. In [9] it was shown that naive application of a mass independent renormalisation scheme, where the renormalisation constants are fixed by conditions at zero physical quark mass, is generally incompatible with $O(a)$ improvement. It is the presence of terms proportional to am_q that tend to spoil the improvement for non-zero quark mass. This can be remedied by modifying the renormalisation so that the renormalised parameters are related to the bare parameters through

$$m_{\mathrm{R}} = Z_m(\tilde{g}_0^2, a\mu)\tilde{m}_q \tag{2.48}$$

$$g_{\mathrm{R}}^2 = Z_g(\tilde{g}_0^2, a\mu)\tilde{g}_0^2 \tag{2.49}$$

where

$$\tilde{m}_q = (1 + b_m(g_0^2)am_q)m_q \tag{2.50}$$

$$\tilde{g}_0^2 = (1 + b_g(g_0^2)am_q)g_0^2 \tag{2.51}$$

and $a\mu$ is the renormalisation scale. The coefficient functions, $b_m(g_0^2)$ and $b_g(g_0^2)$, need to be determined in addition to the standard renormalisation constants, Z_m and Z_g and should be fine tuned so as to remove $O(a)$ cutoff effects associated with a finite quark mass. It should also be mentioned that the b-coefficients are independent of the renormalisation scheme used to fix the renormalisation constants and are scale independent.

Renormalisation of the composite operators introduced earlier proceeds in a similar way with

$$(A_{\mathrm{R}})_\mu^a = Z_A(\tilde{g}_0^2)(1 + b_A(g_0^2)am_q)(A_{\mathrm{I}})_\mu^a \tag{2.52}$$

$$\begin{aligned}(V_{\rm R})^a_\mu &= Z_V(\tilde{g}_0^2)(1+b_V(g_0^2)am_q)(V_{\rm I})^a_\mu &(2.53)\\ (P_{\rm R})^a &= Z_P(\tilde{g}_0^2,a\mu)(1+b_P(g_0^2)am_q)P^a &(2.54)\end{aligned}$$

where again the b-coefficients have to be tuned to cancel $O(a)$ quark mass cutoff effects and the renormalisation factors, Z_X, have to be fixed through renormalisation conditions. The factors Z_V and Z_A, being related to conserved currents in the chiral limit, are scale and scheme independent and correspond to a finite re-scaling of the bare operators.

The renormalised quark mass can also be defined through the following relation which depends on the improved and renormalised composite operators

$$\partial_\mu \langle (A_{\rm R})^a_\mu(x)\mathcal{O}(x_1,\cdots,x_n)\rangle = 2m_{\rm R}\langle (P_{\rm R})^a(x)\mathcal{O}(x_1,\cdots,x_n)\rangle + O(a^2) \qquad (2.55)$$

where $\mathcal{O}(x_1,\cdots,x_n)$ is an arbitrary operator and $x \neq x_i\,\forall i$ to avoid contact terms. This is the renormalised Ward-Takahashi identity associated with axial flavour transformations in the $N_f = 2$ lattice theory [11]. It is also know as the partially conserved axial current (PCAC) relation for obvious reasons. In the continuum limit Equation (2.55) becomes an exact relation whilst at finite lattice spacing the relation is spoiled by $O(a^2)$ discretisation errors if the lattice theory is fully $O(a)$ improved. Treating the relation as exact at finite lattice spacing therefore results in a renormalised mass that differs from Equation (2.48) by terms of $O(a^2)$.

A bare mass, which I will call $m_{\rm PCAC}$ here, can be motivated from Equation (2.55) and is given by

$$2m_{\rm PCAC}\langle P^a(x)\mathcal{O}\rangle = \partial_\mu\langle A^a_\mu(x)\mathcal{O}\rangle + c_A a\partial^2\langle P^a(x)\mathcal{O}\rangle \qquad (2.56)$$

with renormalisation defined through

$$m_{\rm R} = \frac{Z_A}{Z_P}\frac{(1+b_A am_q)}{(1+b_P am_q)}m_{\rm PCAC} + O(a^2). \qquad (2.57)$$

A very useful property of the PCAC mass is that it should not depend on the operator, $\mathcal{O}$, or on the point, x, up to terms of $O(a^2)$ if the theory is fully $O(a)$ improved. Alternatively this property can used as a way of determining the improvement coefficients, c_{SW} and c_A, as will be discussed presently.

Determination of the improvement and renormalisation coefficients

With all the improved and renormalised quantities needed in this work defined our attention can turn to the determination of the improvement coefficients and renormalisation factors. Ideally they should be determined non-perturbatively i.e. by numerical simulation and indeed almost all desired quantities have been calculated using non-perturbative methods in the quenched approximation (which is described in Section 2.3.4). The situation is not so good in the unquenched $N_f = 2$ theory (also described in Section 2.3.4).

The use of Ward identities associated with axial vector and vector flavour transformations has been central to the work of non-perturbative renormalisation and improvement. These equations relate different correlation functions to one another and should be satisfied up to at least $O(a^2)$ in the improved lattice theory. One particular example is the PCAC relation given in Equation (2.55). Requiring that these relations are satisfied identically on the lattice provides a method for the determination of the c-coefficients and scale independent Z factors or scale independent combinations of them. The b-coefficients or combinations of them can also be determined in this way but generally only if the analysis is extended to Ward identities with non-degenerate mass quarks.

These techniques have been applied by the Alpha collaboration to the non-perturbative determination of c_{SW} and c_A [12], Z_A, Z_V and b_V [13], c_V [14] and b_m, $b_A - b_P$ and $Z_m Z_P / Z_A$ [15] in the quenched approximation and to the determination of c_{SW} [16] in the $N_f = 2$ theory.

This work is extended by deDivitiis and Petronzio [17] and by the extensive work of the LANL collaboration [18] in the quenched approximation and recently by Bakeyev *et al.* [19] in a calculation of Z_V and b_V in the $N_f = 2$ theory.

The determination of scale and scheme dependent renormalisation constants such as Z_P presents a more complicated problem. The Alpha collaboration have used finite size techniques with the Schrödinger functional [20] to examine the scaling behaviour of Z_P in the quenched approximation [21] and $N_f = 2$ theory [22]. Results have also been obtained recently by the SPQcdR collaboration [23] for renormalisation constants of all quark bilinears. They use the continuum-like renormalisation condition of projecting matrix elements of the operators with external off-shell quark and gluon states onto their tree level structure. This method looks very promising but has unfortunately only been applied in the quenched approximation.

All of the numerical simulations relating to the work of this thesis have been performed with the fully $O(a)$-improved action where the value of $c_{\rm SW}$ has been set from either [12] or [16]. Since the majority of these simulations are for the $N_f = 2$ theory this work has unfortunately had to rely on perturbative estimates for the remaining coefficients and renormalisation factors. For the b and c-coefficients I have relied on the work of the Alpha collaboration [24, 25, 26, 27]. The majority of the coefficients have been determined by studying the approach of renormalised correlation functions to the continuum limit. In practice this was done by requiring the $O(a)$-improvement of certain combinations of the correlation functions.

The results for the b-coefficients have been expressed in terms of $\alpha_{latt} \equiv g_0^2/4\pi$ so that

$$b_X(g_0^2) = b_X^{(0)} + b_X^{(1)}\alpha_{latt} + O(\alpha_{latt}^2). \tag{2.58}$$

where the expansion coefficients are given in Table 2.1 for an arbitrary number of quark flavours, N_f.

The one-loop results for c_A and c_V are given by

$$c_A(\alpha_{latt}) = -0.09517(3)\ \alpha_{latt} + O(\alpha_{latt}^2) \tag{2.59}$$

$$c_V(\alpha_{latt}) = -0.2053(2)\ \alpha_{latt} + O(\alpha_{latt}^2) \tag{2.60}$$

X	$b_X^{(0)}$	$b_X^{(1)}$
g	0	$0.15080(3) \times N_f$
m	$-\frac{1}{2}$	$-1.2092(3)$
A	1	$1.9124(7)$
V	1	$1.9255(7)$
P	1	$1.9242(3)$

Table 2.1: One-loop results for b-coefficients from the Alpha collaboration [27].

For the renormalisation factors I have relied on the results of [28, 29]. They were determined using the standard technique of requiring that renormalised matrix elements of the operators in question are equal to the tree level results at some renormalisation scale, μ. The results were found with arbitrary values for the improvement coefficients and are given in the $\overline{\mathrm{MS}}$ scheme by

$$Z_X^{\overline{\mathrm{MS}}}(\alpha_{latt}, a\mu) = 1 + \alpha_{latt}\left(\frac{\gamma_X}{\pi}\log(a\mu) + B_X\right) + O(\alpha_{latt}^2) \tag{2.61}$$

where $X \in \{m, A, V, P\}$ and the coefficients γ_X and B_X are given in Table 2.2.

X	γ_X	B_X
m	-2	$1.3742 + 0.8210\ c_{\mathrm{SW}} - 0.1464\ c_{\mathrm{SW}}^2$
A	0	$-1.67604 - 0.02629\ c_{\mathrm{SW}} + 0.23888\ c_{\mathrm{SW}}^2$
V	0	$-2.18762 + 0.50352\ c_{\mathrm{SW}} + 0.05764\ c_{\mathrm{SW}}^2$
P	2	$-2.39745 + 0.23859\ c_{\mathrm{SW}} - 0.21603\ c_{\mathrm{SW}}^2$

Table 2.2: One-loop perturbative results for the renormalisation factors Z_m, Z_A, Z_V and Z_P from [28].

It should be borne in mind that the use of perturbative results here is a temporary measure and that non-perturbative results are always preferable. The two can be compared in the quenched approximation (e.g. [13] for Z_A and Z_V) and although there is generally good agreement at low values of α_{latt} there can be large discrepancies for higher values characteristic of hadronic processes. These discrepancies can be up to around 20% for the renormalisation factors and b-

coefficients and as much as a factor of 2 or 3 for the c-coefficients. This is not so much of a problem for the b-coefficients if only small quark masses are considered or for the c-coefficients when the improvement terms produce small contributions but overall a significant systematic error can be produced.

2.2.6 Improved perturbation theory

An important question to ask at this point is if a cause exists for the poor performance of perturbation theory and if so what can be done about improving the situation. These questions were first discussed in the context of lattice QCD by Lepage and Mackenzie [30].

Their first conclusion was that α_{latt} is generally a poor expansion parameter in the sense that errors coming from truncating the perturbative expansion are large. The solution they suggested was to re-express the perturbation series in terms of some renormalised coupling e.g. $\alpha^{\overline{\mathrm{MS}}}(\mu)$ as is done in continuum perturbation theory. This requires defining the renormalisation scheme and fixing in the scale, μ, in some way appropriate to the quantity being studied.

Further analysis in [30] identified the presence of large contributions from tadpole diagrams as a second cause for the poor performance of perturbation theory. It was found that this problem could be remedied by re-scaling the link variables of the theory by a non-perturbatively determined factor, u_0, representing the mean value of a link variable. If u_0 is chosen sensibly this should lead to a large cancellation of tadpole contributions in perturbative expressions calculated with the new tadpole action. Examples of good choices for u_0 are the fourth root of the expectation value of the averaged plaquette variable, $\langle\frac{1}{3}\mathrm{Tr}\,\overline{U_{\mu\nu}}\rangle^{1/4}$, and $1/8\kappa_{\mathrm{crit}}$.

It is easy to show that the tadpole action can be cast in the form of the original action by equating its parameters ($\tilde{g}_0^2$, $\tilde{\kappa}$ and $\tilde{c}_{\mathrm{SW}}$) with the parameters of the original action rescaled by suitable powers of u_0. In particular one finds that

$$\tilde{g}_0^2 = u_0^{-4} g_0^2, \quad \tilde{\kappa} = u_0 \kappa, \quad \tilde{c}_{\mathrm{SW}} = u_0^3 c_{\mathrm{SW}}. \tag{2.62}$$

and the boosted coupling therefore given by $\tilde{\alpha} = u_0^{-4}\alpha_{\text{latt}}$.

Similar results can be found for any other quantity and this importantly allows tadpole improved quantities to be related to the corresponding quantity calculated with the standard action.

For example, if the perturbative expansion for some quantity, X, calculated with the standard action is

$$X = X^{(0)} + X^{(1)}\alpha_{\text{latt}} + O(\alpha_{\text{latt}}^2) \tag{2.63}$$

then the tadpole improved perturbative result for the corresponding quantity, $\tilde{X}$, can be found by substituting the parameters of the standard action with those of the tadpole action and multiplying by the correct number of u_0 factors (as calculated in perturbation theory) i.e.

$$\tilde{X} = \left(\tilde{X}^{(0)} + \tilde{X}^{(1)}\tilde{\alpha} + O(\tilde{\alpha}^2)\right) u_{0,\text{PT}}^n \tag{2.64}$$

The final tadpole improved result for X is then given through the relation

$$X_{\text{TI}} = u_0^{-n}\ \tilde{X} = \left(\tilde{X}^{(0)} + \tilde{X}^{(1)}\tilde{\alpha} + O(\tilde{\alpha}^2)\right)\left(\frac{u_{0,\text{PT}}}{u_0}\right)^n. \tag{2.65}$$

If this procedure is applied to the one-loop results for the renormalisation factors given previously it gives

$$Z_{m,\text{TI}}^{\overline{\text{MS}}}(a\mu) = u_0^{-1}\left[1 + \tilde{\alpha}\left(\frac{\gamma_m}{\pi}\log(a\mu) + \tilde{B}_m\right) + O(\tilde{\alpha}^2)\right] \tag{2.66}$$

and

$$Z_{X,\text{TI}}^{\overline{\text{MS}}}(a\mu) = u_0\left[1 + \tilde{\alpha}\left(\frac{\gamma_X}{\pi}\log(a\mu) + \tilde{B}_X\right) + O(\tilde{\alpha}^2)\right] \tag{2.67}$$

for $X \in \{A, V, P\}$. The $\tilde{B}$ coefficients can be calculated simply by making the substitution $c_{\mathrm{SW}} \to \tilde{c}_{\mathrm{SW}} = u_0^3 c_{\mathrm{SW}}$ in the original B coefficients and making use of the perturbative expression

$$u_{0,\mathrm{PT}} = 1 + u_0^{(1)}\tilde{\alpha} + O(\tilde{\alpha}^2). \tag{2.68}$$

They are summarised in Table 2.3.

X	$\tilde{B}_X$
m	$1.3742 + 0.8210\ u_0^3 c_{\mathrm{SW}} - 0.1464\ u_0^6 c_{\mathrm{SW}}^2 + u_0^{(1)}$
A	$-1.67604 - 0.02629\ u_0^3 c_{\mathrm{SW}} + 0.23888\ u_0^6 c_{\mathrm{SW}}^2 - u_0^{(1)}$
V	$-2.18762 + 0.50352\ u_0^3 c_{\mathrm{SW}} + 0.05764\ u_0^6 c_{\mathrm{SW}}^2 - u_0^{(1)}$
P	$-2.39745 + 0.23859\ u_0^3 c_{\mathrm{SW}} - 0.21603\ u_0^6 c_{\mathrm{SW}}^2 - u_0^{(1)}$

Table 2.3: $\tilde{B}_X$ coefficients for tadpole improved renormalisation factors.

Tadpole expressions for the b-coefficients are given by

$$b_{X,\mathrm{TI}} = u_0^{-1}\left(b_X^{(0)} + (b_X^{(1)} + b^{(0)}u_0^{(1)})\tilde{\alpha} + O(\tilde{\alpha}^2)\right) \tag{2.69}$$

and for the c-coefficients simply by replacing α_{latt} with $\tilde{\alpha}$.

The boosted coupling, $\tilde{\alpha}$, turns out to be a good expansion parameter in the sense described earlier [30]. It can, however, be eliminated in terms of some renormalised coupling if this is preferable. As an example the relation

$$\alpha^{\overline{\mathrm{MS}}}(\mu) = \tilde{\alpha} + O(\tilde{\alpha}^2) \tag{2.70}$$

would allow one-loop perturbative results to be expressed in terms of $\alpha^{\overline{\mathrm{MS}}}(\mu)$.

In the work of this thesis I have used one-loop tadpole improved expressions for all of the renormalisation factors and improvement coefficients calculated with $u_0 = 1/8\kappa_{\mathrm{crit}}$ and the boosted coupling, $\tilde{\alpha}$.

2.3 Monte Carlo methods and numerical simulation

We are now in a position to discuss the calculation of correlation functions in lattice QCD with the $O(a)$-improved Wilson fermion action, $S_{\mathrm{F}}^{\mathrm{SW}}$, and Wilson gauge field action, S_{G}. I start by explicitly performing the integrations over the fermionic degrees of freedom and then discuss how the remaining integral over gauge field configurations can be estimated using Monte-carlo methods.

2.3.1 Fermionic degrees of freedom

The functional integral representation for the correlation function of a general operator, $\mathcal{O}$, in lattice QCD is given by the following expression

$$\langle \mathcal{O} \rangle = \frac{1}{Z} \int \mathcal{D}\overline{\psi}\mathcal{D}\psi\mathcal{D}U \; \mathcal{O} \; \exp\left(-S_{\mathrm{F}}^{\mathrm{SW}}[\overline{\psi}, \psi, U] - S_{\mathrm{G}}[U]\right). \tag{2.71}$$

In the lattice formulation this is a well defined multiple integral over a finite number of integration variables and can in principle be evaluated analytically. The integration variables here are the Grassmann-valued fermion field variables, $\overline{\psi}_n$ and ψ_n, and the $SU(3)$-valued link variables, U_l, where n is some composite index over lattice sites, spin and colour and the index, l, extends over all the links on the lattice. The fermion action has a particularly simple form in terms of these variables

$$S_{\mathrm{F}}^{\mathrm{SW}} = \sum_{m,n} \overline{\psi}_m K_{mn}(\kappa; U)\psi_n \tag{2.72}$$

where the fermion matrix, $K_{mn}(\kappa; U)$, has been introduced and its dependence on both κ and the gauge field, U, indicated explicitly. The integration measure can be written out explicitly in terms of the integration variables and is given by

$$\mathcal{D}\overline{\psi}\mathcal{D}\psi\mathcal{D}U \equiv \prod_n d\overline{\psi}_n d\psi_n \prod_l dU_l. \tag{2.73}$$

For each link variable, U_l, we therefore have to perform an integration over the $SU(3)$ group manifold as defined through the Haar measure, dU_l, and for each fermion field variable a Grassmann integration has to be performed.

It turns out that the integration rules for Grassmann variables are particularly simple and this allows the integration over the fermion field variables to be done explicitly. The primary algebraic property of Grassmann variables is that they anti-commute e.g.

$$\{\psi_m, \psi_n\} \equiv \psi_m\psi_n + \psi_n\psi_m = 0 \qquad \forall m, n. \tag{2.74}$$

An immediate corollary is that the square of any Grassmann variable is zero, a property that severely restricts the form of any function of Grassmann variables.

The integration measures, $d\overline{\psi}_n$ and $d\psi_n$, also anti-commute with each other and with the integration variables. This means that the following rules suffice in order to calculate an arbitrary multiple integral of any function of Grassmann variables

$$\int d\psi_n = 0, \qquad \int d\psi_m\psi_n = \delta_{mn}. \tag{2.75}$$

A particularly useful quantity to calculate is the fermion generating functional

$$Z[\overline{\eta}, \eta] = \int \mathcal{D}\overline{\psi}\mathcal{D}\psi \;\exp\left(-\sum_{m,n}\overline{\psi}_m K_{mn}\psi_n + \sum_n \overline{\eta}_n\psi_n + \sum_n \overline{\psi}_n\eta_n\right) \tag{2.76}$$

where $\overline{\eta}$ and η are source terms for the fermion field variables. This integral can be evaluated by first "completing the squares" then making use of the anti-commutivity of Grassmann variables to expand the exponential and perform the integrations. The result is that

$$Z[\overline{\eta},\eta] = \det K \exp\left(\sum_{m,n} \overline{\eta}_m G_{mn} \eta_n\right) \tag{2.77}$$

which depends on the fermion determinant, $\det K$, and the inverse of the fermion matrix, G, satisfying

$$K_{mn} G_{np} = \delta_{mp}. \tag{2.78}$$

In the present context the matrix, $G(\kappa; U)$, is the lattice discretisation of the quark propagator calculated on a fixed gauge field background, U.

Now the importance of the fermion generating functional is that any fermion integral can be generated from it by differentiating with respect to the fermion sources. In particular the differentiation rules

$$\frac{\partial}{\partial \overline{\eta}_m} \exp\left(\sum_n \overline{\eta}_n \psi_n\right) = \psi_m \exp\left(\sum_n \overline{\eta}_n \psi_n\right) \tag{2.79}$$

and

$$\frac{\partial}{\partial \eta_m} \exp\left(\sum_n \overline{\psi}_n \eta_n\right) = -\overline{\psi}_m \exp\left(\sum_n \overline{\psi}_n \eta_n\right) \tag{2.80}$$

can be used to show that

$$\begin{aligned} &\int \mathcal{D}\overline{\psi}\mathcal{D}\psi \; \overline{\psi}_{i_1} \cdots \overline{\psi}_{i_p} \psi_{j_1} \cdots \psi_{j_q} \exp\left(-\sum_{m,n} \overline{\psi}_m K_{mn} \psi_n\right) \\ &\quad = \left(-\frac{\partial}{\partial \eta_{i_1}}\right) \cdots \left(-\frac{\partial}{\partial \eta_{i_p}}\right) \left(\frac{\partial}{\partial \overline{\eta}_{j_1}}\right) \cdots \left(\frac{\partial}{\partial \overline{\eta}_{j_q}}\right) Z[\overline{\eta},\eta]\bigg|_{\overline{\eta}=\eta=0} . \end{aligned} \tag{2.81}$$

Along with the result of Equation (2.77) the expression above allows any functional integral over fermionic degrees of freedom to be evaluated. A useful observation here is that only terms in the expansion of the exponential in Equation (2.77) containing all the differentiation variables and no others will contribute to the result. No such terms exist if $p \neq q$ and the functional integral is therefore zero in that case. Otherwise each term contributes a product of elements of K^{-1} to the result weighted by ± 1 as determined by the ordering of the Grassmann variables.

These results can be immediately applied to correlation functions for lattice QCD leaving only the integrations over the link variables to be performed. The result with all gauge field dependence made explicit is that

$$\langle \mathcal{O} \rangle = \frac{\int \mathcal{D}U \; F_{\mathcal{O}}(G(U);U) \; \det K(U) \; \exp\left(-S_{\mathrm{G}}[U]\right)}{\int \mathcal{D}U \; \det K(U) \; \exp\left(-S_{\mathrm{G}}[U]\right)}. \tag{2.82}$$

where $F_{\mathcal{O}}(G(U);U)$ is the result of performing the integrations over $\overline{\psi}$ and ψ for the operator, $\mathcal{O}$.

2.3.2 Monte Carlo methods

The remaining integration over gauge field configurations in Equation (2.82) presents an extremely complex analytical problem. Approximate methods have been used for small and large β and small κ but no exact solution has been found. The use of numerical methods such as the statistical technique of Monte Carlo integration have, in contrast, been very useful in its evaluation.

Monte Carlo integration is most easily explained with a standard integral for a function, $f(x)$, over a single real variable, x,

$$I = \int_a^b f(x)dx. \tag{2.83}$$

This integral can be related to an expectation value with respect to a normalised probability distribution, $\rho(x)$, through

$$I = \langle f(x)/\rho(x) \rangle_\rho \equiv \int_a^b \frac{f(x)}{\rho(x)} \rho(x) dx. \tag{2.84}$$

The expectation value can then be estimated by sampling N points in the range $[a, b]$ distributed according to $\rho(x)$ and calculating the sample mean to give

$$I \simeq \frac{1}{N}\sum_{i=1}^{N}\frac{f(x_i)}{\rho(x_i)}, \tag{2.85}$$

with associated statistical error given by

$$\sqrt{\frac{\langle (f/\rho)^2\rangle_\rho - \langle f/\rho\rangle_\rho^2}{N}} \equiv \frac{\sigma_\rho}{\sqrt{N}}. \tag{2.86}$$

The estimate of the integral, I, can therefore be systematically improved by sampling more points although with diminishing returns due to the presence of the square root. The error can also be made smaller by choosing ρ in such a way that the standard deviation, σ_ρ, is made as small as is practicable. This is the technique of importance sampling. It is not really necessary when the function, f, is slowly varying over the integration range. In that case a uniform distribution will suffice. However, if f is sharply peaked for example then choosing ρ so that points are sampled more where f is large would be vastly more efficient than using a uniform distribution.

Such considerations are particularly important for lattice QCD where the gauge field integrals tend to be dominated by contributions from small parts of the sample space.

2.3.3 Configuration generation

In order to proceed, a probability distribution has to be chosen and a method for generating configurations from this distribution found. I will discuss how to generate configurations for some arbirtrary distribution, P_{F}, here and leave the discussion of the distributions used to generate gauge configuration until Section 2.3.4.

It would be ideal if we could sample configurations directly from P_F as can be done for Gaussian distributions but this is not practicable in general. An alternative method is to use a Markov process which generates a sequence of configurations that are asymptotically distributed as P_{F}. This is described in detail in [31] and I only cover the important features here for the case of a discrete space of configurations.

Consider the situation where at the n^{th} step of the Markov process the configurations are distributed according to P_n. The probability of being in configuration A at step $n+1$ is then given by

$$P_{n+1}(A) = \sum_{B} P_n(B) P_{\mathrm{M}}(B \to A) \tag{2.87}$$

where $P_{\mathrm{M}}(B \to A)$ is the probability of stepping from configuration B to configuration A and defines the Markov process.

A sufficient condition for this Markov process to have P_{F} as a fixed point of the mapping is the detailed balance condition

$$P_{\mathrm{F}}(A) P_{\mathrm{M}}(A \to B) = P_{\mathrm{F}}(B) P_{\mathrm{M}}(B \to A). \tag{2.88}$$

This does not on its own ensure that the sequence will converge to this fixed point but with the additional condition that the mapping is weakly ergodic, meaning that any configuration can eventually be reached from any other, the Markov process will converge to P_{F}.

So after iterating the Markov process from some starting configuration for a sufficiently long time the subsequently generated configurations will be distributed as P_{F} and are said to be equilibrated. This equilibration can be verified by monitoring the value of some variable such as the average plaquette in lattice QCD.

Despite being correctly distributed these configurations are not statistically independent in general. This has repercussions for the estimation of the expectation value of any quantity, $\mathcal{O}$. The variance on such an estimate calculated using N equilibrated configurations is given by the modified formula

$$\sigma^2(\mathcal{O}) = \frac{1}{N}\langle(\mathcal{O} - \langle\mathcal{O}\rangle)^2\rangle \;\; (1 + 2\mathcal{A}_{\mathcal{O}}) \tag{2.89}$$

where $\mathcal{A}_{\mathcal{O}}$ is a measure of the autocorrelations between values of $\mathcal{O}$ calculated on successive configurations. This result is larger than that for statistically independent configurations by a factor that depends on the quantity being studied through $\mathcal{A}_{\mathcal{O}}$. In principle this would mean calculating all quantities on all configurations in order to estimate the errors correctly. However, in practice the factor, $\mathcal{A}$, can be calculated for some suitable quantity and other quantities only calculated on configurations separated by at least $(1 + 2\mathcal{A})$ which are assumed to be statistically independent.

2.3.4 Hybrid Monte Carlo algorithm

Finally I would like to describe the particular algorithm that has been used in the generation of most of the gauge configurations on which the work of this thesis is based.

Looking at the gauge field integral in Equation (2.82) it is clear that the factor, $\exp\left(-S_{\mathrm{G}}[U]\right)$, is a strongly varying function of U. What is perhaps not so obvious is that the fermion determinant is also a strongly varying function of U. Both factors are therefore important as regards importance sampling. The matrix, K, satisfies the γ_5 hermiticity condition

$$K = \gamma_5 K^{\dagger} \gamma_5. \tag{2.90}$$

and its determinant is therefore real. Unfortunately it is not positive semi-definite for arbitrary κ and therefore cannot be used directly in the sampling distribution.

One solution is to ignore the determinant factor altogether by effectively treating it as a constant. This defines the quenched approximation and perturbatively amounts to ignoring the effects of virtual (sea) quark loops. It is also equivalent to taking the value of κ in the fermion determinant, which we will call κ_{sea} from now on, to be zero, therefore making the sea quarks infinitely heavy. Despite this, valence quarks can still be given finite masses in the quenched approximation through the value of κ in the quark propagator, which I call κ_{val} here. Such an approximation may seem a little drastic at first but a definitive study by the CP-PACS collaboration [32] found systematic errors of around only 10% in phenomenologically interesting quantities such as the hadron mass spectrum and meson decay constants.

In the quenched approximation the natural choice for the sampling distribution is

$$P(U) = \frac{1}{Z} e^{-S_{\mathrm{G}}[U]} \quad \text{where} \quad Z = \int \mathcal{D}U \; e^{-S_{\mathrm{G}}[U]}. \tag{2.91}$$

The local form of the gauge field action then allows single variable update algorithms to be used in the generation of gauge configurations. I do not wish to discuss these algorithms here but will say that large datasets are easily achievable on today's supercomputers.

The generation of gauge configurations becomes significantly more difficult if dynamical sea quark effects are to be included. This can be done for Wilson quarks by considering a theory with two mass degenerate quarks, the $N_f = 2$ theory. Physically this models the situation of dynamical up and down quarks but with exact isospin symmetry, an approximation that should have much smaller systematic errors than the quenched approximation. The product of the two fermion determinant factors is now positive semi-definite and an appropriate sampling distribution is then given by

$$P(U) = \frac{1}{Z} \left(\det K(\kappa_{\mathrm{sea}}, U) \right)^2 \; e^{-S_{\mathrm{G}}[U]}. \tag{2.92}$$

The non-local nature of this distribution means that single variable updating methods would depend on calculations involving all link variables. Less expensive methods exist that update all link variables at once such as the hybrid Monte Carlo (HMC) algorithm of Duane *et al.* [33] which has been used here.

In the case of dynamical fermions we start by rewriting the determinant factors in terms of complex scalar fields, $\phi^\dagger$ and ϕ, and introduce fictitious momenta conjugate to the link variables, denoted by P to give

$$P(U) = \frac{1}{Z'} \int \mathcal{D}P\mathcal{D}\phi^\dagger\mathcal{D}\phi e^{-H[P,U,\phi^\dagger,\phi]}. \tag{2.93}$$

where

$$H[P,U,\phi^\dagger,\phi] = \frac{1}{2}\sum_l P_l^2 + S_{\mathrm{G}}[U] + \sum_{m,n} \phi_m^\dagger (K^\dagger K)^{-1}_{mn} \phi_n \tag{2.94}$$

defines a Hamiltonian for our fictitious system. The generation of gauge configurations then proceeds as follows:

i/ Choose momenta at random from their Gaussian distribution and take $\phi = K^\dagger \xi$ for random Gaussian noise, ξ. This ensures that ϕ and $\phi^\dagger$ are distributed according to

$$P(\phi^\dagger, \phi) \propto \exp\left(-\phi^\dagger (K^\dagger K)^{-1} \phi\right). \tag{2.95}$$

ii/ Numerically integrate Hamilton's equations of motion for P and U for some fictitious time, $\tau = n\delta\tau$, whilst keeping ϕ constant. The numerical integration scheme should be area preserving and reversible to ensure detailed balance for the correct distribution. One example is the leapfrog integration scheme.

iii/ Perform a Metropolis accept/reject test i.e. keep the new configurations, P' and U', with probability $\min(1, \exp(H[P', U'] - H[P, U]))$.

iv/ Repeat the process until sufficient gauge configurations have been generated.

Overall this process satisfies detailed balance and ergodicity as necessary. This is true for any step size, $\delta\tau$, and number of steps, n, and these parameters are therefore free to be tuned to minimise the computational cost of generating statistically independent gauge configurations. The cost is already significant because of the need to perform a sparse matrix inversion for every step in the numerical integration. Preconditioning techniques were used to make the inversion steps more efficient. This has the effect of changing the form of the Hamiltonian slightly from the one given above but the basic structure of the algorithm remains the same.

2.4 Hadron masses and meson decay constants

In the final section of this chapter I describe the two-point correlation functions that have been used in the work of this thesis and how they can be used to determine hadron masses and matrix elements associated with the weak decay of pseudoscalar and vector mesons.

2.4.1 Two-point correlation functions

A general two-point correlation function is constructed from two operators at distinct space-time points, $\mathcal{O}_1(x)$ and $\mathcal{O}_2(y)$. In this work we have taken $y = 0$ and studied the Fourier transform of the two-point function over the remaining spatial degrees of freedom as given by

$$C_{\mathcal{O}_1\mathcal{O}_2}(t, \vec{p}) = \sum_{\vec{x}} e^{-i\vec{p}\cdot\vec{x}} \langle \mathcal{O}_1(x)\mathcal{O}_2(0)\rangle \tag{2.96}$$

where $t = x_4/a$ and $\vec{p}$ is a lattice 3-momentum. The function, $C_{\mathcal{O}_1\mathcal{O}_2}(t, \vec{p})$, will be referred to as a correlator in what follows. The momenta are restricted to take discrete values here because of the finite spatial extent of the lattice, aL, and have components given by $ap_i = 2\pi r_i/L$ where the integer $r_i \in [1, L-1]$.

The correlation function in Equation (2.96) corresponds to a functional integral as given by Equation (2.71) with the substitution $\mathcal{O} = \mathcal{O}_1(x)\mathcal{O}_2(0)$. Unfortunately this functional integral does not correspond exactly with a vacuum to vacuum amplitude or Green's function because the lattice has a finite temporal extent,

aT. If we impose periodic (antiperiodic) boundary conditions for the bosonic (fermionic) fields in the temporal direction then

$$\langle \mathcal{O}_1(x)\mathcal{O}_2(0)\rangle = \frac{\mathrm{Tr}\ e^{-aHT}\mathcal{O}_1(x)\mathcal{O}_2(0)}{\mathrm{Tr}\ e^{-aHT}} \tag{2.97}$$

where H is the lattice Hamiltonian operator and $\mathcal{O}_1(x)$ and $\mathcal{O}_2(0)$ are to be taken as Hilbert space operators on the right hand side. The trace over eigenstates of H is given by the following relation

$$\mathrm{Tr}\ \mathcal{O} = \langle 0|\mathcal{O}|0\rangle + \sum_{n,\vec{q}} \frac{1}{2E_n(\vec{p})(aL)^3}\langle n,\vec{q}|\mathcal{O}|n,\vec{q}\rangle. \tag{2.98}$$

where the eigenstates have been normalised appropriately for a lattice of finite spatial extent i.e.

$$\langle m,\vec{q}|n,\vec{p}\rangle = 2E_n(\vec{p})(aL)^3\delta_{mn}\delta_{\vec{q},\vec{p}}. \tag{2.99}$$

and the lattice delta function is given by

$$\delta_{\vec{q},\vec{p}} = \frac{1}{L^3}\sum_{\vec{x}} e^{i(\vec{q}-\vec{p})\cdot\vec{x}} = \left\{ \begin{array}{ll} 1 & \text{if } a(\vec{q}-\vec{p}) = 2\pi\vec{n},\ n_i \in \mathbb{Z} \\ 0 & \text{otherwise} \end{array} \right. . \tag{2.100}$$

The expression for the correlator can be further expanded by inserting a complete set of states as given by

$$\mathbf{1} = |0\rangle\langle 0| + \sum_{n,\vec{p}} \frac{1}{2E_n(\vec{p})(aL)^3}|n,\vec{p}\rangle\langle n,\vec{p}| \tag{2.101}$$

into the numerator of Equation (2.97) and making use of an earlier result that

$$\mathcal{O}_1(x) = e^{Hx_4 - i\vec{P}\cdot\vec{x}}\mathcal{O}_1(0)e^{-Hx_4+i\vec{P}\cdot\vec{x}}. \tag{2.102}$$

Making these changes results in the following expression for a general correlator

$$
\begin{aligned}
C_{\mathcal{O}_1\mathcal{O}_2}(t,\vec{p}) &= \left(1+\sum_{n,\vec{q}} e^{-aE_n(\vec{q})T}\right)^{-1} \Bigg[\langle 0|\mathcal{O}_1(0)|0\rangle\langle 0|\mathcal{O}_2(0)|0\rangle L^3\delta_{\vec{p},\vec{0}} \\
&+ \sum_n \frac{e^{-aE_n(\vec{p})t}}{2aE_n(\vec{p})} \frac{\langle 0|\mathcal{O}_1(0)|n,\vec{p}\rangle}{a} \frac{\langle n,\vec{p}|\mathcal{O}_2(0)|0\rangle}{a} \\
&+ \sum_n \frac{e^{-aE_n(\vec{p})(T-t)}}{2aE_n(\vec{p})} \frac{\langle n,-\vec{p}|\mathcal{O}_1(0)|0\rangle}{a} \frac{\langle 0|\mathcal{O}_2(0)|n,-\vec{p}\rangle}{a} \\
&+ \sum_{m,n} \frac{1}{L^3} \sum_{\vec{q},\vec{k}} \delta_{\vec{k}-\vec{q}-\vec{p},\vec{0}} \left\{ \frac{e^{-aE_m(\vec{q})(T-t)}}{2aE_m(\vec{q})} \frac{\langle m,\vec{q}|\mathcal{O}_1(0)|n,\vec{k}\rangle}{a^2} \right. \\
&\times \left. \frac{e^{-aE_n(\vec{k})t}}{2aE_n(\vec{k})} \frac{\langle n,\vec{k}|\mathcal{O}_2(0)|m,\vec{q}\rangle}{a^2} \right\} \Bigg]. \qquad (2.103)
\end{aligned}
$$

The first thing to note about this expression is the overall multiplicative constant. In the large T limit this constant tends to unity. I ignore it here, effectively including it in a redefinition of the other time independent factors present in Equation (2.103). This will lead to small systematic errors in these factors that disappear in the limit as $T \to \infty$.

The second and perhaps most important thing to note is that many of the terms in Equation (2.103) are zero by symmetry. This is especially so of the first term which is zero unless $\mathcal{O}_1(0)$ and $\mathcal{O}_2(0)$ are flavour and colour singlet operators with the same spin, parity and charge conjugation symmetry as the vacuum. These conditions are not satisfied by the operators used in this work and the term is taken to be zero from now on.

Similar considerations apply for the other matrix elements leaving only those with the appropriate symmetries to contribute. Suitably defining the indices, n and m, to run over non-zero contributions gives the following general structure for a correlator with $\vec{p} = \vec{0}$

$$
C_{\mathcal{O}_1\mathcal{O}_2}(t) = \sum_n \frac{\mathcal{A}^{(n)}_{\mathcal{O}_1\mathcal{O}_2}}{2aM_n}\, e^{-aM_n t} + \sum_m \frac{\mathcal{A}^{(m)}_{\mathcal{O}_2\mathcal{O}_1}}{2aM_m}\, e^{-aM_m(T-t)} + \cdots \qquad (2.104)
$$

where

$$\mathcal{A}^{(n)}_{\mathcal{O}_1\mathcal{O}_2} = \frac{\langle 0|\mathcal{O}_1(0)|n,\vec{0}\rangle}{a}\frac{\langle n,\vec{0}|\mathcal{O}_2(0)|0\rangle}{a} \tag{2.105}$$

is a dimensionless amplitude factor and

$$M_n = E_n(\vec{0}). \tag{2.106}$$

At this point the two operators, $\mathcal{O}_1$ and $\mathcal{O}_2$, are still arbitrary and the two separate sums associated with forward and backward propagating states in Equation (2.104) run over different energy eigenstates in general. Even at this stage, however, it is clear that the masses of at least the lowest lying states can be determined by studying the time dependence of $C_{\mathcal{O}_1\mathcal{O}_2}(t)$.

This observation means that by choosing $\mathcal{O}_1$ and $\mathcal{O}_2$ appropriately we should be able to determine the masses of the associated hadrons in lattice QCD.

2.4.2 Interpolating operators for mesons and baryons

The main criterion used in choosing $\mathcal{O}_1$ and $\mathcal{O}_2$ is that

$$\langle 0|\mathcal{O}_i(0)|n,\vec{q}\rangle \neq 0 \quad \text{for} \quad i=1,2. \tag{2.107}$$

for the hadronic state we wish to study. This requires, as was stated earlier, that these interpolating operators have the same quark content, colour, spin, parity and in some cases charge conjugation symmetry as the hadronic state. I now go on to discuss the operators used to study mesonic and baryonic states in turn.

Meson operators

The basic structure of a meson interpolating operator is as follows

$$\mathcal{M}^{(q_1q_2)}(x) = \overline{\psi}^{(q_1)}(x)\Gamma\psi^{(q_2)}(x), \tag{2.108}$$

where Γ is some combination of Dirac gamma matrices and q_1 and q_2 are flavour labels. This operator is a colour singlet as required and its spin, parity and charge conjugation symmetry are fixed by the particular choice of gamma matrices present. The meson operators used in this thesis and the associated particle states they have been used to study are given in Table 2.4 along with the labels I have used to identify their masses and matrix elements from lattice simulations. The J^{PC} and ${}^{2S+1}L_J$ assignments of each state are also given although the charge conjugation symmetry is only relevant for flavour singlet states. It is worth bearing in mind that the scalar state, $a_0(980)$, may correspond to a more exotic or hybrid state such as a bound state of K and $\overline{K}$ mesons. It will still, however, contribute to the meson correlator.

Operators	J^{PC} $({}^{2S+1}L_J)$	States(MeV)	label
$P^{(q_1q_2)}(x) = \overline{\psi}^{(q_1)}(x)\gamma_5\psi^{(q_2)}(x)$ $A_4^{(q_1q_2)}(x) = \overline{\psi}^{(q_1)}(x)\gamma_4\gamma_5\psi^{(q_2)}(x)$	0^{-+} $({}^1S_0)$	$\pi(140)$,K(494)	PS
$V_i^{(q_1q_2)}(x) = \overline{\psi}^{(q_1)}(x)\gamma_i\psi^{(q_2)}(x)$ $T_{i4}^{(q_1q_2)}(x) = i\overline{\psi}^{(q_1)}(x)\sigma_{i4}\psi^{(q_2)}(x)$	1^{--} $({}^3S_1)$	$\rho(770)$ K$^*(892)$ $\phi(1020)$	V
$S^{(q_1q_2)}(x) = \overline{\psi}^{(q_1)}(x)\psi^{(q_2)}(x)$	0^{++} $({}^3P_0)$	$a_0(980)$	S
$T_{ij}^{(q_1q_2)}(x) = i\overline{\psi}^{(q_1)}(x)\sigma_{ij}\psi^{(q_2)}(x)$	1^{+-} $({}^1P_1)$	$b_1(1235)$	B
$A_i^{(q_1q_2)}(x) = \overline{\psi}^{(q_1)}(x)\gamma_i\gamma_5\psi^{(q_2)}(x)$	1^{++} $({}^3P_1)$	$a_1(1260)$	A

Table 2.4: Summary of interpolating operators for mesons and the associated particle states.

A general meson correlator is constructed by choosing the sink operator,

$$\mathcal{O}_1(x) = \mathcal{M}_1^{(q_1q_2)}(x) = \overline{\psi}^{(q_1)}(x)\Gamma_1\psi^{(q_2)}(x) \tag{2.109}$$

and the source operator,

$$\mathcal{O}_2(0) = \left(\mathcal{M}_2^{(q_1q_2)}(0)\right)^\dagger = \overline{\psi}^{(q_2)}(0)\gamma_4\Gamma_2^\dagger\gamma_4\psi^{(q_1)}(0). \tag{2.110}$$

The source operator can be thought of as acting like a creation operator for all states having the same quantum numbers as the state we wish to study. After creation these states propagate for some time and are annihilated by the operator at sink. This accounts for the forward propagating sum of terms in Equation (2.104). The backward propagating states can be thought of in a similar manner but with the roles of source and sink operators reversed. For meson correlators the backward propagating states correspond to the antiparticles of the forward propagating states. The matrix elements associated with forward and backward propagating states can therefore be related through charge conjugation. This result can be used, along with the fact that the correlators studied here are real, to give the following expression for a meson correlator

$$C_{\mathcal{M}_1\mathcal{M}_2^\dagger}(t) = \sum_n \frac{\mathcal{A}^{(n)}_{\mathcal{M}_1\mathcal{M}_2^\dagger}}{2aM_n} \left(e^{-aM_nt} + \eta_{12}e^{-aM_n(T-t)}\right) + \cdots \tag{2.111}$$

where $\eta_{12} = \pm 1$ depends on the behaviour of the correlator under time reflection $t \to T - t$.

The remaining amplitude factor can be factorised, a result that is of importance when performing simultaneous fits to multiple correlators as discussed in Section 3.6.1. For spin-0 particles the factorisation is simply given by

$$\mathcal{A}^{(n)}_{\mathcal{M}_1\mathcal{M}_2^\dagger} = \mathcal{A}^{(n)}_{\mathcal{M}_1}\mathcal{A}^{(n)\,*}_{\mathcal{M}_2} \tag{2.112}$$

where

$$\mathcal{A}^{(n)}_{\mathcal{M}} = \frac{\langle 0|\mathcal{M}(0)|n,\vec{0}\rangle}{a}. \tag{2.113}$$

The situation for spin-1 particles is more complicated because there are three independent polarisation states for each mass. In this case the state label, n, can be decomposed into a new label for states of distinct mass, which I will also call n, and a polarisation label, r, with associated polarisation vector, $\epsilon^r(\vec{p})$. Matrix elements of any one of V_i, T_{i4}, A_i or $T_i = \frac{1}{2}\epsilon_{ijk}T_{jk}$, which I denote generically by $\mathcal{M}_i$ here, can be decomposed as follows

$$\langle 0|\mathcal{M}_i(0)|n,\epsilon^r(\vec{0}),\vec{0}\rangle = a\mathcal{A}^{(n)}_{\mathcal{M}}\ \epsilon^r_i(\vec{0}). \tag{2.114}$$

The sum over contributions to the correlator coming from distinct polarisation states can be performed by making use of the general result that

$$\sum_r \epsilon^r_i(\vec{p})\epsilon^r_j(\vec{p})^* = \delta_{ij} + \frac{p_i p_j}{M_n^2} \tag{2.115}$$

to give

$$\sum_r \frac{\langle 0|(\mathcal{M}_1)_i|n,\epsilon^r(\vec{0}),\vec{0}\rangle}{a}\frac{\langle n,\epsilon^r(\vec{0}),\vec{0}|(\mathcal{M}_2)^\dagger_j|0\rangle}{a} = \delta_{ij}\mathcal{A}^{(n)}_{\mathcal{M}_1}\mathcal{A}^{(n)\,*}_{\mathcal{M}_2}. \tag{2.116}$$

When substituted into Equation (2.111) this effectively casts the spin-1 correlators into the same form as spin-0 correlators with n running over states of distinct mass in both cases. The dimensionless amplitude factors, $\mathcal{A}^{(n)}_{\mathcal{M}}$, and masses, aM_n, effectively parameterise the meson correlators and it is these quantities that can be directly determined using the data analysis techniques of Chapter 3.

Now that I have described the theoretical form of a general meson correlator I would like to describe how they are calculated numerically using the functional integral methods of Section 2.3. The first step is to perform the integrations over the fermionic degrees of freedom. This can be done using Equations (2.77) and (2.81) and effectively replaces $\overline{\psi}$,ψ pairs by elements of the quark propagator, G.

For a general meson correlator, $C_{\mathcal{M}_1\mathcal{M}_2^\dagger}(t,\vec{p})$, the result is that

$$\begin{aligned} C_{\mathcal{M}_1\mathcal{M}_2^\dagger}(t,\vec{p}) = -\Big\langle \sum_{\vec{x}} e^{-i\vec{p}\cdot\vec{x}}\Big\{ &\mathrm{Tr}_{\mathrm{sc}}\left[\gamma_5 G^{(q_1)\dagger}(x,0;U)\gamma_5\Gamma_1 G^{(q_2)}(x,0;U)\gamma_4\Gamma_2^\dagger\gamma_4\right] \\ -\delta_{q_1q_2}\mathrm{Tr}_{\mathrm{sc}}\left[G^{(q_1)}(x,x;U)\Gamma_1\right]\,&\mathrm{Tr}_{\mathrm{sc}}\left[G^{(q_1)}(0,0;U)\gamma_4\Gamma_2^\dagger\gamma_4\right]\Big\}\Big\rangle_U \end{aligned} \tag{2.117}$$

where G has been written in spin-colour matrix form with the space-time and gauge field dependence made explicit and the γ_5-hermiticity relation,

$$G(x,y;U) = \gamma_5 G^\dagger(y,x;U)\gamma_5, \tag{2.118}$$

has been used to reverse the order of the space-time arguments on the first quark propagator. The traces are over spin and colour indices and $<>_U$ represents the expectation value over gauge fields as defined through the Monte Carlo procedure for the quenched or $N_f = 2$ theory.

As was discussed in Section 2.3 we estimate this expectation value by a finite sum over gauge configurations chosen from the appropriate probability distribution. The dependence on these gauge configurations comes in through the quark propagator only and the first step is therefore to invert the fermion matrix, K, on each configuration. This in itself is a very computationally intensive operation and is only really necessary if we wish to calculate the extra flavour singlet term in the expectation value. With a restriction to flavour non-singlet mesons we only need to calculate elements of G with a fixed space-time source at the lattice origin. This is done in practice by solving the matrix equation,

$$\sum_x K(y,x;U)G(x,0;U) = \delta(y,0), \tag{2.119}$$

using some form of iterative solver such as the conjugate gradient algorithm.

Once this has been done for sufficiently many different flavours the propagators can be tied together by contracting them with the appropriate gamma matrices at source and sink to form a meson correlator. For our general meson correlator the result for a single gauge configuration, $U^{(i)}$, is

$$C^{(i)}_{\mathcal{M}_1\mathcal{M}_2^\dagger}(t,\vec{p}) = -\sum_{\vec{x}} e^{-i\vec{p}\cdot\vec{x}}\mathrm{Tr}_{\mathrm{sc}}\left[\gamma_5 {G^{(q_1)}}^\dagger(x,0;U^{(i)})\gamma_5\Gamma_1 G^{(q_2)}(x,0;U^{(i)})\gamma_4\Gamma_2^\dagger\gamma_4\right]. \tag{2.120}$$

and the full correlator is then estimated by

$$C_{\mathcal{M}_1\mathcal{M}_2^\dagger}(t,\vec{p}) \simeq \frac{1}{N}\sum_i^N C^{(i)}_{\mathcal{M}_1\mathcal{M}_2^\dagger}(t,\vec{p}) \tag{2.121}$$

with some standard error as discussed earlier.

Baryon operators

The basic form of the baryon interpolating operators used here is

$$\mathcal{B}^{(q_1q_2q_3)}(x) = \epsilon_{abc}(\psi_a^{(q_1)}{}^T(x)C\Gamma\psi_b^{(q_2)}(x))\psi_c^{(q_3)}(x) \tag{2.122}$$

where $C = \gamma_4\gamma_2$ is the charge conjugation matrix for Dirac spinors and a, b and c are colour indices. These operators are colour singlets and have a single free spinor index as necessary for describing spin-$\frac{1}{2}$ octet and spin-$\frac{3}{2}$ decuplet baryons. The spin and parity properties are fixed through the choice of the matrix, Γ. In this thesis I have only considered the spin-$\frac{1}{2}$ nucleon and spin-$\frac{3}{2}$ delta baryon and the operators used in their study are given in Table 2.5 along with their isospin and spin-parity assignments.

Operators	$I(J^P)$	Lightest states(MeV)
$N_1^{(q_1q_2q_3)} = \epsilon_{abc}(\psi_a^{(q_1)}{}^T C\gamma_5\psi_b^{(q_2)})\psi_c^{(q_3)}$ $N_2^{(q_1q_2q_3)} = \epsilon_{abc}(\psi_a^{(q_1)}{}^T C\gamma_4\gamma_5\psi_b^{(q_2)})\psi_c^{(q_3)}$	$\frac{1}{2}(\frac{1}{2}^\pm)$	N(940), N(1535)
$\Delta_i^{(q_1q_2q_3)} = \epsilon_{abc}(\psi_a^{(q_1)}{}^T C\gamma_i\psi_b^{(q_2)})\psi_c^{(q_3)}$	$\frac{3}{2}(\frac{3}{2}^\pm)$	$\Delta(1232), \Delta(1700)$

Table 2.5: Summary of interpolating operators for baryons and the associated particle states.

As indicated in Table 2.5 these operators do not have a definite parity and in fact couple to both parity states, transforming under parity as

$$\mathcal{P}\mathcal{B}^{(q_1q_2q_3)}(x_4,\vec{x})\mathcal{P} = \gamma_4\mathcal{B}^{(q_1q_2q_3)}(x_4,-\vec{x}). \tag{2.123}$$

With the representation of $\gamma_4 = diag(1,1,-1,-1)$ used here this shows that the upper two spinor components of $\mathcal{B}$ transform with positive parity whilst the lower two transform with negative parity.

It is also important to realise that the Δ_i operators contain a spin-$\frac{1}{2}$ component, meaning that they will have a non-zero overlap with spin-$\frac{1}{2}$ states in addition to the spin-$\frac{3}{2}$ states we wish to study. I will come back to this problem later.

Finally I should mention that in order to get the flavour symmetries of the baryons being studied correct it is necessary to take linear combinations of the given operators. I only consider the single operator case here for simplicity and refer the reader to [3], [34] and [35] for a more detailed discussion.

A general baryon correlator is constructed by choosing the sink operator,

$$\mathcal{O}_1(x) = \mathcal{B}^{(q_1 q_2 q_3)}(x), \tag{2.124}$$

and source operator

$$\begin{aligned} \mathcal{O}_2(0) &= \overline{\mathcal{B}^{(q_1 q_2 q_3)}(0)} = \mathcal{B}^{(q_1 q_2 q_3)^\dagger}(0)\gamma_4 \\ &= \epsilon_{abc}\, \overline{\psi}_c^{(q_3)}(0)(\overline{\psi}_b^{(q_2)}(0)\gamma_4\Gamma^\dagger\gamma_4 C\overline{\psi}_a^{(q_1)^T}(0)). \end{aligned} \tag{2.125}$$

In order to analyse the functional form of such a correlator I need to introduce some notation for the states involved. As was mentioned earlier the baryon correlator will couple to states of either parity. In addition, the fermionic states have a spin degree of freedom, s, and so in order to simplify notation in what follows I denote the zero momentum baryonic states by $|n, s, +\rangle$ and $|n, s, -\rangle$ for positive and negative parity states respectively. The index, n, runs over distinct mass states as in the mesonic case.

The amplitudes for the forward propagating states can be factorised using the following matrix element identities for spin-$\frac{1}{2}$ states,

$$\begin{aligned}\langle 0|N_i(0)|n,s,+\rangle &= \frac{1}{\sqrt{2}}a\mathcal{A}_{N_i}^{(n,+)}u^s(M_n^+,\vec{0}) && (2.126)\\ \langle 0|N_i(0)|n,s,-\rangle &= \frac{1}{\sqrt{2}}a\mathcal{A}_{N_i}^{(n,-)}\gamma_5 u^s(M_n^-,\vec{0}) && (2.127)\end{aligned}$$

where $i \in \{1,2\}$ and

$$\begin{aligned}\langle 0|\Delta_i(0)|n,s,+\rangle &= \frac{1}{2}a\mathcal{A}_{\Delta}^{(n,+)}u_i^s(M_n^+,\vec{0}) && (2.128)\\ \langle 0|\Delta_i(0)|n,s,-\rangle &= \frac{1}{2}a\mathcal{A}_{\Delta}^{(n,-)}\gamma_5 u_i^s(M_n^-,\vec{0}), && (2.129)\end{aligned}$$

for spin-$\frac{3}{2}$ states where $u^s(p)$ and $u_i^s(p)$ are Dirac and Rarita-Schwinger [36] polarisation spinors respectively. The overall constant factors are purely for convenience here. Results for the backward propagating antiparticle states can be related to the above results by charge conjugation.

The Δ_i operators also have a non-zero overlap with spin-$\frac{1}{2}$ states. The contributions from these states can, however, be projected out using standard projection operators [37]. This has been done here by making use of the fact that the $C_{\Delta_4\overline{\Delta_4}}(t,\vec{p})$ correlator only contains contributions from the spin-$\frac{1}{2}$ states and is proportional to the spin-$\frac{1}{2}$ contribution to the other Delta correlators. In what follows I therefore use the following spin-$\frac{3}{2}$ projected Delta correlator

$$C_{\Delta\overline{\Delta}}(t) = \sum_i C_{\Delta_i\overline{\Delta_i}}(t) - \tfrac{1}{3}C_{\Delta_4\overline{\Delta_4}}(t) \tag{2.130}$$

The contributions to the correlators coming from distinct spin states can be summed over using

$$\sum_s u^s(\vec{0})\overline{u}^s(\vec{0}) = \tfrac{1}{2}(1+\gamma_4), \tag{2.131}$$

for Dirac spinors and the Rarita-Schwinger spin-sum [38] performed using

$$\sum_s u_i^s(\vec{0})\overline{u}_i^s(\vec{0}) = \tfrac{2}{3}\cdot\tfrac{1}{2}(1+\gamma_4). \tag{2.132}$$

Putting this all together gives the following result for a general baryon correlator

$$\begin{aligned} C_{\mathcal{B}\overline{\mathcal{B}}}(t) = \frac{1}{2}\sum_n \tfrac{1}{2}(1+\gamma_4)&\left(\frac{|\mathcal{A}_{\mathcal{B}}^{(n,+)}|^2}{2aM_n^+}e^{-M_n^+ t} + \frac{|\mathcal{A}_{\mathcal{B}}^{(n,-)}|^2}{2aM_n^-}e^{-M_n^-(T-t)}\right) \\ -\tfrac{1}{2}(1-\gamma_4)&\left(\frac{|\mathcal{A}_{\mathcal{B}}^{(n,-)}|^2}{2aM_n^-}e^{-M_n^- t} + \frac{|\mathcal{A}_{\mathcal{B}}^{(n,+)}|^2}{2aM_n^+}e^{-M_n^+(T-t)}\right) \end{aligned} \tag{2.133}$$

where $\mathcal{B} = N_1,\ N_2$ or Δ.

It is useful to project out the positive and negative parity contributions using the projection operators,

$$P_\pm = \tfrac{1}{2}(1\pm\gamma_4), \tag{2.134}$$

to give

$$C_{\mathcal{B}\overline{\mathcal{B}}}^{\pm}(t) = \mathrm{Tr}\left(P_\pm C_{\mathcal{B}\overline{\mathcal{B}}}(t)\right) = \pm\sum_n\left(\frac{|\mathcal{A}_{\mathcal{B}}^{(n,\pm)}|^2}{2aM_n^\pm}e^{-M_n^\pm t} + \frac{|\mathcal{A}_{\mathcal{B}}^{(n,\mp)}|^2}{2aM_n^\mp}e^{-M_n^\mp(T-t)}\right). \tag{2.135}$$

These parity projected baryon correlators have been used in this work to determine the masses of the corresponding baryonic states in a similar way to that for the mesonic correlators. One crucial difference, however, is that the forward and backward propagating exponentials are now governed by different mass factors and there is no time reflection symmetry like that for meson correlators. For baryon correlators there is, however, a corresponding result relating the positive and negative parity projections,

$$C_{\mathcal{B}\overline{\mathcal{B}}}^{+}(t) = -C_{\mathcal{B}\overline{\mathcal{B}}}^{-}(T-t). \tag{2.136}$$

To complete the analysis of baryon correlators I briefly describe how they are calculated in terms of quark propagators. Denoting the gamma matrices at source and sink by

$$\Gamma_{(\mathrm{snk})} = C\Gamma \quad \text{and} \quad \Gamma_{(\mathrm{src})} = \gamma_4 \Gamma^\dagger \gamma_4 C \tag{2.137}$$

gives the following result for the contribution to a general baryon correlator from a single gauge configuration

$$\begin{aligned}
C^{(i)}_{\mathcal{B}\overline{\mathcal{B}}}(t,\vec{p}) &= \epsilon_{abc}\epsilon_{def}\sum_{\vec{x}} e^{-i\vec{p}\cdot\vec{x}}\Big[\\
& G^{(q_3)}_{cf}(x,0;U^{(i)})\mathrm{Tr}(G^{(q_1)}_{ad}{}^T(x,0;U^{(i)})\Gamma_{(\mathrm{snk})}G^{(q_2)}_{be}(x,0;U^{(i)})\Gamma_{(\mathrm{src})}) \\
&- \delta_{q_1q_2}G^{(q_3)}_{cf}(x,0;U^{(i)})\mathrm{Tr}(G^{(q_1)}_{ae}{}^T(x,0;U^{(i)})\Gamma_{(\mathrm{snk})}G^{(q_1)}_{bd}(x,0;U^{(i)})\Gamma^T_{(\mathrm{src})}) \\
&- \delta_{q_2q_3}G^{(q_2)}_{ce}(x,0;U^{(i)})\Gamma_{(\mathrm{src})}G^{(q_1)}_{ad}{}^T(x,0;U^{(i)})\Gamma_{(\mathrm{snk})}G^{(q_2)}_{bf}(x,0;U^{(i)}) \\
&- \delta_{q_1q_3}G^{(q_1)}_{cd}(x,0;U^{(i)})\Gamma^T_{(\mathrm{src})}G^{(q_2)}_{be}{}^T(x,0;U^{(i)})\Gamma^T_{(\mathrm{snk})}G^{(q_1)}_{af}(x,0;U^{(i)}) \\
&+ \delta_{q_1q_2}\delta_{q_2q_3}\Big(G^{(q_1)}_{cd}(x,0;U^{(i)})\Gamma^T_{(\mathrm{src})}G^{(q_1)}_{ae}{}^T(x,0;U^{(i)})\Gamma_{(\mathrm{snk})}G^{(q_1)}_{bf}(x,0;U^{(i)}) \\
&+ G^{(q_1)}_{ce}(x,0;U^{(i)})\Gamma_{(\mathrm{src})}G^{(q_1)}_{bd}{}^T(x,0;U^{(i)})\Gamma^T_{(\mathrm{snk})}G^{(q_1)}_{af}(x,0;U^{(i)})\Big)\Big].
\end{aligned} \tag{2.138}$$

Spinor indices have been kept implicit here and the traces are over these indices only. The baryon correlator is then estimated, as in the meson case, by averaging over all such contributions.

2.4.3 Fuzzed sources and sinks

So far I have only discussed the simplest case of local source and sink operators for mesons and baryons. There is, however, no reason for the interpolating operators to be local and spatially extended, or smeared, operators actually make more physical sense given that mesons and baryons are extended objects.

In this thesis the gauge invariant smearing technique of fuzzing [39] has been used to create extended sources and sinks. For mesons the fuzzed operator is given by

$$\mathcal{M}_{\mathrm{F}}^{(q_1 q_2)}(t,\vec{x}) = \overline{\psi}^{(q_1)}(t,\vec{x})\Gamma\psi_{\mathrm{F}}^{(q_2)}(t,\vec{x}) \tag{2.139}$$

where

$$\psi_{\mathrm{F}}^{(q_2)}(t,\vec{x}) = \sum_{\vec{y}} F(t,\vec{x},\vec{y})\psi^{(q_2)}(t,\vec{y}) \tag{2.140}$$

and the fuzzing function,

$$F(t,\vec{x},\vec{y}) = \frac{1}{6}\sum_{\vec{\mu}}\left[\delta_{\vec{y},\vec{x}+R\vec{\mu}}\prod_{i=0}^{R-1}U_{\mu}^{\dagger}(t,\vec{x}+i\vec{\mu}) + \delta_{\vec{y},\vec{x}-R\vec{\mu}}\prod_{i=1}^{R}U_{\mu}(t,\vec{x}-i\vec{\mu})\right]. \tag{2.141}$$

The vector, $\vec{\mu}$, is used here to denote a vector of length a in one of the three positive spatial directions and the average over both positive and negative spatial directions is present to ensure that the fuzzed operator retains the same J^{PC} assignment as the corresponding local operator.

The chain of link variables in the operator acts like a colour flux tube joining the quark fields which are kept a fixed integer number of lattice spacings, R, apart. Such an operator tends to have a small overlap with the states we wish to study but this can be enhanced by fattening the spatially oriented link variables [40]. This is done by mixing each link with its neighbours in a gauge invariant way as defined by the following iterative procedure

$$U_{\mu}^{(n+1)}(x) = P_{SU(3)}\left[c\,U_{\mu}^{(n)}(x) + \sum_{\hat{\nu}\in S}U_{\nu}^{(n)\dagger}(x+\hat{\mu})U_{\mu}^{(n)}(x+\hat{\nu})U_{\nu}^{(n)}(x)\right] \tag{2.142}$$

where the set, S, consists of the four spatial directions perpendicular to that of the link being fattened. It is necessary to project back into the $SU(3)$ group manifold after summing which can be done using a suitable projection operator, $P_{SU(3)}$.

The parameter, c, and the number of iterations can be tuned to maximise the state overlap. A value of $c = 2$ and $n = 5$ iterations were used here as found to be optimal by Lacock *et al.* [39]. The fuzzing radius, R, can be tuned to minimise contamination of the correlators by states of higher energy. This is to be offset, however, with making the correlators noisier as was found in a study with C. Maynard and J. Gill of the University of Edinburgh early in my Ph.D. work. An intermediate value of $R = 5$ was therefore taken.

All of the above also follows for baryon interpolating operators except that there are more ways that the fuzzing procedure can be implemented since there are now three quark fields. A double fuzzing procedure has been used here and the fuzzed baryon operator defined by

$$\mathcal{B}_{\mathrm{F}}^{(q_1 q_2 q_3)}(t,\vec{x}) = \epsilon_{abc}\,({\psi_a^{(q_1)}}^T(t,\vec{x})\,C\Gamma\,\psi_{F,b}^{(q_2)}(t,\vec{x}))\,\psi_{\mathrm{F},c}^{(q_3)}(t,\vec{x}) \qquad (2.143)$$

The fuzzed operators can be used at source, sink or both making four correlators for every choice of mesonic or baryonic operator at source and sink. The standard nomenclature used here is to denote a correlator fuzzed at source and local at sink as an FL correlator.

The only difference that including fuzzed operators makes to the functional form of the correlators is in the amplitude factors, $\mathcal{A}_{\mathcal{O}}^{(n)}$. The fuzzed correlator is given by replacing the source or sink amplitude in Equations (2.111) and (2.135) by its fuzzed counterpart which I denote by $\mathcal{A}_{\mathcal{O}_{\mathrm{F}}}^{(n)}$.

Finally it is worth mentioning how the use of fuzzed operators changes the form of a correlator as given in terms of quark propagators. This can be seen most simply by introducing quark propagators fuzzed at source,

$$\begin{aligned} G^{\mathrm{FL}}(x_4,\vec{x};y_4,\vec{y}) &= \frac{1}{\det K}\int \mathcal{D}\overline{\psi}\mathcal{D}\psi\ \psi(x_4,\vec{x})\overline{\psi}_{\mathrm{F}}(y_4,\vec{y})\ e^{-S_{\mathrm{F}}[\overline{\psi},\psi,U]} \\ &= \sum_{\vec{z}} G(x_4,\vec{x};y_4,\vec{z})F^{\dagger}(y_4,\vec{y},\vec{z}), \end{aligned} \qquad (2.144)$$

sink,

$$\begin{aligned} G^{\mathrm{LF}}(x_4,\vec{x};y_4,\vec{y}) &= \frac{1}{\det K}\int \mathcal{D}\overline{\psi}\mathcal{D}\psi\ \psi_{\mathrm{F}}(x_4,\vec{x})\overline{\psi}(y_4,\vec{y})\ e^{-S_{\mathrm{F}}[\overline{\psi},\psi,U]} \\ &= \sum_{\vec{z}} F(x_4,\vec{x},\vec{z})G(x_4,\vec{z};y_4,\vec{y}), \end{aligned} \tag{2.145}$$

and both source and sink,

$$\begin{aligned} G^{\mathrm{FF}}(x_4,\vec{x};y_4,\vec{y}) &= \frac{1}{\det K}\int \mathcal{D}\overline{\psi}\mathcal{D}\psi\ \psi_{\mathrm{F}}(x_4,\vec{x})\overline{\psi}_{\mathrm{F}}(y_4,\vec{y})\ e^{-S_{\mathrm{F}}[\overline{\psi},\psi,U]} \\ &= \sum_{\vec{z}} F(x_4,\vec{x},\vec{z})G^{\mathrm{FL}}(x_4,\vec{z};y_4,\vec{y}). \end{aligned} \tag{2.146}$$

The fuzzed propagators can all be derived from the local propagator using the above equations. For the source fuzzed propagator, however, this would mean calculating $G(x_4,\vec{x};y_4,\vec{z})$ for all relevant $\vec{z}$. A far more computationally efficient way of calculating $G^{\mathrm{FL}}(x_4,\vec{x},y_4,\vec{y})$ is to invert the fermion matrix on a fuzzed source by solving the following matrix equation numerically

$$\sum_{x_4,\vec{x}} K(z_4,\vec{z};x_4,\vec{x})G^{\mathrm{FL}}(x_4,\vec{x};y_4,\vec{y}) = \delta(z_4,y_4)\,F^{\dagger}(y_4,\vec{y},\vec{z}). \tag{2.147}$$

Once this has been done the LF and FF propagators can be easily calculated using Equations (2.145) and (2.146).

Fuzzed meson and baryon correlators are then given by replacing some of the standard propagators in Equations (2.120) and (2.138) by one or more of the fuzzed propagators. For example a source fuzzed meson correlator is calculated by contracting an FL propagator and LL propagator together with the appropriate gamma matrices. Sink fuzzed meson correlators are given by contracting LF and LL propagators and source and sink fuzzed correlators given by contracting FF and LL propagators. Similar considerations apply for the baryon correlators.

2.4.4 Meson decay constants

So far I have described how correlators for mesons and baryons can be parameterised in terms of state masses and associated amplitude factors. It is therefore clear that correlators can be used to probe the spectrum of hadron masses. What is not so obvious is that the amplitude factors for some meson correlators are related to matrix elements describing the weak decay of mesonic states. These matrix elements can, in turn, be completely parameterised through what are known as meson decay constants. I define these decay constants in what follows and discuss how they can be measured in lattice simulations.

Pseudoscalar decay constants

The pion decay constant, f_π, can be defined in the continuum Euclidean theory through the following relation,

$$\langle 0|(A_{\mathrm{R}})_4(0)|\pi\rangle = M_\pi f_\pi, \tag{2.148}$$

where $|\pi\rangle$ describes a zero-momentum pion and all quantities are taken to be real and positive. Similar relations exist for other pseudoscalar mesons such as the kaon. The appropriate weak matrix elements, such as in Equation (2.148), can be determined on the lattice by studying the relevant meson correlator. This can be made explicit by defining the bare decay constant on the lattice, f_{PS}, through the following equation,

$$\frac{\langle 0|(A_{\mathrm{I}})_4(0)|\mathrm{PS}\rangle}{a} = aM_{\mathrm{PS}}\, af_{\mathrm{PS}}, \tag{2.149}$$

where $|\mathrm{PS}\rangle$ denotes the lowest mass pseudoscalar state at zero-momentum. Expanding out the improved operator as in Equation (2.46) and making the symmetric choice of lattice derivative i.e.

$$\partial_\mu f(x) = \Delta_\mu^{(+-)} f(x) + O(a^3) \equiv \frac{1}{2a}\left(f(x+\hat{\mu}) - f(x-\hat{\mu})\right) + O(a^3), \tag{2.150}$$

then allows the decay constant to be written as

$$f_{\mathrm{PS}} = f_{\mathrm{PS}}^{(0)} + c_A\, f_{\mathrm{PS}}^{(1)} \tag{2.151}$$

where the components are related to amplitude factors calculable from meson correlators by

$$af_{\mathrm{PS}}^{(0)} = \frac{\mathcal{A}_{A_4}^{\mathrm{PS}}}{aM_{\mathrm{PS}}}, \qquad af_{\mathrm{PS}}^{(1)} = \sinh aM_{\mathrm{PS}} \frac{\mathcal{A}_P^{\mathrm{PS}}}{aM_{\mathrm{PS}}}. \tag{2.152}$$

Alternatively an improved lattice derivative can be used e.g.

$$\partial_\mu f(x) = \tilde{\Delta}_\mu^{(+-)} f(x) \equiv \left[1 - \frac{a^2}{6}\Delta_\mu^+ \Delta_\mu^-\right] \Delta_\mu^{(+-)} f(x) + O(a^5) \tag{2.153}$$

where the forward and backward lattice derivatives are defined by

$$\Delta_\mu^+ \equiv \frac{1}{a}\left(f(x+\hat{\mu}) - f(x)\right), \qquad \Delta_\mu^- \equiv \frac{1}{a}\left(f(x) - f(x-\hat{\mu})\right). \tag{2.154}$$

The resultant expression for the decay constant improvement term is then given by,

$$af_{\mathrm{PS,imp}}^{(1)} = \frac{\mathcal{A}_P^{\mathrm{PS}}}{aM_{\mathrm{PS}}} \left(\frac{4}{3}\sinh aM_{\mathrm{PS}} - \frac{1}{6}\sinh 2aM_{\mathrm{PS}}\right), \tag{2.155}$$

All of the above parameters can be determined from a single simultaneous fit as described in Section 3.6.1, a method that has been used in this thesis.

Vector decay constants

The decay constant analysis for vector mesons proceeds in a similar manner to that for pseudoscalar mesons. Here I use the following dimensionless definition for the rho decay constant

$$\langle 0|(V_{\mathrm{R}})_i(0)|\rho,\epsilon^r\rangle = \frac{M_\rho^2}{f_\rho}\epsilon_i^r, \tag{2.156}$$

with similar expressions for other vector mesons such as the K^* and ϕ. The corresponding lattice expression for the lowest vector meson state, $|\mathrm{V}\rangle$, is given by

$$\frac{\langle 0|(V_{\mathrm{I}})_i(0)|\mathrm{V},\epsilon^r\rangle}{a} = \frac{(aM_{\mathrm{V}})^2}{f_{\mathrm{V}}}\epsilon_i^r. \tag{2.157}$$

Expanding out the improved operator using Equation (2.47) allows the decay constant to be written as

$$\frac{1}{f_{\mathrm{V}}} = f_{\mathrm{V}}^{(0)} + c_V\, f_{\mathrm{V}}^{(1)} \tag{2.158}$$

where

$$f_{\mathrm{V}}^{(0)} = \frac{\mathcal{A}_{V_i}^{\mathrm{V}}}{(aM_{\mathrm{V}})^2}, \qquad f_{\mathrm{V}}^{(1)} = \sinh aM_{\mathrm{V}}\frac{\mathcal{A}_{T_{i4}}^{\mathrm{V}}}{(aM_{\mathrm{V}})^2} \tag{2.159}$$

and the amplitude factors do not depend on the index, i. Alternatively using the improved derivative gives,

$$f_{\mathrm{V,imp}}^{(1)} = \frac{\mathcal{A}_{T_{i4}}^{\mathrm{V}}}{(aM_{\mathrm{V}})^2}\left(\frac{4}{3}\sinh aM_{\mathrm{V}} - \frac{1}{6}\sinh 2aM_{\mathrm{V}}\right). \tag{2.160}$$

All of these parameters can again be determined from a single simultaneous fit.

Axial vector decay constant

The final meson decay constant studied in this thesis is for the axial vector meson, a_1. I follow the same convention the vector meson case and define the decay constant by

$$\langle 0|(A_{\rm R})_i(0)|a_1, \epsilon^r\rangle = \frac{M_{a_1}^2}{f_{a_1}}\,\epsilon_i^r. \qquad (2.161)$$

The corresponding lattice expression for the lowest axial vector state, $|{\rm A}\rangle$, is given by

$$\frac{\langle 0|(A_{\rm I})_i(0)|{\rm A}, \epsilon^r\rangle}{a} = \frac{(aM_{\rm A})^2}{f_{\rm A}}\epsilon_i^r. \qquad (2.162)$$

and the decay constant therefore evaluated through

$$\frac{1}{f_{\rm A}} = f_{\rm A}^{(0)} = \frac{\mathcal{A}_{A_i}^{\rm A}}{(aM_{\rm A})^2}. \qquad (2.163)$$

where the amplitude factor is again constant over i. There is no improvement term in this expression because the corresponding matrix element vanishes at zero momentum.

Chapter 3

Data analysis

Data analysis is an essential part of the work of lattice QCD that allows physical predictions to be made from the numerical simulations. In this chapter I summarise all the statistical and numerical techniques needed to analyse the data from lattice simulations. In particular I describe the technique of least squares estimation (or χ^2 minimisation) that has been used to estimate fit parameters such as hadron masses and amplitude factors from lattice simulation data and also to extrapolate these results to the physical limits. I also give an account of the bootstrap techniques that have been used here to estimate errors on the fit parameters.

The material of this chapter can be found in [41, 42, 43] where it is discussed in greater detail. I have referred to [41] for general statistics and a theoretical discussion of least squares estimation, reference [42] for its discussion of bootstrap and jacknife techniques and [43] for the numerical techniques and algorithms necessary to perform the data analysis.

3.1 Lattice data

In lattice simulations we generally measure n-point correlation functions from which we can extract physical observables. As discussed earlier these correlation functions have functional integral representations which can be approximated by finite sums using Monte-Carlo techniques. In statistical parlance this is just the estimation of an expectation value given a finite sample of points from a probability distribution function.

In what follows I concentrate on the case of meson and baryon correlators but this can be easily generalised to any data modelling situation. As before I denote correlator data by $C^{(k)}(t_i)$, where k runs over statistically independent gauge configurations numbered from 1 to N_{C} and t_i denotes the lattice times to be used in the fitting procedure as indexed by i which runs from 1 to N_{D}. Given this data the expectation value of our operator can be estimated by the sample mean, $\bar{C}(t_i)$, where

$$\bar{C}(t_i) = \frac{1}{N_{\mathrm{C}}} \sum_{k=1}^{N_{\mathrm{C}}} C^{(k)}(t_i). \tag{3.1}$$

These mean values are distributed with a covariance matrix that can be estimated by $(Cov)_{ij}$, where

$$(Cov)_{ij} = \frac{1}{N_{\mathrm{C}}(N_{\mathrm{C}}-1)} \sum_{k=1}^{N_{\mathrm{C}}} (C^{(k)}(t_i) - \bar{C}(t_i))(C^{(k)}(t_j) - \bar{C}(t_j)). \tag{3.2}$$

The diagonal elements of $(Cov)_{ij}$ can be taken as estimates of the variances on the sample means and are related to the standard errors on the means, σ_i, by

$$\sigma_i = \sqrt{(Cov)_{ii}} \tag{3.3}$$

From these quantities we can define the correlation matrix, $(Cor)_{ij}$, by

$$(Cor)_{ij} = \frac{(Cov)_{ij}}{\sigma_i \sigma_j}. \tag{3.4}$$

The elements of $(Cor)_{ij}$ range from $+1$ for totally correlated data to -1 for totally anti-correlated data with $(Cor)_{ij} = 0$ being a necessary condition for the data at t_i and t_j to be statistically independent.

As an example I show in Graph 3.1 the correlations between $\bar{C}(t_1)$ and other times for a pseudoscalar two-point correlator.

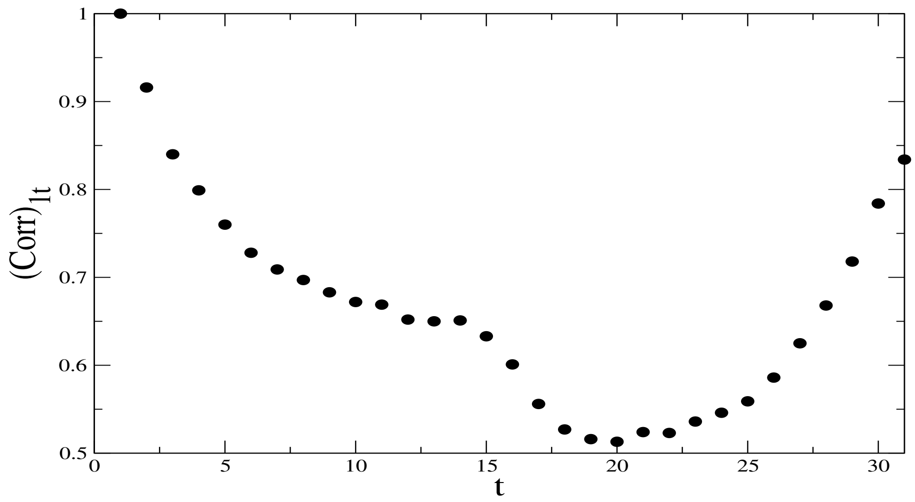

Figure 3.1: Correlation coefficients for a pseudoscalar correlator from the $\beta = 5.2$, $\kappa_{\mathrm{sea}} = 0.1358$ dataset with $\kappa_{\mathrm{val}} = \kappa_{\mathrm{sea}}$.

It can be seen that there is a high level of correlation between all timeslices in this two-point function. This is true generally of all two-point functions with correlations being especially high between adjacent timeslices in one correlator and between the same timeslices of different two-point functions.

3.2 Least squares estimation

With the basic statistical quantities specified our attention can turn to the problem of data modelling. The starting point in this process is to choose a model function, $m(t_i; a)$, which depends on a set of N_{P} parameters, a. This function can be an empirical ansatz or can be theoretically motivated as is the case for the correlators being studied here.

The problem is how to find the parameter values that provide the best fit between model and data. A standard method for doing this is the method of least squares estimation. The procedure is to minimise the following function of the model parameters

$$\chi^2(a) = \sum_{i,j=1}^{N_\mathrm{D}} (y(t_i) - m(t_i;a))(Cov)^{-1}_{ij}(y(t_j) - m(t_j;a)) \tag{3.5}$$

which is called the chi-squared function and depends on N_D datapoints. For two-point correlators we would take $y(t_i) = \bar{C}(t_i)$. The function χ^2 is intuitively a measure of how closely the model function fits the data for particular values of the parameters. The parameter values that minimise this function are called the least squares estimates of the parameters given the data and will be denoted by a^{min} here.

The presence of $(Cov)^{-1}_{ij}$ in χ^2 can be understood intuitively as making χ^2 more sensitive to the data with the smallest associated errors. It can also be justified from the fact that if the values of $y(t_i)$ come from a normal distribution then minimising χ^2 in its present form corresponds to maximising the likelihood of getting these $y(t_i)$ values given the parameters. It is important to realise that this is not the same thing as maximising the probability of getting the parameters given the data and there exist more sophisticated techniques using Bayes theorem to take this discrepancy into account.

3.3 Estimating fit parameter errors

In this work two methods have been used to estimate errors on the minimised parameters. The first method uses the technique of small error propagation and is used only in initial analysis. The second more general method employs bootstrap techniques to estimate error intervals for the parameters. I will discuss each in turn.

3.3.1 Small errors analysis

The starting point for the small errors analysis is to consider the minimised parameters as a function of the input data, $y_i = y(t_i)$. The parameter covariance matrix, V_P, can then be related to the data covariance matrix through

$$(V_{\mathrm{P}})_{kl} = \sum_{i,j=1}^{N_{\mathrm{D}}} \frac{\partial a_k^{min}}{\partial y_i} \, (Cov)_{ij} \, \frac{\partial a_l^{min}}{\partial y_j}. \tag{3.6}$$

This expression can be evaluated and a detailed analysis yields

$$(V_{\mathrm{P}})_{kl} = \alpha_{kl}^{-1} + \sum_{i,j=1}^{N_{\mathrm{D}}} \sum_{p,q=1}^{N_{\mathrm{P}}} \alpha_{kp}^{-1} \alpha_{lq}^{-1} (y_i - m(t_i))(Cov)_{ij}^{-1} \frac{\partial^2 m(t_j)}{\partial a_p \partial a_q} \tag{3.7}$$

where

$$\begin{aligned} \alpha_{kl} &\equiv \frac{1}{2} \frac{\partial^2 \chi^2}{\partial a_k \partial a_l} \qquad (3.8) \\ &= \sum_{i,j=1}^{N_{\mathrm{D}}} \frac{\partial m(t_i)}{\partial a_k} \, (Cov)_{i,j}^{-1} \, \frac{\partial m(t_j)}{\partial a_k} - (y_i - m(t_i))(Cov)_{i,j}^{-1} \, \frac{\partial^2 m(t_j)}{\partial a_k \partial a_l} \end{aligned}$$

and all relevant quantities are evaluated at $a = a^{min}$. If the model fits the data well then taking $(V_{\mathrm{P}})_{kl} = \alpha_{kl}^{-1}(a^{min})$ is a good approximation and has been used in this work. The square root of the diagonal elements of V_{P} provide an estimate of the standard error on the parameters.

3.3.2 Bootstrap errors

The second and more general technique for producing error estimates for the parameters uses bootstrap techniques which I will discuss in the context of data from lattice simulations. The procedure is to construct N_{B} bootstrap data subensembles from the correlator data where each set is generated by choosing N_{C} gauge configurations randomly and with repetition from the total set. The original set is therefore a valid if unlikely choice for a subensemble. A sample mean and covariance matrix can be calculated for each subensemble and the χ^2 minimisation repeated for each set. In practice however the covariance matrix calculated for the original dataset has been used in these fits. Overall the bootstrap method yields a distribution of new minimised parameters $a^{min}(b)$ where b runs over distinct subensembles.

The bootstrap estimate of the parameter covariance matrix is then given by

$$(V_{\mathrm{P}})_{kl} = \frac{1}{N_{\mathrm{B}}-1}\sum_{b=1}^{N_{\mathrm{B}}}(a_k^{min}(b) - a_k^{min}(\cdot))(a_l^{min}(b) - a_l^{min}(\cdot)) \tag{3.9}$$

where

$$a_k^{min}(\cdot) = \frac{1}{N_{\mathrm{B}}}\sum_{b=1}^{N_{\mathrm{B}}} a_k^{min}(b). \tag{3.10}$$

Alternatively confidence intervals can be defined that contain some set proportion of the bootstrap values for the parameters. The extremes of these intervals need not be symmetrical with respect to a^{min} resulting in asymmetrical error values. This is useful since there is no assumption here of any symmetry in the underlying distribution and because large asymmetries can be indicative of some failure in the procedure used to minimise χ^2. Throughout this work I quote results for fit parameters using 68% confidence intervals calculated with $N_{\mathrm{B}} = 500$.

3.4 Goodness of fit

So far I have mentioned how to find estimates of the parameters given the data and how to estimate errors on these parameters. None of this, however, gives an indication of how well the model fits the data. To provide some measure of the goodness of fit it is necessary to assume that the data is distributed about the true model in some particular way. It is also necessary to assume that the data is distributed about the model evaluated with minimised parameters in a similar way.

If a normal distribution is assumed then the statistic, χ^2, can be shown to be distributed with distribution function

$$f(\chi^2, \nu) = \frac{1}{2^{\nu/2}\Gamma(\nu/2)}(\chi^2)^{[\nu/2-1]}exp(-\frac{1}{2}\chi^2) \tag{3.11}$$

where ν is the number of degrees of freedom which here is $N_{\rm D} - N_{\rm P}$ and Γ is the gamma function.

Integrating this probability distribution up to the value of χ^2 obtained from the fit, $\chi^2_{\rm min}$, gives the probability of obtaining a value for χ^2 in the range $[0, \chi^2_{\rm min}]$. This integral can be written in terms of the incomplete gamma function,

$$P(x,a) = \frac{1}{\Gamma(a)} \int_0^x t^{a-1}\, e^{-t}\, dt \tag{3.12}$$

by

$$\int_0^{\chi^2_{\rm min}} f(\chi^2,\nu)\; d\chi^2 = P(\chi^2_{\rm min}/2, \nu/2). \tag{3.13}$$

The value of $P(\chi^2_{\rm min}/2, \nu/2)$, which runs from 0 to 1, can be used as a measure of the goodness of fit with small values indicating a good fit (since statistically, larger values of χ^2 would be expected) and values near 1 indicating a bad fit.

In this work the complement of P, called Q, has been used as an alternative but equally valid measure of the goodness of fit

$$Q(\chi^2_{\rm min}/2, \nu/2) = \int_{\chi^2_{\rm min}}^{\infty} f(\chi^2,\nu)\; d\chi^2 = 1 - P(\chi^2_{\rm min}/2, \nu/2). \tag{3.14}$$

Another rough estimate for goodness of fit is how close $\chi^2_{\rm min}$ comes to the mean value of χ^2. The mean turns out to be ν so for a good fit we are looking for a value of $\chi^2_{\rm min}/\nu \leq 1$. This ratio is commonly called the reduced chi-squared. Large values indicate a poor fit whereas small values can indicate that the errors in the data have been overestimated.

3.5 Numerical techniques

Up to this point I have described how to model lattice data in principle. There is, however, a practical side to this process that relies heavily on numerical techniques.

3.5.1 Marquardt-Levenberg algorithm

In general the model function, $m(t_i; a)$, used in least squares estimation is non-linear in its parameters making an exact solution to the minimisation problem difficult or impossible to find. For this reason the Marquardt-Levenberg algorithm has been used in this work. Starting from some initial values of the parameters this algorithm iteratively steps towards the minimum of χ^2. The algorithm combines the inverse hessian method and the method of steepest descent to work both near and far from the minimum. For this process to work, however, it is important to choose the initial parameter values with care. Bad choices can lead the algorithm to local minima away from the global minimum or even to get stuck in flat areas of parameter space.

Each step of the Marquardt-Levenberg algorithm comes from solving the following matrix equation for the parameter step, δa,

$$\sum_{l=1}^{N_{\mathrm{P}}} \alpha'_{kl}\, \delta a_l = \beta_k \tag{3.15}$$

where α' is related to the matrix α introduced earlier by

$$\alpha' = \alpha + \lambda\ \mathbb{I}_{N_{\mathrm{P}}}. \tag{3.16}$$

and

$$\beta_k \equiv -\frac{1}{2}\frac{\partial \chi^2}{\partial a_k} = \sum_{i,j}^{N_{\mathrm{D}}} \left(y_i - m(t_i; a)\right)\ (Cov)^{-1}_{i,j}\ \frac{\partial m(t_j; a)}{\partial a_k} \tag{3.17}$$

In the equations above the matrix, $\mathbb{I}_{N_{\mathrm{P}}}$, is the unit $N_{\mathrm{P}} \times N_{\mathrm{P}}$ matrix, λ is a tunable parameter of the algorithm and both α' and β are evaluated using the current parameter values.

When α' is non-singular this system of equations can be solved by simply inverting α'. In the case where α' is singular to machine precision i.e. it has some very small eigenvalues the solution is not well defined and can be dominated by very large jumps in the eigen-directions associated with the small eigenvalues. These problems have been remedied here by using the technique of singular value decomposition (SVD) to find a pseudo-inverse for α' that is compatible with χ^2 minimisation.

The first step in the SVD procedure is to write the matrix in the form

$$\alpha' = U\ diag(w_1, \cdots, w_{N_\mathrm{P}})\ V^T \tag{3.18}$$

where U and V are both orthogonal matrices. This process even works if the matrix is singular. The numerical SVD inverse is then defined by

$$\alpha'^{-1} = V\ diag(e_1, \cdots, e_{N_\mathrm{P}})\ U^T \tag{3.19}$$

where

$$e_i = \begin{cases} 1/w_i & \text{if } |w_i| \geq tol \\ 0 & \text{otherwise} \end{cases} \tag{3.20}$$

and *tol* is some numerical tolerance level. Using this inverse to solve the matrix equation gives the best possible parameter step compatible with χ^2 minimisation and stops the algorithm taking large jumps in directions associated with small values of w_i by effectively freezing these directions out.

3.5.2 Initial parameter guesses

In the previous subsection I mentioned how the Marquardt-Levenberg algorithm needs some initial parameter guesses and how in some circumstances it is important to get these guesses close to the global χ^2 minimum.

One general way to do this is to use the data to motivate the guess. For example if the model function is a straight line then any two (t, y) data points can be used to guess the slope and intercept. The situation is similar for an exponential model function, $m(t) = a_1 e^{-a_2 t}$, which can be cast into linear form by taking logarithms.

More importantly, however, is the case where we are fitting correlator data for mesons and baryons to the forms in Equations (2.111) and (2.135) with the sums truncated to a finite number of contributions. In this work these fits have been found to be particularly sensitive to the initial parameter guesses and in particular to the initial values used for the mass parameters. One technique that helps at least in guessing the lowest state mass is the use of an effective mass plot. The effective mass can be defined either through

$$M_{\text{eff}}(t) = \cosh^{-1}\left(\frac{\bar{C}(t+1) + \bar{C}(t-1)}{2\bar{C}(t)}\right) \tag{3.21}$$

or by

$$M_{\text{eff}}(t) = \ln \frac{\bar{C}(t)}{\bar{C}(t+1)} \tag{3.22}$$

as appropriate for the functional form of the correlator being studied and should be roughly equal in value to the lowest state mass when the correlator is dominated by the contribution from that state. As an example I plot the effective mass for a pseudoscalar meson correlator in Figure 3.2 using Equation (3.21).

The characteristic plateau between timeslices 10 and 22 indicates that the contribution from the lowest mass state dominates the correlator there. Values of the effective mass from the plateau therefore make good initial guesses for the lowest state mass. The associated amplitude factor can also be estimated from data in this region, again assuming that the lowest state dominates.

Determining guesses for the masses and amplitudes from higher states becomes increasingly more difficult. The first excited state parameters can be reasonably estimated by subtracting the lowest state contribution from the correlator using

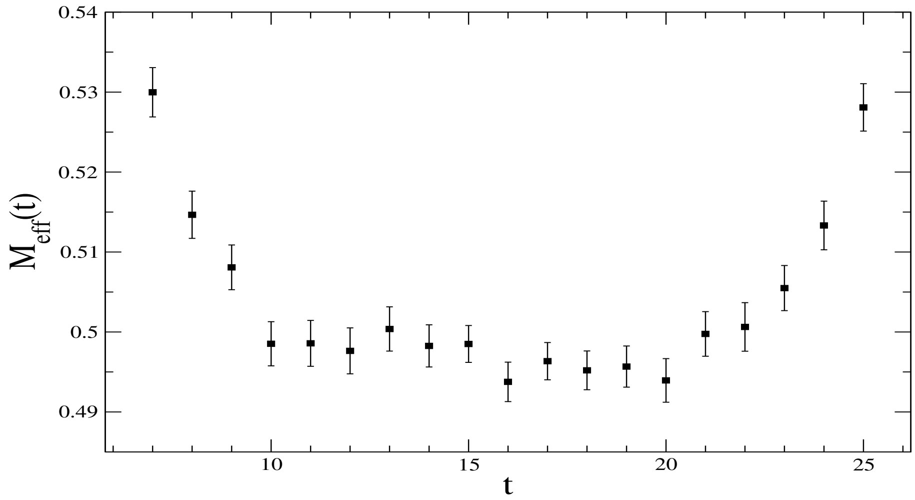

Figure 3.2: Effective mass plot for a pseudoscalar meson correlator from the $\beta = 5.93$ quenched dataset with degenerate $\kappa_{\rm val} = 0.1327$.

the guess parameters for that state and then using the effective mass technique again with data from earlier times. This procedure can, however, run into difficulties and generally fails if applied to even higher states. The problem stems from the need to guess the parameters reasonably accurately in order for the fit to be successful. Such accuracy can be hard to attain with this technique because inaccuracies in lower state guesses become compounded in the higher state guesses. For this reason I have used the following shotgun technique which I have found to be stable in all circumstances.

The basic idea is to perform a number of fits starting from a scatter of parameter guesses at values around those found with the strategy described above. This has the great advantage that it can get around peculiarities of the χ^2 landscape and almost assures that the correct χ^2 minimum will be found by at least one fit. In practice I have found that many fits tend to find the same minimum and have used this as an indicator that the procedure has worked well.

Now at first sight it might seem that this fitting procedure would be computationally prohibitive with costs growing like the number of scatter points per parameter raised to the power $N_{\rm P}$. I have found, however, that it is only necessary to perform the shotgun procedure on the highest state mass (or masses in the baryonic case) with amplitude factors recalculated using the standard guess technique in order to achieve stable results. This is especially so if the lower state parameters have been determined in a previous fit. In this work I have used the shotgun technique for one, two and even three state fits successfully. The three state fits were found to yield no better determination of the lowest state parameters than the two state fits and have not been pursued in this thesis.

3.5.3 Inverting the covariance matrix

Another place where numerical techniques are important is in the evaluation of the χ^2 function which requires a knowledge of the covariance matrix and its inverse. This can be problematic especially when there are insufficient data to accurately determine the covariance matrix, as is common in lattice simulations. The lack of data can lead to the appearance of unphysically small eigenvalues in the covariance matrix which dominate the inverse and hence bias the minimisation procedure.

One simple technique that can help when fitting correlators is data folding. For mesons the time reflection symmetry of the correlator can be used to our advantage by defining the folded correlator,

$$C^{(\text{fold})}_{\mathcal{M}_1\mathcal{M}_2^\dagger}(t) = \frac{1}{2}\left(C_{\mathcal{M}_1\mathcal{M}_2^\dagger}(t) + \eta_{12} C_{\mathcal{M}_1\mathcal{M}_2^\dagger}(T-t)\right). \tag{3.23}$$

Folding the data in this way allows fits to be performed only using data points up to the central lattice time, $T/2$, whilst still including all the correlator measurements in the fit. This has the advantage of improving the statistics on the early measurements and significantly reducing the size of the correlation matrix, both of which help in its evaluation from a finite set of data.

A similar folding procedure exists for baryons and the folded correlators are defined by

$$C^{\pm(\text{fold})}_{\mathcal{B}\overline{\mathcal{B}}}(t) = \frac{1}{2}\left(C^{\pm}_{\mathcal{B}\overline{\mathcal{B}}}(t) - C^{\mp}_{\mathcal{B}\overline{\mathcal{B}}}(T-t)\right). \tag{3.24}$$

This helps to improve the statistics in the measurements but the asymmetry of the correlator prevents a natural reduction of the fit window as was done for the meson correlators. The fit window can be reduced, however, by only fitting the forward propagating exponentials to the data in the first half of the lattice.

Although the folding techniques do help in the determination of the covariance matrix the problem of insufficient data can still arise, especially when fitting multiple correlators simultaneously. In this work the eigenvalue smoothing technique of Michael and McKerrell [44] has been used to model the correlation matrix when there is insufficient data.

The first step is to calculate the correlation matrix as in Equation (3.4) and then to perform the SVD technique on it. The basis of the eigenvalue smoothing technique is then to average over a number of the smallest eigenvalues and then replace all eigenvalues by the larger of themselves and this average. The resulting eigenvalues are then rescaled to preserve the value of the trace of the matrix. The number of eigenvalues averaged over should depend on the number of independent measurements of the data i.e N_{C}. Following a suggestion in [44] the smallest $N_{\mathrm{D}} - N_{\mathrm{E}}$ eigenvalues, where $N_{\mathrm{E}} \simeq \sqrt{N_{\mathrm{C}}}$, have been averaged over in this work. Once this procedure has been done the covarianace matrix and its inverse can be calculated.

3.6 Fitting alternative datatypes

The work of this thesis has involved data modelling situations more complex than that of fitting a single correlator. These situations include fitting multiple correlators, fitting functions of correlators and fitting data in the form of bootstrap sets to some particular model and I will discuss each in turn.

3.6.1 Simultaneous fits

The basis of the simultaneous fitting procedure is that certain correlators can be parameterised by the same mass and sometimes the same amplitude factors. It therefore makes sense to use all the data available in the determination of the shared parameters by fitting the correlators simultaneously. In practice these fits have been performed by setting out the data from each correlator end to end. The model function and its derivatives need to be linearised in a corresponding way. This format makes it particularly easy to implement and simplifies the inclusion of correlations between different correlators in the fits.

In this thesis simultaneous fits have been performed to the LL, FL and FF correlators for each combination of source and sink operator. The LF correlators could also have been included but were found to be too noisy to help constrain the fit parameters. What makes these fits particularly appealing is that all the correlators can be parameterised by only one mass, M_n, and two amplitude factors, $\mathcal{A}_{\mathcal{O}}^{(n)}$ and $\mathcal{A}_{\mathcal{O}_{\mathrm{F}}}^{(n)}$ for each n included in the fit. For baryon fits where the backward propagating states are included the number of parameters doubles but the factorisation remains. The results of such fits are well constrained and the statistical errors on the parameters reduced in comparison to single correlator fits. The extra data also stabilised the progress of the fitting algorithm especially when more than one state contribution is included in the fit.

Similar factorised fits have also been performed to pseudoscalar meson correlators where source and sink operators can be either $P(x)$ or $A_4(x)$. Including local and fuzzed operators gives a maximum of 12 correlators that can used in these simultaneous fits whilst only including two more amplitude factors per state contribution over the LL,FL,FF fits. The parameters in such fits are therefore very well constrained by the data. These considerations also apply to vector meson correlators where both $V_i(x)$ and $T_{i4}(x)$ are relevant operators.

3.6.2 Fitting functions of correlators

It can sometimes be shown from theoretical considerations that certain functions of correlators have a particularly simple functional form. The PCAC quark mass of Equation (2.56) is one example and is given by the ratio of two two-point functions. In these situations modelling functions of correlators can be a more direct and statistically accurate way of evaluating important physical parameters.

Consider the general situation where we wish to model some function,

$$d(t) \equiv d(C_1(t), \cdots, C_n(t)) \tag{3.25}$$

of n correlators, labelled $C_i(t)$.

As in the case of a single correlator the input data consists of a finite number of measurements at a finite number of times. The averages of the n correlators can be estimated at these times by the sample means as in Equation (3.1) giving an estimate for the function $d(t)$ as

$$\bar{d}(t_i) = d(\bar{C}_1(t_i), \cdots, \bar{C}_n(t_i)). \tag{3.26}$$

To perform the χ^2 minimisation procedure an estimate of the covariance matrix of the $\bar{d}(t_i)$ is also needed but unlike in the case of a single correlator there is in general no exact result to motivate an expression. It is possible, however, to estimate the covariance matrix using a jacknife procedure and this has been done for the work of this thesis.

The jacknife procedure used here starts by recalculating $\bar{d}(t_i)$ with the contribution from each independent measurement removed in turn. In this way a set of values $\bar{d}_{(s)}(t_i)$ can be built up where s labels the omitted measurement. The jacknife estimate of the covariance matrix is then given by

$$C(t_i, t_j) = \frac{N_{\mathrm{C}} - 1}{N_{\mathrm{C}}} \sum_{s=1}^{N_{\mathrm{C}}} (\bar{d}_{(s)}(t_i) - \bar{d}_{(\cdot)}(t_i))(\bar{d}_{(s)}(t_j) - \bar{d}_{(\cdot)}(t_j)) \tag{3.27}$$

where

$$\bar{d}_{(\cdot)}(t_i) = \frac{1}{N_{\mathrm{C}}} \sum_{s=1}^{N_{\mathrm{C}}} \bar{d}_{(s)}(t_i) \tag{3.28}$$

Apart from the above changes, χ^2 minimisation and bootstrap error estimation proceed as described previously.

3.6.3 Fitting to bootstrap data

In lattice QCD it is generally necessary to extrapolate the results of initial analyses to physically appropriate limits. This includes the important cases of modelling the dependence of physical parameters on quark masses and of performing extrapolations to the continuum limit. For the work of this thesis such extrapolations necessitate the extension of the data modelling procedures described earlier to the case of bootstrap data.

Consider the situation where we have some data, $y(t_i)$, with associated bootstrap sets, $y_{(b)}(t_i)$, where b runs over distinct bootstrap results. The covariance matrix for the data can be estimated using the bootstrap formula in Equation (3.9), however, a slightly modified form has been used here.

First the covariance matrix is estimated as in Equation (3.9) and the correlation matrix evaluated as in Equation (3.4). Next the positive and negative limits for the 68% confidence intervals, $y^+(t_i)$ and $y^-(t_i)$ respectively, are calculated using the bootstrap data at each t_i. From these the length of the intervals

$$\Delta y(t_i) = \frac{1}{2}\left(y^+(t_i) - y^-(t_i)\right). \tag{3.29}$$

are calculated and the covariance matrix finally estimated by

$$(Cov)_{ij} = \Delta y(t_i)(Corr)_{ij}\Delta y(t_j). \tag{3.30}$$

Best estimates for the model parameters are now determined by minimising χ^2 for the data, $y(t_i)$. Errors for the mininised parameters are calculated by fitting the model to the data from each bootstrap subset $y_{(b)}(t_i)$ to build up bootstrap distributions for the fit parameters. Confidence intervals can then be determined as before.

3.7 Exact solutions

To conclude this chapter I would like to mention a special case where the χ^2 minimisation problem can be solved exactly. This is the case where the model function is linear in its parameters i.e. we can write

$$m(t;a) = \sum_{k=1}^{N_{\mathrm{P}}} a_k f_k(t) \tag{3.31}$$

where $f_k(t)$ are called the basis functions for the fit. When $m(t;a)$ has this form Equation (3.5) for χ^2 can be written as

$$\chi^2(a) = \chi^2(0) - 2\sum_{k=1}^{N_{\mathrm{P}}} a_k\,\beta_k + \sum_{k,l=1}^{N_{\mathrm{P}}} a_k\,\alpha_{kl}\,a_l \tag{3.32}$$

where

$$\beta_k = -\frac{1}{2}\left.\frac{\partial\chi^2}{\partial a_k}\right|_{a=0} = \sum_{i,j}^{N_{\mathrm{D}}} f_k(t_i)(Cov)^{-1}_{ij}y(t_j) \tag{3.33}$$

and

$$\alpha_{kl} = \frac{1}{2}\left.\frac{\partial^2\chi^2}{\partial a_k\partial a_l}\right|_{a=0} = \sum_{i,j}^{N_{\mathrm{D}}} f_k(t_i)(Cov)^{-1}_{ij}f_l(t_j). \tag{3.34}$$

The χ^2 minimisation problem then has a solution, provided that α is invertible, given by

$$a_k^{(min)} = \sum_{l}^{N_{\mathrm{P}}} \alpha^{-1}_{kl}\ \beta_l. \tag{3.35}$$

Alternatively if α is singular then using the SVD inversion procedure will find an appropriate solution as described earlier for the Marquardt-Levenberg algorithm.

I have used this exact solution method when modelling the quark mass dependence of observables such as the hadron masses and hadronic matrix elements.

Chapter 4

Spectrum and decay constant analysis

In this chapter I present the analysis and results for the work of this thesis. I start by describing the details of the dynamical and quenched simulations upon which this work is based and briefly discuss the measurement of correlators for mesons and baryons. This is followed by a description of the analysis procedures used to determine the hadron masses, associated matrix elements and the PCAC quark masses from the correlator data. I then present results for the extrapolation of this data to the chiral limit and for the determination of the physical hadron masses, meson decay constants and the light quark masses. Finally I present the results of an investigation of unquenching effects for the matched datasets.

Some of my early analysis on the hadron spectrum can be found in [45], [46] and [47] and previous results for the light quark masses found in [48]. The work presented here, however, covers more scope and any repeated analysis has been recalculated using improved techniques and in some cases more data.

4.1 Simulation details

All of the lattice simulations studied in this thesis have been performed on a $16^3 \times 32$ space-time lattice using the $O(a)$-improved Sheikholeslami-Wohlert fermion action and the standard Wilson gauge field action as defined in Equations (2.40) and (2.39) respectively. Non-perturbatively determined values of the improvement coefficient, c_{SW}, as determined by the Alpha collaboration [12, 16], have been used in all these simulations. Gauge configurations for the $N_f = 2$ simulations were generated using the HMC algorithm described in Section 2.3.4 and a standard over-relaxed heat-bath update algorithm was used for the single quenched simulation. The details of all the lattice simulations have been summarised in Table 4.1.

β	κ_{sea}	c_{sw}	r_0/a	N_{C}	κ_{val}
5.20	0.1358	2.0171	$5.32\,^{+2}_{-9}$	139	0.1342 0.1350 0.1355 0.13565 0.1358 0.13595
5.20	0.13565	2.0171	$5.25\,^{+3}_{-5}$	141	0.1342 0.1350 0.1355 0.13565 0.1358
5.20	0.1355	2.0171	$5.04\,^{+6}_{-2}$	208	0.1340 0.1345 0.1350 0.1355
5.20	0.1350	2.0171	$4.72\,^{+5}_{-2}$	202	0.1335 0.1340 0.1345 0.1350 0.1355
5.25	0.1352	1.9603	$5.13\,^{+4}_{-5}$	206	0.1342 0.1347 0.1352 0.1357
5.26	0.1345	1.9497	$4.73\,^{+3}_{-7}$	104	0.1335 0.1340 0.1345 0.1350
5.29	0.1340	1.9192	$4.81\,^{+3}_{-7}$	101	0.1335 0.1340 0.1345 0.1350
5.93	-	1.82	$4.714\,^{+11}_{-16}$	623	0.1327 0.1332 0.1334 0.1337 0.1339

Table 4.1: Summary of simulation and correlator measurement details for the datasets studied in this thesis.

4.1.1 Matched datasets

The dynamical simulations at $(\beta, \kappa_{\text{sea}}) = (5.2, 0.1350), (5.26, 0.1345), (5.29, 0.1340)$ and the quenched simulation at $\beta = 5.93$ form a set with parameters chosen to keep the lattice spacing fixed. This has been done in order to study the effect of varying the sea quark mass whilst keeping cutoff and finite-size effects as constant as possible. It also makes these simulations particularly suited to the investigation of unquenching effects. This was the subject of a study by the UKQCD collaboration [45] which contained some of the work presented here.

The techniques used to determine the parameters for these matched simulations are well described in [49] and [45] and I will only give a rough outline here. The basic way that the lattice spacing is determined in a simulation is through some physical observable, f, with mass dimension, $d \neq 0$. It is usually chosen to be something easily calculable in lattice simulations. Denoting the dimensionless lattice equivalent of the observable by F, the lattice spacing is determined by solving the equation

$$F = a^d f. \tag{4.1}$$

This determination of a, which is only really appropriate in the scaling region where the lattice observable has a polynomial dependence on the lattice spacing, is explicitly dependent on the observable used and suffers from cutoff effects particular to that observable. To leading order, however, keeping F fixed provides a practical means of maintaining a constant lattice spacing.

So given one simulation at some $(\beta, \kappa_{\text{sea}})$ combination with a particular value of F other simulation parameters corresponding to the same value of F need to be determined. Cumulant expansion techniques allow the values of operator expectation values at points separated by small parameter changes, $(\delta\beta, \delta\kappa_{\text{sea}})$, to be related. To first order this is given by [45]

$$\langle \mathcal{O} \rangle_2 = \langle \mathcal{O} \rangle_1 + \left[\langle \tilde{\mathcal{O}} \frac{\partial \tilde{S}_G}{\partial \beta} \rangle_1 + \langle \tilde{\mathcal{O}} \frac{\partial \tilde{S}_F^W}{\partial c_{SW}} \rangle_1 \frac{d c_{SW}}{d\beta} \right] \delta\beta + \langle \tilde{\mathcal{O}} \frac{\partial \tilde{S}_F^W}{\partial \kappa_{\text{sea}}} \rangle_1 \, \delta\kappa_{\text{sea}} \tag{4.2}$$

for the operator, $\mathcal{O}$. The tilde in this expression is defined through $\tilde{A} = A - \langle A \rangle$ and the subscript 1 and 2 denote the two points in parameter space. If the observable, $F = \langle \mathcal{O} \rangle$, then the above equation can be used directly to determine the parameter steps needed to keep F fixed. If, however, F is a quantity derived from an expectation value then Equation (4.2) cannot be used directly. It can, however, be used to estimate values of F at nearby points in simulation space and hence to estimate its partial derivatives with respect to the parameters, $\partial F/\partial \beta$ and $\partial F/\partial \kappa_{\text{sea}}$. Solving the following equation then allows, say, the change in β to be calculated given a change in κ_{sea}

$$\delta\beta = -\frac{\partial F}{\partial \kappa_{\text{sea}}} \Big/ \frac{\partial F}{\partial \beta}\, \delta\kappa_{\text{sea}}. \tag{4.3}$$

4.1.2 The Sommer scale parameter

The Sommer scale parameter, r_0, [50] has been used as one way to fix the lattice spacing in this work. It was also the choice of matching variable used to determine the parameters for the matched simulations. It is defined in terms of the static quark potential, $V(r)$, through the following relation

$$r_0^2 \left. \frac{dV}{dr} \right|_{r=r_0} = 1.65 \tag{4.4}$$

with phenomenological potential models yielding a value of $r_0 \simeq 0.5$ fm. The static quark potential is determined in turn from expectation values of Wilson operators and the indirect technique of calculating parameter shifts was therefore used in the matching procedure.

Lattice values of r_0, i.e. r_0/a, have been calculated for the UKQCD Collaboration by Dr. A.C. Irving at the University of Liverpool using the techniques described in [51] and its values for the datasets considered here are given in Table 4.1. For the matched simulations r_0/a is consistent within errors as required although the value for the data set at $\kappa_{\text{sea}} = 0.1340$ seems a little high. For all of the simulations the lattice spacing through r_0 is around 0.1 fm, giving a spatial volume of around 1.6 fm. The relative coarseness of these simulations should be seen as a compromise given the computing resources and the need to avoid finite-size effects. The use of an $O(a)$-improved action, however, makes the level of coarseness acceptable. In a previous study by the UKQCD Collaboration [52] it was found that finite-size effects in the light hadron spectrum were negligible within errors for masses in the range $M_{\mathrm{PS}}/M_{\mathrm{V}} = 0.86 - 0.67$ as long as

$$La/r_0 > 3.2. \tag{4.5}$$

This bound is satisfied by all of the matched simulations. It is not satisfied, however, for most of the lighter quark mass simulations at fixed $\beta = 5.2$ and for the single simulation at $\beta = 5.25$. Further evidence of finite-size effects has been found by the JLQCD Collaboration [53] in a study at $\beta = 5.2$ using the same action as used here. They find significant finite-size effects even at $\kappa_{\mathrm{sea}} = 0.1355$. I will return to this important subject later in this chapter.

4.1.3 Correlator measurements

In Section 2.3.3 I mentioned how the measurements of an observable on successive gauge configurations tend to be correlated and how the number of trajectory steps between statistically independent measurements needs to be determined. This requires measuring the observable on each gauge configuration in order to calculate its integrated autocorrelation time [52]. Unfortunately it is not practical to measure correlators on each gauge configuration due to the significant computational effort required. The average plaquette variable, $\langle \frac{1}{3}\mathrm{Tr}\ \overline{U_{\mu\nu}}\rangle$, however, can be easily measured on all gauge configurations and has been used here to estimate autocorrelations for each dataset. For all but the lightest two datasets at $(5.2, 0.13565)$ and $(5.2, 0.1358)$ a step of 40 trajectories was deemed necessary for independent correlator measurements [45]. Surprisingly the autocorrelation time was found to drop as the sea quark mass was decreased [54] and correlator measurements on the lightest two datasets have therefore been performed on every 20^{th} configuration. The numbers of independent correlator measurements made with these step sizes are given in Table 4.1.

Correlators have been calculated here for all of the operators in Tables 2.4 and 2.5 using the same operator at source and sink. In those situations where more than one mesonic operator has a non-zero overlap with the same state, e.g. the operators $P(x)$ and $A_4(x)$ for the pseudoscalar state, the cross correlators have also been calculated. Each correlator has been calculated with a range of valence quark masses for each dataset. This allows partially quenched chiral extrapolations to be performed in the valence quark mass at fixed sea quark mass or alternatively, interpolations to the strange quark mass. The values of κ_{val} used for each dataset can be found in Table 4.1. Baryon correlators have only been calculated with degenerate valence quark masses. Meson correlators have in addition been calculated with $\kappa_{\mathrm{val},1} \neq \kappa_{\mathrm{val},2}$ for most of the possible non-degenerate combinations. This extra freedom and the increased number of datapoints gives better control over the chiral extrapolations and therefore on the determination of the light quark masses and meson decay constants.

4.2 Correlator analysis

In this section I discuss the general strategies used in this work to analyse correlator data for mesons and baryons in order to determine the masses of the light hadrons, matrix elements associated with the weak decay of light mesons and the PCAC masses. The data folding technique of Section 3.5.3 has been used throughout my analysis as has the shotgun technique for guessing fit parameters described in Section 3.5.2 and I will consider these implicit in the following. The final results from all of the correlator analyses are given in Appendix A.

4.2.1 Sliding window analysis

The basic aim of this data analysis is to model the correlator data for mesons and baryons using the functional forms given in Equations (2.111) and (2.135) respectively. This is, however, an impossible task given that there are an infinite number of undetermined parameters in these models and only a finite number of datapoints to constrain them.

One way to remedy this problem is to truncate the sum over states to a finite number of terms. Looking at the model functions it is clear that the contributions from the omitted higher states become exponentially suppressed with respect to the remaining lower states at times sufficiently far from $t = 0$ and $t = T$. Such truncated fits are therefore acceptable as long as the time range for the fit is chosen appropriately. The problem is then how to maximise the number of datapoints included in the fit in order to constrain the parameters as well as possible but still remain consistent with the model function used.

For single-state fits the effective mass plot can be a useful indicator of fit range. The appropriate fit range can be roughly equated with that where the effective mass has reached a plateau. This method is, however, quite qualitative and is inappropriate when higher state contributions are included in the fits. In this work I have primarily used the measure of the goodness of fit, Q, as a qualitative indicator of a good fit range. I have also used the secondary requirement that small changes in the fit range leave the fit parameters unchanged within errors. This measure keeps the systematic errors associated with choice of fit range to a minimum.

In order to find the best fit range I have used a sliding window analysis technique where either the minimum fit time, t_{min}, or the maximum fit time, t_{max}, is systematically varied whilst holding the other fixed. Parameter errors for these fits have been estimated from the parameter covariance matrix in order to speed up the analysis with the calculation of full bootstrap errors reserved for the best fit range.

In Figure 4.1 I show the result of a sliding window analysis for a single-state fit using the function

$$C(t) = A\left(e^{-aM_{\mathrm{PS}}t} + e^{-aM_{\mathrm{PS}}(T-t)}\right), \tag{4.6}$$

to an LL pseudoscalar correlator with $t_{max} = 15$. The lowest-state mass, aM_{PS}, clearly reaches a plateau at $t_{min} = 9$. This is also where the goodness of fit value, Q, becomes significant indicating the appropriateness of the model function over this fit range. A natural choice of fit range in this circumstance would therefore

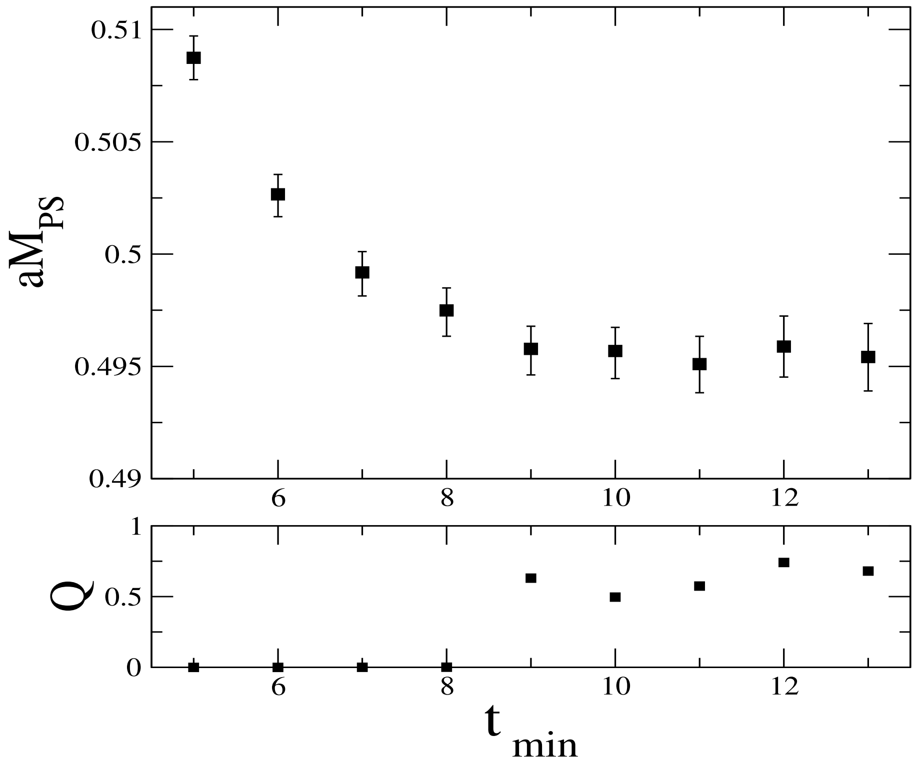

Figure 4.1: Sliding window plot for a single-state fit to an LL pseudoscalar correlator from the quenched simulation at $\beta = 5.93$ with $\kappa_{\mathrm{val}\,1} = \kappa_{\mathrm{val}\,2} = 0.1327$.

be $9-15$ or $10-15$ with the latter having the advantage that changing t_{min} by ± 1 has very little effect on aM_{PS}. Similar considerations apply in all other situations and I would estimate that systematic variations from choice of fit range amount to no more than the size of the quoted statistical errors and in most cases to only half of that.

4.2.2 Fits to meson correlators

Fits to meson correlators have all been performed keeping $t_{max} = 15$ fixed throughout. Data from the temporal midpoint of the lattice at $t = 16$ could also have been included but were found to give no improvement in the final results and so have been omitted.

In order to discuss my fitting strategy for meson correlators I note that these fits can be split into two distinct subsets. The first includes fits to correlators constructed out of a single type of operator and its fuzzed equivalent and the second to fits involving correlators constructed from two different types of operator and their fuzzed equivalents. I will discuss each in turn.

Single operator fits

Single operator fits can be defined as fits to correlators of the form $C_{\mathcal{M}_{S_1}\mathcal{M}^\dagger_{S_2}}(t)$ where S_1 and S_2 indicate the smearing of the operator, $\mathcal{M}$, at sink and source respectively which can be either local (L) or fuzzed (F). The important point here is that $\mathcal{M}$ is the same at source and sink. In those cases where $\mathcal{M}$ has either one or two free spatial indices, e.g. $\mathcal{M} = V_i$, the indices have been averaged over before fitting. This makes theoretical sense given that the actual form of the correlators is independent of the spatial indices.

The basic fitting strategy I have followed here starts with a sliding window analysis for separate single-state, single correlator fits to the LL, FL and FF correlators with a model function of the form

$$C(t) = \mathcal{A}\left(e^{-aMt} + e^{-aM(T-t)}\right), \tag{4.7}$$

and a simultaneous fit to the LL, FL and FF correlators, which I will call an LL,FL,FF fit from now on, with model function

$$C(t) = \mathcal{A}_{S_1}\mathcal{A}_{S_2}\left(e^{-aMt} + e^{-aM(T-t)}\right), \tag{4.8}$$

where S_1 and S_2 again denote sink and source smearing respectively. The amplitude factors have been taken to be real here. The result of such a sliding window analysis is given in Figure 4.2 for a set of pseudoscalar correlators.

The primary reason for performing all of these fits is to check for consistency between the single correlator fits and the simultaneous fit. This is clearly verified in the example above with all fits finding the same plateau for aM_{PS}. It is also

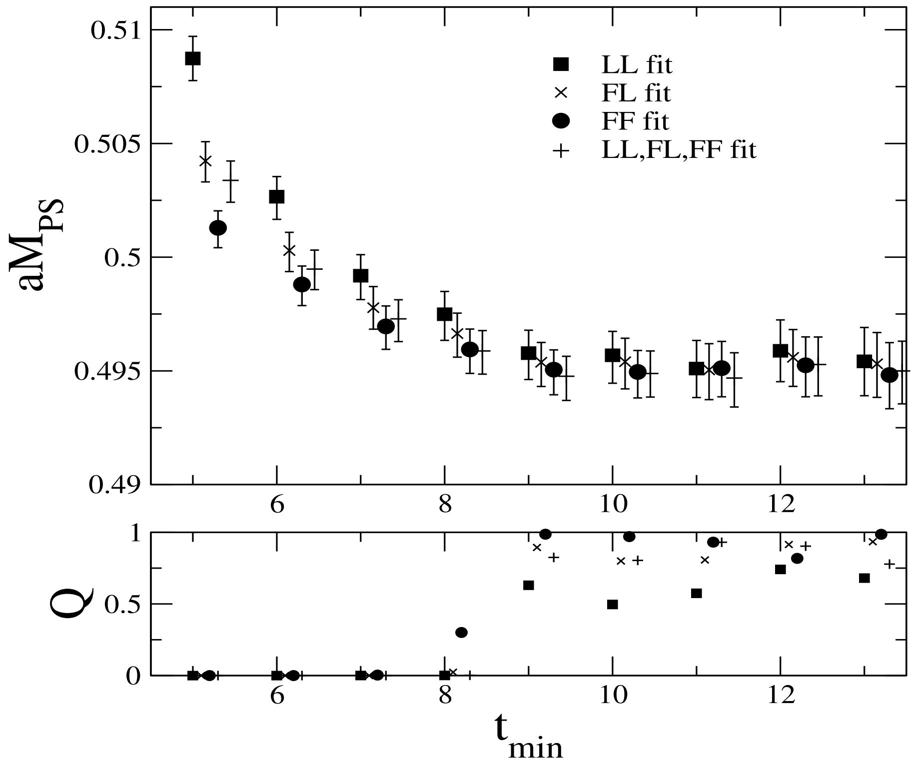

Figure 4.2: Sliding window plot for single-state LL, FL, FF, and LL,FL,FF fits to pseudoscalar correlators from the quenched simulation at $\beta = 5.93$ with $\kappa_{\mathrm{val}1} = \kappa_{\mathrm{val}2} = 0.1327$.

interesting to note that fits to fuzzed correlators tend to approach the plateau more quickly than the local correlator as expected. They do all, however, plateau at roughly the same value of t_{min}. This is a direct result of the fuzzing not being optimised to minimise excited-state contamination in the correlators as was discussed in Section 2.4.3. Overall from these single-state fits I determine the best fit range for the LL,FL,FF fit which I then repeat with full bootstrap errors.

In the second stage of the analysis I use the best result from the single-state LL,FL,FF fit as part of an initial guess for a two-state fit with model function,

$$C(t) = \sum_{n=1}^{N_{\mathrm{S}}} \mathcal{A}_{S_1}^{(n)} \mathcal{A}_{S_2}^{(n)} \left(e^{-aM_n t} + e^{-aM_n (T-t)} \right) . \tag{4.9}$$

where the number of states, $N_{\mathrm{S}} = 2$. Two-state fits were also attempted for single correlators but the results found to be too unstable to be of any use. The reason for performing these two-state fits is to take some account of the excited-state contamination that is present in the data. In this way the lowest-state parameters from these fits should be better determined and the associated systematic errors made smaller.

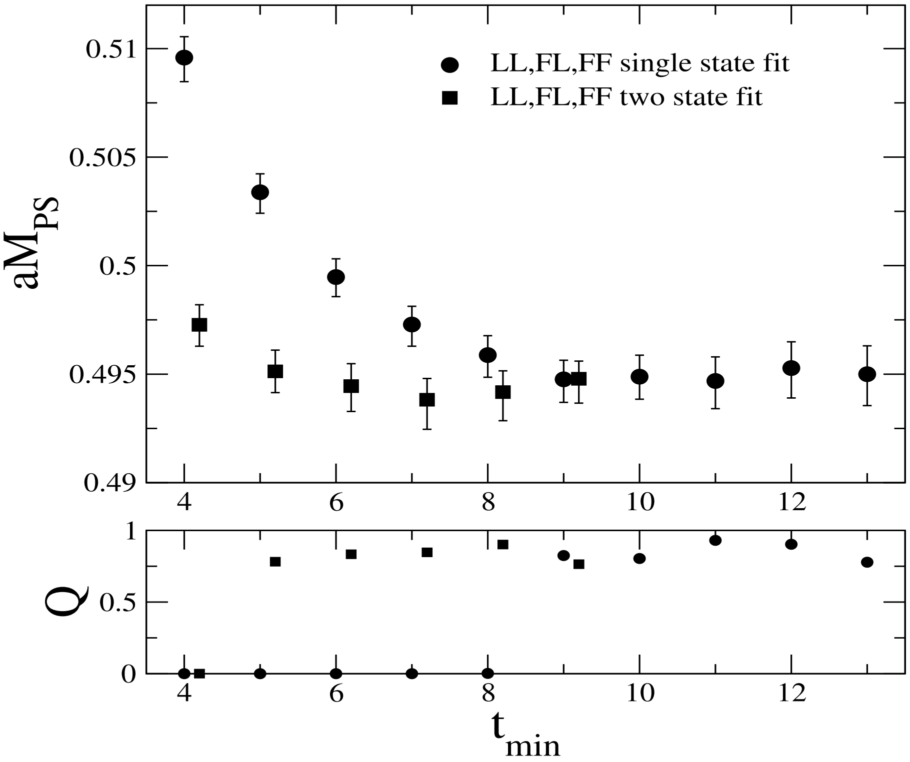

Figure 4.3: Sliding window plot for single and two-state LL,FL,FF fits to pseudoscalar correlators from the quenched simulation at $\beta = 5.93$ with $\kappa_{\mathrm{val}\,1} = \kappa_{\mathrm{val}\,2} = 0.1327$.

As an example I show the result of a sliding window analysis for a two-state fit in Figure 4.3 along with the results of the corresponding single-state fit for comparison. The fit parameter, aM_{PS}, can again be seen to reach a plateau although at earlier times than the single-state fit. What is more important is that this plateau is at the same value of the fit mass as the single-state fit. I use this as an important consistency check. To complete the analysis I choose a best fit range for the two-state fit, which in this example would be $5-15$ or $6-15$, and repeat the fit with full bootstrap errors. It is possible to continue this strategy to three-state fits and higher and although such fits were investigated they did not, in my opinion, improve upon the results of the two-state fits.

The above strategy was successful for all of the mesonic states studied in this thesis although some problems were encountered in scalar meson fits. Further investigation found that the cause of the problem was the high level of noise in the scalar correlators with data at times near the mid-point of the lattice being consistent with zero. This was particularly apparent for the quenched dataset at $\beta = 5.93$ and for the two dynamical datasets at $(5.2, 0.13565)$ and $(5.2, 0.1358)$. It also became worse as the bare quark mass was lowered for all datasets. Despite this there was enough signal in the data at earlier times to allow the above fitting strategy to be followed although with some unusual consequences as will be discussed in Section 4.3.1.

Double operator fits

In those situations where more than one operator has a non-zero overlap with the state we wish to study many more correlators can be used in the fitting process. In the pseudoscalar case, correlators of the form $C_{\mathcal{M}_{1,S_1}\mathcal{M}^\dagger_{2,S_2}}(t)$ have been calculated for all possible combinations of operators $\mathcal{M}_{1,S_1}, \mathcal{M}_{2,S_2} \in \{P_{\mathrm{L}}, P_{\mathrm{F}}, A_{4,\mathrm{L}}A_{4,\mathrm{F}}\}$. Excluding those correlators that are local at source and fuzzed at sink this gives a total of 12 possible correlators that can be fitted simultaneously. A similar situation exists for vector mesons where $\mathcal{M}_{1,S_1}, \mathcal{M}_{2,S_2} \in \{V_{i,\mathrm{L}}, V_{i,\mathrm{F}}, T_{i4,\mathrm{L}}T_{i4,\mathrm{F}}\}$ and the free spatial index, i, has again been averaged over before fitting.

The fitting strategy for double operator fits proceeds in a similar manner to the single operator case. I again start by performing single-state fits although this time to all local correlators (LL fits), all fuzzed correlators (FF fits), all local and fuzzed correlators (LL,FF fits) and finally to all possible correlators (LL,FL,FF fits). Fits to these different correlator combinations again act as a consistency check for the fitted parameters. After choosing the best fit ranges for these single-state fits I perform two-state fits to the same correlator combinations. This is in contrast to the single operator case where LL and FF fits to two-states were found to be unstable. The advantage here is that consistency checks can now be performed between different two-state fits as well as between those to one or two-states.

In the pseudoscalar meson case I have chosen the final results of this analysis from the LL,FL,FF fits, if possible, as they tended to yield parameters with the lowest statistical errors. This was not found to be the case for the datasets at ($\beta = 5.2, \kappa_{\rm sea} = 0.1358$) and ($\beta = 5.2, \kappa_{\rm sea} = 0.13565$), however, where the LL,FF fits gave the smallest errors and their results therefore used. Problems were also encountered in LL,FL,FF fits to correlators from the datasets at $(5.26, 0.1345)$ and $(5.29, 0.1340)$. These problems, which consisted of unstable and inconsistent results and unusually low values of χ^2, arose when the fit range was made longer than $8-15$. This suggests that in these cases even the eigenvalue smoothing technique of Michael and McKerrell was not able to compensate for the lack of data. Fortunately the LL,FF fits were found to give consistent and stable results and have been used instead.

In the vector meson case all two-state simultaneous fits were found to be problematic yielding no identifiable plateaus in the sliding window analyses and poor χ^2 values. This was despite the single-state fits working as expected. On further investigation it was found that those correlators with $\mathcal{M}_1 \neq \mathcal{M}_2$ reached a single-state plateau significantly earlier than the others. As a result no common fit range could be found for these two sets of correlators in the two-state fits. This problem could have been remedied by allowing different fit ranges for each correlator, a measure that would have required rewriting a significant proportion of the analysis code and has not been pursued here. I have proceeded instead by omitting the cross correlators from the fits. This seemingly drastic measure only led to a slight increase in statistical errors in the pseudoscalar case where the comparison could be made. With these changes implemented the simultaneous fits to the remaining correlators worked successfully. In particular the LL,FL,FF fits were found to yield parameters with the smallest statistical errors and have therefore been taken to provide the final results in the vector meson analysis.

4.2.3 Fits to baryon correlators

In the baryon sector correlators of the form $C_{N_{1,S_1}\overline{N_{1,S_2}}}(t)$ and $C_{N_{2,S_1}\overline{N_{2,S_2}}}(t)$ have been calculated for the nucleon channel and of the form $C_{\Delta_{S_1}\overline{\Delta_{S_2}}}(t)$ for the delta baryon channel. Both single and double operator fits could therefore be performed to the nucleon correlators whereas only single operator fits are possible for the delta baryon. A small initial study of the double operator nucleon fits, however, found them to be slow and unstable due to the large number of parameters and gave no marked improvement over the single operator fit results. For this reason nucleon fits have been performed to an average of the two operator channels.

Fits to baryon correlators proceed in a similar fashion to single operator meson fits although with the added complication of distinct forward and backward propagating states. Both $t_{\rm min}$ and $t_{\rm max}$ therefore have to be determined from a sliding window analysis. I again start with single-state, single correlator fits to LL, FL and FF correlators with model function

$$C(t) = \mathcal{A}^{+}e^{-aM^{+}t} + \mathcal{A}^{-}e^{-aM^{-}(T-t)}, \tag{4.10}$$

and a single-state simultaneous LL,FL,FF fit with model function

$$C(t) = \mathcal{A}^{+}_{S_1}\mathcal{A}^{+}_{S_2}e^{-aM^{+}t} + \mathcal{A}^{-}_{S_1}\mathcal{A}^{-}_{S_2}e^{-aM^{-}(T-t)}, \tag{4.11}$$

where all amplitude factors are again taken to be positive. The sliding window analysis proceeds in two stages.

Firstly I fix $t_{\rm max}$ to some reasonable value for a single-state fit and vary $t_{\rm min}$. In Figure 4.4 I show the result of such a sliding window analysis for the positive and negative parity nucleon masses. The positive parity nucleon mass reaches a clear plateau at $t_{\rm min} = 11$ in a similar manner to the meson case. In contrast the negative parity nucleon mass remains invariant to changes in $t_{\rm min}$ for a large range of values and only begins to deviate when $t_{\rm min}$ is significantly far from the plateau region. This can be useful as a further consistency check and validates that the fit is proceeding well.

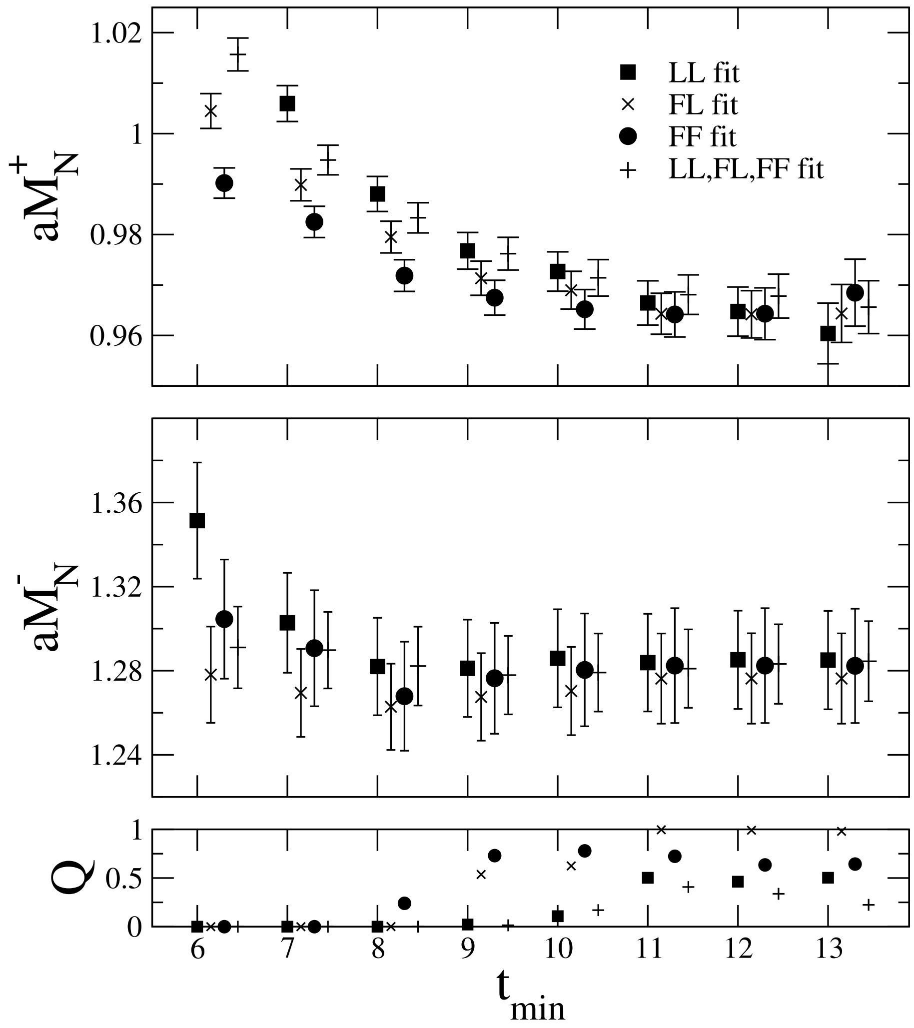

Figure 4.4: Sliding window plot for aM_{N}^{+} and aM_{N}^{-} from single-state LL, FL, FF, and LL,FL,FF fits with $t_{\mathrm{max}} = 24$ to nucleon correlators from the quenched simulation at $\beta = 5.93$ and $\kappa_{\mathrm{val}} = 0.1327$.

With a best t_{min} chosen, a second sliding window analysis can be performed but this time varying t_{max}. In Figure 4.5 I plot the results of such an analysis. The observed behaviour is similar to the case where t_{max} was fixed but with the roles of the positive and negative parity states reversed. The negative parity nucleon mass can be seen to reach a plateau at around $t_{\mathrm{max}} = 24$ although with much larger errors than for the positive parity state. This is a direct result of the correlators being much noisier in the back half of the lattice where the negative parity state dominates.

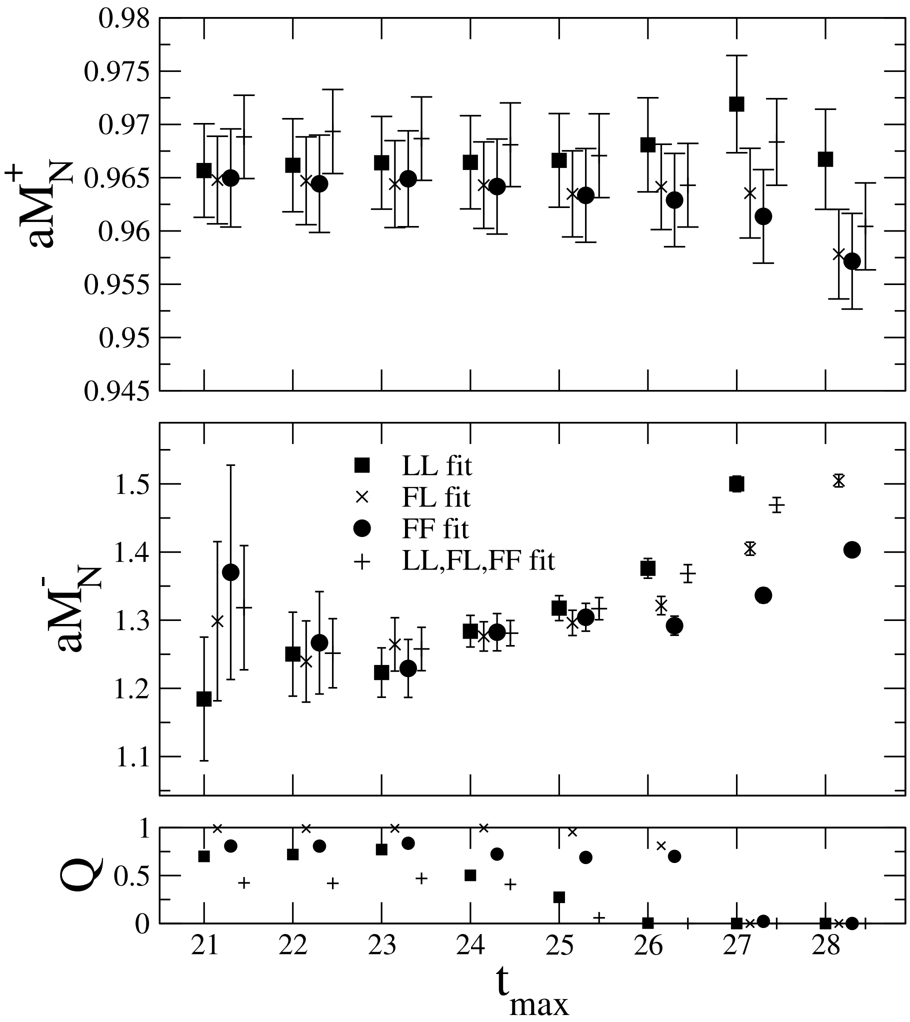

Figure 4.5: Sliding window plot for aM_{N}^{+} and aM_{N}^{-} from single-state LL, FL, FF, and LL,FL,FF fits with $t_{\mathrm{min}} = 11$ to nucleon correlators from the quenched simulation at $\beta = 5.93$ and $\kappa_{\mathrm{val}} = 0.1327$.

Two-state fits have been performed in a similar fashion to the single-state fits and build on their results as in the meson case. Again I only perform two-state simultaneous LL,FL,FF fits but this time to the modified model function,

$$C(t) = \sum_{n=1}^{N_{\mathrm{S}}} \mathcal{A}_{S_1}^{(n,+)} \mathcal{A}_{S_2}^{(n,+)} e^{-aM_n^{+} t} + \mathcal{A}_{S_1}^{(n,-)} \mathcal{A}_{S_2}^{(n,-)} e^{-aM_n^{-}(T-t)}. \tag{4.12}$$

where $N_{\mathrm{S}} = 2$. Sliding window analysis results for positive and negative parity nucleon masses from two-state fits are shown in Figures 4.6 and 4.7 respectively.

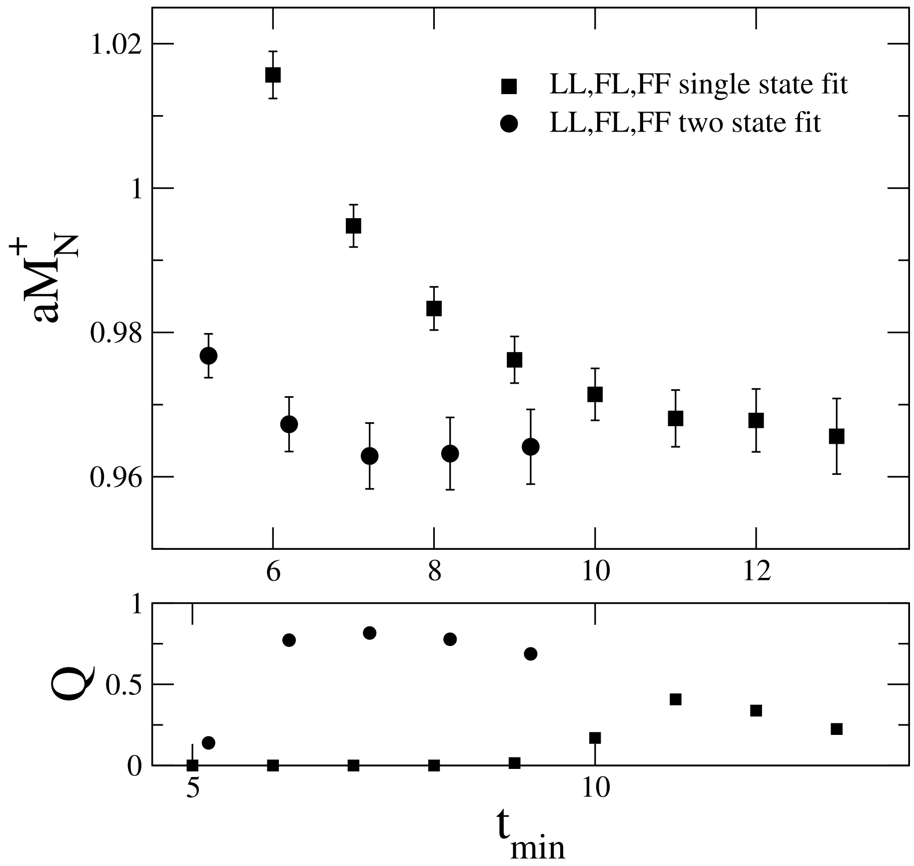

Figure 4.6: Sliding window plot for aM_{N}^{+} from single and two-state LL,FL,FF fits with $t_{\max} = 24$ and $t_{\max} = 27$ respectively to nucleon correlators from the quenched simulation at $\beta = 5.93$ and $\kappa_{\mathrm{val}} = 0.1327$.

In both of these cases the respective mass can be seen to plateau earlier than for the single-state fit and with a similar value as would be expected. With these final consistency checks performed all that remains is to choose a best fit range, which in this example is $7 - 27$, and repeat the fit with full bootstrap errors.

4.2.4 PCAC mass fits

In Equation (2.56) I gave an alternative definition of a bare quark mass which was motivated from the PCAC relation in Equation (2.55) i.e.

$$2m_{\mathrm{PCAC}} \langle P_{\mu}^{a}(x)\mathcal{O}\rangle = \partial_{\mu} \langle A_{\mu}^{a}(x)\mathcal{O}\rangle + c_{A} a \partial^{2} \langle P_{\mu}^{a}(x)\mathcal{O}\rangle$$

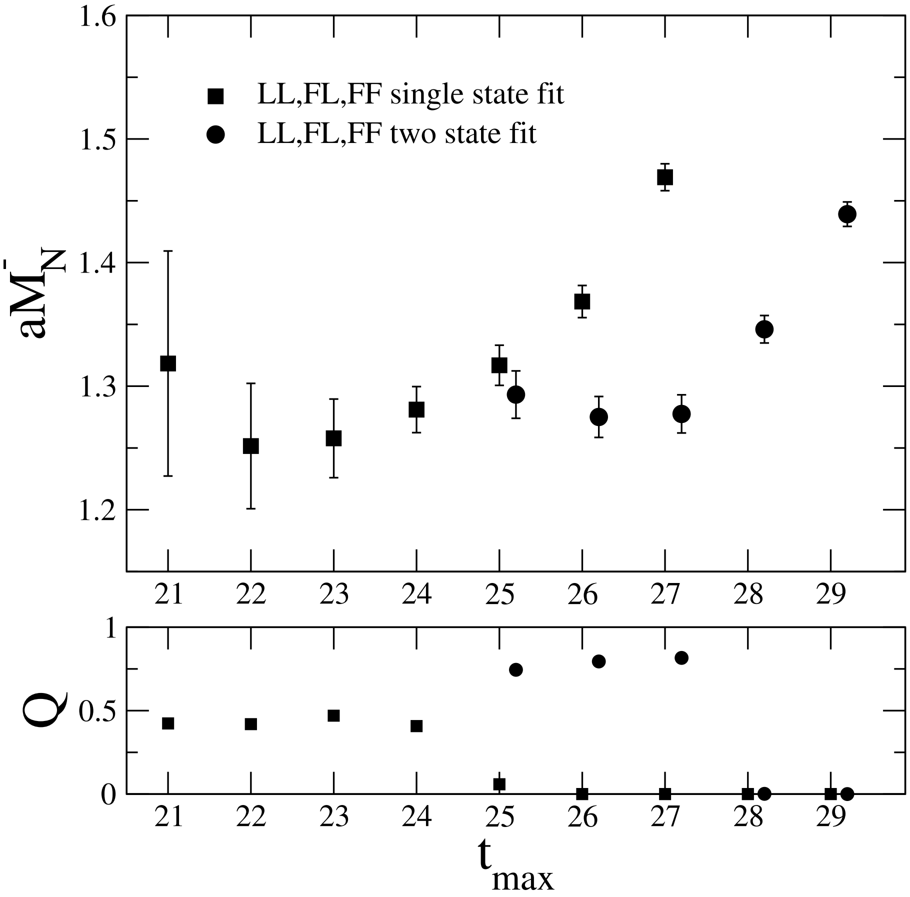

Figure 4.7: Sliding window plot for aM_{N}^{-} from single and two-state LL,FL,FF fits with $t_{\mathrm{min}} = 11$ and $t_{\mathrm{min}} = 7$ respectively to nucleon correlators from the quenched simulation at $\beta = 5.93$ and $\kappa_{\mathrm{val}} = 0.1327$.

This mass can be directly measured from pseudoscalar correlators by choosing $\mathcal{O} = P_S^{\dagger}(0)$ where S is either F or L and performing a spatial fourier transform at zero momentum. Making the standard choices for lattice derivatives i.e.

$$\partial_\mu f(x) = \Delta_\mu^{(+-)} f(x) + O(a^3)$$

and

$$\partial^2 f(x) = \sum_\mu \Delta_\mu^+ \Delta_\mu^- f(x) + O(a^2), \tag{4.13}$$

gives the following relation for m_{PCAC},

$$m_{\mathrm{PCAC}}(t) = r(t) + c_A\ s(t) + O(a^2) \tag{4.14}$$

with component functions

$$r(t) = \frac{1}{2}\frac{C_{A_4P^\dagger}(t+1) - C_{A_4P^\dagger}(t-1)}{2C_{PP^\dagger}(t)}, \tag{4.15}$$

and

$$s(t) = \frac{C_{PP^\dagger}(t+1) - 2C_{PP^\dagger}(t) + C_{PP^\dagger}(t-1)}{2C_{PP^\dagger}(t)}. \tag{4.16}$$

Alternatively using the following improved definitions of the lattice derivatives,

$$\partial_\mu f(x) = \tilde{\Delta}_\mu^{(+-)} f(x) + O(a^5) \tag{4.17}$$

and

$$\partial^2 f(x) = \sum_\mu \left[1 - \frac{a^2}{12}\Delta_\mu^+\Delta_\mu^-\right] \Delta_\mu^+\Delta_\mu^- f(x) + O(a^4), \tag{4.18}$$

gives

$$m_{\mathrm{PCAC}} = r_{\mathrm{imp}}(t) + c_A\ s_{\mathrm{imp}}(t) + O(a^2) \tag{4.19}$$

where,

$$r_{\mathrm{imp}}(t) = \frac{2}{3}\frac{C_{A_4P^\dagger}(t+1) - C_{A_4P^\dagger}(t-1)}{2C_{PP^\dagger}(t)} - \frac{1}{12}\frac{C_{A_4P^\dagger}(t+2) - C_{A_4P^\dagger}(t-2)}{2C_{PP^\dagger}(t)} \tag{4.20}$$

and

$$s_{\text{imp}}(t) = \frac{4}{3}\frac{C_{PP^\dagger}(t+1) - 2C_{PP^\dagger}(t) + C_{PP^\dagger}(t-1)}{2C_{PP^\dagger}(t)} - \frac{1}{12}\frac{C_{PP^\dagger}(t+2) - 2C_{PP^\dagger}(t) + C_{PP^\dagger}(t-2)}{2C_{PP^\dagger}(t)}. \tag{4.21}$$

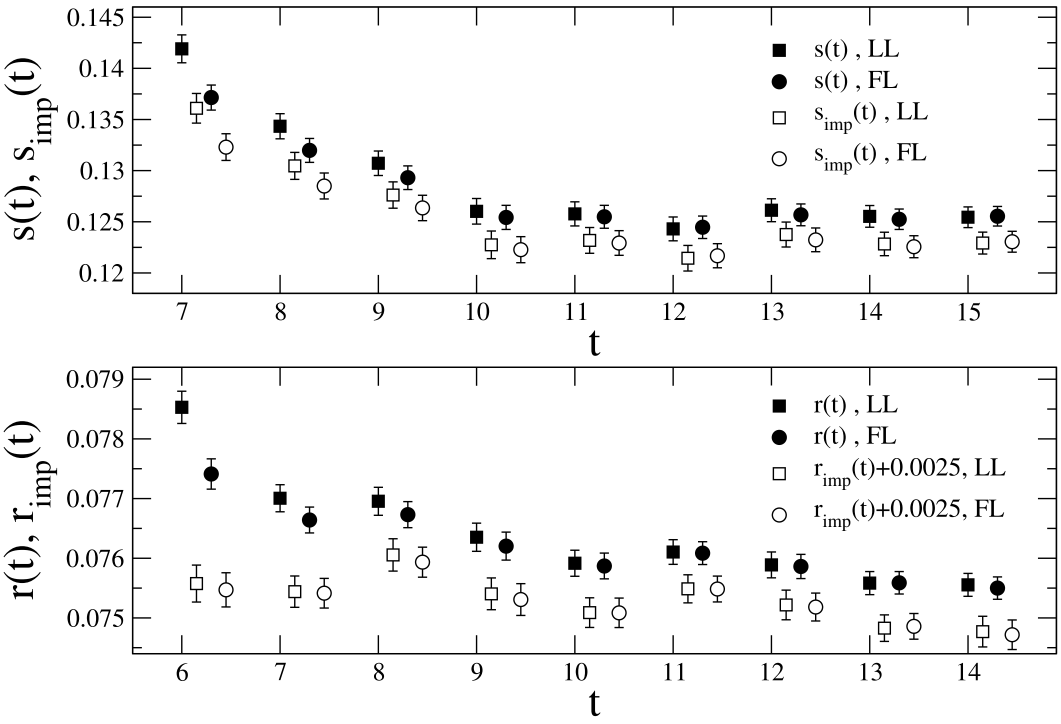

Figure 4.8: Plot of $r(t)$, $r_{\text{imp}}(t)$, $s(t)$ and $s_{\text{imp}}(t)$ for LL and FL correlators from the quenched simulation at $\beta = 5.93$ with $\kappa_{\text{val}} = 0.1327$.

In Figure 4.8 I plot examples of $r(t)$, $r_{\text{imp}}(t)$, $s(t)$ and $s_{\text{imp}}(t)$ for both LL and FL correlators. In the continuum limit the functions, $r(t)$ and $r_{\text{imp}}(t)$, should be equal and independent of both t and choice of $\mathcal{O}$. This is clearly not the case at finite a although LL and FL definitions of $r(t)$ and $r_{\text{imp}}(t)$ do reach consistent plateaus at later times. The deviations at earlier times and differences between $r(t)$ and $r_{\text{imp}}(t)$ are directly attributable to discretisation errors from the operator at $O(a)$, from the action at $O(a^2)$ and from choice of derivative at $O(a^3)$ and $O(a^5)$ respectively. What is perhaps surprising is quite how much difference the choice of derivative can make with $r_{\text{imp}}(t)$ reaching a plateau significantly earlier than $r(t)$.

The time dependence of these two functions can be investigated directly by substituting the following expressions for $C_{A_4P^\dagger}(t)$ and $C_{PP^\dagger}(t)$ into $r(t)$ and $r_{\rm imp}(t)$

$$C_{A_4P^\dagger}(t) = \sum_{n=1}^{2} C^{(n)}_{A_4P^\dagger}(t) = \sum_{n=1}^{2} \mathcal{A}^{(n)}_{A_4}\mathcal{A}^{(n)}_{P}\left(e^{-aM_nt} + e^{-aM_n(T-t)}\right), \tag{4.22}$$

$$C_{PP^\dagger}(t) = \sum_{n=1}^{2} C^{(n)}_{PP^\dagger}(t) = \sum_{n=1}^{2} \mathcal{A}^{(n)2}_{P}\left(e^{-aM_nt} + e^{-aM_n(T-t)}\right). \tag{4.23}$$

The result for $r(t)$ can be written as a weighted sum of fractional state contributions

$$r(t) = \sum_{n=1}^{2} r^{(n)}\frac{C^{(n)}_{PP^\dagger}(t)}{C_{PP^\dagger}(t)} = r^{(1)} + \left(r^{(2)} - r^{(1)}\right)\frac{C^{(2)}_{PP^\dagger}(t)}{C_{PP^\dagger}(t)} \tag{4.24}$$

with weight coefficients, $r^{(n)}$, given by

$$r^{(n)} = \frac{1}{2}\frac{\mathcal{A}^{(n)}_{A_4}}{\mathcal{A}^{(n)}_{P}}\sinh(aM_n). \tag{4.25}$$

This function will reach a plateau at $r(t) = r^{(1)}$ when the lowest-state contribution is dominant to within errors. A similar result exists for $r_{\rm imp}(t)$ with weight coefficients,

$$r^{(n)}_{\rm imp}(t) = \frac{\mathcal{A}^{(n)}_{A_4}}{\mathcal{A}^{(n)}_{P}}\left[\frac{2}{3}\sinh(aM_n) - \frac{1}{12}\sinh(2aM_n)\right]. \tag{4.26}$$

and a similar plateau at $r_{\rm imp}(t) = r^{(1)}_{\rm imp}$. This plateau will be reached more quickly in the improved case if the following inequality holds,

$$\frac{r^{(2)}_{\rm imp} - r^{(1)}_{\rm imp}}{r^{(1)}_{\rm imp}} < \frac{r^{(2)} - r^{(1)}}{r^{(1)}}. \tag{4.27}$$

A direct calculation of the weight coefficients from the results of double operator fits to pseudoscalar correlators verified that this inequality is indeed satisfied for all the datasets and κ_{val} combinations studied here. The results tended to range from a factor of two reduction in the excited-state contribution to only a marginal improvement at small quark masses.

The functions, $s(t)$ and $s_{\text{imp}}(t)$, contain contributions proportional to the $O(a)$ operator errors present in both $r(t)$ and $r_{\text{imp}}(t)$ although each also comes with distinct discretisation errors. Despite this they can still be used to eliminate operator errors at $O(a)$ in $r(t)$ and $r_{\text{imp}}(t)$ if c_A is tuned appropriately. Alternatively this argumentation can be reversed to give a possible way of determining c_A as done by Collins *et al.* [55]. As can be seen in Figure 4.8 there is not so much of a marked difference between $s(t)$ and $s_{\text{imp}}(t)$ and no real extension of the plateau region as was the case for $r(t)$ and $r_{\text{imp}}(t)$. The primary reason for this can be seen by substituting the expression for $C_{PP^\dagger}(t)$ in Equation (4.23) into Equations (4.16) and (4.21) for $s(t)$ and $s_{\text{imp}}(t)$ respectively to give

$$s(t) = \sum_{n=1}^{2} s^{(n)} \frac{C^{(n)}_{PP^\dagger}(t)}{C_{PP^\dagger}(t)} \tag{4.28}$$

with weight coefficients given by

$$s^{(n)} = (\cosh(aM_n) - 1) \tag{4.29}$$

and a similar expression for $s_{\text{imp}}(t)$ with weight coefficients given by

$$s^{(n)}_{\text{imp}} = \frac{4}{3}\left(\cosh(aM_n) - 1\right) - \frac{1}{12}\left(\cosh(2aM_n) - 1\right). \tag{4.30}$$

Although it is true that

$$\frac{s^{(2)}_{\text{imp}} - s^{(1)}_{\text{imp}}}{s^{(1)}_{\text{imp}}} < \frac{s^{(2)} - s^{(1)}}{s^{(1)}} \tag{4.31}$$

in all the cases I investigated the improvement was found to be minimal. When coupled with the result that $s^{(2)}$ was found to be significantly larger than $s^{(1)}$ in general this also explains the late plateaus seen for both $s(t) = s^{(1)}$ and $s_{\text{imp}}(t) = s_{\text{imp}}^{(1)}$.

Results for the plateau values of $r(t)$, $s(t)$, $r_{\text{imp}}(t)$ and $s_{\text{imp}}(t)$ have been determined from the results of pseudoscalar correlator fits and by directly fitting the data to a constant model function. Both methods gave consistent results although the results from the pseudoscalar fits had lower or comparable statistical errors and have therefore been taken as the final results.

4.3 Chiral extrapolations

With current computational resources and lattice actions it is impossible to simulate directly with quark masses near those of the up and down quarks. This is especially true of simulations with the Wilson quark action. As an example the pseudoscalar meson masses in the dynamical simulations at $\kappa_{\text{val}} = \kappa_{\text{sea}}$ range from 440 MeV to 1099 MeV with the lattice spacing set through r_0. When compared to the mass of the kaon, $M_{\text{K}} = 498$ MeV, and pion, $M_\pi = 135$ MeV, this indicates that the simulations are some way from the up/down quark mass regime with masses ranging around or above that of the strange quark. Extrapolations of the measured observables are therefore necessary in order to make physical predictions.

Chiral perturbation theory (χPT) [56] is a low energy effective theory that can be used to determine the dependence of many physical observables on quark masses near the chiral limit. This is particularly useful for guiding the chiral extrapolations of measured quantities in lattice simulations and is systematically improvable order by order although at the cost of an increasing number of undetermined coefficients.

Of particular use in the context of lattice QCD are the generalisations of χPT to the partially quenched case (PQχPT) [57, 58] where sea and valence masses can be different and to the quenched case (QχPT) [59]. Extending the parameter space in this way gives far more predictive power to the lattice simulations because it is much cheaper to vary valence quark masses than sea quark masses and the valence quark masses can be pushed significantly lower.

It is worth mentioning that these chiral theories are defined in the continuum limit. In a strict sense they can therefore only be used to guide chiral extrapolations of lattice results if a continuum extrapolation is performed first. Despite this they are often applied at finite lattice spacing. A more sound solution has been given by Rupak and Shoresh [60] who have determined the chiral lagrangian up to terms of $O(a)$ for the lattice theory with Wilson quarks. This work has been extended to $O(a^2)$ and to a mixed lattice theory by Bär, Rupak and Shoresh [61]. These results offer the possibility of guiding both chiral and continuum extrapolations and allow the low energy constants of full QCD to be determined from partially quenched simulations at finite a. Such a program has been carried out successfully by the qq+q collaboration [62, 63, 64] who have simulated with sufficiently small quark masses to make contact with NLO results from χPT. This is, unfortunately, not true of all but the lightest simulations presented here which may yet show evidence of the characteristic chiral logarithms although this has still to be investigated. For this reason χPT has not been used to motivate the chiral extrapolations performed in this thesis and general polynomial forms have been used instead.

There are two basic types of chiral extrapolation that can be performed on the lattice data presented here. The first of these is to independently extrapolate the results for each dataset in the valence quark mass only. These are the quenched and partially quenched extrapolations. The second type of extrapolation performed here includes the results from different datasets with either the same lattice spacing or β value in the one fit. This is ideal for the matched simulations and those at $\beta = 5.2$. For want of a better term I call these full chiral extrapolations since they are performed simultaneously in the sea and valence quark masses and include all the unitary points with $\kappa_{\rm sea} = \kappa_{\rm val}$. All of the chiral extrapolations in this thesis have been performed assuming that the data are uncorrelated. Correlated fits were found to consistently produce very poor χ^2/dof and Q values despite the fact that the data and model looked like they were in agreement. Because of this and the fact that the errors are taken care of through the bootstrap process uncorrelated fits were used instead. The results for the chiral extrapolations are given in Appendix B.

4.3.1 Partially quenched chiral extrapolations

In Section 2.2 two separate definitions were given for the bare quark mass. They are the standard definition,

$$am = \frac{1}{2}\left(\frac{1}{\kappa} - \frac{1}{\kappa_{\text{crit}}}\right), \tag{4.32}$$

and the definition from the PCAC relation, am_{PCAC}. Both of these masses are suitable for performing extrapolations. A third option is to extrapolate in the pseudoscalar meson mass, aM_{PS}, which has the advantage that it is a directly measurable physical quantity. The basic strategy I follow here is to fit aM_{PS} directly to the standard quark mass and am_{PCAC} and fit all other quantities to aM_{PS}. This is effectively the same as fitting all quantities to both the standard quark mass and PCAC mass.

Extrapolations of aM_{PS}

The basic lattice observables are measured at particular values of κ_{val} and simulation parameters, β and κ_{sea}, although these are fixed in partially quenched extrapolations. In order to perform extrapolations in the standard quark mass the value of κ_{crit} therefore needs be determined first. This can be done by requiring that the pseudoscalar meson mass, which I now write as $aM_{\text{PS}}(\kappa_{\text{val},1}, \kappa_{\text{val},2})$, vanishes in the chiral limit i.e. $aM_{\text{PS}}(\kappa_{\text{crit}}, \kappa_{\text{crit}}) = 0$. Extrapolations of aM_{PS} in $\kappa_{\text{val},1}$ and $\kappa_{\text{val},2}$ have been performed for this purpose with the following fit ansatz,

$$(aM_{\text{PS}})^2(\kappa_{\text{val},1}, \kappa_{\text{val},2}) = A + B(\frac{1}{\kappa_{\text{val},1}} + \frac{1}{\kappa_{\text{val},2}}) + C(\frac{1}{\kappa_{\text{val},1}} + \frac{1}{\kappa_{\text{val},2}})^2 + D\frac{1}{\kappa_{\text{val},1}}\frac{1}{\kappa_{\text{val},2}}. \tag{4.33}$$

This is the most general quadratic fit ansatz that is consistent with the symmetry condition, $aM_{\rm PS}(\kappa_{\rm val,1},\kappa_{\rm val,2}) = aM_{\rm PS}(\kappa_{\rm val,2},\kappa_{\rm val,1})$. The results of such extrapolations have been used to determine $\kappa_{\rm crit}$ for the dataset being studied and then transformed to give $aM_{\rm PS}$ in terms of standard quark masses i.e.

$$(aM_{\rm PS})^2(am_1,am_2) = B_{\rm PS}(am_1+am_2)+C_{\rm PS}(am_1+am_2)^2+D_{\rm PS}am_1am_2, \quad (4.34)$$

where

$$am_{\rm i} = \frac{1}{2}\left(\frac{1}{\kappa_{val,i}} - \frac{1}{\kappa_{\rm crit}}\right). \quad (4.35)$$

Fits with C, D or both C and D set to zero have also been performed in order to find the fit function that best models the data as measured through χ^2/dof. Fits with $C = D = 0$ were found to have the lowest errors but did not model the data as well as those with square terms included. When freed, both C and D generally assumed non-zero values except for the quenched dataset, where the $D = 0$ fit modelled the data better, and for the $(5.25, 0.1352)$ dataset where the $C = 0$ fit did best. In addition the quadratic fits tended to produce much larger errors than the linear fit near the chiral limit. This goes some way to incorporating the systematic effect coming from choice of fit function although the effect of not matching onto chiral perturbation theory is expected to be larger. Results from these fits are plotted against $1/\kappa_{\rm eff} = 1/2(1/\kappa_{\rm val,1} + 1/\kappa_{\rm val,2})$ in Figures B.1 and B.2 and the coefficients summarised in Table B.1.

Fits to the PCAC mass have been performed with the mass calculated from both improved, $am_{\rm PCAC,imp}$, and unimproved, $am_{\rm PCAC}$, definitions of r and s. A one-loop tadpole improved value was taken for c_A calculated using the boosted coupling, $\tilde{\alpha}$. The data has been modelled using the following fit ansatz,

$$\begin{aligned}(aM_{\rm PS})^2 &= B'_{\rm PS}(am_1^{\rm PCAC} + am_2^{\rm PCAC}) + C'_{\rm PS}(am_1^{\rm PCAC} + am_2^{\rm PCAC})^2 \\ &+ D'_{\rm PS}am_1^{\rm PCAC}am_2^{\rm PCAC}, \end{aligned} \quad (4.36)$$

where

$$am_{\rm i}^{\rm PCAC} = am^{\rm PCAC}(\kappa_{{\rm val},i}, \kappa_{{\rm val},i}). \tag{4.37}$$

The above model is consistent with the condition that $aM_{\rm PS}$ and $am_{\rm PCAC}$ vanish at the same point. Fits have also been performed with $C'_{\rm PS} = 0$, $D'_{\rm PS} = 0$ and $C'_{\rm PS} = D'_{\rm PS} = 0$ as was done for the standard quark mass fits to allow the model best fitting the data to be chosen. The results from these fits with $am_{\rm PCAC} = r + c_A(\tilde{\alpha})s$ are plotted against the average PCAC mass in Figures B.3 and B.4 and the coefficients summarised in Table B.2. Results with $am_{\rm PCAC,imp} = r_{\rm imp} + c_A(\tilde{\alpha})s_{\rm imp}$ are plotted in Figures B.5 and B.6 and the coefficients summarised in Table B.3.

It is worth mentioning that the χ^2/dof values for these fits are quite large when compared to the results of the standard quark mass analysis. Further investigation found that the fits vastly improved with the addition of a constant term to the model. In general the values of the intercept were found to be significantly different from zero. Choice of coupling and definition of $am_{\rm PCAC}$ had no significant effect on this result indicating that the problem lies with the actual model itself. This is backed up by Collins *et al.* [55] who found for the quenched dataset at $\beta = 5.93$ that the addition of a chiral log term restored the expected behaviour in the chiral limit. Such an analysis has not been attempted here although it would be interesting to apply it to the other datasets.

Extrapolations in $aM_{\rm PS}$

Fits to variables calculated with non-degenerate values of κ have been performed with the following ansatz,

$$X(\kappa_{\rm val,1}, \kappa_{\rm val,2}) = A_X + B_X(aM_{\rm PS,val})^2 + C_X(aM_{\rm PS,val})^4, \tag{4.38}$$

where $X \in \{aM_{\rm V}, aM_{\rm A}, aM_{\rm B}, aM_{\rm S}, af_{\rm PS}^{(0)}, af_{\rm PS}^{(1)}, af_{\rm PS,imp}^{(1)}, f_{\rm V}^{(0)}, f_{\rm V}^{(1)}, f_{\rm V,imp}^{(1)}, f_{\rm A}^{(0)}\}$ and

$$aM_{\mathrm{PS,val}} = aM_{\mathrm{PS}}(\kappa_{\mathrm{val},1}, \kappa_{\mathrm{val},2}). \tag{4.39}$$

The decay constants have not been improved and renormalised before fitting and their components fitted instead. This has the advantage that any future improvements in the determination of the improvement coefficients and renormalisation factors can be immediately transferred to the results given here.

The fit form in Equation (4.38) was used in order to model curvature in the data and to give more realistic error estimates than those of a linear model where $C_X = 0$. The results of these fits are plotted in Figures B.7 to B.28 and the coefficients collected in Tables B.4 to B.14.

What is clear from the results is that all of the fits worked extremely well. This would be perfect if all systematic errors in the data were well under control and the model function was motivated from theory. Unfortunately neither of these is true and this means that any trends in the systematic errors will be modelled along with the actual signal. I am particularly concerned here with finite-size effects in the data although other systematic effects such as that coming from the sliding window analysis procedure may introduce trends.

The JLQCD collaboration found clear evidence of finite-size effects [53] in simulations with Wilson quarks at $\beta = 5.2$. In their analysis they found that smaller volumes tended to overestimate the mass and that the size of the effect increased as both κ_{val} and κ_{sea} were decreased. The implications for the partial quenched chiral extrapolations performed here is that such an effect should show up as a slowing in the decrease of the hadron mass as the valence quark mass is reduced. This behaviour is, for example, seen in the extrapolation of aM_{V} for the dataset at $(5.2, 0.1355)$ on page 198. It is most obvious, however, in the extrapolations of aM_{S} on page 204 with the dataset at $(5.2, 0.1358)$ even exhibiting a turning point in the data. Although such behaviour cannot be definitively attributed to finite-size effects without performing further simulations with larger volumes it does, where necessary, demand a certain caution with the data and any results derived from it.

The baryon masses, which were only calculated with degenerate values of κ_{val}, have been fitted to the following ansatz,

$$X(\kappa_{\mathrm{val}}) = A_X + B_X(aM_{\mathrm{PS,val}})^2 + C_X(aM_{\mathrm{PS,val}})^4, \tag{4.40}$$

where $X \in \{aM_{\mathrm{N}}^+, aM_{\mathrm{N}}^-, aM_{\Delta}^+, aM_{\Delta}^-\}$. Results for these fits can be found in Figures B.29 to B.36 and Tables B.15 to B.18. Fits to the lighter positive parity states generally show the expected monotonic decrease with valence quark mass with the exception of the aM_{Δ}^+ fit for the lightest dataset at $(5.2, 0.1358)$ shown on page 224 which reaches a plateau within errors for low valence quark masses. Finite-size effects are expected to be large in this case although, unusually, the same behaviour is not exhibited by the dataset at $(5.2, 0.13565)$.

Fits to aM_{N}^- also show the expected decrease with quark mass and agree well with the data except at $(5.2, 0.1358)$ where $\chi^2/\mathrm{dof} = 1.543$ and the data has a clear turning point. Results for aM_{Δ}^-, in contrast to the nucleon, show no clear signals except for the datasets at $(5.2, 0.1350)$ and $(5.26, 0.1345)$.

4.3.2 Full chiral extrapolations

Full chiral extrapolations have been performed in a similar manner to the partially quenched case with the addition that they are performed simultaneously in the sea and valence directions. The matched dynamical datasets allow such an extrapolation to be performed at a fixed value of the lattice spacing whilst the datasets at $\beta = 5.2$ allow fixed β extrapolations to be performed in a similar manner to the JLQCD collaboration [53] and the CP-PACS collaboration [65]. Before performing these extrapolations the masses and decay constants were examined to check for the expected trends as the sea quark mass is reduced. Some of the hadron masses for the dataset at $(5.2, 0.1358)$ were found to lie above comparable values from datasets at higher sea quark mass. Such behaviour is consistent with sea quark induced finite-size effects and the dataset has therefore been omitted from any extrapolations.

Extrapolations of $aM_{\rm PS}$

Extrapolations of $aM_{\rm PS}$ have again been performed to the standard and PCAC definitions of the quark mass. For the standard quark mass the following ansatz has been used to model the data,

$$\begin{aligned}(aM_{\rm PS})^2(am_{\rm sea};am_1,am_2) = B^{\rm PS}_{\rm s} am_{\rm sea} + B^{\rm PS}_{\rm v}\,(am_1+am_2) + C^{\rm PS}_{\rm ss}(am_{\rm sea})^2\\ +C^{\rm PS}_{\rm vv}\,(am_1+am_2)^2 + C^{\rm PS}_{\rm sv} am_{\rm sea}\,(am_1+am_2) + D^{\rm PS}_{\rm vv} am_1 am_2\end{aligned} \tag{4.41}$$

where

$$am_{\rm sea} = \frac{1}{2}\left(\frac{1}{\kappa_{\rm sea}} - \frac{1}{\kappa_{\rm crit}}\right). \tag{4.42}$$

and the valence quark masses are defined as before. Because there were only three datasets involved in the full fits, however, it was also necessary to ensure that only terms linear in $am_{\rm sea}$ survived when $am_1 = am_2 = am_{\rm sea}$ i.e. in the unitary direction. This was done by making sure the constraint,

$$C^{\rm PS}_{\rm ss} + 4\;C^{\rm PS}_{\rm vv} + 2\;C^{\rm PS}_{\rm sv} + D^{\rm PS}_{\rm vv} = 0, \tag{4.43}$$

was satisfied during the fitting process.

It is important to realise that the above fit form implies a unique value of $\kappa_{\rm crit}$ for all of the datasets involved as defined through $(aM_{\rm PS})^2(0;0,0) = 0$. Such a definition is consistent with an extrapolation in full QCD where only the unitary points are included. The above fit can therefore be seen as an attempt to make use of the data at $\kappa_{\rm val} \neq \kappa_{\rm sea}$ which, as discussed earlier, is less expensive to calculate in lattice simulations and can be used to improve the determination of physical quantities in full QCD.

Instead of performing extrapolations using the non-linear model function in Equation (4.41) the pseudoscalar mass has been extrapolated directly in $\kappa_{\rm sea}$, $\kappa_{\rm val,1}$ and

$\kappa_{\mathrm{val},2}$ using the following fit ansatz,

$$(aM_{\mathrm{PS}})^2(\kappa_{\mathrm{sea}};\kappa_{\mathrm{val},1},\kappa_{\mathrm{val},2}) = A + B_{\mathrm{s}}\frac{1}{\kappa_{\mathrm{sea}}} + B_{\mathrm{v}}\left(\frac{1}{\kappa_{\mathrm{val},1}} + \frac{1}{\kappa_{\mathrm{val},2}}\right) + C_{\mathrm{ss}}\frac{1}{\kappa_{\mathrm{sea}}{}^2}$$
$$+C_{\mathrm{vv}}\left(\frac{1}{\kappa_{\mathrm{val},1}} + \frac{1}{\kappa_{\mathrm{val},2}}\right)^2 + C_{\mathrm{sv}}\frac{1}{\kappa_{\mathrm{sea}}}\left(\frac{1}{\kappa_{\mathrm{val},1}} + \frac{1}{\kappa_{\mathrm{val},2}}\right) + D_{\mathrm{vv}}\frac{1}{\kappa_{\mathrm{val},1}}\frac{1}{\kappa_{\mathrm{val},2}}, \tag{4.44}$$

with the following constraint on the parameters,

$$C_{\mathrm{ss}} + 4\ C_{\mathrm{vv}} + 2\ C_{\mathrm{sv}} + D_{\mathrm{vv}} = 0. \tag{4.45}$$

The results from these fits have then been used to determine κ_{crit} and transformed to the form of Equation (4.41). The fit coefficients are given in Tables B.19 and B.20 and plots of aM_{PS} versus $1/\kappa_{\mathrm{eff}}$ given in Figures B.37 and B.38 for the matched and $\beta = 5.2$ extrapolations respectively. The plots show a single curve for each dataset, generated by holding κ_{sea} fixed, and a unitary curve, generated by taking $\kappa_{\mathrm{val},1} = \kappa_{\mathrm{val},2} = \kappa_{\mathrm{sea}}$. A detailed comparison of the single dataset curves was made with the results of the partially quenched extrapolations by fixing κ_{sea} in Equation (4.44). The effective fit coefficients from the full fits were found to be consistent with those from the partially quenched extrapolations within errors for all datasets within the matched and $\beta = 5.2$ sets. In addition the effective values of κ_{crit} were also found to be consistent.

An important difference, however, arises when the κ values are translated into quark masses. In the full fits it is clear that $aM_{\mathrm{PS}} > 0$ when $am_1 = am_2 = 0$ if $am_{\mathrm{sea}} > 0$. This is in stark contrast to the partially quenched case where aM_{PS} is defined to vanish with the valence quark mass. The primary cause of this discrepancy is the explicit chiral symmetry breaking introduced by the Wilson term in the quark action [66]. The result is that the value of κ_{val} where aM_{PS} vanishes, i.e. κ_{crit} from the partially quenched extrapolations, is dependent on κ_{sea} with limiting value given by κ_{crit} from the full chiral extrapolation. Any discrepancy between physical predictions of the two methods should, however, vanish after extrapolating the partially quenched results in am_{sea} and performing a continuum extrapolation.

Full chiral extrapolations of aM_{PS} versus the PCAC mass were attempted using the following ansatz,

$$\begin{aligned}(aM_{\mathrm{PS}})^2 = {B'}^{\mathrm{PS}}_{\mathrm{v}}\left(am_1^{\mathrm{PCAC}} + am_2^{\mathrm{PCAC}}\right) + {C'}^{\mathrm{PS}}_{\mathrm{vv}}\left(am_1^{\mathrm{PCAC}} + am_2^{\mathrm{PCAC}}\right)^2 \\ + {C'}^{\mathrm{PS}}_{\mathrm{sv}} am_{\mathrm{sea}}^{\mathrm{PCAC}}\left(am_1^{\mathrm{PCAC}} + am_2^{\mathrm{PCAC}}\right) + {D'}^{\mathrm{PS}}_{\mathrm{vv}} am_1^{\mathrm{PCAC}} am_2^{\mathrm{PCAC}}\end{aligned} \tag{4.46}$$

where

$$am_{\mathrm{sea}}^{\mathrm{PCAC}} = am^{\mathrm{PCAC}}(\kappa_{\mathrm{sea}}, \kappa_{\mathrm{sea}}). \tag{4.47}$$

The absence of a constant term or any monomials exclusively in $am_{\mathrm{sea}}^{\mathrm{PCAC}}$ is to ensure that $(aM_{\mathrm{PS}})^2$ vanishes with $am_{\mathrm{val}}^{\mathrm{PCAC}}$ for each value of $am_{\mathrm{sea}}^{\mathrm{PCAC}}$ and a constraint has again been applied in order to ensure the unitary fit contains no quadratic contributions. These fits did not model the data well with $\chi^2/\mathrm{dof} = 7.21$ for the matched sets and $\chi^2/\mathrm{dof} = 4.24$ for the $\beta = 5.2$ case. I plot the result of the matched fit in Figure B.39 and collect the fit coefficients in Table B.21. It is clear from the plot that the data for the set at $(5.2, 0.1350)$ lies above that of the other sets and therefore does not follow the trend set by $(5.26, 0.1345)$ and $(5.29, 0.1340)$. Comparing Equation (4.46) to the partially quenched formula in Equation (4.36) shows that the trend implicit in Equation (4.46) is given by

$$B'_{\mathrm{PS}} = {B'}^{\mathrm{PS}}_{\mathrm{s}} + {C'}^{\mathrm{PS}}_{\mathrm{sv}} am_{\mathrm{sea}}^{\mathrm{PCAC}}. \tag{4.48}$$

In addition the following relations must hold,

$$C'_{\mathrm{PS}} = {C'}^{\mathrm{PS}}_{\mathrm{vv}} \qquad \text{and} \qquad D'_{\mathrm{PS}} = {D'}^{\mathrm{PS}}_{\mathrm{vv}}, \tag{4.49}$$

for all of the datasets included in the fit. None of these relations are, however, satisfied for the matched datasets as can be seen in Table B.2. This result is therefore unusable in any further analysis and casts some doubt on the results from the dataset at $(5.2, 0.1350)$.

In contrast the data at $\beta = 5.2$ does appear to meet the requirements above as a comparison of the partially quenched results shows. The problem was found to stem from attempting the combined constraint of using Equation (4.46) and requiring a linear unitary fit form as a relaxation of these constraints confirmed. For example I plot the result of a fit to

$$\begin{aligned}(aM_{\mathrm{PS}})^2 = {} & B'^{\mathrm{PS}}_{\mathrm{s}} am^{\mathrm{PCAC}}_{\mathrm{sea}} + B'^{\mathrm{PS}}_{\mathrm{v}} \left(am^{\mathrm{PCAC}}_1 + am^{\mathrm{PCAC}}_2\right) + C'^{\mathrm{PS}}_{\mathrm{ss}} (am^{\mathrm{PCAC}}_{\mathrm{sea}})^2 \\ & + C'^{\mathrm{PS}}_{\mathrm{vv}} \left(am^{\mathrm{PCAC}}_1 + am^{\mathrm{PCAC}}_2\right)^2 + C'^{\mathrm{PS}}_{\mathrm{sv}} am^{\mathrm{PCAC}}_{\mathrm{sea}} \left(am^{\mathrm{PCAC}}_1 + am^{\mathrm{PCAC}}_2\right) \\ & + D'^{\mathrm{PS}}_{\mathrm{vv}} am^{\mathrm{PCAC}}_1 am^{\mathrm{PCAC}}_2 \end{aligned} \tag{4.50}$$

for the $\beta = 5.2$ datasets in Figure B.40 with coefficients summarised in Table B.22. This fit clearly models the data well although it does relax the constraint that $aM_{\mathrm{PS}}(am^{\mathrm{PCAC}}_{\mathrm{sea}}; 0, 0) = 0$ for each dataset. The unitary contraint that $(aM_{\mathrm{PS}})^2(0; 0, 0) = 0$ still holds, however, and this is enough to allow the results of this fit to be used in a determination of the light quark masses.

Extrapolations in aM_{PS}

All of the remaining observables studied in this thesis have been extrapolated using the following fit ansatz,

$$\begin{aligned} X(\kappa_{\mathrm{sea}}; \kappa_{\mathrm{val},1}, \kappa_{\mathrm{val},2}) = {} & A^X + B^X_{\mathrm{s}} (aM_{\mathrm{PS,sea}})^2 + B^X_{\mathrm{v}} (aM_{\mathrm{PS,val}})^2 \\ & + C^X_{\mathrm{ss}} (aM_{\mathrm{PS,sea}})^4 + C^X_{\mathrm{vv}} (aM_{\mathrm{PS,val}})^4 + C^X_{\mathrm{sv}} (aM_{\mathrm{PS,sea}})^2 (aM_{\mathrm{PS,val}})^2, \end{aligned} \tag{4.51}$$

where

$$aM_{\mathrm{PS,sea}} = aM_{\mathrm{PS}}(\kappa_{\mathrm{sea}}, \kappa_{\mathrm{sea}}) \tag{4.52}$$

and the quadratic parameters have been constrained to satisfy

$$C^X_{\rm ss} + C^X_{\rm vv} + C^X_{\rm sv} = 0. \tag{4.53}$$

In contrast to the partially quenched case it was necessary to improve and renormalise the decay constants before performing the fits. The renormalised pseudoscalar decay constant is defined by

$$af^{(R)}_{\rm PS} = Z_A\left(1 + b_A\tfrac{1}{2}(am_1 + am_2)\right)\left(af^{(0)}_{\rm PS} + c_A\, af^{(1)}_{\rm PS}\right), \tag{4.54}$$

with the expression for $af^{(R)}_{\rm PS,imp}$ given by replacing $af^{(1)}_{\rm PS}$ with $af^{(1)}_{\rm PS,imp}$. For the vector meson the corresponding expression is

$$\frac{1}{f^{(R)}_{\rm V}} = Z_V\left(1 + b_V\tfrac{1}{2}(am_1 + am_2)\right)\left(f^{(0)}_{\rm V} + c_V\, f^{(1)}_{\rm V}\right), \tag{4.55}$$

again with a similar expression for $f^{(R)}_{\rm V,imp}$. Finally, the axial vector meson decay constant is given by

$$\frac{1}{f^{(R)}_{\rm A}} = Z_A\left(1 + b_A\tfrac{1}{2}(am_1 + am_2)\right) f^{(0)}_{\rm A}. \tag{4.56}$$

Results for full chiral extrapolations to $aM_{\rm PS}$ are given in Section B.2.

The basic expectations built into Equation (4.51) are that the intercept and slope of the data from each dataset, as measured at $aM_{\rm PS,val} = 0$, should be expressible as a quadratic and linear function in $(aM_{\rm PS,sea})^2$ respectively. Furthermore it is expected that the intercept and slope are either increasing or decreasing functions of $(aM_{\rm PS,sea})^2$. This is especially so of the intercept which is expected to decrease with $(aM_{\rm PS,sea})^2$ and therefore with $am_{\rm sea}$. Any deviation from this would tend to indicate the presence of significant finite-size effects associated with small $am_{\rm sea}$.

Fits to the meson masses were generally found to agree with expectations. One small exception, however, is the $aM_{\rm V}$ fit to the matched data for which the unitary curve, although consistent with the partially quenched curves within errors, does have a higher value of $aM_{\rm V}$ in the chiral limit. Another more serious situation exists in the matched fit for $aM_{\rm B}$ shown on page 236 where the data for the $(5.29, 0.1340)$ dataset can clearly be seen to lie between the other two sets. This is not what is expected or built into Equation (4.51) and the fit clearly fails to model the data correctly. One final point is that in some cases the lower two datasets overlap within errors. This does not pose a serious problem but may indicate the presence of finite-size effects associated with $am_{\rm sea}$ in the data.

In the baryon sector fits to $aM_{\rm N}^{+}$ were found to model the data reasonably well although the unitary curve in the matched fit has a significantly higher value in the chiral limit than the partially quenched curves. This is consistent with finite size effects although it could also be an artefact caused by the use of an effectively linear model in the unitary direction. No such problems were found for the $\beta = 5.2$ fit. Fits to aM_{Δ}^{+} show good agreement with expectations within errors although the data for the lightest two sets overlap in both the matched and $\beta = 5.2$ cases.

For the negative parity baryons only the $\beta = 5.2$ fit to $aM_{\rm N}^{-}$ appears to work although even in this case the two lightest sets overlap within errors. The other three fits show all the signs of significant finite-size effects. For the matched datasets the ordering of the masses from different sets is contrary to expectations. This is especially so for aM_{Δ}^{-} where the masses from the different datasets lie in reverse order. At $\beta = 5.2$, the fit to aM_{Δ}^{-} shows that the lightest two sets lie along consistent curves. These curves, however, are roughly constant functions of $aM_{\rm PS,val}$ which as mentioned earlier is an expected sign of finite-size effects associated with the valence quark mass.

The pseudoscalar meson decay constant fits do not agree with the data. In the matched case this is due to the unexpected position of the data for the $(5.2, 0.1350)$ dataset. Such a trend is not seen in similar fits perormed by the CP-PACS [65] and JLQCD [53] collaborations or in the $\beta = 5.2$ fit which shows the expected trends in the data. This makes it unlikely that finite-size effects are the cause, a conclusion that is supported by the findings of [52]. The same unusual trends were also observed for $af_{\rm PS}^{(0)}$, $af_{\rm PS}^{(1)}$ and in the matrix elements, $\mathcal{A}_{A_4}^{\rm PS}$

and $\mathcal{A}_P^{\mathrm{PS}}$ as a function of aM_{PS}. This could account for the unexpected result found in the fits to am_{PCAC} which depends explicitly on these matrix elements. At present no known cause has been found for these discrepancies and the results of the fit to $af_{\mathrm{PS}}^{(R)}$ for the matched datasets have not been used in any further analysis.

The discussion above can maybe also explain the failure of the $\beta = 5.2$ fit. The data at $\kappa_{\mathrm{sea}} = 0.1350$ clearly exhibits a significantly different dependence on $aM_{\mathrm{PS,val}}$ than the other sets at $\beta = 5.2$ and could therefore cause an already constrained fit to fail totally. Overall these results mean that no prediction of the physical pseudoscalar decay constants is possible from the full fits.

Fits of the vector meson decay constant for the matched datasets behave as expected although this is within large errors. For the $\beta = 5.2$ datasets, however, the ordering of the data is not as expected with the data from the set at $(5.2, 0.1350)$ having lower values of $f_{\mathrm{V}}^{(R)}$ than the two lighter sets at comparable $aM_{\mathrm{PS,val}}$. In order to investigate this further a comparison with the results of the CP-PACS collaboration [65], who define the vector decay constant in a similar way to the pseudoscalar decay constant, was made. Their results show a clear reduction of the decay constant with $aM_{\mathrm{PS,sea}}$ at fixed $aM_{\mathrm{PS,val}}$ whereas the simulations presented here show that the data for $(5.2, 0.13565)$ is consistent with or above those of the set at $(5.2, 0.1355)$. Finite-size effects are therefore expected.

For the case of the axial vector meson decay constant both the matched data and the data at $\beta = 5.2$ can be seen to overlap and there is some indication that the data does not follow the expected trends. Because of this the unitary fit curves can be seen to predict higher values for $f_{\mathrm{A}}^{(R)}$ in the chiral limit than the partially quenched fits although this is less pronounced in the $\beta = 5.2$ fit. Finite-size effects are again a possibility although no firm conclusion can be made without more data.

Fitting r_0

Fits have been performed to r_0/a and a/r_0 as a function of $aM_{\mathrm{PS,sea}}$ for the matched and $\beta = 5.2$ datasets respectively. Such fits were necessary in order to use r_0/a to set the scale and make physical predictions from the full extrapolations. For the matched datasets the fit was performed to a constant function since r_0/a is supposed to be constant for these datasets. For the $\beta = 5.2$ datasets a/r_0 was fit in preference to r_0/a in order to simplify its use in setting the scale. The following expression was used to perform the fit,

$$a/r_0 = A_{r_0} + B_{r_0}(aM_{\mathrm{PS,sea}})^2, \tag{4.57}$$

although there is no theoretical motivation for this particular form. Higher polynomial terms were excluded since there are only three data points. The results for these fits are plotted in Figure B.63 and the coefficients given in Table B.45. The values of χ^2/dof may seem quite high, especially for the $\beta = 5.2$ set, but the Q values indicate that the results are reasonable.

4.4 Determination of the physical points

In this section I present results for the hadron masses, meson decay constants and quark masses calculated using the results of the partially quenched and full chiral extrapolations. In order to make such predictions it is necessary to set the mass scale (through a), fix the light point i.e. determine the normal (or average up/down) quark mass, $am_{\mathrm{n}} = (am_{\mathrm{u}} + am_{\mathrm{d}})/2$, and fix the strange point i.e. determine am_{s}. I now discuss each of these in turn.

4.4.1 Setting the scale

In this work I have used two distinct variables to set the mass scale, namely the rho mass, $M_\rho = 771.1$ MeV, and the Sommer scale parameter, $r_0^{\mathrm{phys}} = 0.5$ fm.

Setting the scale with r_0 is a simple procedure for the partially quenched analysis and for the full matched extrapolation where r_0 is fixed. The lattice spacing is defined in these situations by

$$a_{r_0} = r_0^{\mathrm{phys}}/(r_0/a), \tag{4.58}$$

where (r_0/a) denotes the value from lattice simulations. For the $\beta = 5.2$ simulations, however, (r_0/a) varies with $aM_{\mathrm{PS,sea}}$ and the determination of a must therefore be done at the light point. This has been done by solving the following equation for $aM_{\mathrm{PS,sea}}$,

$$(r_0/a)(aM_{\mathrm{PS,sea}}) = \frac{aM_{\mathrm{PS,sea}}}{A_{r_0} + B_{r_0}(aM_{\mathrm{PS,sea}})^2} = r_0^{\mathrm{phys}} M_\pi, \tag{4.59}$$

where the pion mass, $M_\pi = 134.9766$ MeV. The value of (r_0/a) at the light point was then used to fix the lattice spacing from Equation (4.58).

Setting the scale with M_ρ also has to be performed at the light point. For partially quenched simulations this has been done by solving the following equation

$$\frac{aM_{\mathrm{V}}}{aM_{\mathrm{PS,val}}} = \frac{A_{\mathrm{V}} + B_{\mathrm{V}}(aM_{\mathrm{PS,val}})^2 + C_{\mathrm{V}}(aM_{\mathrm{PS,val}})^4}{aM_{\mathrm{PS,val}}} = \frac{M_\rho}{M_\pi} \tag{4.60}$$

for $aM^2_{\mathrm{PS,val}}$. The value of aM_{V} at this point was then be used to fix the lattice spacing by solving,

$$a_\rho = aM_{\mathrm{V}}/M_\rho. \tag{4.61}$$

For the full fits the lattice spacing has been set in a similar way using the unitary fit result i.e. by setting $aM_{\mathrm{PS,val}} = aM_{\mathrm{PS,sea}}$ in Equation (4.51) and solving

$$\frac{aM_{\mathrm{V}}(aM_{\mathrm{PS,sea}}; aM_{\mathrm{PS,sea}})}{aM_{\mathrm{PS,sea}}} = \frac{M_\rho}{M_\pi}. \tag{4.62}$$

Results for the lattice spacing (in fm) are summarised in Table 4.2.

Dataset	a_ρ	a_{r_0}
$(5.2, 0.1350)$	$0.1144\,^{+36}_{-53}$	$0.1060\,^{+\ 5}_{-10}$
$(5.2, 0.1355)$	$0.1211\,^{+70}_{-94}$	$0.0992\,^{+\ 5}_{-11}$
$(5.2, 0.13565)$	$0.1062\,^{+51}_{-59}$	$0.09532\,^{+94}_{-58}$
$(5.2, 0.1358)$	$0.1135\,^{+41}_{-44}$	$0.0940\,^{+16}_{-\ 3}$
$(5.25, 0.1352)$	$0.1109\,^{+46}_{-59}$	$0.09753\,^{+87}_{-70}$
$(5.26, 0.1345)$	$0.1128\,^{+31}_{-42}$	$0.1057\,^{+16}_{-\ 7}$
$(5.29, 0.1340)$	$0.1144\,^{+77}_{-84}$	$0.1039\,^{+14}_{-\ 7}$
$(5.93, \text{quen.})$	$0.1208\,^{+27}_{-25}$	$0.10607\,^{+35}_{-24}$
matched	$0.1197\,^{+31}_{-35}$	$0.10539\,^{+63}_{-55}$
$\beta = 5.2$	$0.1057\,^{+32}_{-37}$	$0.0907\,^{+13}_{-\ 9}$

Table 4.2: Summary of results for the lattice spacing as determined through r_0 and M_ρ. Results are in fm.

The matched sets have a consistent value of a_{r_0} as expected although the value at $(5.29, 0.1340)$ is slightly low, especially when compared to the quenched result. Results for a_ρ also show consistency although with a lattice spacing around 10% higher than the a_{r_0} value. This increase is consistently true of a_ρ in all the datasets studied here and can be up to 20% larger than a_{r_0} as is the case at $(5.2, 0.1355)$ and $(5.2, 0.1358)$. Such a discrepancy between the two estimates of the lattice spacing would be expected purely on the grounds of discretisation errors. In this case, however, the sensitivity of a_ρ to the behaviour of aM_{V} in the chiral limit and therefore to the particular fit form used to model the data could induce a larger systematic effect. This would be compounded by any peculiar trends in the data as is the case at $(5.2, 0.1355)$ and offers an explanation of the large discrepancy between a_ρ and a_{r_0} in that case.

4.4.2 Determination of the normal quark mass

With the lattice spacing fixed the value of the normal quark mass can be determined. This has been done using the results of the pseudoscalar mass fits to both the standard and PCAC quark masses although only the standard quark results have been used to determine the spectrum. In the partially quenched case $am_{\rm n}$ has been fixed by solving the following equation,

$$(aM_{\rm PS})^2(am_{\rm n}, am_{\rm n}) = (aM_\pi)^2, \tag{4.63}$$

where $aM_{\rm PS}$ is defined either with Equation (4.34) or Equation (4.36) for the standard and PCAC quark masses respectively.

For the full fits $am_{\rm n}$ has been similarly defined through

$$(aM_{\rm PS})^2(am_{\rm n}; am_{\rm n}, am_{\rm n}) = (aM_\pi)^2. \tag{4.64}$$

using Equations (4.41) and (4.46) with $am_1 = am_2 = am_{\rm sea}$ and $am_1^{\rm PCAC} = am_2^{\rm PCAC} = am_{\rm sea}^{\rm PCAC}$ respectively. In this way the normal quark is treated as being fully dynamical.

4.4.3 Determination of the strange quark mass

The strange quark mass has been set in this thesis using $M_{\rm K} = 497.672$ MeV, $M_{\rm K^*} = 896.10$ MeV and $M_\phi = 1019.456$ MeV as inputs, where the ϕ meson is assumed to be a pure $\rm s\overline{s}$ state.

$M_{\rm K}$ input

For the partially quenched case, $am_{\rm s}$ has been defined using the K meson mass through the following equation,

$$aM_{\mathrm{PS}}(am_{\mathrm{n}}, am_{\mathrm{s}}) = aM_{\mathrm{K}}. \tag{4.65}$$

using the previous definitions of a. For the full fits the sea quark mass is fixed to am_{n} and the following equation then used to define am_{s},

$$aM_{\mathrm{PS}}(am_{\mathrm{n}}; am_{\mathrm{n}}, am_{\mathrm{s}}) = aM_{\mathrm{K}}. \tag{4.66}$$

With this done the mass of the unphysical η_{ss} state can be defined by

$$aM_{\eta_{\mathrm{ss}}} = aM_{\mathrm{PS}}(am_{\mathrm{n}}; am_{\mathrm{s}}, am_{\mathrm{s}}), \tag{4.67}$$

a result that has been used along with aM_{K} and aM_{π} to determine the rest of the hadron spectrum by substitution into Equations (4.38) and (4.51) for the partially quenched and full extrapolations respectively.

M_{K^*} input

The K* mass has been used to define am_{s} by first solving

$$aM_{\mathrm{V}}(aM_{\mathrm{PS,val}}) = aM_{\mathrm{K}^*} \tag{4.68}$$

for $aM_{\mathrm{PS,val}}$ which is then a lattice prediction of aM_{K}. The strange quark mass and η_{ss} mass have then been determined in an identical way to the M_{K} method. The procedure for the full fit works similarly after setting $aM_{\mathrm{PS,sea}} = aM_{\pi}$ in Equation (4.51).

M_{ϕ} input

The last method used here to fix the strange quark sector uses the ϕ meson mass as input. This was done by first solving

$$aM_{\mathrm{V}}(aM_{\mathrm{PS,val}}) = aM_{\phi}, \tag{4.69}$$

or a similar equation in the full fit case to give a lattice prediction for $aM_{\eta_{\mathrm{ss}}}$ and then

$$aM_{\mathrm{PS}}(am_{\mathrm{s}}, am_{\mathrm{s}}) = aM_{\eta_{\mathrm{ss}}} \tag{4.70}$$

solved to determine the bare strange quark mass. The K meson mass was then determined and the strange spectrum built from these results as before.

Overall the methods using strange vector meson masses were only successful if the scale was set by M_ρ. For this reason only the K mass was used to determine the strange sector when the scale was set by r_0.

4.4.4 Hadron mass spectrum

Results for the spectrum of light and strange mesons and light baryons have been tabulated in Sections C.1 and C.2 respectively. I have plotted results for the pseudoscalar and vector meson and the positive parity baryons in Figure 4.9 with the scale set using r_0 and the strange mass fixed through M_{K}.

In the meson sector the order of the states agrees with experiment within errors. What is clear, however, is that the lattice values all overestimate the physical masses indicating the presence of substantial discretisation errors. The overestimation is smallest in the matched dynamical sets where there is a reasonable agreement with the experimental K^* and ϕ mesons masses. The agreement is not as good for M_ρ or for the unphysical η_{ss} meson mass where the 'experimental' value is given from the Gell-Mann-Okubo mass formula

$$M_{\eta_{\mathrm{ss}}}^2 = \frac{1}{3}\left(4M_{\mathrm{K}}^2 - M_\pi^2\right) = 569.35 \text{ MeV}. \tag{4.71}$$

Despite having small statistical errors and the lattice results showing a surprising degree of consistency the values are still around 20% greater than the GMO

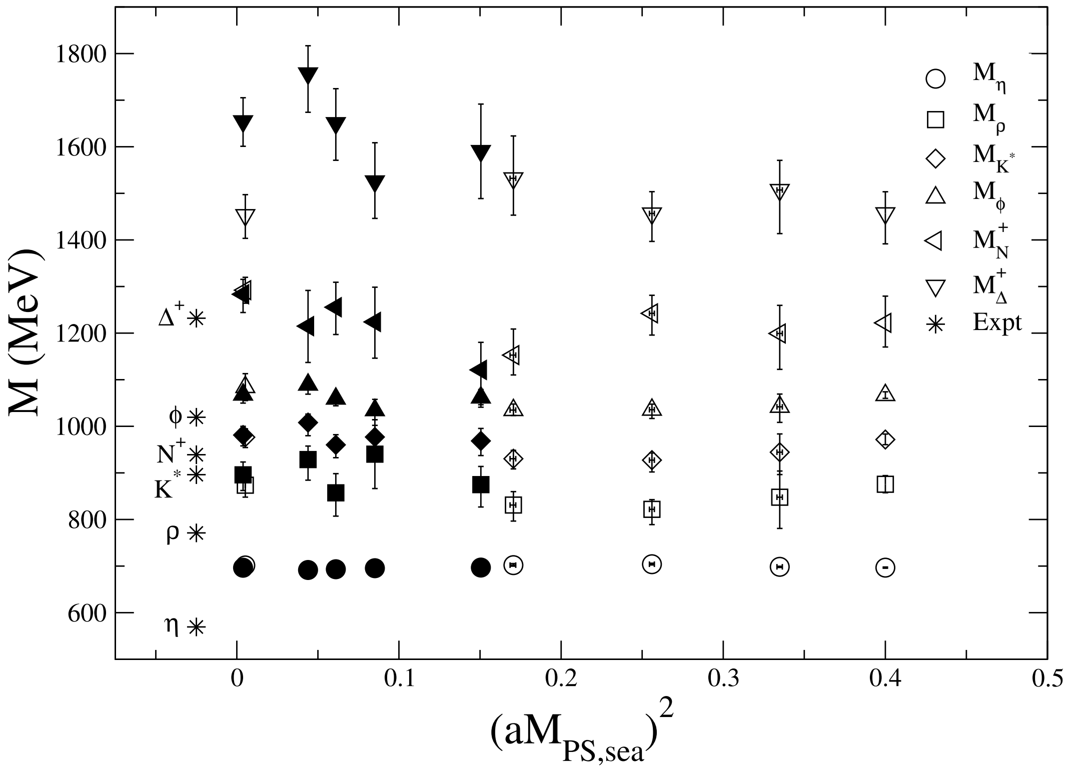

Figure 4.9: Plot of the hadron spectrum for all partially quenched and full fits with scale set by r_0 and am_s fixed by M_K. The matched datasets are indicated by transparent symbols and all others by solid symbols. The quenched set is plotted with $(aM_{PS,sea})^2 = 0.4$. Stars indicate the experimental points.

formula suggests. It is difficult, however, to say anything about the cause of this discrepancy.

In the baryon sector the correct order of positive parity states is maintained. The lattice results do, however, show a marked overestimation of the masses by as much as 40% in some cases. This could be simply due to discretisation errors although finite-size effects would explain such an effect. This hypothesis is consistent with the behaviour of M_Δ^+ for the $\beta = 5.2$ sets which actually increases as $(aM_{PS,sea})^2$ is reduced.

In Figure 4.10 I show similar results for the hadron spectrum with the scale set by M_ρ. The most obvious difference in this case is the general decrease in the lattice predictions. This is a direct result of a_ρ being consistently larger than a_{r_0} in all

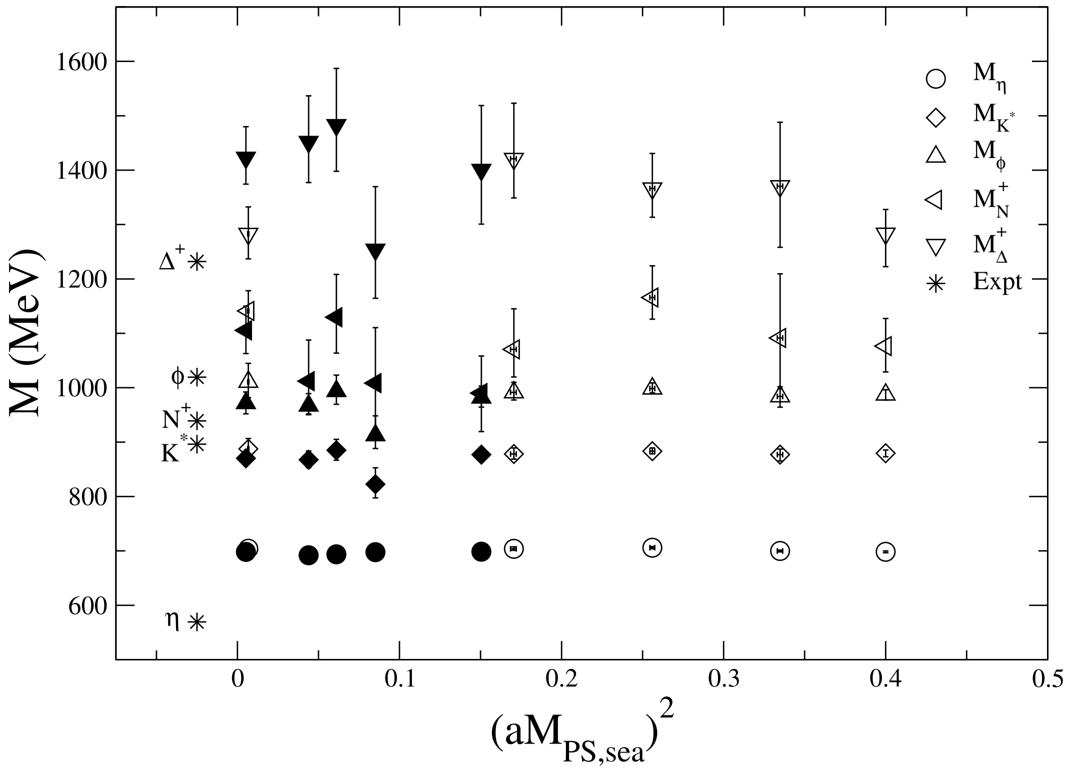

Figure 4.10: Plot of the hadron spectrum for all partially quenched and full fits with scale set by M_ρ and am_{s} fixed by M_{K}. The matched datasets are indicated by transparent symbols and all others by solid symbols. The quenched set is plotted with $(aM_{\mathrm{PS,sea}})^2 = 0.4$. Stars indicate the experimental points.

of the cases studied here and has the effect of bringing the lattice determinations of the hadron masses into much better agreement with the experimental values. This is true for all but the η_{ss} mass which stays relatively invariant at around 20% greater than the GMO value.

I have also investigated how the hadron spectrum is modified by the different choices of parameter used to fix the strange quark mass. The effect here is much less pronounced than that of the choice of parameter used to fix the lattice spacing but some observations can be made.

Perhaps the most important observation is that the strange meson masses increased slightly when the parameter used to fix m_{s} was changed from M_{K} to either M_{K^*} or M_ϕ. This change resulted in a better agreement of the lattice results for the K* and ϕ meson masses with the experimental value which was underestimated when using $M_{\rm K}$ to set the strange quark mass. The K meson mass was also predicted when the K* and ϕ inputs were used. Both of these choices gave consistent values for $M_{\rm K}$ but tended to overestimate it slightly. Some of the lattice results did agree with experiment, however, and this was most pronounced when using the results of the full chiral extrapolations to the matched datasets.

4.4.5 Meson decay constants

Results for the meson decay constants are summarised in Section C.3. Results from the full fits are only given for $f_{\rm V}^{(R)}$ in the matched case as all the other fits failed to produce sensible results.

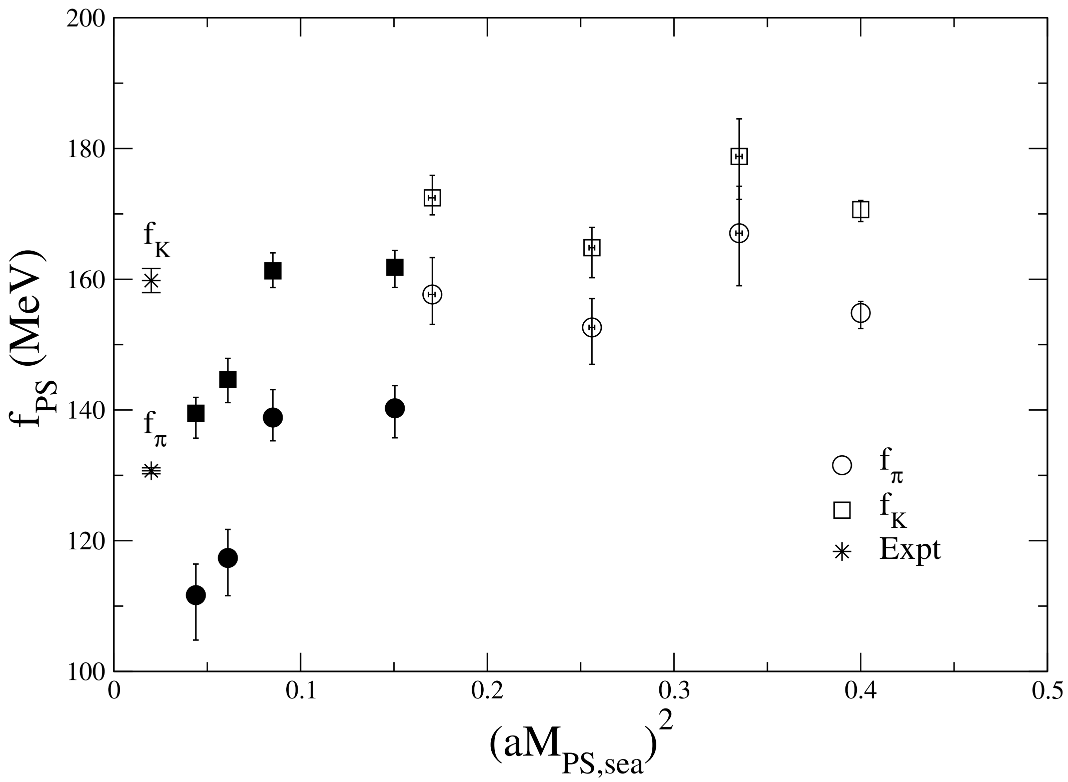

Figure 4.11: Plot of the pseudoscalar decay constants from partially quenched fits with scale set by r_0 and $am_{\rm s}$ fixed by $M_{\rm K}$. The matched datasets are indicated by transparent symbols and all others by solid symbols. The quenched set is plotted with $(aM_{\rm PS,sea})^2 = 0.4$. Stars indicate the experimental points.

In Figure 4.11 I plot the lattice predictions for the pseudoscalar decay constants along with the experimental results. As with the hadron spectrum the lattice results maintain the correct experimentally determined order although the results do fluctuate around the experimental values. The matched sets consistently overestimate the values of both f_π and f_K although the discrepancy is smaller for f_K. The opposite is true of the two lightest sets at $(5.2, 0.13565)$ and $(5.2, 0.1358)$ which underestimate both decay constants by around 15%.

When M_ρ was used to set the scale the matched results for f_π and f_K showed a much improved agreement with experiment. Results for the other datasets, however, tended to underestimate the physical values and this is especially noticeable at $(5.2, 0.13565)$ and $(5.2, 0.1358)$. Choice of the parameter used to fix the strange quark mass again has a small effect with the K^* and ϕ inputs yielding slightly larger value of f_K.

The large discrepancies seen between lattice and experimental values for f_π and f_K could be a result of systematic errors coming from the use of perturbative results for the renormalisation factor and improvement coefficients which also allow some $O(a)$ effects to remain. A useful dimensionless quantity in which most of these effects cancel is f_K/f_π. This ratio has been calculated for all of the datasets and the results given in Table 4.3.

Comparison with the experimental result, $f_\mathrm{K}/f_\pi = 1.223(15)$, shows that the matched datasets consistently fall short of this value whereas the other datasets are either consistent with or tend to overestimate it. There is some indication of a trend in the matched dynamical results toward the experimental value although this is gradual and the results are consistent within errors. A clearer trend is visible in the partially quenched results at $\beta = 5.2$ which also increase as the chiral limit is approached. Except in the r_0, M_K case, however, this trend appears to overshoot the experimental value by the time the $(5.2, 0.1358)$ dataset is reached. Discretisation effects are therefore expected to be large at the physical point.

Results for the vector and axial vector meson decay constants are plotted in Figure 4.12. The general ordering of their values is consistent with the expectation that they should increase with the quark masses. All of the datasets produce

Dataset	r_0, M_{K}	M_ρ, M_{K}	M_ρ, M_{K^*}	M_ρ, M_ϕ
$(5.2, 0.1350)$	$1.094\ ^{+20}_{-22}$	$1.108\ ^{+26}_{-29}$	$1.125\ ^{+35}_{-37}$	$1.121\ ^{+33}_{-36}$
$(5.2, 0.1355)$	$1.162\ ^{+16}_{-16}$	$1.231\ ^{+31}_{-34}$	$1.40\ ^{+\ 8}_{-11}$	$1.318\ ^{+40}_{-60}$
$(5.2, 0.13565)$	$1.233\ ^{+36}_{-24}$	$1.281\ ^{+49}_{-44}$	$1.307\ ^{+85}_{-71}$	$1.312\ ^{+70}_{-67}$
$(5.2, 0.1358)$	$1.249\ ^{+52}_{-38}$	$1.346\ ^{+64}_{-56}$	$1.43\ ^{+11}_{-10}$	$1.424\ ^{+86}_{-86}$
$(5.25, 0.1352)$	$1.154\ ^{+17}_{-12}$	$1.194\ ^{+28}_{-24}$	$1.227\ ^{+52}_{-44}$	$1.227\ ^{+47}_{-41}$
$(5.26, 0.1345)$	$1.080\ ^{+13}_{-11}$	$1.091\ ^{+13}_{-14}$	$1.101\ ^{+16}_{-16}$	$1.099\ ^{+15}_{-16}$
$(5.29, 0.1340)$	$1.070\ ^{+15}_{-14}$	$1.085\ ^{+23}_{-21}$	$1.099\ ^{+35}_{-28}$	$1.098\ ^{+32}_{-27}$
$(5.93, \mathrm{quen.})$	$1.1020\ ^{+68}_{-58}$	$1.1289\ ^{+97}_{-89}$	$1.147\ ^{+17}_{-15}$	$1.147\ ^{+15}_{-14}$

Table 4.3: Ratio of f_{K} over f_π for all datasets. Column headings indicate the choice of scale setting parameter and input used to fix the strange quark mass.

roughly consistent determinations of the decay constants although there is some sign of a trend in the matched results towards smaller values as the chiral limit is approached. This effect is most noticeable for f_ρ.

4.4.6 Quark masses

Renormalised quark masses have been calculated in the $\overline{\mathrm{MS}}$ scheme at a reference scale of 2 GeV for both the standard and PCAC definitions of the bare quark mass. This process required the bare quark masses to be renormalised and matched onto the continuum scheme at a particular scale, μ. When using tadpole improved perturbative results this should be done at a scale which minimises the systematic error coming from the truncation of the perturbation series [30]. Determination this best scale, q^*, is a non-trivial problem and has not been attempted here. Instead I have renormalised the quark masses with $\mu = 1/a$ and $\mu = \pi/a$ in order to gauge the likely systematic effect associated with the choice of matching scale. Once renormalised the quark masses have to be run to the reference scale of 2 GeV. This has been done using the Mathematica package RunDec [67] which implements four-loop running of the quark masses from perturbation theory. The

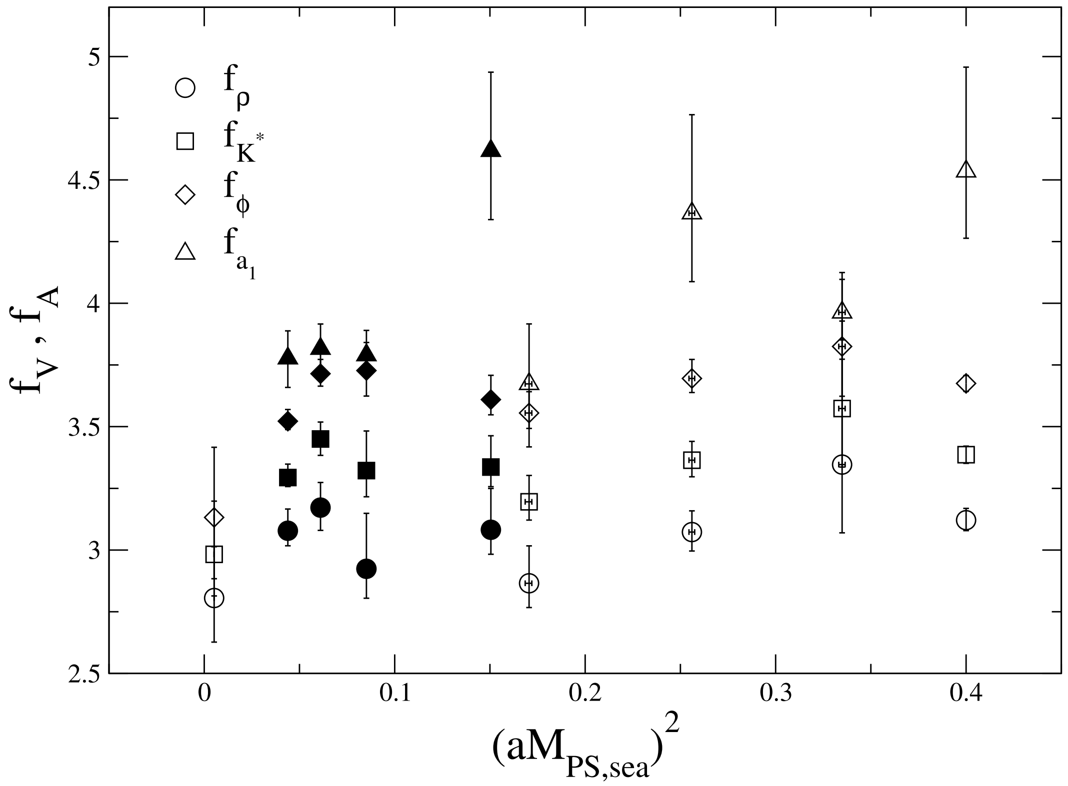

Figure 4.12: Plot of the vector and axial vector decay constants with scale set by r_0 and am_s fixed by M_K. The matched datasets are indicated by transparent symbols and all others by solid symbols. The quenched set is plotted with $(aM_\mathrm{PS,sea})^2 = 0.4$. Stars indicate the experimental points.

results for the quark masses are summarised in Section C.4.

A clear systematic difference exists between the renormalised quark masses determined from the standard and PCAC definitions of the bare quark mass in these results. PCAC mass determinations of both the normal and strange quark masses are consistently around 20% smaller than the standard definition gives. The two definitions need not, however, give the same results at finite lattice spacing with each having its own particular discretisation errors. They should, however, converge to the same answer in the continuum limit.

The effect coming from the choice of scale setting parameter is around $5 - 10\%$ with the a_{r_0} results being consistently smaller. At first glance this appears to be contrary to expectations given the relative sizes of the two lattice spacings and the role they play in setting the scale. The lattice spacing does, however, enter at the point where the bare quark masses are fixed using hadron masses and the effect here is for the quark masses to increace with the lattice spacing. This must be the more influential effect as it dominates the dependence of the renormalised mass on the lattice spacing. Again, variation with the choice of lattice spacing can be put down to discretisation errors and consistent results should be found in the continuum limit.

The strange quark mass, not surprisingly, shows a clear dependence on the parameter used to fix it. There is a significant difference of around $10-15\%$ between the K and K* determinations with results from K* and ϕ giving consistent values for the quark mass within errors. This is true of all but the results for the $(5.2, 0.1355)$ dataset which show an unusually high value for $m_{\mathrm{s}}^{\overline{MS}}$ when either the K* or ϕ mass is used. Again, these discrepancies can be put down to discretisation effects and tends to indicate that such effects are significant at the lattice spacings studied here.

Finally the systematic effect coming from the choice of matching scale should be discussed. For the standard definition of the quark mass the results with $\mu = \pi/a$ were found to lie around 5% higher than the results with $\mu = 1/a$. This is a clear systematic difference and the resulting error should be included in the determined values of the quark masses. For the PCAC definition of the quark mass the results at $\mu = \pi/a$ and $\mu = 1/a$ show very little difference within errors with the masses at $\mu = \pi/a$ being at most 1% larger than those at $\mu = 1/a$. This clear difference between the standard and PCAC quark masses is possibly due to the differences in the way the scale enters their calculation.

In order to discuss any trends between the different datasets I have plotted $m_{\mathrm{n}}^{\overline{MS}}$ and $m_{\mathrm{s}}^{\overline{MS}}$ with the lattice spacing fixed through M_ρ and M_{K} used to determine am_{s} for both the standard and PCAC definitions of the quark mass in Figures 4.13 and 4.14 respectively.

One of the most unexpected observations is the striking similarity between the plots for $m_{\mathrm{n}}^{\overline{MS}}$ and $m_{\mathrm{s}}^{\overline{MS}}$. This is certainly due to the fact that both masses were determined exclusively from the pseudoscalar fit data. The only clear difference

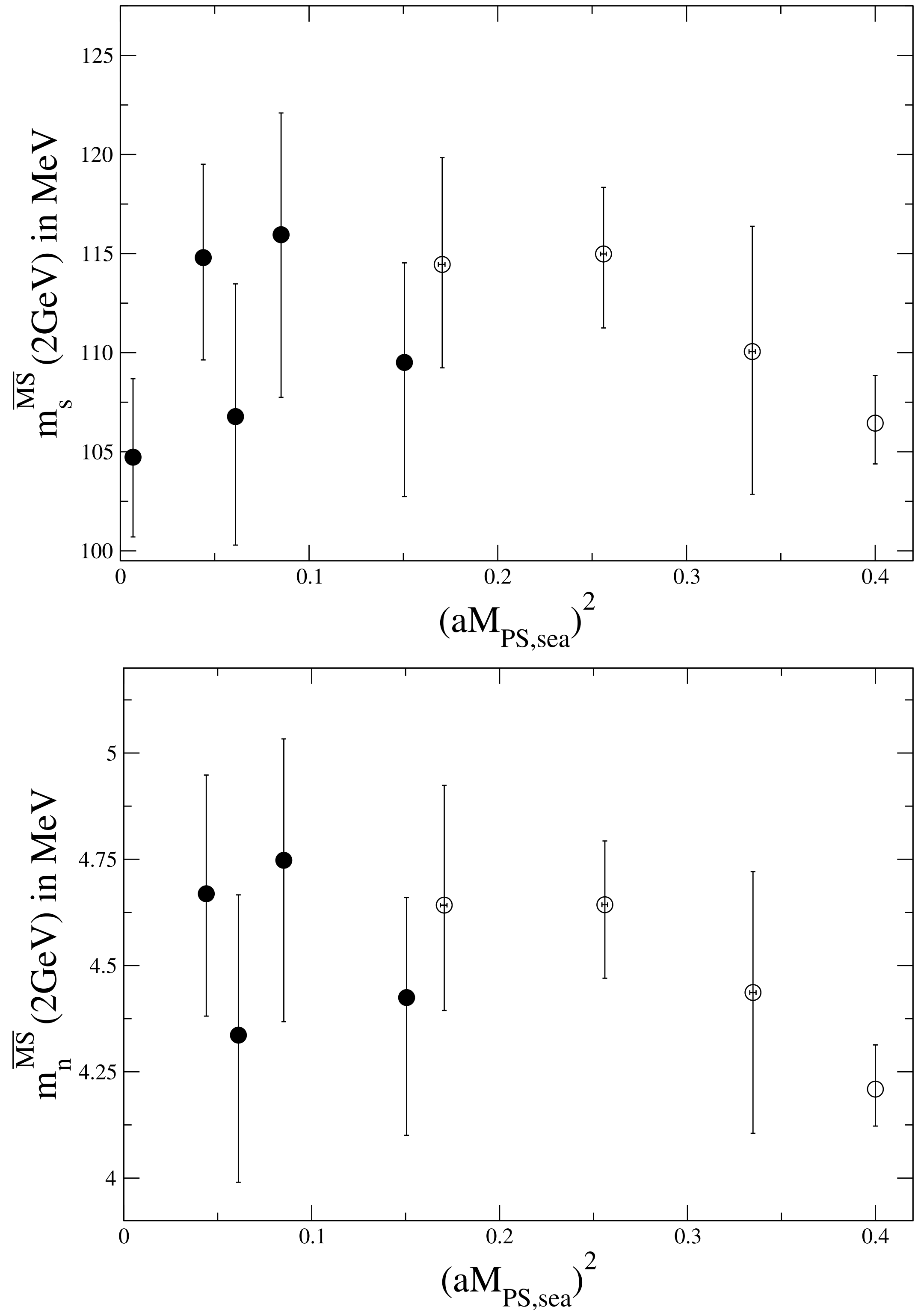

Figure 4.13: Renormalised normal (below) and strange (above) standard quark masses in the $\overline{\text{MS}}$ scheme at a reference scale of 2 GeV for all datasets. The lattice spacing has been determined through M_ρ and the strange quark mass fixed by M_{K}. The matched set results are distinguished by transparent symbols and the quenched results have been placed at $aM_{\text{PS,sea}} = 0.4$.

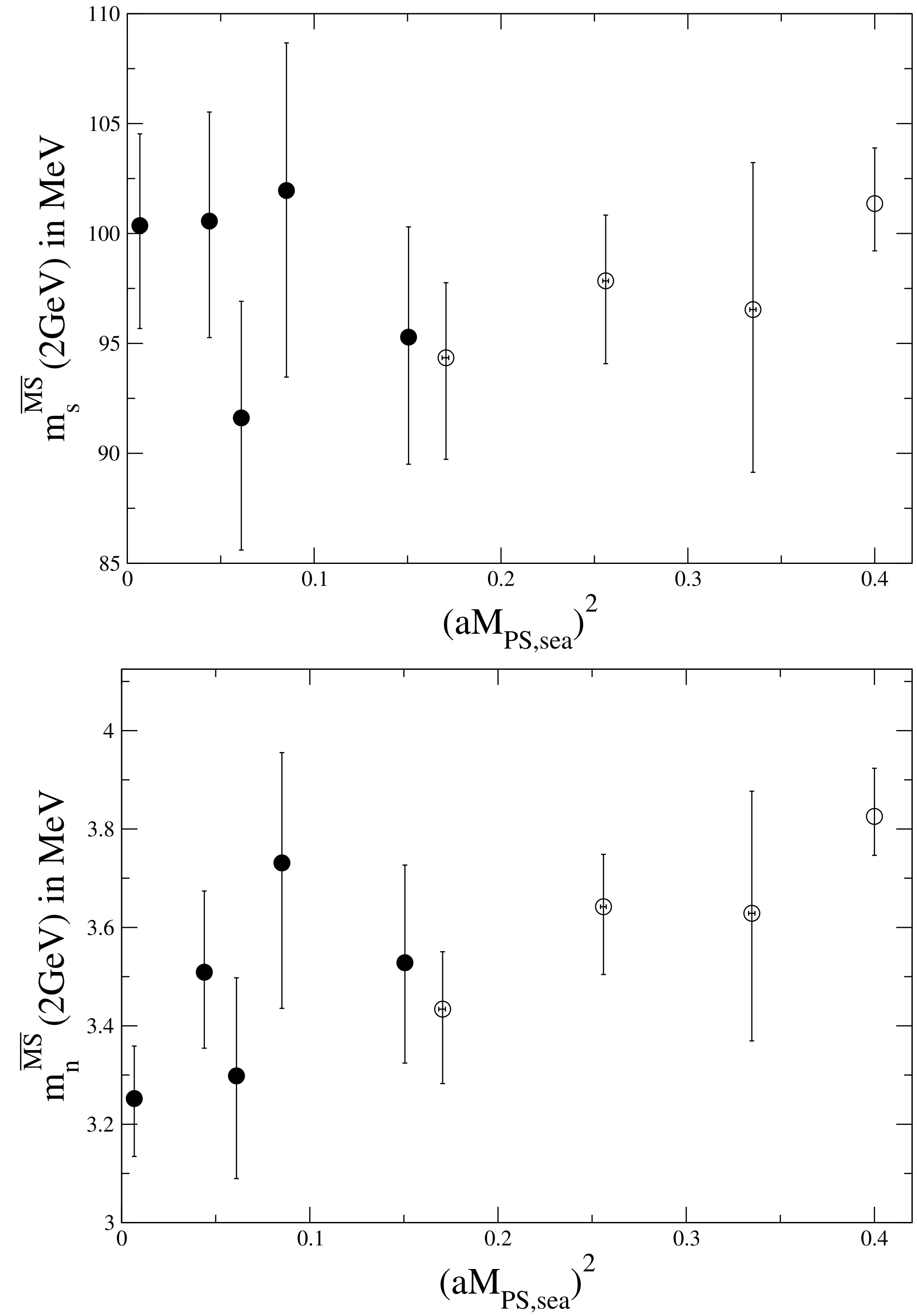

Figure 4.14: Renormalised normal (below) and strange (above) PCAC quark masses in the $\overline{\mathrm{MS}}$ scheme at a reference scale of 2 GeV for all datasets. The lattice spacing has been determined through M_ρ and the strange quark mass fixed by M_{K}. The matched set results are distinguished by transparent symbols and the quenched results have been placed at $aM_{\mathrm{PS,sea}} = 0.4$.

is the absence of a result for $m_{\mathrm{n}}^{\overline{MS}}$ for the standard quark mass from the full $\beta = 5.2$ fit. I have excluded this quantity from the plot because of its low value at $m_{\mathrm{n}}^{\overline{MS}} = 2.093\ {}^{+89}_{-82}$ which is a result of the unitary fit to the standard quark mass being much steeper than the partially quenched fits. The effect is much less pronounced for the PCAC mass and the value therefore included in the respective plot. The quark mass results in these plots show a high degree of consistency although some trends can be picked out in the matched results. Standard quark mass determinations of both $m_{\mathrm{n}}^{\overline{MS}}$ and $m_{\mathrm{s}}^{\overline{MS}}$ show a tendency to increase as the chiral limit is approached. The effect is strong enough to show a clear difference between the quark masses from the $(5.2, 0.1350)$ and quenched datasets at the $1\,\sigma$ level. A trend is also visible in the PCAC quark mass results although the tendency is for the masses to reduce as the chiral limit is approached. Results from the $(5.2, 0.1350)$ and quenched datasets again show at a $1\,\sigma$ difference.

Most of the results presented here show consistency with the best lattice determinations from the Particle data group [68] where $m_{\mathrm{n}}^{\overline{MS}}(2\text{ GeV}) = 4.2 \pm 1.0$ MeV and $m_{\mathrm{s}}^{\overline{MS}}(2\text{ GeV}) = 105 \pm 25$ MeV. The few exceptions are the standard quark mass determination of $m_{\mathrm{n}}^{\overline{MS}}$ from the full fits at $\beta = 5.2$ and determinations of $m_{\mathrm{s}}^{\overline{MS}}$ for the dataset at $(5.2, 0.1355)$ when the strange quark is set using aM_{V} fit data. Overall this is a very encouraging result.

A more accurate comparison of lattice and continuum determinations of the quark masses can be made from the results of χPT [69] where the ratios of the light quark masses can be determined from phenomenological input. These ratios have the distinct advantage that the renormalisation constants cancel in them and the results are therefore independent of matching scale. Other systematic effects may also cancel to some degree.

The result from χPT is that $m_{\mathrm{s}}/m_{\mathrm{n}} = 24.4 \pm 1.0$. Lattice results for this ratio are in general agreement when the strange quark mass is set by M_{K} with values between 25 and 26 for the standard mass definition and between 26 and 28 for the PCAC mass. No difference was observed between results calculated with a_ρ and a_{r_0} as expected. When the strange quark mass was set by M_{K^*} or M_ϕ the quark mass ratio increased to between 30 and 35. This result may indicate the presence of significant discretisation errors when the strange quark mass is fixed through either the K* or ϕ mass.

4.5 Investigation of unquenching effects

In this final section I present the results of an investigation to determine if any effects associated with a finite sea quark mass are present in the data analysed so far. This analysis has been done exclusively with data from the matched datasets i.e. with cutoff effects held fixed. Some of this analysis was performed using earlier results for the hadron mass spectrum by Dr. C.R. Allton from the University of Wales Swansea and presented in [45]. I update that analysis here using more recent results.

4.5.1 Edinburgh plot

The Edinburgh plot [70] is a particularly effective way of analysing lattice data calculated with different actions and at different values of the lattice spacing. An important benefit of this method is that the data can be compared directly without the need for chiral extrapolations. In the current context it has been used primarily to uncover any significant differences in the data from the matched simulations and therefore to look for unquenching effects although the other simulations have also been examined. In Figure 4.15 the mass ratio, $M_{\rm N}^{+}/M_{\rm V}$, has been plotted against $M_{\rm PS}/M_{\rm V}$ for all degenerate values of $\kappa_{\rm val}$ in all of the datasets. Points at $\kappa_{\rm val} = \kappa_{\rm sea}$ are shown with solid symbols and the matched simulations are presented on a separate plot for clarity. Also plotted on these graphs are the results from a phenomenological model for the hadron masses [71] in order to guide the eye. In this model the masses of the baryons and mesons are given in terms of quark masses, m_i, and quark spins, $\vec{S}_i$, by

$$M_{\rm baryon} \;=\; M_{\rm b} + \sum_{i=1}^{3} m_i + \xi_{\rm b} \sum_{i>j} \frac{\vec{S}_i \cdot \vec{S}_j}{m_i m_j}, \tag{4.72}$$

$$M_{\mathrm{meson}} = M_{\mathrm{m}} + \sum_{i=\mathrm{q},\overline{\mathrm{q}}} m_i + \xi_{\mathrm{m}} \frac{\vec{S}_{\mathrm{q}} \cdot \vec{S}_{\overline{\mathrm{q}}}}{m_i m_j}, \tag{4.73}$$

where the coefficients have values $M_{\mathrm{b}} = 0.077\mathrm{GeV}$, $\xi_{\mathrm{b}} = 0.02205\mathrm{GeV}^3$, $M_{\mathrm{m}} = -0.057\mathrm{GeV}$ and $\xi_{\mathrm{m}} = 0.0715\mathrm{GeV}^3$. The experimental point and the point in the static quark limit are also included in the plots.

Overall the data from the simulations can be seen to follow the trend of the phenomenological model. This is quite surprising considering that finite-size effects are expected to be large for the lighter datasets although they may cancel to some extent in the ratios. For the lightest dataset at $(5.2, 0.1358)$ there is an especially clear trend towards the experimental point within errors. The very lightest point is even consistent with the experimental value of $M_{\mathrm{N}}^{+}/M_{\mathrm{V}}$ although not with $M_{\mathrm{PS}}/M_{\mathrm{V}}$. This is not surprising given the different sensitivities of these two ratios to changes in the quark masses.

It is clear from the matched plot that the dynamical data are consistently above the phenomenological model whereas the quenched data sit below. This could be a signal of unquenching effects although there is no clear signal of a variation with κ_{sea} in the dynamical data and there are few dynamical points at comparable values of $M_{\mathrm{PS}}/M_{\mathrm{V}}$ to those for the quenched data. As was explained in Section 4.1.1, finite-size effects, which would have a similar effect to that observed, can be ruled out as an explanation and this result can at least be taken as an observed difference between quenched and unquenched simulations.

4.5.2 The J parameter

The J parameter [72] is a dimensionless variable that provides another means of comparing lattice data without having to perform a chiral extrapolation. It is defined by the following relation,

$$J = M_{\mathrm{V}} \frac{\mathrm{d}M_{\mathrm{V}}}{\mathrm{d}M_{\mathrm{PS}}^2}\bigg|_{M_{\mathrm{V}}/M_{\mathrm{PS}} = M_{\mathrm{K}}^{*}/M_{\mathrm{K}}}, \tag{4.74}$$

and therefore gives some measure of the relative difference between pseudoscalar

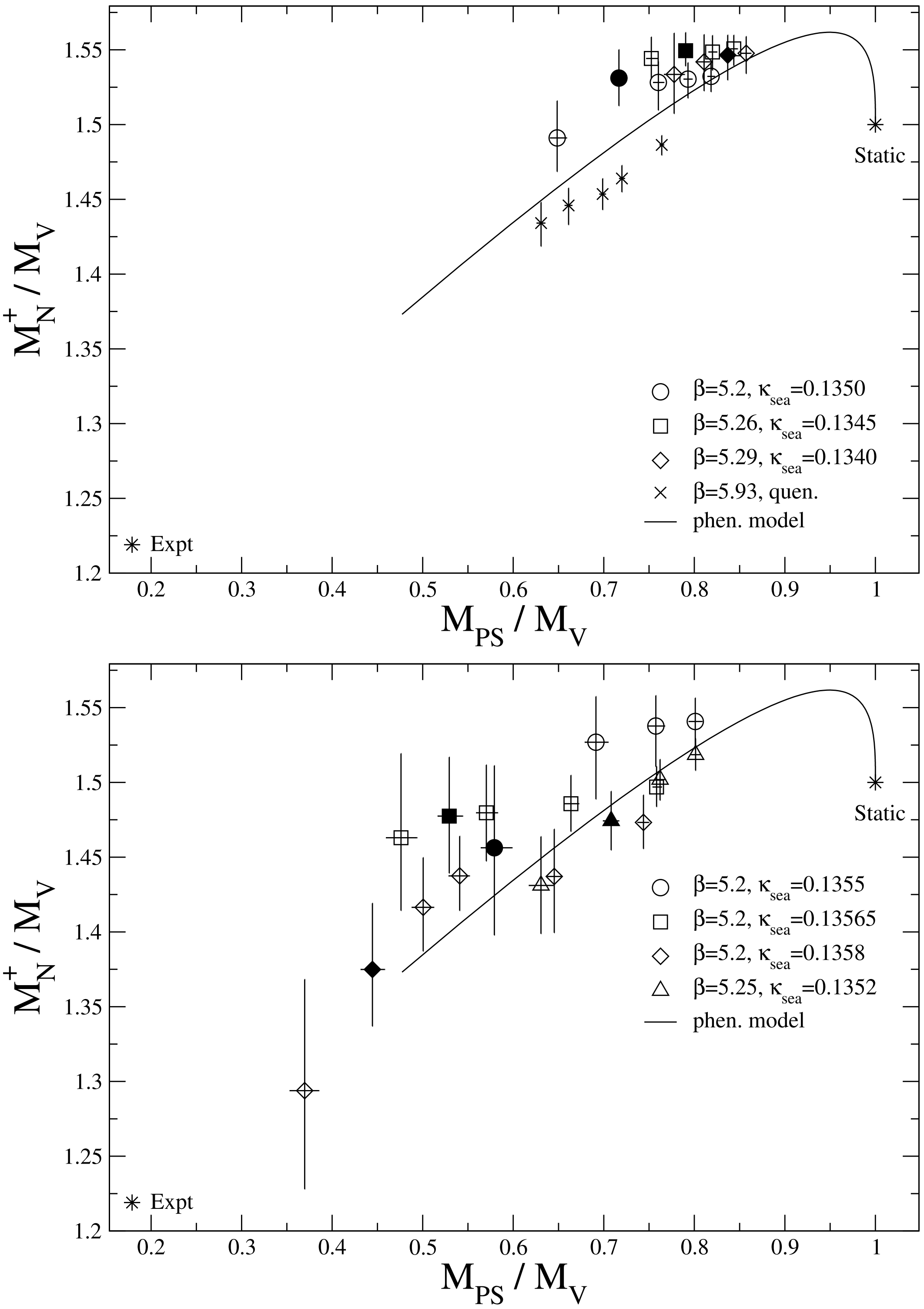

Figure 4.15: Edinburgh plot for all datasets. Data points have been calculated with degenerate κ_{val} and solid symbols indicate $\kappa_{\text{val}} = \kappa_{\text{sea}}$. The static quark limit and experimental points are shown along with the phenomenological model from [71].

and vector mesons at the scale of the strange quark. These masses are directly accessible in lattice simulations.

The J parameter has been measured in this thesis in three different ways. The first is from the results of partially quenched chiral extrapolations of aM_V to $(aM_\mathrm{PS})^2$. In this case the derivative in Equation (4.74) is with respect to $M_\mathrm{PS,val}$ and J is calculated at fixed $(aM_\mathrm{PS,sea})^2$. The physical point is fixed by solving the following equation for $(aM_\mathrm{PS,val})^2$,

$$\frac{aM_\mathrm{V}}{aM_\mathrm{PS,val}} = \frac{A_\mathrm{V} + B_\mathrm{V}(aM_\mathrm{PS,val})^2 + C_\mathrm{V}(aM_\mathrm{PS,val})^4}{aM_\mathrm{PS,val}} = \frac{M_{\mathrm{K}^*}}{M_\mathrm{K}} = 1.8 \qquad (4.75)$$

This has been done in both the linear case, where $C_\mathrm{V} = 0$, and for the full quadratic fit. The corresponding results for J, which I call $J_\mathrm{pq}^\mathrm{lin}$ and $J_\mathrm{pq}^\mathrm{quad}$, are summarised in Table 4.4.

Dataset	$J_\mathrm{pq}^\mathrm{lin}$	$J_\mathrm{eff}^\mathrm{lin}$	$J_\mathrm{pq}^\mathrm{quad}$	$J_\mathrm{eff}^\mathrm{quad}$
$(5.2, 0.1350)$	0.3899^{+85}_{-87}	0.3757^{+63}_{-55} 0.391^{+10}_{-10}	0.407^{+50}_{-42}	0.404^{+50}_{-42} 0.411^{+52}_{-45}
$(5.2, 0.1355)$	0.339^{+29}_{-24}	0.373^{+11}_{-9}	0.17^{+13}_{-11}	0.391^{+45}_{-36}
$(5.2, 0.13565)$	0.401^{+24}_{-24}	0.368^{+12}_{-10}	0.439^{+93}_{-83}	0.385^{+45}_{-36}
$(5.2, 0.1358)$	0.369^{+27}_{-24}		0.361^{+73}_{-66}	
$(5.25, 0.1352)$	0.363^{+14}_{-12}		0.403^{+58}_{-52}	
$(5.26, 0.1345)$	0.3609^{+56}_{-54}	0.3712^{+48}_{-44}	0.431^{+27}_{-22}	0.390^{+48}_{-39}
$(5.29, 0.1340)$	0.3538^{+78}_{-78}	0.3671^{+61}_{-52}	0.403^{+45}_{-51}	0.382^{+50}_{-42}
$(5.93, \text{quen.})$	0.3816^{+73}_{-82}		0.415^{+27}_{-29}	

Table 4.4: Values of the J parameter from the first and second methods.

The other two methods of calculating J use the results of the full chiral extrapolations of aM_V. The first of these starts by calculating an effective partially quenched fit formula from Equation (4.51) by fixing $(aM_\mathrm{PS,sea})^2$ to the appropriate value for the dataset we wish to study. The J parameter can then be calculated in exactly the same way as the partially quenched case. I have again performed this analysis using both linear and quadratic fit models and the results, which I write as J_{eff}, are also give in Table 4.4.

The final method involves calculating J along the unitary trajectory defined by setting $aM_{\text{PS,val}} = aM_{\text{PS,sea}}$ in Equation (4.51). The derivative in Equation (4.74) is therefore with respect to $(M_{\text{PS,sea}})^2$. A linear fit to the matched datasets resulted in a value of $J_{\text{full}} = 0.351\ {}^{+18}_{-16}$ and a quadratic fit gave a similar value of $J_{\text{full}} = 0.356\ {}^{+20}_{-19}$. For the $\beta = 5.2$ datasets the linear fit gave a very successful $J_{\text{full}} = 0.470\ {}^{+24}_{-24}$ and the quadratic fit again yielded a similar value of $J_{\text{full}} = 0.476\ {}^{+35}_{-39}$.

I have collected all of these results in two separate plots for linear and quadratic fits in Figure 4.16. The experimental value, which is defined as

$$J_{\text{exp}} = M_{\text{K}^*} \frac{M_{\text{K}^*} - M_\rho}{M_{\text{K}}^2 - M_\pi^2} = 0.48(2), \tag{4.76}$$

is also included.

The results of the lattice calculations can be seen to consistently underestimate J by as much as 25% in the case of partially quenched linear extrapolations. The use of a quadratic fit function for aM_{V} appears to improve the situation although at the cost of much larger errors. Values of J from partially quenched and effective partially quenched extrapolations are consistent within errors except at $(5.2, 0.1355)$ where the partially quenched quadratic fit drastically underestimates J. This is a direct result of the levelling out of the aM_{V} data at low $aM_{\text{PS,val}}$ which as discussed earlier could be a finite-size effect. The J parameter is particularly suited as an indicator of such trends in the data.

The values for J found from the full linear and quadratic fits to the matched datasets, despite being consistent, are actually below those from the partially quenched extrapolations. This is the result of a small but negative value for the coefficient, B_{s}^{V}, in these fits. In contrast, the results for both the linear and quadratic unitary fits to the $\beta = 5.2$ data are in surprisingly good agreement

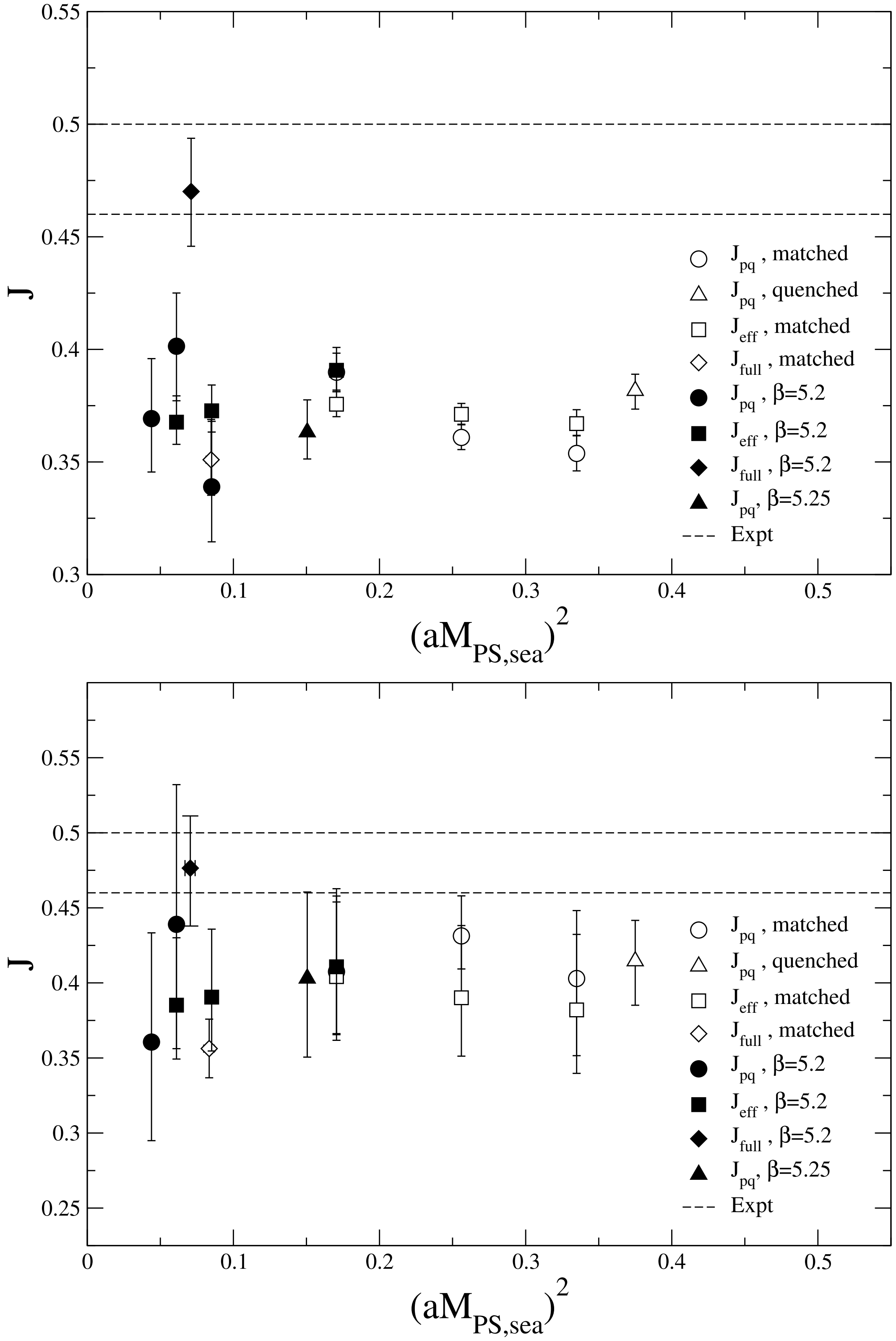

Figure 4.16: Plot of the J parameter from linear (above) and quadratic (below) partially quenched and full fits. Results for $(5.2, 0.1350)$ have been included with the matched set.

with the experimental value.

The search for unquenching effects in the matched data gives inconclusive results. In the linear fit case there is some evidence of a tendency for both $J_{\rm pq}$ and $J_{\rm eff}$ to increase as $aM_{\rm PS,sea}$ is reduced. This is indicative of sea quark effects and the trend is towards the experimental value. The value of J from the quenched dataset, however, lies above those for the sets at $(5.26, 0.1345)$ and $(5.29, 0.1340)$ and is consistent with the results at $(5.2, 0.1350)$. This result is hard to explain since the expectation is that unquenching should bring J closer to the continuum value. The results from the quadratic fits bring no further illumination, yielding consistent results for all of the matched datasets.

4.5.3 Unquenching in the chiral extrapolations

Unquenching effects have been investigated in the results of both partially quenched and full chiral extrapolations to the pseudoscalar meson mass. In the partially quenched case unquenching effects would show up as a systematic variation of the coefficients, A_X, B_X and C_X with $aM_{\rm PS,val}$ and a clear difference between the dynamical and quenched values. For the full fits, a sea quark dependence in the dynamical simulation data would manifest as non-zero values of the coefficients, $B^X_{\rm s}$, $C^X_{\rm ss}$ and $C^X_{\rm sv}$.

In the meson sector there are no clear signals of unquenching effects although some tantalising hints do exist. For example, partially quenched extrapolations to $aM_{\rm V}$ do show a lower value of the intercept, $A_{\rm V}$, in the dynamical simulations than the quenched value although only at the $1\,\sigma$ level. This is not statistically significant but is indicative of unquenching. No clear trend was observed within the dynamical results which were consistent within errors. This was backed up by the full fit results where all of the coefficients sensitive to unquenching were found to be consistent with zero within errors.

For $aM_{\rm A}$ results again show no clear signal of unquenching. There is, however, some indication of a trend for the partially quenched coefficient $A_{\rm A}$ towards lower values as $aM_{\rm PS,sea}$ is reduced for the heavier two dynamical sets. The result for $(5.2, 0.1350)$, however, appears to break the trend although the results are consistent within errors. The full fit verifies that this is the case with data from the lowest two sets overlapping within errors. As discussed in Section 4.3 this could be a finite-size effect, a result that raises the possibility that finite-size effects could be masking any unquenching effects in the data. The situation could, however, improve with increased statistics.

For aM_{B} the relative ordering of the data from the three sets clearly causes problems when looking for unquenching effects and the full fit result cannot be used. The partially quenched results also confirm this unusual ordering and in addition show that the quenched data is lower than the dynamical data at comparable $aM_{\mathrm{PS,val}}$. This result does require explanation but certainly does not indicate the presence of unquenching.

For aM_{S} the quenched result rules out any direct comparison. For the dynamical sets alone there is an expected trend towards lower values for A_{S} although the results are still consistent with each other. This trend is also picked up in the full fit where the coefficients, $C^{\mathrm{S}}_{\mathrm{ss}}$ and $C^{\mathrm{S}}_{\mathrm{sv}}$ lie roughly $1.5\,\sigma$ from zero. The negative value of $C^{\mathrm{S}}_{\mathrm{sv}}$ also indicates a trend towards a more pronounced dependence of aM_{S} on $aM_{\mathrm{PS,val}}$ as $aM_{\mathrm{PS,sea}}$ is reduced. This result is not confirmed by the partially quenched extrapolations, however, and despite there being strong indications of unquenching in the full fit this is only within statistical errors and at $1.5\,\sigma$.

Results for the pseudoscalar and axial vector meson decay constants, as discussed in Section 4.3, exhibit clear problems in the data and cannot therefore be used to investigate unquenching effects. The results for the vector meson decay constant are free of such problems. Partially quenched extrapolations of $f^{(0)}_{\mathrm{V}}$ show the clearest signal of an unquenching effect in the meson sector with all three fit coefficients showing trends away from the quenched result. This amounts to roughly a $2\,\sigma$ deviation of the $(5.2, 0.1350)$ coefficients from the quenched coefficients. No clear evidence for such a signal was found, however, in the full fit to $f^{(R)}_{\mathrm{V}}$. This suggests that the trend vanishes with improvement and renormalisation.

The search for any signal of unquenching in the baryon sector was marred by the presence of finite-size effects for the negative parity states. Partially quenched results for aM_{N}^{+} show no sign of unquenching effects. There is some indication of a sea quark effect in the unitary fit where $B_{\mathrm{s}} = -0.41\ {}^{+19}_{-16}$ but this goes contrary to expectations and as discussed before results in a higher value of aM_{N}^{+} in the chiral limit than found for the partially quenched fits. Fit results for aM_{Δ}^{+} show no clear sign of unquenching in either the partially quenched or full fits but there is some indication of a signal in the full fit where $C_{\mathrm{ss}} = 0.85\ {}^{+66}_{-69}$. With B_{s} consistent with zero this indicates a reduction of aM_{Δ}^{+} in the chiral limit as $aM_{\mathrm{PS,sea}}$ is decreaced as can be seen in the fit. This is the expected trend if unquenching effects were present although the results is also still consistent with there being no effect within errors.

Overall there are no clear signals of unquenching in the chiral extrapolations. This analysis does, however, highlight the need to ensure that finite-size effects are well under control as their presence will tend to obscure the potentially subtle unquenching effects.

4.5.4 Unquenching in the physical observables

In the final part of this analysis I have studied unquenching effects in the lattice predictions for the physical observables. Although there are some indications for the presence of such effects in the data this is not enough to make any firm conclusions.

In the hadron mass sector most results from the matched datasets are consistent within errors. The only exceptions are the K^* and ϕ masses when the lattice spacing is set by r_0. Both masses show a gradual decrease as $aM_{\mathrm{PS,sea}}$ is reduced which amounts to a difference of just over $1\,\sigma$ between the quenched and $(5.2, 0.1350)$ results. The same behaviour is not seen when the lattice spacing is set by M_ρ which is not too surprising given that the ρ, K^* and ϕ meson masses are all determined from the same vector meson data.

A systematic decrease with $aM_{\mathrm{PS,sea}}$ was also observed for the vector and axial vector meson decay constants. The effect was present when the lattice spacing was fixed by either M_ρ or r_0 and was independent of the way the strange quark mass was fixed. The size of the reduction was over $1.5\,\sigma$ in all cases although this still does not unambiguously indicate the presence unquenching effects. It does, however, lend more weight to the observations for $f_{\mathrm{V}}^{(0)}$ where a similarly sized deviation was seen.

Finally I reiterate the findings of the quark mass analysis in Section 4.4.6 where a $1\,\sigma$ deviation was seen between results from the quenched dataset and the results at $(5.2, 0.1350)$. Again such a trend although indicative of unquenching is not statistically significant and may even be an artefact of some systematic effect in the data or analysis procedures.

Chapter 5

Summary and conclusions

In this work I have presented results for the light hadron spectrum, light meson decay constants and light quark masses from numerical simulations of lattice QCD with $N_\mathrm{f} = 2$ flavours of $O(a)$-improved Wilson quarks. This analysis has been performed with the results from seven dynamical simulations, three of which were generated with the lattice spacing fixed along with one additional quenched simulation in order to study effects associated with a finite sea quark mass.

Partially quenched chiral extrapolations have been performed for each dataset in addition to full extrapolations for the data at fixed lattice spacing and independently at fixed $\beta = 5.2$. The full extrapolations allowed the lattice results to be extrapolated simultaneously in the sea and valence quark masses with a reduced number of parameters to the combined partially quenched extrapolations. In this way lattice predictions of the hadron masses and decay constants have been made with the normal quark mass treated in a fully dynamical manner. The results of such extrapolations were encouraging although they did identify the need for accurate lattice data free from finite-size effects in order to work effectively.

Lattice results for the J parameter have been calculated using the results of both the partially quenched and full extrapolations. The results were found to consistently underestimate the experimental value. This situation was found to be improved by using higher order polynomial fits of aM_V to $(aM_\mathrm{PS})^2$ although at the cost of larger errors. Of particular note were the determinations of J from the full extrapolation at fixed β which gave $J = 0.470\ {}^{+24}_{-24}$ using a linear fit ansatz and $J = 0.476\ {}^{+35}_{-39}$ from a quadratic fit. Both of these values are consistent with the experimental value of $J = 0.48(2)$.

Predictions for the light hadron spectrum from both partially quenched and full chiral extrapolations have been determined using both r_0 and M_ρ to set the physical scale and using either M_{K}, M_{K^*} or M_ϕ to set the strange quark mass. M_π was used consistently to fix the normal quark mass. The results generally overestimated the experimental values although some predictions, particularly for M_{K^*} and M_ϕ showed surprising agreement despite being at finite lattice spacing. The general agreement was found to improve when M_ρ was used to set the scale.

Pseudoscalar meson decay constants have also been determined for each dataset although the full extrapolations failed to produce sensible results. Results for the matched datasets showed good agreement with the experimental values when the physical scale was set by M_ρ although most other situations only gave qualitative agreement. The ratio f_{K}/f_π was also calculated and the results for the matched simulations found to underestimate it by around 15%. Deviations from the experimental value were found to be less pronounced for the other simulations. Vector and axial meson decay constants have also been calculated and showed the expected trend with varying quark mass.

Results for the the quark masses have been calculated using both the standard and PCAC mass definitions. The results have been given in the $\overline{\mathrm{MS}}$ scheme at a reference scale of 2 GeV with matching onto the continuum scheme performed at scales of $\mu = 1/a$ and $\mu = \pi/a$ in order to study the systematic effect. Changing the scale from $\mu = 1/a$ to $\mu = \pi/a$ resulted in a 5% increase of the quark masses when using the standard definition of the quark mass but showed difference for the PCAC masses. Results show general agreement with the lattice averages of $m_{\mathrm{n}}^{\overline{MS}}(2\ \mathrm{GeV}) = 4.2 \pm 1.0$ MeV and $m_{\mathrm{s}}^{\overline{MS}}(2\ \mathrm{GeV}) = 105 \pm 25$ MeV with the PCAC quark masses being consistently smaller than the standard quark mass results by around 20%. The choice of scale setting parameter was found to have a $5 - 10\%$ effect on the values of the quark masses with r_0 consistently giving smaller results. Strange quark masses showed an increase of around $10 - 15\%$

when M_{K^*} or M_ϕ were used as input in preference to M_{K}. In addition the ratio, $m_{\mathrm{s}}/m_{\mathrm{n}}$, was calculated and compared to the value from chiral perturbation theory of 24.4 ± 1.0. Lattice results were found to be in agreement when the strange quark mass was set with M_{K} but were as high as 35 when either M_{K^*} or M_ϕ was used.

Unquenching effects have been studied using the Edinburgh plot, J parameter, chiral extrapolation results and the results for hadron masses, decay constants and quark masses. No statistically significant results were found that could be confidently identified as unquenching effects although some tantalising hints were shown. This was especially so of the Edinburgh plot which showed a clear difference between the quenched and matched dynamical simulations. What this analysis really identified, however, was the need to have good control over systematic errors such as finite-size effects that may otherwise obscure the results of unquenching. This is one way in which the above work could be extended although resources are probably better spent on more modern lattice approaches such as those using G-W fermions.

Appendix A

Correlator analysis results

$\kappa_{\mathrm{val},1}$	$\kappa_{\mathrm{val},2}$	$\mathcal{A}^{\mathrm{PS}}_{A_{4,\mathrm{L}}}$	$\mathcal{A}^{\mathrm{PS}}_{P_{\mathrm{L}}}$	aM_{PS}	Fit range	χ^2/dof
0.1335	0.1335	$0.0814\ ^{+12}_{-12}$	$0.2688\ ^{+41}_{-43}$	$0.5674\ ^{+16}_{-17}$	$5-15$	0.543
0.1340	0.1335	$0.0767\ ^{+11}_{-12}$	$0.2635\ ^{+40}_{-43}$	$0.5438\ ^{+16}_{-18}$	$5-15$	0.527
0.1340	0.1340	$0.0722\ ^{+10}_{-11}$	$0.2586\ ^{+40}_{-42}$	$0.5195\ ^{+16}_{-19}$	$5-15$	0.507
0.1345	0.1335	$0.0719\ ^{+10}_{-11}$	$0.2576\ ^{+40}_{-44}$	$0.5194\ ^{+17}_{-19}$	$5-15$	0.511
0.1345	0.1340	$0.0673\ ^{+10}_{-11}$	$0.2530\ ^{+38}_{-43}$	$0.4944\ ^{+17}_{-21}$	$5-15$	0.492
0.1345	0.1345	$0.0626\ ^{+\ 9}_{-10}$	$0.2479\ ^{+37}_{-44}$	$0.4684\ ^{+17}_{-22}$	$5-15$	0.473
0.1350	0.1335	$0.0667\ ^{+\ 9}_{-11}$	$0.2508\ ^{+39}_{-46}$	$0.4942\ ^{+17}_{-22}$	$5-15$	0.498
0.1350	0.1340	$0.0622\ ^{+\ 9}_{-11}$	$0.2466\ ^{+37}_{-45}$	$0.4683\ ^{+17}_{-23}$	$5-15$	0.479
0.1350	0.1345	$0.0575\ ^{+\ 8}_{-10}$	$0.2418\ ^{+37}_{-48}$	$0.4413\ ^{+18}_{-24}$	$5-15$	0.461
0.1350	0.1350	$0.0526\ ^{+\ 8}_{-11}$	$0.2366\ ^{+38}_{-52}$	$0.4130\ ^{+18}_{-25}$	$5-15$	0.443
0.1355	0.1355	$0.04290\ ^{+53}_{-61}$	$0.2308\ ^{+30}_{-38}$	$0.3526\ ^{+18}_{-22}$	$4-15$	0.795

Table A.1: Fit results for LL,FL,FF fits to $C_{PP^\dagger}(t)$, $C_{A_4P^\dagger}(t)$, $C_{PA_4^\dagger}(t)$ and $C_{A_4A_4^\dagger}(t)$ correlators from the dataset at $\beta = 5.2$, $\kappa_{\mathrm{sea}} = 0.1350$

$\kappa_{\mathrm{val},1}$	$\kappa_{\mathrm{val},2}$	$\mathcal{A}^{\mathrm{PS}}_{A_{4,\mathrm{L}}}$	$\mathcal{A}^{\mathrm{PS}}_{P_{\mathrm{L}}}$	aM_{PS}	Fit range	χ^2/dof
0.1340	0.1340	$0.06188\ ^{+66}_{-79}$	$0.2319\ ^{+27}_{-29}$	$0.4759\ ^{+15}_{-15}$	$4-15$	1.037
0.1345	0.1340	$0.05683\ ^{+62}_{-76}$	$0.2252\ ^{+28}_{-30}$	$0.4494\ ^{+16}_{-16}$	$4-15$	0.94
0.1345	0.1345	$0.05186\ ^{+60}_{-73}$	$0.2186\ ^{+30}_{-30}$	$0.4216\ ^{+17}_{-16}$	$4-15$	0.856
0.1350	0.1340	$0.05155\ ^{+62}_{-74}$	$0.2176\ ^{+29}_{-31}$	$0.4219\ ^{+18}_{-17}$	$4-15$	0.831
0.1350	0.1345	$0.04659\ ^{+58}_{-73}$	$0.2112\ ^{+31}_{-32}$	$0.3926\ ^{+18}_{-18}$	$4-15$	0.76
0.1350	0.1350	$0.04144\ ^{+54}_{-70}$	$0.2044\ ^{+31}_{-34}$	$0.3617\ ^{+21}_{-20}$	$4-15$	0.682
0.1355	0.1340	$0.04607\ ^{+57}_{-71}$	$0.2092\ ^{+30}_{-32}$	$0.3934\ ^{+20}_{-19}$	$4-15$	0.716
0.1355	0.1345	$0.04114\ ^{+54}_{-70}$	$0.2031\ ^{+30}_{-33}$	$0.3621\ ^{+22}_{-21}$	$4-15$	0.658
0.1355	0.1350	$0.03598\ ^{+51}_{-65}$	$0.1969\ ^{+32}_{-36}$	$0.3287\ ^{+24}_{-21}$	$4-15$	0.588
0.1355	0.1355	$0.03048\ ^{+49}_{-61}$	$0.1900\ ^{+36}_{-40}$	$0.2918\ ^{+26}_{-26}$	$4-15$	0.499

Table A.2: Fit results for LL,FL,FF fits to $C_{PP^\dagger}(t)$, $C_{A_4P^\dagger}(t)$, $C_{PA_4^\dagger}(t)$ and $C_{A_4A_4^\dagger}(t)$ correlators from the dataset at $\beta = 5.2$, $\kappa_{\mathrm{sea}} = 0.1355$

$\kappa_{\mathrm{val},1}$	$\kappa_{\mathrm{val},2}$	$\mathcal{A}^{\mathrm{PS}}_{A_{4,\mathrm{L}}}$	$\mathcal{A}^{\mathrm{PS}}_{P_{\mathrm{L}}}$	aM_{PS}	Fit range	χ^2/dof
0.1342	0.1342	$0.05042\,^{+78}_{-77}$	$0.1981\,^{+32}_{-33}$	$0.4374\,^{+20}_{-20}$	$4-15$	0.911
0.1350	0.1342	$0.04259\,^{+70}_{-74}$	$0.1865\,^{+36}_{-35}$	$0.3925\,^{+22}_{-23}$	$4-15$	0.802
0.1350	0.1350	$0.03479\,^{+68}_{-68}$	$0.1752\,^{+40}_{-39}$	$0.3428\,^{+26}_{-26}$	$4-15$	0.769
0.1355	0.1342	$0.03753\,^{+69}_{-74}$	$0.1789\,^{+39}_{-40}$	$0.3633\,^{+25}_{-26}$	$4-15$	0.753
0.1355	0.1350	$0.02978\,^{+66}_{-62}$	$0.1683\,^{+44}_{-42}$	$0.3095\,^{+31}_{-30}$	$4-15$	0.753
0.1355	0.1355	$0.02461\,^{+63}_{-63}$	$0.1614\,^{+55}_{-51}$	$0.2722\,^{+39}_{-35}$	$4-15$	0.723
0.13565	0.1342	$0.03604\,^{+68}_{-73}$	$0.1770\,^{+39}_{-42}$	$0.3543\,^{+27}_{-27}$	$4-15$	0.742
0.13565	0.1350	$0.02826\,^{+65}_{-63}$	$0.1663\,^{+47}_{-44}$	$0.2990\,^{+33}_{-31}$	$4-15$	0.747
0.13565	0.1355	$0.02303\,^{+65}_{-65}$	$0.1592\,^{+56}_{-53}$	$0.2600\,^{+41}_{-37}$	$4-15$	0.705
0.13565	0.13565	$0.02137\,^{+64}_{-66}$	$0.1567\,^{+61}_{-57}$	$0.2470\,^{+42}_{-40}$	$4-15$	0.68
0.1358	0.1342	$0.03460\,^{+72}_{-71}$	$0.1754\,^{+41}_{-43}$	$0.3450\,^{+29}_{-29}$	$4-15$	0.729
0.1358	0.1350	$0.02672\,^{+69}_{-67}$	$0.1643\,^{+51}_{-47}$	$0.2878\,^{+36}_{-35}$	$4-15$	0.734
0.1358	0.1355	$0.02140\,^{+68}_{-66}$	$0.1566\,^{+63}_{-57}$	$0.2468\,^{+42}_{-40}$	$4-15$	0.679
0.1358	0.13565	$0.01970\,^{+70}_{-67}$	$0.1538\,^{+67}_{-63}$	$0.2331\,^{+44}_{-44}$	$4-15$	0.647
0.1358	0.1358	$0.01790\,^{+70}_{-67}$	$0.1502\,^{+73}_{-71}$	$0.2181\,^{+49}_{-53}$	$4-15$	0.604

Table A.3: Fit results for LL,FF fits to $C_{PP^\dagger}(t)$, $C_{A_4P^\dagger}(t)$, $C_{PA_4^\dagger}(t)$ and $C_{A_4A_4^\dagger}(t)$ correlators from the dataset at $\beta = 5.2$, $\kappa_{\mathrm{sea}} = 0.13565$

$\kappa_{\mathrm{val},1}$	$\kappa_{\mathrm{val},2}$	$\mathcal{A}^{\mathrm{PS}}_{A_{4,\mathrm{L}}}$	$\mathcal{A}^{\mathrm{PS}}_{P_{\mathrm{L}}}$	aM_{PS}	Fit range	χ^2/dof
0.1342	0.1342	$0.0477\,^{+\ 9}_{-11}$	$0.1874\,^{+38}_{-47}$	$0.4270\,^{+24}_{-27}$	$6-15$	0.425
0.1350	0.1342	$0.0398\,^{+\ 9}_{-11}$	$0.1749\,^{+44}_{-53}$	$0.3814\,^{+28}_{-32}$	$6-15$	0.415
0.1350	0.1350	$0.03250\,^{+59}_{-76}$	$0.1659\,^{+37}_{-41}$	$0.3331\,^{+27}_{-30}$	$5-15$	0.435
0.1355	0.1342	$0.03486\,^{+69}_{-81}$	$0.1680\,^{+38}_{-40}$	$0.3541\,^{+26}_{-30}$	$5-15$	0.461
0.1355	0.1350	$0.02744\,^{+62}_{-78}$	$0.1576\,^{+39}_{-46}$	$0.2995\,^{+30}_{-35}$	$5-15$	0.436
0.1355	0.1355	$0.02260\,^{+58}_{-77}$	$0.1504\,^{+41}_{-53}$	$0.2620\,^{+30}_{-45}$	$5-15$	0.435
0.13565	0.1342	$0.03325\,^{+68}_{-82}$	$0.1649\,^{+39}_{-42}$	$0.3450\,^{+28}_{-30}$	$5-15$	0.464
0.13565	0.1350	$0.02587\,^{+64}_{-76}$	$0.1547\,^{+41}_{-49}$	$0.2890\,^{+31}_{-37}$	$5-15$	0.444
0.13565	0.1355	$0.02118\,^{+52}_{-57}$	$0.1499\,^{+36}_{-41}$	$0.2515\,^{+28}_{-33}$	$4-15$	0.514
0.13565	0.13565	$0.01957\,^{+51}_{-55}$	$0.1470\,^{+38}_{-41}$	$0.2386\,^{+29}_{-34}$	$4-15$	0.511
0.1358	0.1342	$0.03156\,^{+69}_{-83}$	$0.1612\,^{+42}_{-45}$	$0.3356\,^{+30}_{-33}$	$5-15$	0.473
0.1358	0.1350	$0.02425\,^{+62}_{-80}$	$0.1513\,^{+42}_{-52}$	$0.2780\,^{+33}_{-38}$	$5-15$	0.455
0.1358	0.1355	$0.01950\,^{+51}_{-57}$	$0.1464\,^{+39}_{-44}$	$0.2384\,^{+30}_{-35}$	$4-15$	0.506
0.1358	0.13565	$0.01787\,^{+54}_{-55}$	$0.1436\,^{+42}_{-47}$	$0.2245\,^{+33}_{-37}$	$4-15$	0.5
0.1358	0.1358	$0.01617\,^{+53}_{-58}$	$0.1404\,^{+43}_{-55}$	$0.2096\,^{+35}_{-42}$	$4-15$	0.492
0.13595	0.13595	$0.01230\,^{+57}_{-74}$	$0.1321\,^{+56}_{-82}$	$0.1738\,^{+46}_{-64}$	$4-15$	0.451

Table A.4: Fit results for LL,FF fits to $C_{PP^\dagger}(t)$, $C_{A_4P^\dagger}(t)$, $C_{PA_4^\dagger}(t)$ and $C_{A_4A_4^\dagger}(t)$ correlators from the dataset at $\beta = 5.2$, $\kappa_{\mathrm{sea}} = 0.1358$

$\kappa_{\mathrm{val},1}$	$\kappa_{\mathrm{val},2}$	$\mathcal{A}^{\mathrm{PS}}_{A_{4,\mathrm{L}}}$	$\mathcal{A}^{\mathrm{PS}}_{P_{\mathrm{L}}}$	aM_{PS}	Fit range	χ^2/dof
0.1342	0.1342	$0.06494\ ^{+69}_{-73}$	$0.2290\ ^{+29}_{-28}$	$0.4963\ ^{+15}_{-19}$	$5-15$	0.67
0.1347	0.1342	$0.06012\ ^{+68}_{-70}$	$0.2227\ ^{+30}_{-30}$	$0.4709\ ^{+17}_{-20}$	$5-15$	0.68
0.1347	0.1347	$0.05535\ ^{+65}_{-70}$	$0.2166\ ^{+32}_{-32}$	$0.4444\ ^{+18}_{-21}$	$5-15$	0.686
0.1352	0.1342	$0.05507\ ^{+67}_{-70}$	$0.2157\ ^{+32}_{-31}$	$0.4446\ ^{+18}_{-21}$	$5-15$	0.707
0.1352	0.1347	$0.05035\ ^{+68}_{-64}$	$0.2100\ ^{+32}_{-33}$	$0.4170\ ^{+19}_{-24}$	$5-15$	0.712
0.1352	0.1352	$0.04540\ ^{+63}_{-65}$	$0.2038\ ^{+31}_{-36}$	$0.3880\ ^{+20}_{-27}$	$5-15$	0.715
0.1357	0.1342	$0.04966\ ^{+71}_{-69}$	$0.2074\ ^{+33}_{-37}$	$0.4173\ ^{+20}_{-26}$	$5-15$	0.76
0.1357	0.1347	$0.04501\ ^{+68}_{-67}$	$0.2022\ ^{+34}_{-39}$	$0.3883\ ^{+21}_{-29}$	$5-15$	0.759
0.1357	0.1352	$0.04011\ ^{+63}_{-75}$	$0.1964\ ^{+36}_{-45}$	$0.3574\ ^{+23}_{-32}$	$5-15$	0.747
0.1357	0.1357	$0.03484\ ^{+66}_{-93}$	$0.1897\ ^{+41}_{-60}$	$0.3237\ ^{+28}_{-41}$	$5-15$	0.723

Table A.5: Fit results for LL,FL,FF fits to $C_{PP^\dagger}(t)$, $C_{A_4P^\dagger}(t)$, $C_{PA_4^\dagger}(t)$ and $C_{A_4A_4^\dagger}(t)$ correlators from the dataset at $\beta = 5.25$, $\kappa_{\mathrm{sea}} = 0.1352$

$\kappa_{\mathrm{val},1}$	$\kappa_{\mathrm{val},2}$	$\mathcal{A}^{\mathrm{PS}}_{A_{4,\mathrm{L}}}$	$\mathcal{A}^{\mathrm{PS}}_{P_{\mathrm{L}}}$	aM_{PS}	Fit range	χ^2/dof
0.1335	0.1335	$0.0835\,^{+10}_{-11}$	$0.2537\,^{+34}_{-36}$	$0.6000\,^{+14}_{-16}$	$4-15$	0.577
0.1340	0.1335	$0.0790\,^{+10}_{-11}$	$0.2479\,^{+33}_{-36}$	$0.5772\,^{+13}_{-16}$	$4-15$	0.564
0.1340	0.1340	$0.0746\,^{+\ 9}_{-10}$	$0.2428\,^{+32}_{-35}$	$0.5542\,^{+14}_{-16}$	$4-15$	0.559
0.1345	0.1335	$0.0743\,^{+\ 9}_{-10}$	$0.2418\,^{+31}_{-35}$	$0.5539\,^{+14}_{-16}$	$4-15$	0.545
0.1345	0.1340	$0.0700\,^{+\ 9}_{-10}$	$0.2369\,^{+31}_{-35}$	$0.5303\,^{+15}_{-16}$	$4-15$	0.54
0.1345	0.1345	$0.0657\,^{+\ 9}_{-10}$	$0.2318\,^{+31}_{-34}$	$0.5060\,^{+15}_{-15}$	$4-15$	0.538
0.1350	0.1335	$0.0695\,^{+\ 9}_{-10}$	$0.2353\,^{+32}_{-35}$	$0.5301\,^{+15}_{-16}$	$4-15$	0.521
0.1350	0.1340	$0.06533\,^{+86}_{-95}$	$0.2307\,^{+31}_{-35}$	$0.5058\,^{+15}_{-15}$	$4-15$	0.516
0.1350	0.1345	$0.06100\,^{+85}_{-92}$	$0.2259\,^{+30}_{-34}$	$0.4807\,^{+15}_{-14}$	$4-15$	0.517
0.1350	0.1350	$0.05654\,^{+80}_{-90}$	$0.2208\,^{+30}_{-34}$	$0.4548\,^{+15}_{-15}$	$4-15$	0.528

Table A.6: Fit results for LL,FF fits to $C_{PP^\dagger}(t)$, $C_{A_4P^\dagger}(t)$, $C_{PA_4^\dagger}(t)$ and $C_{A_4A_4^\dagger}(t)$ correlators from the dataset at $\beta = 5.26$, $\kappa_{\mathrm{sea}} = 0.1345$

$\kappa_{\mathrm{val},1}$	$\kappa_{\mathrm{val},2}$	$\mathcal{A}^{\mathrm{PS}}_{A_{4,\mathrm{L}}}$	$\mathcal{A}^{\mathrm{PS}}_{P_{\mathrm{L}}}$	aM_{PS}	Fit range	χ^2/dof
0.1335	0.1335	0.0921^{+13}_{-13}	0.2734^{+37}_{-36}	0.6232^{+12}_{-14}	$4-15$	0.633
0.1340	0.1335	0.0876^{+12}_{-13}	0.2681^{+37}_{-37}	0.6013^{+13}_{-14}	$4-15$	0.622
0.1340	0.1340	0.0832^{+12}_{-13}	0.2631^{+38}_{-38}	0.5787^{+14}_{-15}	$4-15$	0.61
0.1345	0.1335	0.0829^{+13}_{-13}	0.2624^{+38}_{-38}	0.5788^{+14}_{-14}	$4-15$	0.607
0.1345	0.1340	0.0786^{+12}_{-13}	0.2576^{+39}_{-40}	0.5557^{+15}_{-16}	$4-15$	0.596
0.1345	0.1345	0.0740^{+12}_{-12}	0.2525^{+40}_{-41}	0.5320^{+15}_{-16}	$4-15$	0.583
0.1350	0.1335	0.0781^{+12}_{-13}	0.2562^{+39}_{-39}	0.5558^{+15}_{-15}	$4-15$	0.59
0.1350	0.1340	0.0738^{+12}_{-12}	0.2516^{+41}_{-41}	0.5322^{+15}_{-16}	$4-15$	0.578
0.1350	0.1345	0.0693^{+12}_{-12}	0.2467^{+43}_{-43}	0.5078^{+16}_{-17}	$4-15$	0.565
0.1350	0.1350	0.0647^{+12}_{-12}	0.2415^{+44}_{-46}	0.4826^{+16}_{-19}	$4-15$	0.549

Table A.7: Fit results for LL,FF fits to $C_{PP^\dagger}(t)$, $C_{A_4P^\dagger}(t)$, $C_{PA_4^\dagger}(t)$ and $C_{A_4A_4^\dagger}(t)$ correlators from the dataset at $\beta = 5.29$, $\kappa_{\mathrm{sea}} = 0.1340$

$\kappa_{\mathrm{val},1}$	$\kappa_{\mathrm{val},2}$	$\mathcal{A}^{\mathrm{PS}}_{A_{4,\mathrm{L}}}$	$\mathcal{A}^{\mathrm{PS}}_{P_{\mathrm{L}}}$	aM_{PS}	Fit range	χ^2/dof
0.1327	0.1327	0.06400^{+42}_{-43}	0.2175^{+16}_{-15}	0.49493^{+83}_{-92}	$5-15$	0.916
0.1332	0.1327	0.05946^{+41}_{-41}	0.2127^{+16}_{-17}	$0.4687^{+\ 9}_{-10}$	$5-15$	0.897
0.1332	0.1332	0.05493^{+39}_{-41}	0.2081^{+16}_{-18}	$0.4413^{+\ 9}_{-11}$	$5-15$	0.876
0.1334	0.1327	0.05761^{+40}_{-42}	0.2108^{+16}_{-17}	$0.4580^{+\ 9}_{-10}$	$5-15$	0.885
0.1334	0.1332	0.05306^{+39}_{-40}	0.2062^{+16}_{-18}	$0.4300^{+\ 9}_{-11}$	$5-15$	0.866
0.1334	0.1334	0.05119^{+38}_{-41}	0.2044^{+17}_{-19}	$0.4184^{+\ 9}_{-11}$	$5-15$	0.856
0.1337	0.1337	0.04541^{+37}_{-39}	0.1991^{+17}_{-21}	0.3818^{+10}_{-12}	$5-15$	0.81
0.1339	0.1337	0.04342^{+36}_{-39}	0.1975^{+18}_{-21}	0.3688^{+11}_{-13}	$5-15$	0.78
0.1339	0.1339	0.04140^{+36}_{-39}	0.1958^{+19}_{-23}	0.3553^{+11}_{-13}	$5-15$	0.753

Table A.8: Fit results for LL,FL,FF fits to $C_{PP^\dagger}(t)$, $C_{A_4P^\dagger}(t)$, $C_{PA_4^\dagger}(t)$ and $C_{A_4A_4^\dagger}(t)$ correlators from the quenched dataset at $\beta = 5.93$

$\kappa_{\mathrm{val},1}$	$\kappa_{\mathrm{val},2}$	$\mathcal{A}^{\mathrm{V}}_{V_i,\mathrm{L}}$	$\mathcal{A}^{\mathrm{V}}_{T_{i4},\mathrm{L}}$	aM_{V}	Fit range	χ^2/dof
0.1335	0.1335	$0.1388\,^{+33}_{-36}$	$0.0989\,^{+25}_{-27}$	$0.6932\,^{+33}_{-39}$	$6-15$	0.469
0.1340	0.1335	$0.1344\,^{+34}_{-39}$	$0.0950\,^{+25}_{-28}$	$0.6743\,^{+35}_{-42}$	$6-15$	0.466
0.1340	0.1340	$0.1300\,^{+34}_{-39}$	$0.0912\,^{+24}_{-28}$	$0.6551\,^{+38}_{-45}$	$6-15$	0.451
0.1345	0.1335	$0.1293\,^{+36}_{-41}$	$0.0907\,^{+24}_{-29}$	$0.6549\,^{+38}_{-46}$	$6-15$	0.47
0.1345	0.1340	$0.1251\,^{+35}_{-44}$	$0.0870\,^{+25}_{-30}$	$0.6355\,^{+40}_{-47}$	$6-15$	0.463
0.1345	0.1345	$0.1208\,^{+36}_{-45}$	$0.0832\,^{+24}_{-30}$	$0.6161\,^{+45}_{-53}$	$6-15$	0.473
0.1350	0.1335	$0.1236\,^{+36}_{-46}$	$0.0860\,^{+25}_{-33}$	$0.6349\,^{+41}_{-52}$	$6-15$	0.471
0.1350	0.1340	$0.1194\,^{+39}_{-49}$	$0.0824\,^{+25}_{-35}$	$0.6153\,^{+44}_{-56}$	$6-15$	0.48
0.1350	0.1345	$0.1151\,^{+38}_{-51}$	$0.0787\,^{+26}_{-34}$	$0.5956\,^{+45}_{-63}$	$6-15$	0.511
0.1350	0.1350	$0.1108\,^{+41}_{-55}$	$0.0749\,^{+27}_{-34}$	$0.5762\,^{+53}_{-73}$	$6-15$	0.573
0.1355	0.1355	$0.1064\,^{+39}_{-58}$	$0.0707\,^{+26}_{-38}$	$0.5437\,^{+59}_{-89}$	$6-15$	0.694

Table A.9: Fit results for LL,FL,FF fits to $C_{V_iV_i^\dagger}(t)$ and $C_{T_{i4}T_{i4}^\dagger}(t)$ correlators from the dataset at $\beta = 5.2$, $\kappa_{\mathrm{sea}} = 0.1350$

$\kappa_{\mathrm{val},1}$	$\kappa_{\mathrm{val},2}$	$\mathcal{A}^{\mathrm{V}}_{V_i,\mathrm{L}}$	$\mathcal{A}^{\mathrm{V}}_{T_{i4},\mathrm{L}}$	aM_{V}	Fit range	χ^2/dof
0.1340	0.1340	$0.1020\,^{+43}_{-41}$	$0.0701\,^{+28}_{-28}$	$0.5940\,^{+55}_{-59}$	$6-15$	0.799
0.1345	0.1340	$0.0981\,^{+43}_{-43}$	$0.0666\,^{+28}_{-29}$	$0.5748\,^{+64}_{-63}$	$6-15$	0.728
0.1345	0.1345	$0.0949\,^{+45}_{-47}$	$0.0637\,^{+30}_{-33}$	$0.5566\,^{+68}_{-73}$	$6-15$	0.665
0.1350	0.1340	$0.0941\,^{+44}_{-46}$	$0.0631\,^{+30}_{-31}$	$0.5564\,^{+72}_{-70}$	$6-15$	0.662
0.1350	0.1345	$0.0916\,^{+48}_{-53}$	$0.0606\,^{+31}_{-35}$	$0.5388\,^{+79}_{-83}$	$6-15$	0.597
0.1350	0.1350	$0.0896\,^{+55}_{-61}$	$0.0584\,^{+32}_{-41}$	$0.523\,^{+\ 9}_{-10}$	$6-15$	0.516
0.1355	0.1340	$0.0911\,^{+54}_{-55}$	$0.0602\,^{+35}_{-34}$	$0.5410\,^{+90}_{-94}$	$6-15$	0.647
0.1355	0.1345	$0.0895\,^{+59}_{-64}$	$0.0583\,^{+37}_{-39}$	$0.525\,^{+10}_{-11}$	$6-15$	0.572
0.1355	0.1350	$0.0889\,^{+63}_{-70}$	$0.0570\,^{+37}_{-43}$	$0.511\,^{+11}_{-13}$	$6-15$	0.494
0.1355	0.1355	$0.0902\,^{+68}_{-87}$	$0.0568\,^{+40}_{-53}$	$0.504\,^{+14}_{-17}$	$6-15$	0.439

Table A.10: Fit results for LL,FL,FF fits to $C_{V_i V_i^\dagger}(t)$ and $C_{T_{i4}T_{i4}^\dagger}(t)$ correlators from the dataset at $\beta = 5.2$, $\kappa_{\mathrm{sea}} = 0.1355$

$\kappa_{\mathrm{val},1}$	$\kappa_{\mathrm{val},2}$	$\mathcal{A}^{\mathrm{V}}_{V_i,\mathrm{L}}$	$\mathcal{A}^{\mathrm{V}}_{T_{i4},\mathrm{L}}$	aM_{V}	Fit range	χ^2/dof
0.1342	0.1342	0.1020^{+20}_{-21}	0.0685^{+14}_{-15}	0.5768^{+36}_{-43}	$5-15$	0.761
0.1350	0.1342	0.0955^{+21}_{-24}	0.0626^{+15}_{-16}	0.5476^{+44}_{-50}	$5-15$	0.698
0.1350	0.1350	0.0889^{+25}_{-27}	0.0566^{+18}_{-18}	0.5165^{+54}_{-60}	$5-15$	0.721
0.1355	0.1342	0.0906^{+26}_{-27}	0.0583^{+19}_{-18}	0.5292^{+54}_{-61}	$5-15$	0.634
0.1355	0.1350	0.0842^{+31}_{-32}	0.0525^{+21}_{-20}	0.4975^{+71}_{-75}	$5-15$	0.634
0.1355	0.1355	0.0799^{+36}_{-39}	0.0486^{+23}_{-25}	0.477^{+9}_{-10}	$5-15$	0.572
0.13565	0.1342	0.0888^{+29}_{-29}	0.0568^{+20}_{-20}	0.5233^{+61}_{-65}	$5-15$	0.605
0.13565	0.1350	0.0825^{+32}_{-34}	0.0511^{+22}_{-23}	0.4914^{+75}_{-81}	$5-15$	0.592
0.13565	0.1355	0.0786^{+39}_{-43}	0.0475^{+25}_{-27}	0.472^{+9}_{-11}	$5-15$	0.518
0.13565	0.13565	0.0775^{+44}_{-45}	0.0465^{+26}_{-29}	0.467^{+10}_{-12}	$5-15$	0.48
0.1358	0.1342	0.0866^{+34}_{-33}	0.0552^{+22}_{-22}	0.5168^{+68}_{-73}	$5-15$	0.569
0.1358	0.1350	0.0805^{+36}_{-42}	0.0495^{+24}_{-25}	0.485^{+8}_{-10}	$5-15$	0.538
0.1358	0.1355	0.0772^{+45}_{-47}	0.0463^{+27}_{-31}	0.467^{+11}_{-12}	$5-15$	0.454
0.1358	0.13565	0.0764^{+51}_{-53}	0.0455^{+29}_{-32}	0.462^{+12}_{-14}	$5-15$	0.417
0.1358	0.1358	0.0757^{+59}_{-62}	0.0448^{+34}_{-38}	0.458^{+14}_{-16}	$5-15$	0.38

Table A.11: Fit results for LL,FL,FF fits to $C_{V_iV_i^\dagger}(t)$ and $C_{T_{i4}T_{i4}^\dagger}(t)$ correlators from the dataset at $\beta = 5.2$, $\kappa_{\mathrm{sea}} = 0.13565$

$\kappa_{\mathrm{val},1}$	$\kappa_{\mathrm{val},2}$	$\mathcal{A}^{\mathrm{V}}_{V_i,\mathrm{L}}$	$\mathcal{A}^{\mathrm{V}}_{T_{i4},\mathrm{L}}$	aM_{V}	Fit range	χ^2/dof
0.1342	0.1342	$0.1056\,^{+22}_{-19}$	$0.0703\,^{+14}_{-14}$	$0.5741\,^{+39}_{-33}$	$5-15$	0.719
0.1350	0.1342	$0.0997\,^{+23}_{-22}$	$0.0647\,^{+16}_{-15}$	$0.5461\,^{+48}_{-46}$	$5-15$	0.625
0.1350	0.1350	$0.0936\,^{+25}_{-23}$	$0.0592\,^{+17}_{-15}$	$0.5162\,^{+56}_{-51}$	$5-15$	0.643
0.1355	0.1342	$0.0965\,^{+28}_{-26}$	$0.0618\,^{+18}_{-17}$	$0.5323\,^{+62}_{-61}$	$5-15$	0.638
0.1355	0.1350	$0.0913\,^{+32}_{-28}$	$0.0568\,^{+20}_{-17}$	$0.5032\,^{+71}_{-66}$	$5-15$	0.672
0.1355	0.1355	$0.0867\,^{+36}_{-32}$	$0.0531\,^{+23}_{-19}$	$0.4845\,^{+91}_{-81}$	$5-15$	0.716
0.13565	0.1342	$0.0960\,^{+30}_{-28}$	$0.0611\,^{+19}_{-18}$	$0.5296\,^{+66}_{-64}$	$5-15$	0.649
0.13565	0.1350	$0.0910\,^{+34}_{-31}$	$0.0564\,^{+22}_{-19}$	$0.5009\,^{+79}_{-73}$	$5-15$	0.682
0.13565	0.1355	$0.0865\,^{+40}_{-37}$	$0.0529\,^{+24}_{-22}$	$0.482\,^{+10}_{-\ 9}$	$5-15$	0.734
0.13565	0.13565	$0.0849\,^{+41}_{-39}$	$0.0518\,^{+25}_{-22}$	$0.477\,^{+10}_{-\ 9}$	$5-15$	0.737
0.1358	0.1342	$0.0958\,^{+33}_{-29}$	$0.0608\,^{+20}_{-19}$	$0.5278\,^{+71}_{-70}$	$5-15$	0.652
0.1358	0.1350	$0.0912\,^{+36}_{-35}$	$0.0563\,^{+23}_{-21}$	$0.4999\,^{+89}_{-85}$	$5-15$	0.685
0.1358	0.1355	$0.0869\,^{+44}_{-41}$	$0.0531\,^{+26}_{-25}$	$0.482\,^{+11}_{-10}$	$5-15$	0.747
0.1358	0.13565	$0.0853\,^{+44}_{-44}$	$0.0522\,^{+26}_{-25}$	$0.476\,^{+11}_{-10}$	$5-15$	0.742
0.1358	0.1358	$0.0840\,^{+44}_{-48}$	$0.0516\,^{+27}_{-28}$	$0.472\,^{+11}_{-12}$	$5-15$	0.716
0.13595	0.13595	$0.0834\,^{+54}_{-64}$	$0.0534\,^{+32}_{-37}$	$0.470\,^{+13}_{-15}$	$5-15$	0.687

Table A.12: Fit results for LL,FL,FF fits to $C_{V_iV_i^\dagger}(t)$ and $C_{T_{i4}T_{i4}^\dagger}(t)$ correlators from the dataset at $\beta = 5.2$, $\kappa_{\mathrm{sea}} = 0.1358$

$\kappa_{\text{val},1}$	$\kappa_{\text{val},2}$	$\mathcal{A}^{\text{V}}_{V_i,\text{L}}$	$\mathcal{A}^{\text{V}}_{T_{i4},\text{L}}$	aM_{V}	Fit range	χ^2/dof
0.1342	0.1342	$0.1130\ ^{+26}_{-27}$	$0.0786\ ^{+18}_{-19}$	$0.6193\ ^{+39}_{-37}$	$6-15$	0.869
0.1347	0.1342	$0.1096\ ^{+28}_{-29}$	$0.0754\ ^{+19}_{-20}$	$0.6016\ ^{+42}_{-42}$	$6-15$	0.847
0.1347	0.1347	$0.1058\ ^{+30}_{-30}$	$0.0721\ ^{+20}_{-22}$	$0.5831\ ^{+47}_{-46}$	$6-15$	0.869
0.1352	0.1342	$0.1063\ ^{+32}_{-35}$	$0.0724\ ^{+22}_{-24}$	$0.5848\ ^{+51}_{-54}$	$6-15$	0.82
0.1352	0.1347	$0.1027\ ^{+34}_{-37}$	$0.0692\ ^{+24}_{-26}$	$0.5663\ ^{+58}_{-59}$	$6-15$	0.834
0.1352	0.1352	$0.0990\ ^{+38}_{-42}$	$0.0659\ ^{+25}_{-28}$	$0.5479\ ^{+67}_{-67}$	$6-15$	0.842
0.1357	0.1342	$0.1031\ ^{+38}_{-46}$	$0.0694\ ^{+25}_{-28}$	$0.5692\ ^{+68}_{-67}$	$6-15$	0.785
0.1357	0.1347	$0.0998\ ^{+41}_{-47}$	$0.0664\ ^{+26}_{-32}$	$0.5507\ ^{+72}_{-77}$	$6-15$	0.773
0.1357	0.1352	$0.0962\ ^{+43}_{-53}$	$0.0632\ ^{+28}_{-34}$	$0.5323\ ^{+76}_{-88}$	$6-15$	0.749
0.1357	0.1357	$0.0918\ ^{+49}_{-64}$	$0.0597\ ^{+34}_{-38}$	$0.513\ ^{+\ 9}_{-11}$	$6-15$	0.687

Table A.13: Fit results for LL,FL,FF fits to $C_{V_iV_i^\dagger}(t)$ and $C_{T_{i4}T_{i4}^\dagger}(t)$ correlators from the dataset at $\beta = 5.25$, $\kappa_{\text{sea}} = 0.1352$

$\kappa_{\text{val},1}$	$\kappa_{\text{val},2}$	$\mathcal{A}^{\text{V}}_{V_i,\text{L}}$	$\mathcal{A}^{\text{V}}_{T_{i4},\text{L}}$	aM_{V}	Fit range	χ^2/dof
0.1335	0.1335	$0.1349\,^{+28}_{-31}$	$0.0981\,^{+21}_{-22}$	$0.7113\,^{+36}_{-40}$	$5-15$	0.578
0.1340	0.1335	$0.1313\,^{+28}_{-32}$	$0.0949\,^{+20}_{-23}$	$0.6936\,^{+39}_{-44}$	$5-15$	0.56
0.1340	0.1340	$0.1279\,^{+29}_{-32}$	$0.0917\,^{+21}_{-24}$	$0.6758\,^{+40}_{-47}$	$5-15$	0.52
0.1345	0.1335	$0.1277\,^{+29}_{-32}$	$0.0915\,^{+21}_{-24}$	$0.6760\,^{+40}_{-48}$	$5-15$	0.541
0.1345	0.1340	$0.1244\,^{+30}_{-32}$	$0.0884\,^{+21}_{-24}$	$0.6581\,^{+42}_{-52}$	$5-15$	0.502
0.1345	0.1345	$0.1209\,^{+31}_{-35}$	$0.0852\,^{+21}_{-25}$	$0.6402\,^{+45}_{-55}$	$5-15$	0.463
0.1350	0.1335	$0.1239\,^{+31}_{-33}$	$0.0882\,^{+21}_{-24}$	$0.6585\,^{+44}_{-53}$	$5-15$	0.522
0.1350	0.1340	$0.1207\,^{+30}_{-34}$	$0.0851\,^{+22}_{-24}$	$0.6404\,^{+44}_{-55}$	$5-15$	0.483
0.1350	0.1345	$0.1172\,^{+32}_{-36}$	$0.0819\,^{+22}_{-25}$	$0.6223\,^{+47}_{-58}$	$5-15$	0.445
0.1350	0.1350	$0.1137\,^{+33}_{-40}$	$0.0786\,^{+22}_{-25}$	$0.6045\,^{+50}_{-64}$	$5-15$	0.411

Table A.14: Fit results for LL,FL,FF fits to $C_{V_iV_i^\dagger}(t)$ and $C_{T_{i4}T_{i4}^\dagger}(t)$ correlators from the dataset at $\beta = 5.26$, $\kappa_{\text{sea}} = 0.1345$

$\kappa_{\mathrm{val},1}$	$\kappa_{\mathrm{val},2}$	$\mathcal{A}^{\mathrm{V}}_{V_i,\mathrm{L}}$	$\mathcal{A}^{\mathrm{V}}_{T_{i4},\mathrm{L}}$	aM_{V}	Fit range	χ^2/dof
0.1335	0.1335	$0.1359\,^{+44}_{-49}$	$0.0991\,^{+30}_{-33}$	$0.7269\,^{+50}_{-51}$	$6-15$	0.924
0.1340	0.1335	$0.1323\,^{+45}_{-49}$	$0.0958\,^{+32}_{-35}$	$0.7091\,^{+53}_{-55}$	$6-15$	0.912
0.1340	0.1340	$0.1288\,^{+49}_{-53}$	$0.0926\,^{+33}_{-36}$	$0.6915\,^{+57}_{-56}$	$6-15$	0.895
0.1345	0.1335	$0.1287\,^{+49}_{-52}$	$0.0925\,^{+33}_{-37}$	$0.6914\,^{+58}_{-59}$	$6-15$	0.891
0.1345	0.1340	$0.1252\,^{+53}_{-57}$	$0.0894\,^{+35}_{-37}$	$0.6737\,^{+64}_{-63}$	$6-15$	0.871
0.1345	0.1345	$0.1216\,^{+59}_{-61}$	$0.0861\,^{+39}_{-39}$	$0.6562\,^{+71}_{-71}$	$6-15$	0.849
0.1350	0.1335	$0.1250\,^{+51}_{-57}$	$0.0891\,^{+35}_{-39}$	$0.6739\,^{+63}_{-66}$	$6-15$	0.862
0.1350	0.1340	$0.1215\,^{+57}_{-65}$	$0.0859\,^{+38}_{-42}$	$0.6560\,^{+70}_{-73}$	$6-15$	0.842
0.1350	0.1345	$0.1177\,^{+65}_{-69}$	$0.0826\,^{+43}_{-45}$	$0.6382\,^{+79}_{-80}$	$6-15$	0.821
0.1350	0.1350	$0.1138\,^{+72}_{-80}$	$0.0792\,^{+47}_{-52}$	$0.6205\,^{+90}_{-92}$	$6-15$	0.803

Table A.15: Fit results for LL,FL,FF fits to $C_{V_iV_i^\dagger}(t)$ and $C_{T_{i4}T_{i4}^\dagger}(t)$ correlators from the dataset at $\beta = 5.29$, $\kappa_{\mathrm{sea}} = 0.1340$

$\kappa_{\mathrm{val},1}$	$\kappa_{\mathrm{val},2}$	$\mathcal{A}^{\mathrm{V}}_{V_i,\mathrm{L}}$	$\mathcal{A}^{\mathrm{V}}_{T_{i4},\mathrm{L}}$	aM_{V}	Fit range	χ^2/dof
0.1327	0.1327	$0.1220\,^{+16}_{-15}$	$0.0865\,^{+11}_{-10}$	$0.6478\,^{+22}_{-22}$	$6-15$	1.093
0.1332	0.1327	$0.1185\,^{+17}_{-16}$	$0.0833\,^{+11}_{-11}$	$0.6303\,^{+24}_{-25}$	$6-15$	1.011
0.1332	0.1332	$0.1152\,^{+18}_{-17}$	$0.0803\,^{+12}_{-11}$	$0.6129\,^{+28}_{-27}$	$6-15$	1.015
0.1334	0.1327	$0.1170\,^{+17}_{-16}$	$0.0820\,^{+11}_{-11}$	$0.6233\,^{+26}_{-26}$	$6-15$	0.97
0.1334	0.1332	$0.1138\,^{+19}_{-17}$	$0.0790\,^{+12}_{-11}$	$0.6058\,^{+29}_{-28}$	$6-15$	0.969
0.1334	0.1334	$0.1124\,^{+19}_{-17}$	$0.0778\,^{+13}_{-12}$	$0.5988\,^{+30}_{-28}$	$6-15$	0.968
0.1337	0.1337	$0.1081\,^{+22}_{-19}$	$0.0739\,^{+14}_{-13}$	$0.5776\,^{+37}_{-36}$	$6-15$	0.87
0.1339	0.1337	$0.1066\,^{+23}_{-20}$	$0.0726\,^{+15}_{-14}$	$0.5704\,^{+40}_{-38}$	$6-15$	0.797
0.1339	0.1339	$0.1051\,^{+23}_{-22}$	$0.0714\,^{+16}_{-14}$	$0.5633\,^{+43}_{-41}$	$6-15$	0.787

Table A.16: Fit results for LL,FL,FF fits to $C_{V_iV_i^\dagger}(t)$ and $C_{T_{i4}T_{i4}^\dagger}(t)$ correlators from the quenched dataset at $\beta = 5.93$

$\kappa_{\mathrm{val},1}$	$\kappa_{\mathrm{val},2}$	$\mathcal{A}^{\mathrm{A}}_{A_i,\mathrm{L}}$	aM_{A}	Fit range	χ^2/dof
0.1335	0.1335	$0.175\ ^{+15}_{-17}$	$0.949\ ^{+20}_{-24}$	$4-15$	1.122
0.1340	0.1335	$0.175\ ^{+16}_{-18}$	$0.933\ ^{+22}_{-25}$	$4-15$	1.135
0.1340	0.1340	$0.177\ ^{+16}_{-18}$	$0.920\ ^{+22}_{-26}$	$4-15$	1.141
0.1345	0.1335	$0.175\ ^{+17}_{-19}$	$0.919\ ^{+24}_{-27}$	$4-15$	1.124
0.1345	0.1340	$0.177\ ^{+17}_{-19}$	$0.906\ ^{+24}_{-28}$	$4-15$	1.123
0.1345	0.1345	$0.180\ ^{+16}_{-20}$	$0.894\ ^{+23}_{-29}$	$4-15$	1.104
0.1350	0.1335	$0.178\ ^{+18}_{-21}$	$0.906\ ^{+26}_{-30}$	$4-15$	1.07
0.1350	0.1340	$0.180\ ^{+17}_{-21}$	$0.894\ ^{+24}_{-31}$	$4-15$	1.062
0.1350	0.1345	$0.182\ ^{+14}_{-21}$	$0.882\ ^{+21}_{-32}$	$4-15$	1.04
0.1350	0.1350	$0.185\ ^{+13}_{-19}$	$0.870\ ^{+19}_{-29}$	$4-15$	0.984
0.1355	0.1355	$0.189\ ^{+10}_{-11}$	$0.846\ ^{+16}_{-18}$	$4-15$	0.748

Table A.17: Fit results for LL,FL,FF fits to $C_{A_iA_i^\dagger}(t)$ correlators from the dataset at $\beta = 5.2$, $\kappa_{\mathrm{sea}} = 0.1350$

$\kappa_{\text{val},1}$	$\kappa_{\text{val},2}$	$\mathcal{A}^{\text{A}}_{A_i,\text{L}}$	aM_{A}	Fit range	χ^2/dof
0.1340	0.1340	$0.1772\ ^{+77}_{-71}$	$0.878\ ^{+12}_{-11}$	$4-15$	0.476
0.1345	0.1340	$0.1753\ ^{+77}_{-71}$	$0.859\ ^{+13}_{-12}$	$4-15$	0.456
0.1345	0.1345	$0.1730\ ^{+79}_{-74}$	$0.840\ ^{+13}_{-12}$	$4-15$	0.476
0.1350	0.1340	$0.1732\ ^{+82}_{-75}$	$0.840\ ^{+13}_{-12}$	$4-15$	0.465
0.1350	0.1345	$0.1709\ ^{+82}_{-78}$	$0.821\ ^{+14}_{-13}$	$4-15$	0.486
0.1350	0.1350	$0.1686\ ^{+86}_{-83}$	$0.803\ ^{+15}_{-14}$	$4-15$	0.517
0.1355	0.1340	$0.1709\ ^{+84}_{-81}$	$0.821\ ^{+13}_{-13}$	$4-15$	0.581
0.1355	0.1345	$0.1685\ ^{+85}_{-85}$	$0.802\ ^{+15}_{-14}$	$4-15$	0.586
0.1355	0.1350	$0.1661\ ^{+90}_{-93}$	$0.783\ ^{+16}_{-16}$	$4-15$	0.579
0.1355	0.1355	$0.163\ ^{+10}_{-10}$	$0.763\ ^{+18}_{-18}$	$4-15$	0.572

Table A.18: Fit results for LL,FL,FF fits to $C_{A_i A_i^\dagger}(t)$ correlators from the dataset at $\beta = 5.2$, $\kappa_{\text{sea}} = 0.1355$

$\kappa_{\mathrm{val},1}$	$\kappa_{\mathrm{val},2}$	$\mathcal{A}^{\mathrm{A}}_{A_i,\mathrm{L}}$	aM_{A}	Fit range	χ^2/dof
0.1342	0.1342	$0.1428\ ^{+76}_{-76}$	$0.803\ ^{+13}_{-15}$	$4-15$	1.307
0.1350	0.1342	$0.1410\ ^{+79}_{-82}$	$0.773\ ^{+14}_{-16}$	$4-15$	1.247
0.1350	0.1350	$0.1396\ ^{+84}_{-84}$	$0.746\ ^{+16}_{-17}$	$4-15$	1.074
0.1355	0.1342	$0.1401\ ^{+83}_{-87}$	$0.755\ ^{+16}_{-18}$	$4-15$	1.197
0.1355	0.1350	$0.1388\ ^{+82}_{-93}$	$0.729\ ^{+16}_{-20}$	$4-15$	1.094
0.1355	0.1355	$0.139\ ^{+8}_{-10}$	$0.714\ ^{+17}_{-21}$	$4-15$	1.115
0.13565	0.1342	$0.1402\ ^{+82}_{-90}$	$0.751\ ^{+16}_{-18}$	$4-15$	1.201
0.13565	0.1350	$0.139\ ^{+8}_{-10}$	$0.725\ ^{+16}_{-20}$	$4-15$	1.119
0.13565	0.1355	$0.139\ ^{+8}_{-10}$	$0.709\ ^{+17}_{-21}$	$4-15$	1.139
0.13565	0.13565	$0.139\ ^{+9}_{-10}$	$0.705\ ^{+17}_{-21}$	$4-15$	1.158
0.1358	0.1342	$0.1413\ ^{+87}_{-93}$	$0.748\ ^{+16}_{-19}$	$4-15$	1.234
0.1358	0.1350	$0.141\ ^{+9}_{-10}$	$0.723\ ^{+16}_{-21}$	$4-15$	1.164
0.1358	0.1355	$0.140\ ^{+9}_{-11}$	$0.706\ ^{+17}_{-22}$	$4-15$	1.166
0.1358	0.13565	$0.139\ ^{+9}_{-11}$	$0.700\ ^{+18}_{-22}$	$4-15$	1.179
0.1358	0.1358	$0.138\ ^{+10}_{-10}$	$0.692\ ^{+19}_{-22}$	$4-15$	1.189

Table A.19: Fit results for LL,FL,FF fits to $C_{A_iA_i^\dagger}(t)$ correlators from the dataset at $\beta = 5.2$, $\kappa_{\mathrm{sea}} = 0.13565$

$\kappa_{\mathrm{val},1}$	$\kappa_{\mathrm{val},2}$	$\mathcal{A}^{\mathrm{A}}_{A_i,\mathrm{L}}$	aM_{A}	Fit range	χ^2/dof
0.1342	0.1342	$0.1362\ ^{+65}_{-59}$	$0.779\ ^{+12}_{-12}$	$4-15$	0.724
0.1350	0.1342	$0.1313\ ^{+62}_{-61}$	$0.742\ ^{+13}_{-12}$	$4-15$	0.655
0.1350	0.1350	$0.1288\ ^{+64}_{-68}$	$0.712\ ^{+13}_{-14}$	$4-15$	0.588
0.1355	0.1342	$0.1276\ ^{+65}_{-65}$	$0.717\ ^{+14}_{-13}$	$4-15$	0.607
0.1355	0.1350	$0.1252\ ^{+67}_{-75}$	$0.688\ ^{+13}_{-15}$	$4-15$	0.611
0.1355	0.1355	$0.1223\ ^{+73}_{-77}$	$0.666\ ^{+15}_{-17}$	$4-15$	0.623
0.13565	0.1342	$0.1266\ ^{+66}_{-66}$	$0.710\ ^{+14}_{-14}$	$4-15$	0.601
0.13565	0.1350	$0.1239\ ^{+68}_{-76}$	$0.680\ ^{+14}_{-16}$	$4-15$	0.63
0.13565	0.1355	$0.1208\ ^{+78}_{-81}$	$0.657\ ^{+16}_{-19}$	$4-15$	0.648
0.13565	0.13565	$0.1192\ ^{+81}_{-84}$	$0.648\ ^{+16}_{-19}$	$4-15$	0.636
0.1358	0.1342	$0.1258\ ^{+73}_{-73}$	$0.704\ ^{+14}_{-16}$	$4-15$	0.606
0.1358	0.1350	$0.1223\ ^{+73}_{-79}$	$0.672\ ^{+16}_{-18}$	$4-15$	0.655
0.1358	0.1355	$0.1189\ ^{+86}_{-91}$	$0.648\ ^{+18}_{-20}$	$4-15$	0.676
0.1358	0.13565	$0.1171\ ^{+89}_{-94}$	$0.639\ ^{+19}_{-22}$	$4-15$	0.665
0.1358	0.1358	$0.115\ ^{+\ 9}_{-10}$	$0.627\ ^{+21}_{-24}$	$4-15$	0.644
0.13595	0.13595	$0.107\ ^{+12}_{-12}$	$0.596\ ^{+26}_{-30}$	$4-15$	0.627

Table A.20: Fit results for LL,FL,FF fits to $C_{A_i A_i^\dagger}(t)$ correlators from the dataset at $\beta = 5.2$, $\kappa_{\mathrm{sea}} = 0.1358$

$\kappa_{\mathrm{val},1}$	$\kappa_{\mathrm{val},2}$	$\mathcal{A}^{\mathrm{A}}_{A_i,\mathrm{L}}$	aM_{A}	Fit range	χ^2/dof
0.1342	0.1342	$0.140\ ^{+9}_{-11}$	$0.838\ ^{+14}_{-18}$	$5-15$	0.621
0.1347	0.1342	$0.136\ ^{+10}_{-12}$	$0.816\ ^{+16}_{-19}$	$5-15$	0.596
0.1347	0.1347	$0.133\ ^{+10}_{-12}$	$0.795\ ^{+16}_{-20}$	$5-15$	0.59
0.1352	0.1342	$0.132\ ^{+10}_{-12}$	$0.793\ ^{+17}_{-20}$	$5-15$	0.574
0.1352	0.1347	$0.128\ ^{+11}_{-12}$	$0.771\ ^{+18}_{-21}$	$5-15$	0.575
0.1352	0.1352	$0.124\ ^{+11}_{-12}$	$0.748\ ^{+19}_{-23}$	$5-15$	0.575
0.1357	0.1342	$0.128\ ^{+10}_{-12}$	$0.770\ ^{+17}_{-21}$	$5-15$	0.581
0.1357	0.1347	$0.123\ ^{+11}_{-12}$	$0.746\ ^{+18}_{-23}$	$5-15$	0.596
0.1357	0.1352	$0.118\ ^{+11}_{-12}$	$0.719\ ^{+21}_{-24}$	$5-15$	0.616
0.1357	0.1357	$0.111\ ^{+11}_{-12}$	$0.690\ ^{+23}_{-25}$	$5-15$	0.646

Table A.21: Fit results for LL,FL,FF fits to $C_{A_i A_i^\dagger}(t)$ correlators from the dataset at $\beta = 5.25$, $\kappa_{\mathrm{sea}} = 0.1352$

$\kappa_{\mathrm{val},1}$	$\kappa_{\mathrm{val},2}$	$\mathcal{A}^{\mathrm{A}}_{A_i,\mathrm{L}}$	aM_{A}	Fit range	χ^2/dof
0.1335	0.1335	$0.186\,^{+12}_{-13}$	$0.991\,^{+15}_{-18}$	$4-15$	0.874
0.1340	0.1335	$0.185\,^{+12}_{-13}$	$0.975\,^{+15}_{-17}$	$4-15$	0.895
0.1340	0.1340	$0.184\,^{+12}_{-13}$	$0.958\,^{+16}_{-18}$	$4-15$	0.904
0.1345	0.1335	$0.184\,^{+12}_{-13}$	$0.958\,^{+15}_{-18}$	$4-15$	0.92
0.1345	0.1340	$0.183\,^{+12}_{-14}$	$0.942\,^{+16}_{-19}$	$4-15$	0.924
0.1345	0.1345	$0.182\,^{+12}_{-14}$	$0.925\,^{+17}_{-19}$	$4-15$	0.917
0.1350	0.1335	$0.183\,^{+12}_{-13}$	$0.941\,^{+16}_{-19}$	$4-15$	0.943
0.1350	0.1340	$0.181\,^{+12}_{-14}$	$0.924\,^{+17}_{-20}$	$4-15$	0.937
0.1350	0.1345	$0.180\,^{+13}_{-14}$	$0.907\,^{+18}_{-20}$	$4-15$	0.921
0.1350	0.1350	$0.177\,^{+13}_{-15}$	$0.889\,^{+18}_{-22}$	$4-15$	0.9

Table A.22: Fit results for LL,FL,FF fits to $C_{A_i A_i^\dagger}(t)$ correlators from the dataset at $\beta = 5.26$, $\kappa_{\mathrm{sea}} = 0.1345$

$\kappa_{\mathrm{val},1}$	$\kappa_{\mathrm{val},2}$	$\mathcal{A}^{\mathrm{A}}_{A_i,\mathrm{L}}$	aM_{A}	Fit range	χ^2/dof
0.1335	0.1335	$0.218\,^{+8}_{-11}$	$1.048\,^{+13}_{-15}$	$4-15$	0.896
0.1340	0.1335	$0.216\,^{+8}_{-11}$	$1.031\,^{+13}_{-16}$	$4-15$	0.871
0.1340	0.1340	$0.215\,^{+9}_{-11}$	$1.015\,^{+13}_{-16}$	$4-15$	0.849
0.1345	0.1335	$0.214\,^{+9}_{-12}$	$1.014\,^{+14}_{-17}$	$4-15$	0.852
0.1345	0.1340	$0.213\,^{+9}_{-12}$	$0.998\,^{+13}_{-17}$	$4-15$	0.829
0.1345	0.1345	$0.212\,^{+9}_{-12}$	$0.983\,^{+14}_{-18}$	$4-15$	0.811
0.1350	0.1335	$0.213\,^{+9}_{-13}$	$0.998\,^{+13}_{-18}$	$4-15$	0.837
0.1350	0.1340	$0.212\,^{+9}_{-12}$	$0.982\,^{+14}_{-18}$	$4-15$	0.812
0.1350	0.1345	$0.211\,^{+10}_{-12}$	$0.967\,^{+14}_{-19}$	$4-15$	0.788
0.1350	0.1350	$0.211\,^{+10}_{-12}$	$0.953\,^{+15}_{-18}$	$4-15$	0.764

Table A.23: Fit results for LL,FL,FF fits to $C_{A_iA_i^\dagger}(t)$ correlators from the dataset at $\beta = 5.29$, $\kappa_{\mathrm{sea}} = 0.1340$

$\kappa_{\mathrm{val},1}$	$\kappa_{\mathrm{val},2}$	$\mathcal{A}^{\mathrm{A}}_{A_i,\mathrm{L}}$	aM_{A}	Fit range	χ^2/dof
0.1327	0.1327	$0.1599\,^{+66}_{-79}$	$0.899\,^{+10}_{-12}$	$5-15$	1.175
0.1332	0.1327	$0.1594\,^{+72}_{-82}$	$0.884\,^{+11}_{-13}$	$5-15$	1.242
0.1332	0.1332	$0.1576\,^{+83}_{-89}$	$0.867\,^{+12}_{-14}$	$5-15$	1.305
0.1334	0.1327	$0.1594\,^{+76}_{-84}$	$0.878\,^{+11}_{-14}$	$5-15$	1.275
0.1334	0.1332	$0.1573\,^{+87}_{-92}$	$0.861\,^{+12}_{-15}$	$5-15$	1.341
0.1334	0.1334	$0.157\,^{+9}_{-10}$	$0.854\,^{+13}_{-16}$	$5-15$	1.375
0.1337	0.1337	$0.155\,^{+10}_{-12}$	$0.836\,^{+16}_{-19}$	$5-15$	1.492
0.1339	0.1337	$0.155\,^{+11}_{-13}$	$0.830\,^{+18}_{-21}$	$5-15$	1.537
0.1339	0.1339	$0.154\,^{+11}_{-14}$	$0.824\,^{+18}_{-22}$	$5-15$	1.561

Table A.24: Fit results for LL,FL,FF fits to $C_{A_iA_i^\dagger}(t)$ correlators from the quenched dataset at $\beta = 5.93$

$\kappa_{\mathrm{val},1}$	$\kappa_{\mathrm{val},2}$	aM_{B}	Fit range	χ^2/dof
0.1335	0.1335	$0.977\ ^{+21}_{-24}$	$4-15$	0.943
0.1340	0.1335	$0.960\ ^{+21}_{-25}$	$4-15$	0.896
0.1340	0.1340	$0.945\ ^{+22}_{-26}$	$4-15$	0.895
0.1345	0.1335	$0.943\ ^{+22}_{-25}$	$4-15$	0.854
0.1345	0.1340	$0.928\ ^{+23}_{-27}$	$4-15$	0.853
0.1345	0.1345	$0.912\ ^{+25}_{-30}$	$4-15$	0.857
0.1350	0.1335	$0.927\ ^{+21}_{-27}$	$4-15$	0.828
0.1350	0.1340	$0.912\ ^{+24}_{-29}$	$4-15$	0.831
0.1350	0.1345	$0.897\ ^{+26}_{-32}$	$4-15$	0.842
0.1350	0.1350	$0.883\ ^{+30}_{-38}$	$4-15$	0.865
0.1355	0.1355	$0.858\ ^{+23}_{-27}$	$4-15$	0.798

Table A.25: Fit results for LL,FL,FF fits to $C_{T_{ij}T_{ij}^\dagger}(t)$ correlators from the dataset at $\beta = 5.2$, $\kappa_{\mathrm{sea}} = 0.1350$

$\kappa_{\mathrm{val},1}$	$\kappa_{\mathrm{val},2}$	aM_{B}	Fit range	χ^2/dof
0.1340	0.1340	$0.882\ ^{+14}_{-16}$	$4-15$	1.183
0.1345	0.1340	$0.863\ ^{+15}_{-18}$	$4-15$	1.179
0.1345	0.1345	$0.846\ ^{+15}_{-19}$	$4-15$	1.218
0.1350	0.1340	$0.841\ ^{+17}_{-20}$	$4-15$	1.178
0.1350	0.1345	$0.825\ ^{+17}_{-22}$	$4-15$	1.164
0.1350	0.1350	$0.809\ ^{+18}_{-25}$	$4-15$	1.161
0.1355	0.1340	$0.818\ ^{+19}_{-25}$	$4-15$	1.203
0.1355	0.1345	$0.803\ ^{+20}_{-28}$	$4-15$	1.139
0.1355	0.1350	$0.789\ ^{+22}_{-32}$	$4-15$	1.079
0.1355	0.1355	$0.779\ ^{+23}_{-36}$	$4-15$	1.055

Table A.26: Fit results for LL,FL,FF fits to $C_{T_{ij}T_{ij}^{\dagger}}(t)$ correlators from the dataset at $\beta = 5.2$, $\kappa_{\mathrm{sea}} = 0.1355$

$\kappa_{\mathrm{val},1}$	$\kappa_{\mathrm{val},2}$	aM_{B}	Fit range	χ^2/dof
0.1342	0.1342	$0.775\ ^{+16}_{-18}$	$4-15$	1.221
0.1350	0.1342	$0.740\ ^{+19}_{-21}$	$4-15$	1.165
0.1350	0.1350	$0.715\ ^{+20}_{-22}$	$4-15$	1.076
0.1355	0.1342	$0.719\ ^{+22}_{-24}$	$4-15$	1.091
0.1355	0.1350	$0.696\ ^{+24}_{-27}$	$4-15$	0.994
0.1355	0.1355	$0.686\ ^{+26}_{-30}$	$4-15$	0.928
0.13565	0.1342	$0.712\ ^{+24}_{-26}$	$4-15$	1.039
0.13565	0.1350	$0.689\ ^{+26}_{-29}$	$4-15$	0.943
0.13565	0.1355	$0.679\ ^{+29}_{-34}$	$4-15$	0.892
0.13565	0.13565	$0.678\ ^{+30}_{-36}$	$4-15$	0.87
0.1358	0.1342	$0.703\ ^{+27}_{-30}$	$4-15$	0.959
0.1358	0.1350	$0.683\ ^{+29}_{-34}$	$4-15$	0.877
0.1358	0.1355	$0.674\ ^{+33}_{-39}$	$4-15$	0.849
0.1358	0.13565	$0.672\ ^{+34}_{-39}$	$4-15$	0.835
0.1358	0.1358	$0.669\ ^{+37}_{-45}$	$4-15$	0.796

Table A.27: Fit results for LL,FL,FF fits to $C_{T_{ij}T_{ij}^{\dagger}}(t)$ correlators from the dataset at $\beta = 5.2$, $\kappa_{\mathrm{sea}} = 0.13565$

$\kappa_{\mathrm{val},1}$	$\kappa_{\mathrm{val},2}$	aM_{B}	Fit range	χ^2/dof
0.1342	0.1342	$0.806\ ^{+16}_{-16}$	$4-15$	0.836
0.1350	0.1342	$0.772\ ^{+19}_{-19}$	$4-15$	0.8
0.1350	0.1350	$0.737\ ^{+21}_{-20}$	$4-15$	0.724
0.1355	0.1342	$0.753\ ^{+22}_{-20}$	$4-15$	0.731
0.1355	0.1350	$0.717\ ^{+25}_{-23}$	$4-15$	0.691
0.1355	0.1355	$0.681\ ^{+29}_{-29}$	$4-15$	0.693
0.13565	0.1342	$0.750\ ^{+22}_{-21}$	$4-15$	0.686
0.13565	0.1350	$0.713\ ^{+24}_{-24}$	$4-15$	0.672
0.13565	0.1355	$0.677\ ^{+31}_{-31}$	$4-15$	0.689
0.13565	0.13565	$0.663\ ^{+35}_{-35}$	$4-15$	0.705
0.1358	0.1342	$0.750\ ^{+22}_{-24}$	$4-15$	0.621
0.1358	0.1350	$0.713\ ^{+26}_{-28}$	$4-15$	0.646
0.1358	0.1355	$0.675\ ^{+34}_{-35}$	$4-15$	0.677
0.1358	0.13565	$0.659\ ^{+40}_{-39}$	$4-15$	0.69
0.1358	0.1358	$0.643\ ^{+46}_{-46}$	$4-15$	0.694
0.13595	0.13595	$0.644\ ^{+63}_{-75}$	$4-15$	0.631

Table A.28: Fit results for LL,FL,FF fits to $C_{T_{ij}T^{\dagger}_{ij}}(t)$ correlators from the dataset at $\beta = 5.2$, $\kappa_{\mathrm{sea}} = 0.1358$

$\kappa_{\mathrm{val},1}$	$\kappa_{\mathrm{val},2}$	aM_{B}	Fit range	χ^2/dof
0.1342	0.1342	$0.871\ ^{+16}_{-23}$	$5-15$	0.565
0.1347	0.1342	$0.854\ ^{+16}_{-24}$	$5-15$	0.55
0.1347	0.1347	$0.839\ ^{+15}_{-24}$	$5-15$	0.543
0.1352	0.1342	$0.838\ ^{+17}_{-24}$	$5-15$	0.554
0.1352	0.1347	$0.823\ ^{+16}_{-25}$	$5-15$	0.572
0.1352	0.1352	$0.809\ ^{+15}_{-26}$	$5-15$	0.609
0.1357	0.1342	$0.824\ ^{+15}_{-25}$	$5-15$	0.57
0.1357	0.1347	$0.808\ ^{+16}_{-26}$	$5-15$	0.612
0.1357	0.1352	$0.793\ ^{+16}_{-26}$	$5-15$	0.672
0.1357	0.1357	$0.781\ ^{+16}_{-27}$	$5-15$	0.734

Table A.29: Fit results for LL,FL,FF fits to $C_{T_{ij}T_{ij}^{\dagger}}(t)$ correlators from the dataset at $\beta = 5.25$, $\kappa_{\mathrm{sea}} = 0.1352$

$\kappa_{\mathrm{val},1}$	$\kappa_{\mathrm{val},2}$	aM_{B}	Fit range	χ^2/dof
0.1335	0.1335	$1.061\ ^{+11}_{-13}$	$3-15$	0.789
0.1340	0.1335	$1.049\ ^{+11}_{-13}$	$3-15$	0.751
0.1340	0.1340	$1.037\ ^{+11}_{-14}$	$3-15$	0.715
0.1345	0.1335	$1.038\ ^{+11}_{-14}$	$3-15$	0.711
0.1345	0.1340	$1.027\ ^{+11}_{-14}$	$3-15$	0.678
0.1345	0.1345	$1.017\ ^{+12}_{-15}$	$3-15$	0.651
0.1350	0.1335	$1.028\ ^{+11}_{-14}$	$3-15$	0.661
0.1350	0.1340	$1.017\ ^{+12}_{-14}$	$3-15$	0.635
0.1350	0.1345	$1.008\ ^{+12}_{-14}$	$3-15$	0.613
0.1350	0.1350	$0.999\ ^{+12}_{-15}$	$3-15$	0.599

Table A.30: Fit results for LL,FL,FF fits to $C_{T_{ij}T^{\dagger}_{ij}}(t)$ correlators from the dataset at $\beta = 5.26$, $\kappa_{\mathrm{sea}} = 0.1345$

$\kappa_{\mathrm{val},1}$	$\kappa_{\mathrm{val},2}$	aM_{B}	Fit range	χ^2/dof
0.1335	0.1335	$1.047\ ^{+16}_{-23}$	$4-15$	0.778
0.1340	0.1335	$1.030\ ^{+16}_{-23}$	$4-15$	0.748
0.1340	0.1340	$1.017\ ^{+16}_{-22}$	$4-15$	0.7
0.1345	0.1335	$1.014\ ^{+17}_{-24}$	$4-15$	0.726
0.1345	0.1340	$1.000\ ^{+17}_{-23}$	$4-15$	0.684
0.1345	0.1345	$0.987\ ^{+17}_{-21}$	$4-15$	0.649
0.1350	0.1335	$0.998\ ^{+17}_{-26}$	$4-15$	0.717
0.1350	0.1340	$0.984\ ^{+17}_{-24}$	$4-15$	0.681
0.1350	0.1345	$0.971\ ^{+17}_{-23}$	$4-15$	0.652
0.1350	0.1350	$0.960\ ^{+17}_{-23}$	$4-15$	0.637

Table A.31: Fit results for LL,FL,FF fits to $C_{T_{ij}T_{ij}^\dagger}(t)$ correlators from the dataset at $\beta = 5.29$, $\kappa_{\mathrm{sea}} = 0.1340$

$\kappa_{\mathrm{val},1}$	$\kappa_{\mathrm{val},2}$	aM_{B}	Fit range	χ^2/dof
0.1327	0.1327	$0.927\ ^{+12}_{-14}$	$5-15$	0.964
0.1332	0.1327	$0.914\ ^{+12}_{-15}$	$5-15$	0.945
0.1332	0.1332	$0.899\ ^{+14}_{-17}$	$5-15$	0.957
0.1334	0.1327	$0.909\ ^{+13}_{-16}$	$5-15$	0.944
0.1334	0.1332	$0.894\ ^{+14}_{-18}$	$5-15$	0.978
0.1334	0.1334	$0.888\ ^{+14}_{-18}$	$5-15$	0.996
0.1337	0.1337	$0.871\ ^{+17}_{-20}$	$5-15$	1.118
0.1339	0.1337	$0.865\ ^{+18}_{-20}$	$5-15$	1.188
0.1339	0.1339	$0.857\ ^{+20}_{-20}$	$5-15$	1.249

Table A.32: Fit results for LL,FL,FF fits to $C_{T_{ij}T_{ij}^\dagger}(t)$ correlators from the quenched dataset at $\beta = 5.93$

$\kappa_{\mathrm{val},1}$	$\kappa_{\mathrm{val},2}$	aM_{S}	Fit range	χ^2/dof
0.1335	0.1335	$0.858\,^{+21}_{-27}$	$4-15$	0.75
0.1340	0.1335	$0.835\,^{+22}_{-28}$	$4-15$	0.767
0.1340	0.1340	$0.807\,^{+24}_{-31}$	$4-15$	0.765
0.1345	0.1335	$0.812\,^{+23}_{-30}$	$4-15$	0.789
0.1345	0.1340	$0.782\,^{+26}_{-34}$	$4-15$	0.788
0.1345	0.1345	$0.750\,^{+29}_{-40}$	$4-15$	0.784
0.1350	0.1335	$0.788\,^{+26}_{-35}$	$4-15$	0.818
0.1350	0.1340	$0.757\,^{+29}_{-39}$	$4-15$	0.813
0.1350	0.1345	$0.724\,^{+33}_{-44}$	$4-15$	0.803
0.1350	0.1350	$0.691\,^{+39}_{-46}$	$4-15$	0.787
0.1355	0.1355	$0.655\,^{+37}_{-39}$	$4-15$	0.757

Table A.33: Fit results for LL,FL,FF fits to $C_{SS^\dagger}(t)$ correlators from the dataset at $\beta = 5.2$, $\kappa_{\mathrm{sea}} = 0.1350$

$\kappa_{\mathrm{val},1}$	$\kappa_{\mathrm{val},2}$	aM_{S}	Fit range	χ^2/dof
0.1340	0.1340	$0.776\ ^{+16}_{-15}$	$4-15$	0.495
0.1345	0.1340	$0.749\ ^{+17}_{-16}$	$4-15$	0.512
0.1345	0.1345	$0.723\ ^{+18}_{-19}$	$4-15$	0.537
0.1350	0.1340	$0.722\ ^{+19}_{-19}$	$4-15$	0.542
0.1350	0.1345	$0.695\ ^{+22}_{-21}$	$4-15$	0.565
0.1350	0.1350	$0.670\ ^{+24}_{-24}$	$4-15$	0.582
0.1355	0.1340	$0.697\ ^{+22}_{-22}$	$4-15$	0.593
0.1355	0.1345	$0.671\ ^{+24}_{-26}$	$4-15$	0.601
0.1355	0.1350	$0.649\ ^{+29}_{-33}$	$4-15$	0.599
0.1355	0.1355	$0.632\ ^{+31}_{-42}$	$4-15$	0.582

Table A.34: Fit results for LL,FL,FF fits to $C_{SS^\dagger}(t)$ correlators from the dataset at $\beta = 5.2$, $\kappa_{\mathrm{sea}} = 0.1355$

$\kappa_{\mathrm{val},1}$	$\kappa_{\mathrm{val},2}$	aM_{S}	Fit range	χ^2/dof
0.1342	0.1342	$0.677\ ^{+16}_{-15}$	$4-15$	0.881
0.1350	0.1342	$0.639\ ^{+19}_{-18}$	$4-15$	0.86
0.1350	0.1350	$0.600\ ^{+23}_{-23}$	$4-15$	0.831
0.1355	0.1342	$0.616\ ^{+22}_{-22}$	$4-15$	0.8
0.1355	0.1350	$0.576\ ^{+31}_{-31}$	$4-15$	0.747
0.1355	0.1355	$0.548\ ^{+54}_{-51}$	$4-15$	0.704
0.13565	0.1342	$0.611\ ^{+25}_{-26}$	$4-15$	0.763
0.13565	0.1350	$0.572\ ^{+37}_{-38}$	$4-15$	0.71
0.13565	0.1355	$0.542\ ^{+61}_{-60}$	$4-15$	0.697
0.13565	0.13565	$0.526\ ^{+78}_{-64}$	$4-15$	0.717
0.1358	0.1342	$0.609\ ^{+31}_{-32}$	$4-15$	0.717
0.1358	0.1350	$0.572\ ^{+45}_{-45}$	$4-15$	0.677
0.1358	0.1355	$0.549\ ^{+63}_{-83}$	$4-15$	0.716
0.1358	0.13565	$0.496\ ^{+95}_{-77}$	$4-15$	0.754
0.1358	0.1358	$0.43\ ^{+10}_{-\ 8}$	$4-15$	0.817

Table A.35: Fit results for LL,FL,FF fits to $C_{SS^\dagger}(t)$ correlators from the dataset at $\beta = 5.2$, $\kappa_{\mathrm{sea}} = 0.13565$

$\kappa_{\mathrm{val},1}$	$\kappa_{\mathrm{val},2}$	aM_{S}	Fit range	χ^2/dof
0.1342	0.1342	$0.657\ ^{+12}_{-13}$	$4-15$	0.36
0.1350	0.1342	$0.613\ ^{+14}_{-14}$	$4-15$	0.358
0.1350	0.1350	$0.567\ ^{+17}_{-17}$	$4-15$	0.334
0.1355	0.1342	$0.586\ ^{+18}_{-16}$	$4-15$	0.353
0.1355	0.1350	$0.540\ ^{+20}_{-19}$	$4-15$	0.312
0.1355	0.1355	$0.515\ ^{+29}_{-26}$	$4-15$	0.283
0.13565	0.1342	$0.579\ ^{+19}_{-18}$	$4-15$	0.361
0.13565	0.1350	$0.533\ ^{+25}_{-22}$	$4-15$	0.312
0.13565	0.1355	$0.511\ ^{+36}_{-31}$	$4-15$	0.289
0.13565	0.13565	$0.510\ ^{+42}_{-37}$	$4-15$	0.291
0.1358	0.1342	$0.574\ ^{+22}_{-20}$	$4-15$	0.382
0.1358	0.1350	$0.530\ ^{+30}_{-26}$	$4-15$	0.322
0.1358	0.1355	$0.513\ ^{+46}_{-40}$	$4-15$	0.305
0.1358	0.13565	$0.518\ ^{+50}_{-51}$	$4-15$	0.308
0.1358	0.1358	$0.543\ ^{+51}_{-69}$	$4-15$	0.315
0.13595	0.13595	$0.606\ ^{+48}_{-58}$	$4-15$	0.407

Table A.36: Fit results for LL,FL,FF fits to $C_{SS^\dagger}(t)$ correlators from the dataset at $\beta = 5.2$, $\kappa_{\mathrm{sea}} = 0.1358$

$\kappa_{\mathrm{val},1}$	$\kappa_{\mathrm{val},2}$	aM_{S}	Fit range	χ^2/dof
0.1342	0.1342	$0.799\ ^{+20}_{-21}$	$4-15$	0.69
0.1347	0.1342	$0.780\ ^{+22}_{-23}$	$4-15$	0.641
0.1347	0.1347	$0.761\ ^{+24}_{-26}$	$4-15$	0.619
0.1352	0.1342	$0.762\ ^{+24}_{-26}$	$4-15$	0.602
0.1352	0.1347	$0.743\ ^{+26}_{-28}$	$4-15$	0.577
0.1352	0.1352	$0.727\ ^{+27}_{-31}$	$4-15$	0.556
0.1357	0.1342	$0.749\ ^{+26}_{-28}$	$4-15$	0.598
0.1357	0.1347	$0.731\ ^{+28}_{-31}$	$4-15$	0.569
0.1357	0.1352	$0.716\ ^{+31}_{-33}$	$4-15$	0.542
0.1357	0.1357	$0.712\ ^{+36}_{-39}$	$4-15$	0.541

Table A.37: Fit results for LL,FL,FF fits to $C_{SS^\dagger}(t)$ correlators from the dataset at $\beta = 5.25$, $\kappa_{\mathrm{sea}} = 0.1352$

$\kappa_{\mathrm{val},1}$	$\kappa_{\mathrm{val},2}$	aM_{S}	Fit range	χ^2/dof
0.1335	0.1335	$0.875\ ^{+34}_{-38}$	$4-15$	0.778
0.1340	0.1335	$0.858\ ^{+34}_{-40}$	$4-15$	0.781
0.1340	0.1340	$0.840\ ^{+36}_{-42}$	$4-15$	0.777
0.1345	0.1335	$0.841\ ^{+37}_{-44}$	$4-15$	0.787
0.1345	0.1340	$0.823\ ^{+38}_{-44}$	$4-15$	0.785
0.1345	0.1345	$0.805\ ^{+41}_{-44}$	$4-15$	0.779
0.1350	0.1335	$0.826\ ^{+39}_{-45}$	$4-15$	0.786
0.1350	0.1340	$0.807\ ^{+40}_{-45}$	$4-15$	0.782
0.1350	0.1345	$0.788\ ^{+45}_{-45}$	$4-15$	0.767
0.1350	0.1350	$0.766\ ^{+52}_{-48}$	$4-15$	0.733

Table A.38: Fit results for LL,FL,FF fits to $C_{SS^\dagger}(t)$ correlators from the dataset at $\beta = 5.26$, $\kappa_{\mathrm{sea}} = 0.1345$

$\kappa_{\mathrm{val},1}$	$\kappa_{\mathrm{val},2}$	aM_{S}	Fit range	χ^2/dof
0.1335	0.1335	$0.929\ ^{+28}_{-22}$	$4-15$	1.015
0.1340	0.1335	$0.915\ ^{+30}_{-23}$	$4-15$	0.962
0.1340	0.1340	$0.902\ ^{+30}_{-26}$	$4-15$	0.922
0.1345	0.1335	$0.901\ ^{+30}_{-25}$	$4-15$	0.905
0.1345	0.1340	$0.888\ ^{+28}_{-26}$	$4-15$	0.865
0.1345	0.1345	$0.875\ ^{+26}_{-31}$	$4-15$	0.828
0.1350	0.1335	$0.889\ ^{+29}_{-27}$	$4-15$	0.847
0.1350	0.1340	$0.876\ ^{+27}_{-30}$	$4-15$	0.81
0.1350	0.1345	$0.865\ ^{+23}_{-36}$	$4-15$	0.777
0.1350	0.1350	$0.859\ ^{+16}_{-44}$	$4-15$	0.747

Table A.39: Fit results for LL,FL,FF fits to $C_{SS^\dagger}(t)$ correlators from the dataset at $\beta = 5.29$, $\kappa_{\mathrm{sea}} = 0.1340$

$\kappa_{\mathrm{val},1}$	$\kappa_{\mathrm{val},2}$	aM_{S}	Fit range	χ^2/dof
0.1327	0.1327	$0.863\ ^{+16}_{-18}$	$5-15$	1.186
0.1332	0.1327	$0.857\ ^{+18}_{-19}$	$5-15$	1.181
0.1332	0.1332	$0.852\ ^{+21}_{-22}$	$5-15$	1.184
0.1334	0.1327	$0.856\ ^{+19}_{-20}$	$5-15$	1.179
0.1334	0.1332	$0.864\ ^{+13}_{-14}$	$4-15$	1.071
0.1334	0.1334	$0.862\ ^{+14}_{-15}$	$4-15$	1.062
0.1337	0.1337	$0.865\ ^{+17}_{-19}$	$4-15$	1.051
0.1339	0.1337	$0.871\ ^{+18}_{-20}$	$4-15$	1.07
0.1339	0.1339	$0.878\ ^{+21}_{-23}$	$4-15$	1.091

Table A.40: Fit results for LL,FL,FF fits to $C_{SS^\dagger}(t)$ correlators from the quenched dataset at $\beta = 5.93$

κ_{val}	aM_{N}^{+}	aM_{N}^{-}	Fit range	χ^2/dof
0.1335	$1.0622\,^{+56}_{-79}$	$1.377\,^{+26}_{-30}$	$6-27$	0.443
0.1340	$1.0026\,^{+66}_{-86}$	$1.327\,^{+27}_{-34}$	$6-27$	0.47
0.1345	$0.942\,^{+\ 8}_{-11}$	$1.284\,^{+30}_{-42}$	$6-27$	0.521
0.1350	$0.8823\,^{+69}_{-83}$	$1.303\,^{+20}_{-27}$	$5-28$	0.672
0.1355	$0.8107\,^{+69}_{-82}$	$1.250\,^{+23}_{-27}$	$5-28$	0.691

Table A.41: Fit results for LL,FL,FF fits to $C_{N\overline{N}}(t)$ correlators from the dataset at $\beta = 5.2$, $\kappa_{\text{sea}} = 0.1350$

κ_{val}	aM_{N}^{+}	aM_{N}^{-}	Fit range	χ^2/dof
0.1340	$0.915\,^{+\ 8}_{-11}$	$1.181\,^{+24}_{-24}$	$6-27$	0.804
0.1345	$0.856\,^{+\ 9}_{-14}$	$1.125\,^{+27}_{-26}$	$6-27$	0.769
0.1350	$0.799\,^{+11}_{-17}$	$1.069\,^{+34}_{-34}$	$6-27$	0.812
0.1355	$0.734\,^{+14}_{-19}$	$1.033\,^{+43}_{-47}$	$6-27$	0.721

Table A.42: Fit results for LL,FL,FF fits to $C_{N\overline{N}}(t)$ correlators from the dataset at $\beta = 5.2$, $\kappa_{\text{sea}} = 0.1355$

κ_{val}	aM_{N}^{+}	aM_{N}^{-}	Fit range	χ^2/dof
0.1342	$0.8635\,^{+74}_{-82}$	$1.141\,^{+23}_{-25}$	$6-27$	0.242
0.1350	$0.7673\,^{+72}_{-75}$	$1.084\,^{+23}_{-31}$	$5-27$	0.347
0.1355	$0.706\,^{+\ 9}_{-11}$	$1.050\,^{+27}_{-36}$	$5-27$	0.352
0.13565	$0.689\,^{+11}_{-12}$	$1.045\,^{+35}_{-37}$	$5-27$	0.397
0.1358	$0.670\,^{+15}_{-14}$	$1.014\,^{+49}_{-54}$	$5-27$	0.428

Table A.43: Fit results for LL,FL,FF fits to $C_{N\overline{N}}(t)$ correlators from the dataset at $\beta = 5.2$, $\kappa_{\text{sea}} = 0.13565$

κ_{val}	aM_{N}^{+}	aM_{N}^{-}	Fit range	χ^2/dof
0.1342	$0.846\ ^{+13}_{-11}$	$1.090\ ^{+28}_{-29}$	$6-27$	0.85
0.1350	$0.742\ ^{+17}_{-19}$	$0.979\ ^{+39}_{-42}$	$6-27$	0.732
0.1355	$0.696\ ^{+13}_{-13}$	$0.899\ ^{+45}_{-53}$	$5-27$	0.657
0.13565	$0.675\ ^{+14}_{-13}$	$0.897\ ^{+42}_{-56}$	$5-27$	0.625
0.1358	$0.648\ ^{+18}_{-16}$	$0.911\ ^{+40}_{-60}$	$5-27$	0.626
0.13595	$0.608\ ^{+29}_{-29}$	$1.042\ ^{+47}_{-51}$	$5-28$	0.761

Table A.44: Fit results for LL,FL,FF fits to $C_{N\overline{N}}(t)$ correlators from the dataset at $\beta = 5.2$, $\kappa_{\text{sea}} = 0.1358$

κ_{val}	aM_{N}^{+}	aM_{N}^{-}	Fit range	χ^2/dof
0.1342	$0.9404\ ^{+65}_{-74}$	$1.238\ ^{+15}_{-19}$	$6-27$	0.7
0.1347	$0.8757\ ^{+77}_{-83}$	$1.176\ ^{+19}_{-22}$	$6-27$	0.543
0.1352	$0.808\ ^{+\ 9}_{-11}$	$1.115\ ^{+22}_{-24}$	$6-27$	0.504
0.1357	$0.735\ ^{+12}_{-16}$	$1.059\ ^{+27}_{-32}$	$6-27$	0.645

Table A.45: Fit results for LL,FL,FF fits to $C_{N\overline{N}}(t)$ correlators from the dataset at $\beta = 5.25$, $\kappa_{\text{sea}} = 0.1352$

κ_{val}	aM_{N}^{+}	aM_{N}^{-}	Fit range	χ^2/dof
0.1335	$1.1030\ ^{+68}_{-94}$	$1.373\ ^{+34}_{-31}$	$6-27$	0.566
0.1340	$1.0465\ ^{+68}_{-91}$	$1.307\ ^{+36}_{-32}$	$6-27$	0.502
0.1345	$0.9919\ ^{+64}_{-68}$	$1.240\ ^{+38}_{-34}$	$5-27$	0.448
0.1350	$0.9334\ ^{+64}_{-63}$	$1.186\ ^{+44}_{-43}$	$5-27$	0.419

Table A.46: Fit results for LL,FL,FF fits to $C_{N\overline{N}}(t)$ correlators from the dataset at $\beta = 5.26$, $\kappa_{\text{sea}} = 0.1345$

$\kappa_{\rm val}$	$aM_{\rm N}^{+}$	$aM_{\rm N}^{-}$	Fit range	χ^2/dof
0.1335	$1.1251\ ^{+67}_{-80}$	$1.458\ ^{+46}_{-60}$	$6-27$	0.949
0.1340	$1.0694\ ^{+74}_{-88}$	$1.432\ ^{+36}_{-56}$	$6-27$	0.878
0.1345	$1.0118\ ^{+81}_{-95}$	$1.395\ ^{+30}_{-42}$	$6-27$	0.829
0.1350	$0.952\ ^{+10}_{-11}$	$1.353\ ^{+31}_{-40}$	$6-27$	0.844

Table A.47: Fit results for LL,FL,FF fits to $C_{N\overline{N}}(t)$ correlators from the dataset at $\beta = 5.29$, $\kappa_{\rm sea} = 0.1340$

$\kappa_{\rm val}$	$aM_{\rm N}^{+}$	$aM_{\rm N}^{-}$	Fit range	χ^2/dof
0.1327	$0.9629\ ^{+36}_{-48}$	$1.278\ ^{+14}_{-17}$	$7-27$	0.82
0.1332	$0.8973\ ^{+48}_{-58}$	$1.228\ ^{+19}_{-21}$	$7-27$	0.841
0.1334	$0.8704\ ^{+52}_{-64}$	$1.210\ ^{+22}_{-25}$	$7-27$	0.852
0.1337	$0.8351\ ^{+57}_{-63}$	$1.188\ ^{+31}_{-33}$	$6-27$	0.845
0.1339	$0.8079\ ^{+62}_{-70}$	$1.179\ ^{+37}_{-43}$	$6-27$	0.823

Table A.48: Fit results for LL,FL,FF fits to $C_{N\overline{N}}(t)$ correlators from the quenched dataset at $\beta = 5.93$

κ_{val}	aM_{Δ}^{+}	aM_{Δ}^{-}	Fit range	χ^2/dof
0.1335	$1.133\,^{+10}_{-13}$	$1.515\,^{+22}_{-27}$	$6-28$	0.765
0.1340	$1.078\,^{+12}_{-16}$	$1.474\,^{+22}_{-28}$	$6-28$	0.71
0.1345	$1.030\,^{+14}_{-19}$	$1.427\,^{+23}_{-30}$	$6-28$	0.673
0.1350	$0.988\,^{+13}_{-18}$	$1.379\,^{+29}_{-33}$	$6-28$	0.633
0.1355	$0.936\,^{+13}_{-15}$	$1.255\,^{+42}_{-65}$	$6-27$	0.573

Table A.49: Fit results for LL,FL,FF fits to $C_{\Delta\overline{\Delta}}(t)$ correlators from the dataset at $\beta = 5.2$, $\kappa_{\mathrm{sea}} = 0.1350$

κ_{val}	aM_{Δ}^{+}	aM_{Δ}^{-}	Fit range	χ^2/dof
0.1340	$0.981\,^{+11}_{-10}$	$1.267\,^{+36}_{-33}$	$6-27$	1.083
0.1345	$0.934\,^{+13}_{-13}$	$1.231\,^{+38}_{-38}$	$6-27$	1.095
0.1350	$0.897\,^{+14}_{-15}$	$1.221\,^{+49}_{-50}$	$6-27$	1.017
0.1355	$0.847\,^{+18}_{-19}$	$1.233\,^{+47}_{-58}$	$6-27$	0.708

Table A.50: Fit results for LL,FL,FF fits to $C_{\Delta\overline{\Delta}}(t)$ correlators from the dataset at $\beta = 5.2$, $\kappa_{\mathrm{sea}} = 0.1355$

κ_{val}	aM_{Δ}^{+}	aM_{Δ}^{-}	Fit range	χ^2/dof
0.1342	$0.963\,^{+10}_{-10}$	$1.173\,^{+41}_{-57}$	$6-27$	0.899
0.1350	$0.887\,^{+13}_{-16}$	$1.116\,^{+51}_{-73}$	$6-27$	0.722
0.1355	$0.857\,^{+14}_{-15}$	$1.193\,^{+32}_{-36}$	$5-28$	0.715
0.13565	$0.843\,^{+16}_{-18}$	$1.204\,^{+32}_{-36}$	$5-28$	0.644
0.1358	$0.825\,^{+18}_{-21}$	$1.224\,^{+32}_{-43}$	$5-28$	0.576

Table A.51: Fit results for LL,FL,FF fits to $C_{\Delta\overline{\Delta}}(t)$ correlators from the dataset at $\beta = 5.2$, $\kappa_{\mathrm{sea}} = 0.13565$

$\kappa_{\rm val}$	aM_Δ^+	aM_Δ^-	Fit range	χ^2/dof
0.1342	$0.9326\ ^{+90}_{-91}$	$1.179\ ^{+21}_{-29}$	$6-27$	0.692
0.1350	$0.838\ ^{+13}_{-14}$	$1.106\ ^{+32}_{-49}$	$6-27$	0.725
0.1355	$0.795\ ^{+20}_{-19}$	$1.041\ ^{+53}_{-87}$	$6-27$	0.599
0.13565	$0.791\ ^{+21}_{-23}$	$1.00\ ^{+\ 7}_{-11}$	$6-27$	0.599
0.1358	$0.822\ ^{+16}_{-16}$	$1.156\ ^{+48}_{-67}$	$5-28$	0.754
0.13595	$0.822\ ^{+21}_{-22}$	$1.176\ ^{+50}_{-75}$	$5-28$	0.711

Table A.52: Fit results for LL,FL,FF fits to $C_{\Delta\overline{\Delta}}(t)$ correlators from the dataset at $\beta = 5.2$, $\kappa_{\rm sea} = 0.1358$

$\kappa_{\rm val}$	aM_Δ^+	aM_Δ^-	Fit range	χ^2/dof
0.1342	$1.009\ ^{+10}_{-10}$	$1.318\ ^{+25}_{-28}$	$7-27$	0.694
0.1347	$0.952\ ^{+13}_{-12}$	$1.282\ ^{+25}_{-29}$	$7-27$	0.564
0.1352	$0.922\ ^{+11}_{-11}$	$1.254\ ^{+26}_{-33}$	$6-27$	0.652
0.1357	$0.868\ ^{+16}_{-16}$	$1.225\ ^{+25}_{-37}$	$6-27$	0.695

Table A.53: Fit results for LL,FL,FF fits to $C_{\Delta\overline{\Delta}}(t)$ correlators from the dataset at $\beta = 5.25$, $\kappa_{\rm sea} = 0.1352$

$\kappa_{\rm val}$	aM_Δ^+	aM_Δ^-	Fit range	χ^2/dof
0.1335	$1.1656\ ^{+79}_{-66}$	$1.494\ ^{+30}_{-35}$	$5-27$	0.622
0.1340	$1.1137\ ^{+78}_{-71}$	$1.474\ ^{+26}_{-28}$	$5-28$	0.653
0.1345	$1.0620\ ^{+79}_{-78}$	$1.425\ ^{+28}_{-30}$	$5-28$	0.69
0.1350	$1.0103\ ^{+94}_{-87}$	$1.372\ ^{+33}_{-37}$	$5-28$	0.742

Table A.54: Fit results for LL,FL,FF fits to $C_{\Delta\overline{\Delta}}(t)$ correlators from the dataset at $\beta = 5.26$, $\kappa_{\rm sea} = 0.1345$

$\kappa_{\rm val}$	aM_Δ^+	aM_Δ^-	Fit range	$\chi^2/\rm dof$
0.1335	$1.221\,^{+\ 8}_{-10}$	$1.433\,^{+67}_{-77}$	$6-27$	1.697
0.1340	$1.172\,^{+\ 9}_{-10}$	$1.38\,^{+\ 8}_{-10}$	$6-27$	1.68
0.1345	$1.120\,^{+10}_{-12}$	$1.34\,^{+\ 9}_{-13}$	$6-27$	1.64
0.1350	$1.068\,^{+12}_{-14}$	$1.32\,^{+\ 8}_{-12}$	$6-27$	1.502

Table A.55: Fit results for LL,FL,FF fits to $C_{\Delta\overline{\Delta}}(t)$ correlators from the dataset at $\beta = 5.29$, $\kappa_{\rm sea} = 0.1340$

$\kappa_{\rm val}$	aM_Δ^+	aM_Δ^-	Fit range	$\chi^2/\rm dof$
0.1327	$1.0595\,^{+57}_{-56}$	$1.369\,^{+14}_{-17}$	$7-27$	0.769
0.1332	$1.0070\,^{+70}_{-71}$	$1.337\,^{+17}_{-20}$	$7-27$	0.747
0.1334	$0.9859\,^{+74}_{-85}$	$1.326\,^{+18}_{-21}$	$7-27$	0.719
0.1337	$0.953\,^{+\ 8}_{-11}$	$1.310\,^{+22}_{-25}$	$7-27$	0.671
0.1339	$0.931\,^{+10}_{-11}$	$1.299\,^{+26}_{-29}$	$7-27$	0.676

Table A.56: Fit results for LL,FL,FF fits to $C_{\Delta\overline{\Delta}}(t)$ correlators from the quenched dataset at $\beta = 5.93$

$\kappa_{\mathrm{val},1}$	$\kappa_{\mathrm{val},2}$	r	s	r_{imp}	s_{imp}
0.1335	0.1335	$0.09055\ ^{+24}_{-23}$	$0.1653\ ^{+10}_{-10}$	$0.08556\ ^{+20}_{-21}$	$0.1608\ ^{+9}_{-10}$
0.1340	0.1335	$0.08311\ ^{+23}_{-23}$	$0.1515\ ^{+9}_{-10}$	$0.07892\ ^{+21}_{-21}$	$0.1477\ ^{+9}_{-10}$
0.1340	0.1340	$0.07577\ ^{+22}_{-23}$	$0.1380\ ^{+9}_{-10}$	$0.07228\ ^{+20}_{-20}$	$0.1348\ ^{+9}_{-10}$
0.1345	0.1335	$0.07574\ ^{+22}_{-24}$	$0.1380\ ^{+9}_{-10}$	$0.07226\ ^{+20}_{-21}$	$0.1348\ ^{+9}_{-10}$
0.1345	0.1340	$0.06849\ ^{+22}_{-24}$	$0.1247\ ^{+9}_{-11}$	$0.06564\ ^{+20}_{-21}$	$0.1221\ ^{+8}_{-10}$
0.1345	0.1345	$0.06131\ ^{+22}_{-25}$	$0.1117\ ^{+8}_{-11}$	$0.05903\ ^{+21}_{-22}$	$0.1097\ ^{+8}_{-10}$
0.1350	0.1335	$0.06843\ ^{+22}_{-26}$	$0.1246\ ^{+9}_{-11}$	$0.06559\ ^{+21}_{-22}$	$0.1220\ ^{+8}_{-11}$
0.1350	0.1340	$0.06127\ ^{+22}_{-25}$	$0.1117\ ^{+8}_{-11}$	$0.05899\ ^{+20}_{-22}$	$0.1096\ ^{+8}_{-11}$
0.1350	0.1345	$0.05419\ ^{+22}_{-26}$	$0.0989\ ^{+8}_{-11}$	$0.05240\ ^{+20}_{-23}$	$0.0973\ ^{+8}_{-10}$
0.1350	0.1350	$0.04719\ ^{+21}_{-26}$	$0.0865\ ^{+8}_{-11}$	$0.04583\ ^{+20}_{-24}$	$0.0852\ ^{+7}_{-10}$
0.1355	0.1355	$0.03346\ ^{+20}_{-23}$	$0.06281\ ^{+65}_{-81}$	$0.03276\ ^{+19}_{-22}$	$0.06215\ ^{+64}_{-79}$

Table A.57: Results for r, s, r_{imp} and s_{imp} from pseudoscalar fits for the dataset at $\beta = 5.2$, $\kappa_{\mathrm{sea}} = 0.1350$

$\kappa_{\mathrm{val},1}$	$\kappa_{\mathrm{val},2}$	r	s	r_{imp}	s_{imp}
0.1340	0.1340	$0.06591\ ^{+18}_{-22}$	$0.11537\ ^{+76}_{-76}$	$0.06338\ ^{+16}_{-20}$	$0.11315\ ^{+73}_{-73}$
0.1345	0.1340	$0.05865\ ^{+18}_{-22}$	$0.10269\ ^{+76}_{-73}$	$0.05664\ ^{+17}_{-21}$	$0.10093\ ^{+73}_{-70}$
0.1345	0.1345	$0.05150\ ^{+18}_{-23}$	$0.09020\ ^{+74}_{-70}$	$0.04995\ ^{+17}_{-21}$	$0.08885\ ^{+72}_{-68}$
0.1350	0.1340	$0.05148\ ^{+19}_{-23}$	$0.09035\ ^{+77}_{-74}$	$0.04993\ ^{+18}_{-21}$	$0.08899\ ^{+75}_{-72}$
0.1350	0.1345	$0.04443\ ^{+20}_{-23}$	$0.07806\ ^{+74}_{-72}$	$0.04327\ ^{+18}_{-22}$	$0.07704\ ^{+73}_{-70}$
0.1350	0.1350	$0.03748\ ^{+20}_{-24}$	$0.06614\ ^{+78}_{-73}$	$0.03665\ ^{+19}_{-23}$	$0.06541\ ^{+76}_{-72}$
0.1355	0.1340	$0.04443\ ^{+21}_{-23}$	$0.07838\ ^{+81}_{-77}$	$0.04327\ ^{+20}_{-22}$	$0.07736\ ^{+78}_{-75}$
0.1355	0.1345	$0.03747\ ^{+21}_{-23}$	$0.06628\ ^{+82}_{-77}$	$0.03664\ ^{+19}_{-22}$	$0.06555\ ^{+81}_{-75}$
0.1355	0.1350	$0.03058\ ^{+20}_{-25}$	$0.05451\ ^{+80}_{-71}$	$0.03003\ ^{+19}_{-24}$	$0.05401\ ^{+79}_{-70}$
0.1355	0.1355	$0.02374\ ^{+20}_{-26}$	$0.04288\ ^{+78}_{-76}$	$0.02340\ ^{+19}_{-25}$	$0.04258\ ^{+76}_{-75}$

Table A.58: Results for r, s, r_{imp} and s_{imp} from pseudoscalar fits for the dataset at $\beta = 5.2$, $\kappa_{\mathrm{sea}} = 0.1355$

$\kappa_{\mathrm{val},1}$	$\kappa_{\mathrm{val},2}$	r	s	r_{imp}	s_{imp}
0.1342	0.1342	0.05746^{+21}_{-23}	0.09721^{+88}_{-91}	0.05560^{+19}_{-22}	0.09563^{+86}_{-88}
0.1350	0.1342	0.04598^{+23}_{-24}	0.07802^{+91}_{-92}	0.04479^{+21}_{-22}	0.07700^{+88}_{-90}
0.1350	0.1350	0.03470^{+24}_{-25}	0.05932^{+92}_{-90}	0.03402^{+23}_{-24}	0.05873^{+91}_{-88}
0.1355	0.1342	0.03894^{+25}_{-26}	0.0667^{+9}_{-10}	0.03808^{+24}_{-24}	0.06598^{+92}_{-94}
0.1355	0.1350	0.02782^{+26}_{-26}	0.0483^{+10}_{-9}	0.02737^{+25}_{-25}	0.0479^{+10}_{-9}
0.1355	0.1355	0.02101^{+27}_{-28}	0.0373^{+11}_{-10}	0.02075^{+27}_{-27}	0.0370^{+11}_{-10}
0.13565	0.1342	0.03683^{+26}_{-26}	0.0634^{+10}_{-10}	0.03606^{+24}_{-25}	0.0628^{+10}_{-10}
0.13565	0.1350	0.02578^{+27}_{-26}	0.0450^{+10}_{-9}	0.02539^{+26}_{-25}	0.0447^{+10}_{-9}
0.13565	0.1355	0.01901^{+27}_{-28}	0.0340^{+11}_{-10}	0.01880^{+27}_{-28}	0.0338^{+11}_{-10}
0.13565	0.13565	0.01702^{+27}_{-28}	0.0307^{+10}_{-10}	0.01684^{+26}_{-28}	0.0305^{+10}_{-10}
0.1358	0.1342	0.03471^{+26}_{-27}	0.0601^{+10}_{-10}	0.03401^{+25}_{-26}	0.0595^{+10}_{-10}
0.1358	0.1350	0.02373^{+27}_{-27}	0.0417^{+11}_{-10}	0.02340^{+27}_{-26}	0.0414^{+10}_{-10}
0.1358	0.1355	0.01704^{+27}_{-30}	0.0306^{+11}_{-10}	0.01687^{+27}_{-29}	0.0305^{+10}_{-10}
0.1358	0.13565	0.01507^{+27}_{-29}	0.0273^{+11}_{-10}	0.01493^{+26}_{-28}	0.0272^{+10}_{-10}
0.1358	0.1358	0.01310^{+27}_{-29}	0.0239^{+11}_{-12}	0.01299^{+27}_{-28}	0.0238^{+11}_{-11}

Table A.59: Results for r, s, r_{imp} and s_{imp} from pseudoscalar fits for the dataset at $\beta = 5.2$, $\kappa_{\mathrm{sea}} = 0.13565$

$\kappa_{\mathrm{val},1}$	$\kappa_{\mathrm{val},2}$	r	s	r_{imp}	s_{imp}
0.1342	0.1342	$0.05597\,^{+26}_{-30}$	$0.0926\,^{+11}_{-12}$	$0.05424\,^{+24}_{-28}$	$0.0911\,^{+10}_{-11}$
0.1350	0.1342	$0.04444\,^{+27}_{-31}$	$0.0736\,^{+11}_{-13}$	$0.04335\,^{+25}_{-29}$	$0.0727\,^{+11}_{-12}$
0.1350	0.1350	$0.03323\,^{+24}_{-29}$	$0.0560\,^{+9}_{-10}$	$0.03261\,^{+24}_{-28}$	$0.0555\,^{+9}_{-10}$
0.1355	0.1342	$0.03750\,^{+26}_{-27}$	$0.0633\,^{+10}_{-11}$	$0.03671\,^{+24}_{-26}$	$0.0627\,^{+9}_{-11}$
0.1355	0.1350	$0.02647\,^{+26}_{-31}$	$0.0452\,^{+9}_{-11}$	$0.02607\,^{+25}_{-30}$	$0.0448\,^{+9}_{-11}$
0.1355	0.1355	$0.01991\,^{+27}_{-36}$	$0.0345\,^{+8}_{-12}$	$0.01968\,^{+26}_{-35}$	$0.0343\,^{+8}_{-12}$
0.13565	0.1342	$0.03547\,^{+26}_{-29}$	$0.0601\,^{+10}_{-11}$	$0.03476\,^{+25}_{-27}$	$0.0595\,^{+10}_{-10}$
0.13565	0.1350	$0.02450\,^{+27}_{-34}$	$0.0420\,^{+9}_{-11}$	$0.02416\,^{+26}_{-33}$	$0.0418\,^{+9}_{-10}$
0.13565	0.1355	$0.01795\,^{+24}_{-29}$	$0.03180\,^{+72}_{-84}$	$0.01776\,^{+23}_{-29}$	$0.03164\,^{+71}_{-83}$
0.13565	0.13565	$0.01603\,^{+24}_{-29}$	$0.02859\,^{+71}_{-82}$	$0.01588\,^{+24}_{-29}$	$0.02846\,^{+70}_{-82}$
0.1358	0.1342	$0.03347\,^{+27}_{-31}$	$0.0568\,^{+10}_{-11}$	$0.03283\,^{+26}_{-29}$	$0.0563\,^{+10}_{-11}$
0.1358	0.1350	$0.02256\,^{+27}_{-34}$	$0.0389\,^{+9}_{-11}$	$0.02227\,^{+26}_{-33}$	$0.0386\,^{+9}_{-10}$
0.1358	0.1355	$0.01602\,^{+25}_{-29}$	$0.02855\,^{+73}_{-83}$	$0.01587\,^{+24}_{-28}$	$0.02841\,^{+72}_{-82}$
0.1358	0.13565	$0.01409\,^{+25}_{-29}$	$0.02530\,^{+74}_{-83}$	$0.01397\,^{+24}_{-28}$	$0.02520\,^{+74}_{-82}$
0.1358	0.1358	$0.01215\,^{+25}_{-27}$	$0.02204\,^{+74}_{-88}$	$0.01206\,^{+25}_{-27}$	$0.02196\,^{+74}_{-87}$
0.13595	0.13595	$0.00813\,^{+24}_{-31}$	$0.0151\,^{+8}_{-11}$	$0.00809\,^{+24}_{-31}$	$0.0151\,^{+8}_{-11}$

Table A.60: Results for r, s, r_{imp} and s_{imp} from pseudoscalar fits for the dataset at $\beta = 5.2$, $\kappa_{\mathrm{sea}} = 0.1358$

$\kappa_{\mathrm{val},1}$	$\kappa_{\mathrm{val},2}$	r	s	r_{imp}	s_{imp}
0.1342	0.1342	0.07330^{+20}_{-20}	0.1257^{+8}_{-10}	0.07023^{+18}_{-18}	0.12306^{+77}_{-93}
0.1347	0.1342	0.06594^{+20}_{-20}	0.1129^{+8}_{-10}	0.06346^{+18}_{-18}	0.11081^{+79}_{-94}
0.1347	0.1347	0.05866^{+20}_{-21}	0.1004^{+8}_{-10}	0.05670^{+18}_{-19}	0.09869^{+78}_{-93}
0.1352	0.1342	0.05864^{+19}_{-21}	0.1005^{+8}_{-10}	0.05668^{+18}_{-19}	0.09881^{+80}_{-94}
0.1352	0.1347	0.05145^{+19}_{-22}	0.0882^{+8}_{-10}	0.04994^{+19}_{-21}	0.0869^{+8}_{-10}
0.1352	0.1352	0.04432^{+20}_{-23}	0.0762^{+8}_{-11}	0.04319^{+19}_{-21}	0.0752^{+8}_{-10}
0.1357	0.1342	0.05141^{+20}_{-23}	0.0883^{+8}_{-11}	0.04990^{+19}_{-21}	0.0870^{+8}_{-11}
0.1357	0.1347	0.04431^{+22}_{-25}	0.0763^{+8}_{-11}	0.04318^{+20}_{-22}	0.0754^{+8}_{-11}
0.1357	0.1352	0.03727^{+24}_{-25}	0.0645^{+9}_{-12}	0.03647^{+22}_{-23}	0.0638^{+8}_{-11}
0.1357	0.1357	0.03025^{+25}_{-27}	0.0528^{+9}_{-14}	0.02971^{+24}_{-26}	0.0524^{+9}_{-13}

Table A.61: Results for r, s, r_{imp} and s_{imp} from pseudoscalar fits for the dataset at $\beta = 5.25$, $\kappa_{\mathrm{sea}} = 0.1352$

$\kappa_{\mathrm{val},1}$	$\kappa_{\mathrm{val},2}$	r	s	r_{imp}	s_{imp}
0.1335	0.1335	0.10475^{+28}_{-28}	0.1855^{+9}_{-10}	0.09827^{+23}_{-25}	0.17976^{+83}_{-94}
0.1340	0.1335	0.09711^{+28}_{-28}	0.1713^{+8}_{-10}	0.09156^{+24}_{-25}	0.16638^{+77}_{-90}
0.1340	0.1340	0.08958^{+27}_{-28}	0.1575^{+8}_{-10}	0.08488^{+23}_{-24}	0.15339^{+78}_{-90}
0.1345	0.1335	0.08953^{+27}_{-27}	0.15736^{+82}_{-92}	0.08483^{+24}_{-24}	0.15323^{+77}_{-87}
0.1345	0.1340	0.08210^{+27}_{-27}	0.14391^{+81}_{-86}	0.07816^{+24}_{-25}	0.14046^{+78}_{-82}
0.1345	0.1345	0.07475^{+27}_{-27}	0.13077^{+77}_{-81}	0.07149^{+24}_{-25}	0.12792^{+74}_{-77}
0.1350	0.1335	0.08202^{+27}_{-27}	0.14384^{+82}_{-89}	0.07809^{+25}_{-25}	0.14039^{+78}_{-85}
0.1350	0.1340	0.07469^{+26}_{-27}	0.13067^{+81}_{-80}	0.07144^{+24}_{-24}	0.12782^{+77}_{-76}
0.1350	0.1345	0.06744^{+26}_{-26}	0.11780^{+75}_{-72}	0.06479^{+24}_{-24}	0.11549^{+72}_{-69}
0.1350	0.1350	0.06026^{+27}_{-26}	0.10524^{+72}_{-68}	0.05814^{+25}_{-23}	0.10339^{+69}_{-66}

Table A.62: Results for r, s, r_{imp} and s_{imp} from pseudoscalar fits for the dataset at $\beta = 5.26$, $\kappa_{\mathrm{sea}} = 0.1345$

$\kappa_{\mathrm{val},1}$	$\kappa_{\mathrm{val},2}$	r	s	r_{imp}	s_{imp}
0.1335	0.1335	0.11187^{+31}_{-36}	0.20054^{+83}_{-94}	0.10439^{+26}_{-32}	0.19384^{+77}_{-88}
0.1340	0.1335	0.10423^{+31}_{-35}	0.18626^{+82}_{-92}	0.09776^{+26}_{-31}	0.18048^{+77}_{-86}
0.1340	0.1340	0.09664^{+31}_{-35}	0.17217^{+85}_{-91}	0.09110^{+26}_{-30}	0.16723^{+80}_{-86}
0.1345	0.1335	0.09664^{+32}_{-34}	0.17224^{+87}_{-88}	0.09110^{+26}_{-30}	0.16730^{+82}_{-83}
0.1345	0.1340	0.08916^{+31}_{-34}	0.15843^{+87}_{-91}	0.08445^{+26}_{-30}	0.15425^{+82}_{-86}
0.1345	0.1345	0.08174^{+30}_{-33}	0.14489^{+86}_{-90}	0.07779^{+27}_{-30}	0.14139^{+81}_{-86}
0.1350	0.1335	0.08912^{+31}_{-34}	0.15850^{+89}_{-90}	0.08441^{+27}_{-29}	0.15431^{+84}_{-85}
0.1350	0.1340	0.08174^{+32}_{-33}	0.14498^{+84}_{-91}	0.07779^{+28}_{-30}	0.14147^{+80}_{-86}
0.1350	0.1345	0.07442^{+32}_{-35}	0.13171^{+84}_{-92}	0.07115^{+28}_{-31}	0.12882^{+81}_{-88}
0.1350	0.1350	0.06716^{+32}_{-35}	0.11871^{+80}_{-93}	0.06451^{+29}_{-32}	0.11636^{+77}_{-89}

Table A.63: Results for r, s, r_{imp} and s_{imp} from pseudoscalar fits for the dataset at $\beta = 5.29$, $\kappa_{\mathrm{sea}} = 0.1340$

$\kappa_{\mathrm{val},1}$	$\kappa_{\mathrm{val},2}$	r	s	r_{imp}	s_{imp}
0.1327	0.1327	0.07581^{+9}_{-11}	0.12500^{+43}_{-47}	0.072654^{+79}_{-91}	0.12239^{+41}_{-45}
0.1332	0.1327	0.06795^{+9}_{-11}	0.11188^{+43}_{-49}	0.065412^{+81}_{-95}	0.10980^{+41}_{-47}
0.1332	0.1332	0.06015^{+9}_{-10}	0.09897^{+40}_{-49}	0.05817^{+8}_{-10}	0.09734^{+39}_{-47}
0.1334	0.1327	0.06480^{+9}_{-10}	0.10671^{+42}_{-49}	0.062496^{+82}_{-94}	0.10482^{+41}_{-48}
0.1334	0.1332	0.05704^{+9}_{-11}	0.09389^{+40}_{-49}	0.05525^{+9}_{-10}	0.09242^{+39}_{-47}
0.1334	0.1334	0.05393^{+10}_{-10}	0.08882^{+39}_{-49}	0.052333^{+88}_{-92}	0.08751^{+38}_{-48}
0.1337	0.1337	0.04461^{+10}_{-10}	0.07379^{+40}_{-48}	0.04351^{+9}_{-10}	0.07288^{+39}_{-47}
0.1339	0.1337	0.04148^{+10}_{-10}	0.06880^{+41}_{-47}	0.04053^{+9}_{-10}	0.06801^{+41}_{-46}
0.1339	0.1339	0.03836^{+10}_{-10}	0.06379^{+41}_{-47}	0.03755^{+10}_{-10}	0.06311^{+40}_{-46}

Table A.64: Results for r, s, r_{imp} and s_{imp} from pseudoscalar fits for the quenched dataset at $\beta = 5.93$

Appendix B

Chiral extrapolation results

B.1 Partially quenched chiral extrapolations

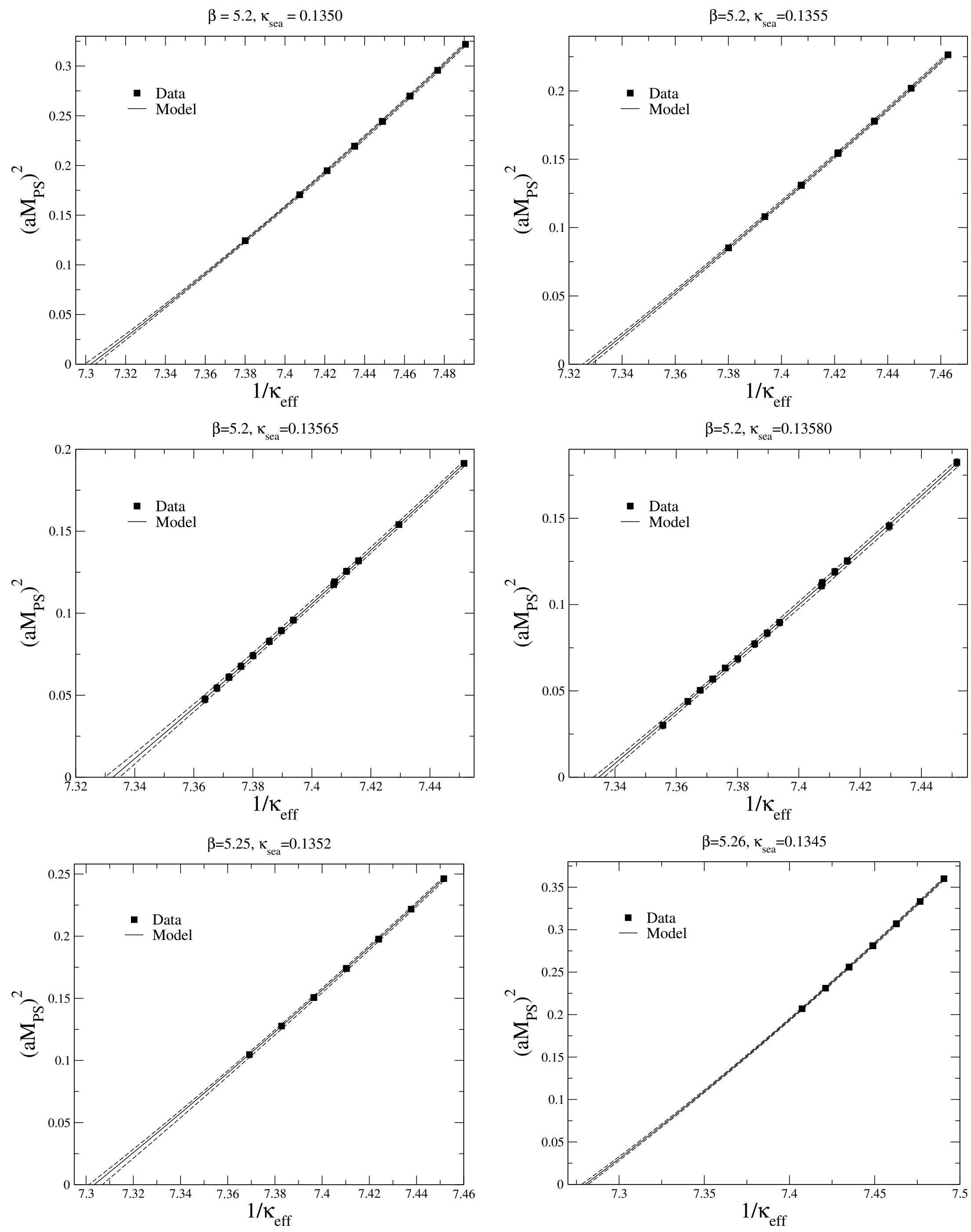

Figure B.1: Plot of fit results for partially quenched chiral extrapolations of $(aM_{\mathrm{PS}})^2$ versus $1/\kappa_{\mathrm{eff}}$ using Equation (4.33) for the datasets at $\beta = 5.2$, $(5.25, 0.1352)$ and $(5.26, 0.1345)$.

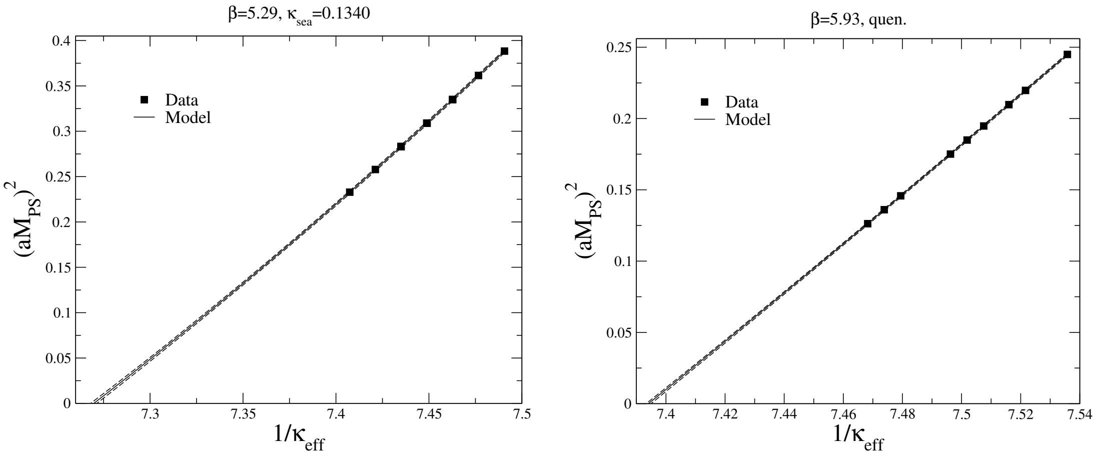

Figure B.2: Plot of fit results for partially quenched chiral extrapolations of $(aM_{\mathrm{PS}})^2$ versus $1/\kappa_{\mathrm{eff}}$ using Equation (4.33) for the datasets at $(5.29, 0.1340)$ and $(5.93, \mathrm{quen.})$

Dataset	κ_{crit}	B_{PS}	C_{PS}	D_{PS}	χ^2/dof
$(5.2, 0.1350)$	$0.136941\,^{+55}_{-44}$	$1.521\,^{+60}_{-87}$	$0.76\,^{+35}_{-24}$	$1.00\,^{+45}_{-56}$	0.00859
$(5.2, 0.1355)$	$0.136485\,^{+31}_{-30}$	$1.560\,^{+48}_{-44}$	$0.94\,^{+34}_{-31}$	$-0.62\,^{+80}_{-87}$	0.00373
$(5.2, 0.13565)$	$0.136378\,^{+51}_{-43}$	$1.517\,^{+86}_{-93}$	$1.16\,^{+64}_{-62}$	$-1.6\,^{+11}_{-12}$	0.0159
$(5.2, 0.1358)$	$0.136338\,^{+33}_{-31}$	$1.496\,^{+83}_{-73}$	$0.88\,^{+74}_{-73}$	$-1.5\,^{+18}_{-20}$	0.118
$(5.25, 0.1352)$	$0.136922\,^{+42}_{-65}$	$1.542\,^{+76}_{-55}$	$0.81\,^{+21}_{-28}$	0	0.00335
$(5.26, 0.1345)$	$0.137361\,^{+39}_{-31}$	$1.494\,^{+30}_{-37}$	$0.61\,^{+13}_{-14}$	$1.65\,^{+54}_{-51}$	0.00203
$(5.29, 0.1340)$	$0.137556\,^{+31}_{-31}$	$1.581\,^{+27}_{-28}$	$0.66\,^{+13}_{-13}$	$0.55\,^{+49}_{-50}$	0.000588
$(5.93, \mathrm{quen.})$	$0.135244\,^{+14}_{-16}$	$1.675\,^{+22}_{-21}$	0	$1.51\,^{+29}_{-32}$	0.00510

Table B.1: Summary of fit results for partially quenched chiral extrapolations of $(aM_{\mathrm{PS}})^2$ versus the standard quark mass using Equation (4.34).

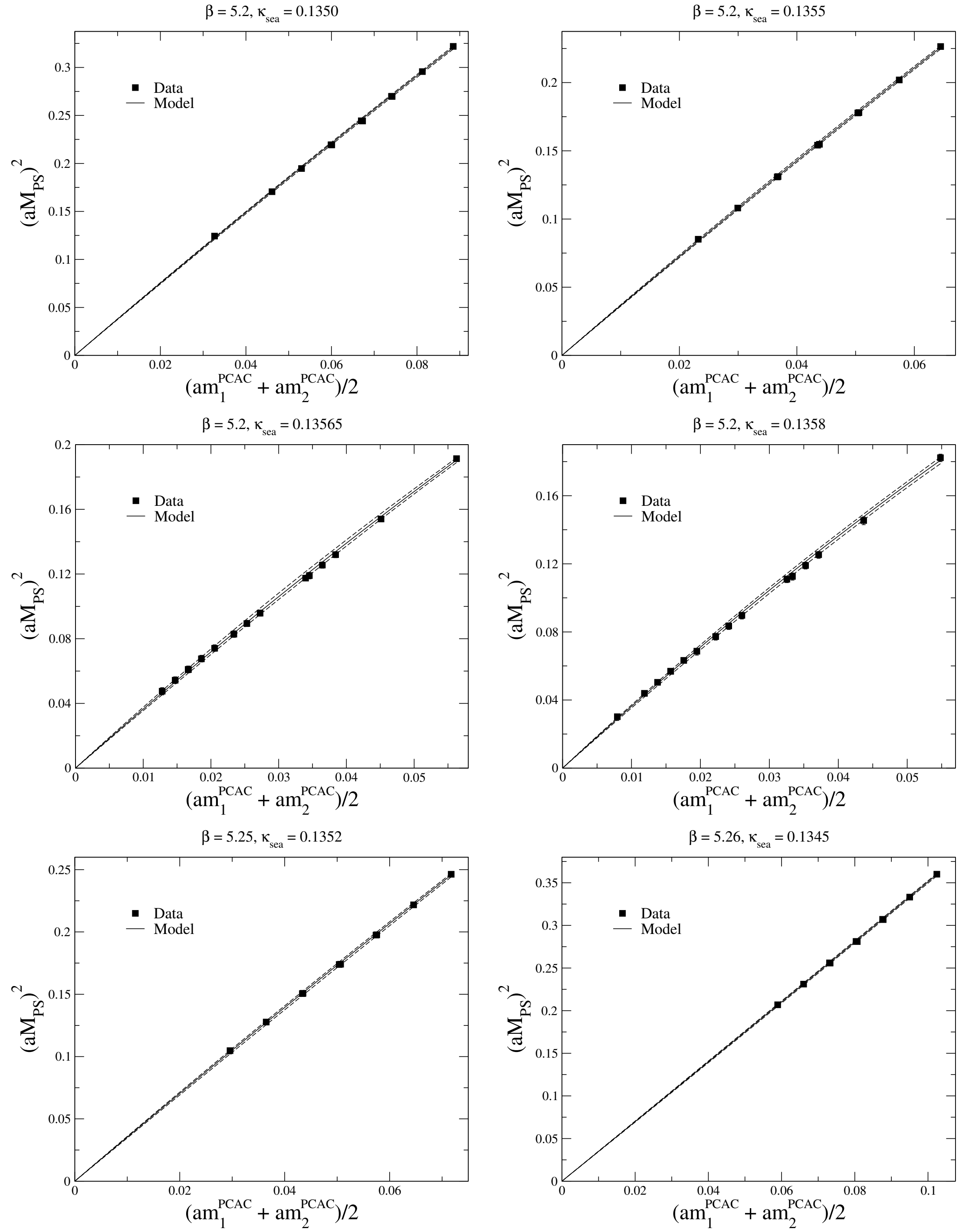

Figure B.3: Plot of fit results for partially quenched chiral extrapolations of $(aM_{\mathrm{PS}})^2$ versus am_{PCAC} using Equation (4.36) for the datasets at $\beta = 5.2$, $(5.25, 0.1352)$ and $(5.26, 0.1345)$.

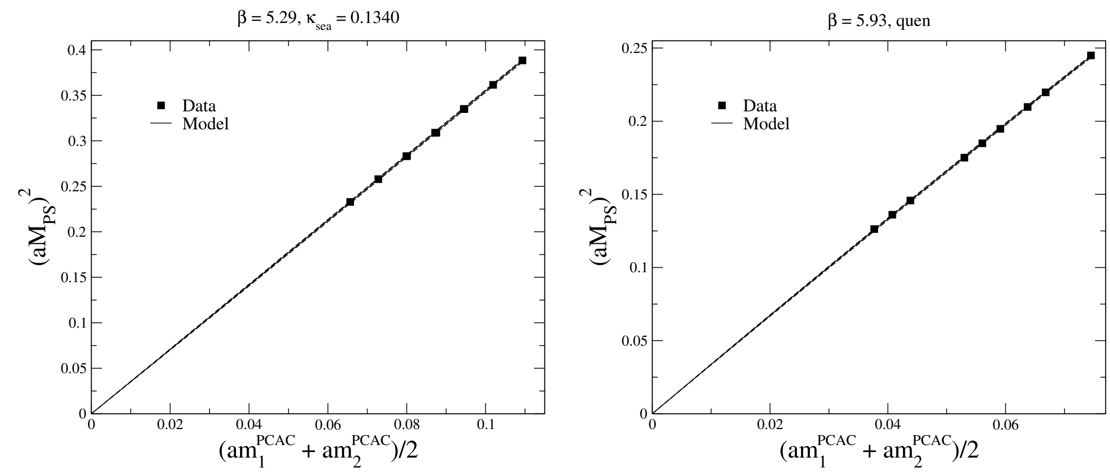

Figure B.4: Plot of fit results for partially quenched chiral extrapolations of $(aM_{\mathrm{PS}})^2$ versus am_{PCAC} using Equation (4.36) for the datasets at $(5.29, 0.1340)$ and $(5.93, \mathrm{quen.})$

Dataset	B'_{PS}	C'_{PS}	D'_{PS}	χ^2/dof
$(5.2, 0.1350)$	$1.901\ ^{+19}_{-24}$	$-2.12\ ^{+24}_{-22}$	$6.50\ ^{+78}_{-74}$	0.512
$(5.2, 0.1355)$	$1.842\ ^{+32}_{-28}$	$-1.56\ ^{+32}_{-31}$	$3.40\ ^{+72}_{-77}$	0.217
$(5.2, 0.13565)$	$1.853\ ^{+68}_{-60}$	$-2.76\ ^{+86}_{-88}$	$5.3\ ^{+18}_{-17}$	0.233
$(5.2, 0.1358)$	$1.851\ ^{+50}_{-58}$	$-3.51\ ^{+85}_{-79}$	$6.7\ ^{+21}_{-23}$	0.322
$(5.25, 0.1352)$	$1.779\ ^{+32}_{-42}$	$-1.29\ ^{+44}_{-27}$	$3.30\ ^{+69}_{-91}$	0.106
$(5.26, 0.1345)$	$1.746\ ^{+17}_{-18}$	$-1.04\ ^{+14}_{-16}$	$4.36\ ^{+55}_{-47}$	0.0430
$(5.29, 0.1340)$	$1.765\ ^{+17}_{-18}$	$-0.64\ ^{+14}_{-14}$	$2.78\ ^{+48}_{-46}$	0.0128
$(5.93, \mathrm{quen.})$	$1.694\ ^{+13}_{-17}$	$-0.368\ ^{+90}_{-69}$	0	0.295

Table B.2: Summary of fit results for partially quenched chiral extrapolations of $(aM_{\mathrm{PS}})^2$ versus am_{PCAC} using Equation (4.36).

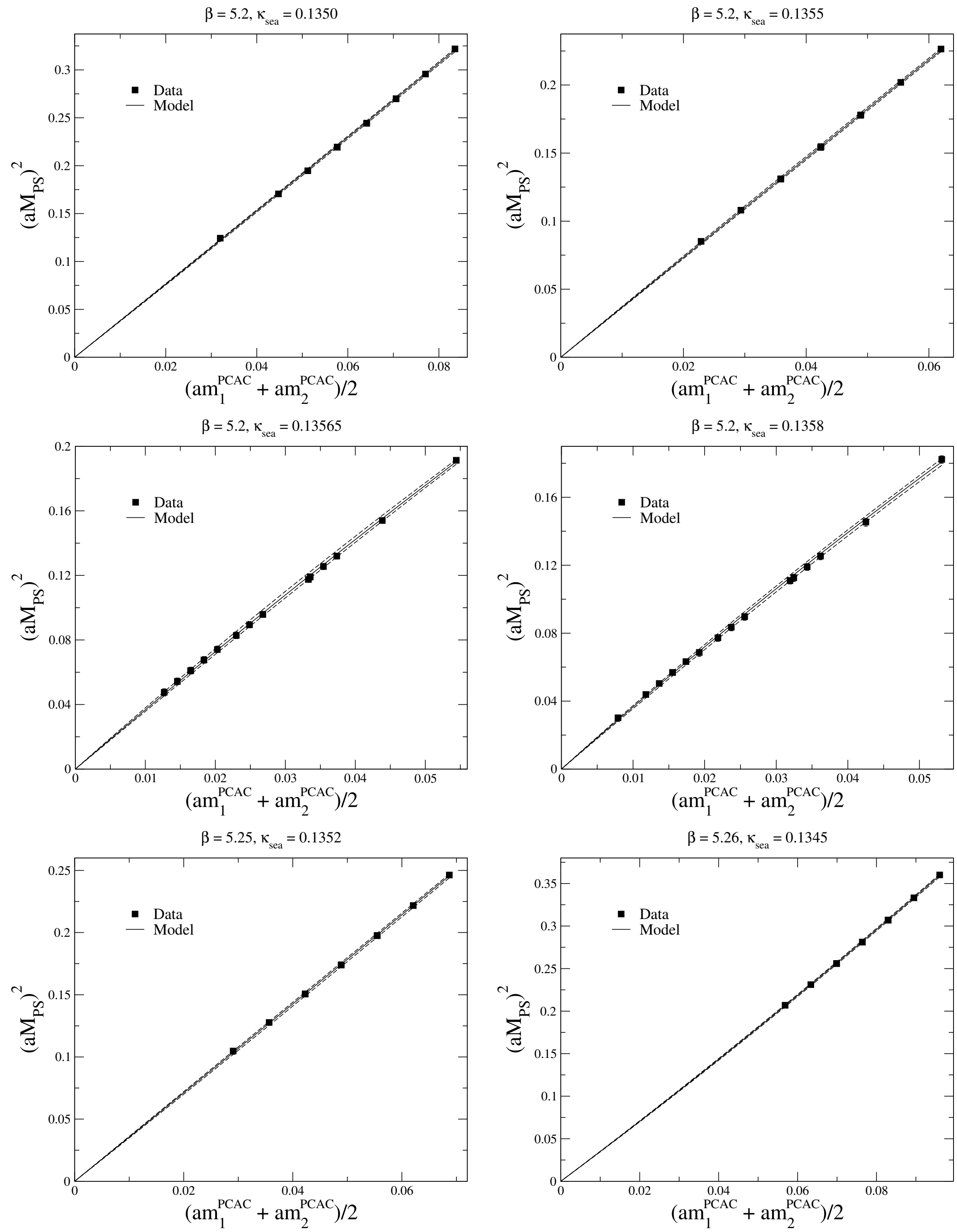

Figure B.5: Plot of fit results for partially quenched chiral extrapolations of $(aM_{\mathrm{PS}})^2$ versus $am_{\mathrm{PCAC,imp}}$ using Equation (4.36) for the datasets at $\beta = 5.2$, $(5.25, 0.1352)$ and $(5.26, 0.1345)$.

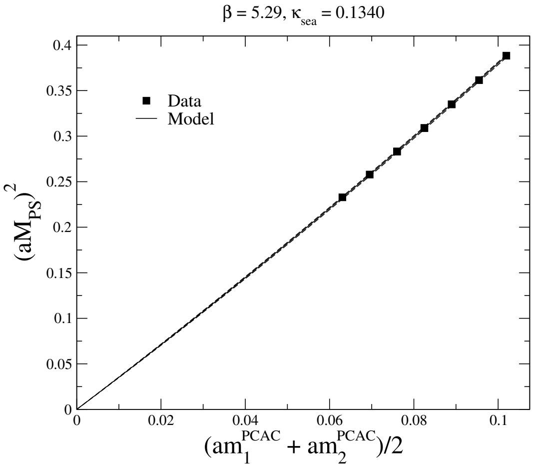

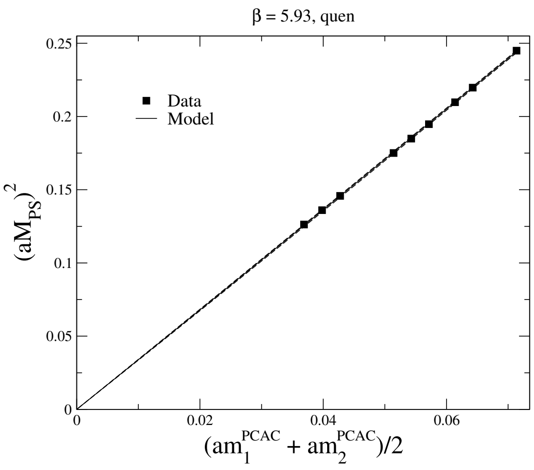

Figure B.6: Plot of fit results for partially quenched chiral extrapolations of $(aM_{\mathrm{PS}})^2$ versus $am_{\mathrm{PCAC,imp}}$ using Equation (4.36) for the datasets at $(5.29, 0.1340)$ and $(5.93, \mathrm{quen.})$

Dataset	B'_{PS}	C'_{PS}	D'_{PS}	χ^2/dof
$(5.2, 0.1350)$	$1.902\ ^{+20}_{-25}$	$-1.13\ ^{+29}_{-26}$	$4.94\ ^{+93}_{-88}$	0.542
$(5.2, 0.1355)$	$1.841\ ^{+33}_{-29}$	$-0.16\ ^{+21}_{-22}$	0	0.204
$(5.2, 0.13565)$	$1.858\ ^{+71}_{-63}$	$-1.88\ ^{+90}_{-93}$	$3.6\ ^{+20}_{-18}$	0.226
$(5.2, 0.1358)$	$1.856\ ^{+52}_{-60}$	$-2.72\ ^{+92}_{-84}$	$5.1\ ^{+22}_{-24}$	0.308
$(5.25, 0.1352)$	$1.776\ ^{+30}_{-38}$	0	$0.34\ ^{+92}_{-69}$	0.102
$(5.26, 0.1345)$	$1.733\ ^{+18}_{-19}$	0	$2.90\ ^{+31}_{-30}$	0.0577
$(5.29, 0.1340)$	$1.747\ ^{+19}_{-20}$	$0.765\ ^{+65}_{-69}$	0	0.0237
$(5.93, \mathrm{quen.})$	$1.693\ ^{+14}_{-18}$	0	$0.52\ ^{+41}_{-30}$	0.290

Table B.3: Summary of fit results for partially quenched chiral extrapolations of $(aM_{\mathrm{PS}})^2$ versus $am_{\mathrm{PCAC,imp}}$ using Equation (4.36).

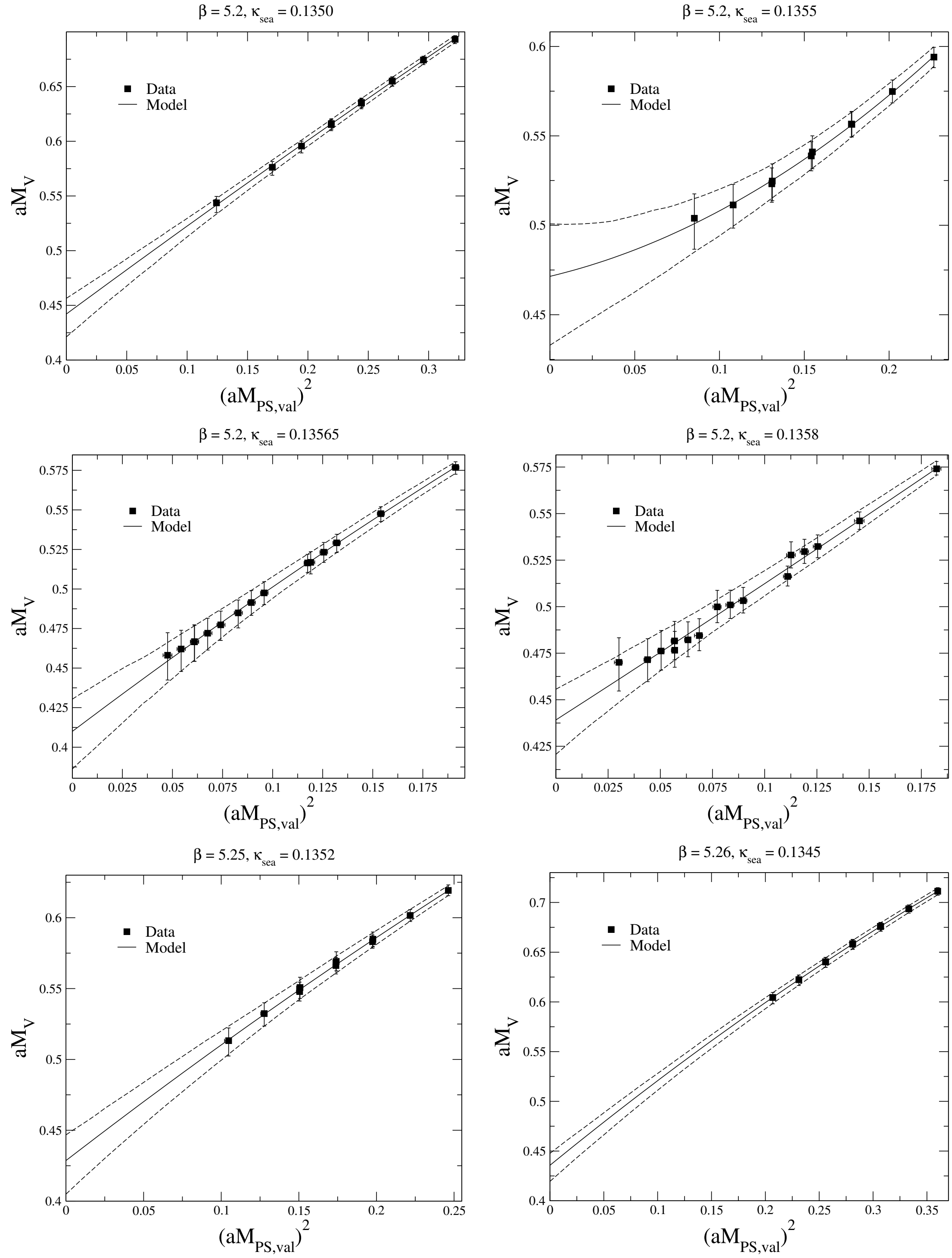

Figure B.7: Plot of fit results for partially quenched chiral extrapolations of $aM_{\rm V}$ versus $(aM_{\rm PS})^2$ using Equation (4.38) for the datasets at $\beta = 5.2$, $(5.25, 0.1352)$ and $(5.26, 0.1345)$.

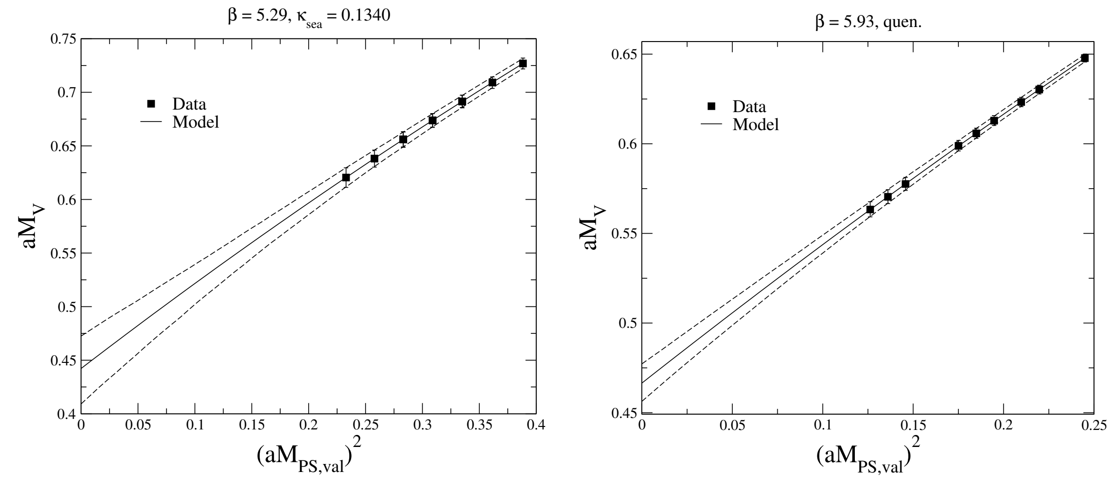

Figure B.8: Plot of fit results for partially quenched chiral extrapolations of $aM_{\rm V}$ versus $(aM_{\rm PS})^2$ using Equation (4.38) for the datasets at $(5.29, 0.1340)$ and $(5.93, \text{quen.})$

Dataset	A	B	C	χ^2/dof
$(5.2, 0.1350)$	0.442^{+14}_{-21}	0.81^{+14}_{-11}	-0.09^{+21}_{-27}	0.0351
$(5.2, 0.1355)$	0.471^{+29}_{-39}	0.23^{+35}_{-27}	1.40^{+71}_{-84}	0.0183
$(5.2, 0.13565)$	0.410^{+20}_{-24}	0.96^{+28}_{-23}	-0.42^{+79}_{-90}	0.0133
$(5.2, 0.1358)$	0.439^{+16}_{-18}	0.72^{+22}_{-19}	0.11^{+62}_{-71}	0.225
$(5.25, 0.1352)$	0.429^{+18}_{-24}	0.84^{+18}_{-15}	-0.28^{+32}_{-36}	0.0383
$(5.26, 0.1345)$	0.436^{+12}_{-16}	0.884^{+81}_{-61}	$-0.32^{+\ 9}_{-12}$	0.00245
$(5.29, 0.1340)$	0.442^{+30}_{-33}	0.81^{+15}_{-15}	-0.20^{+19}_{-22}	0.000327
$(5.93, \text{quen.})$	0.466^{+11}_{-10}	0.795^{+71}_{-77}	-0.22^{+15}_{-14}	0.000630

Table B.4: Summary of fit results for partially quenched chiral extrapolations of $aM_{\rm V}$ versus $(aM_{\rm PS})^2$ using Equation (4.38).

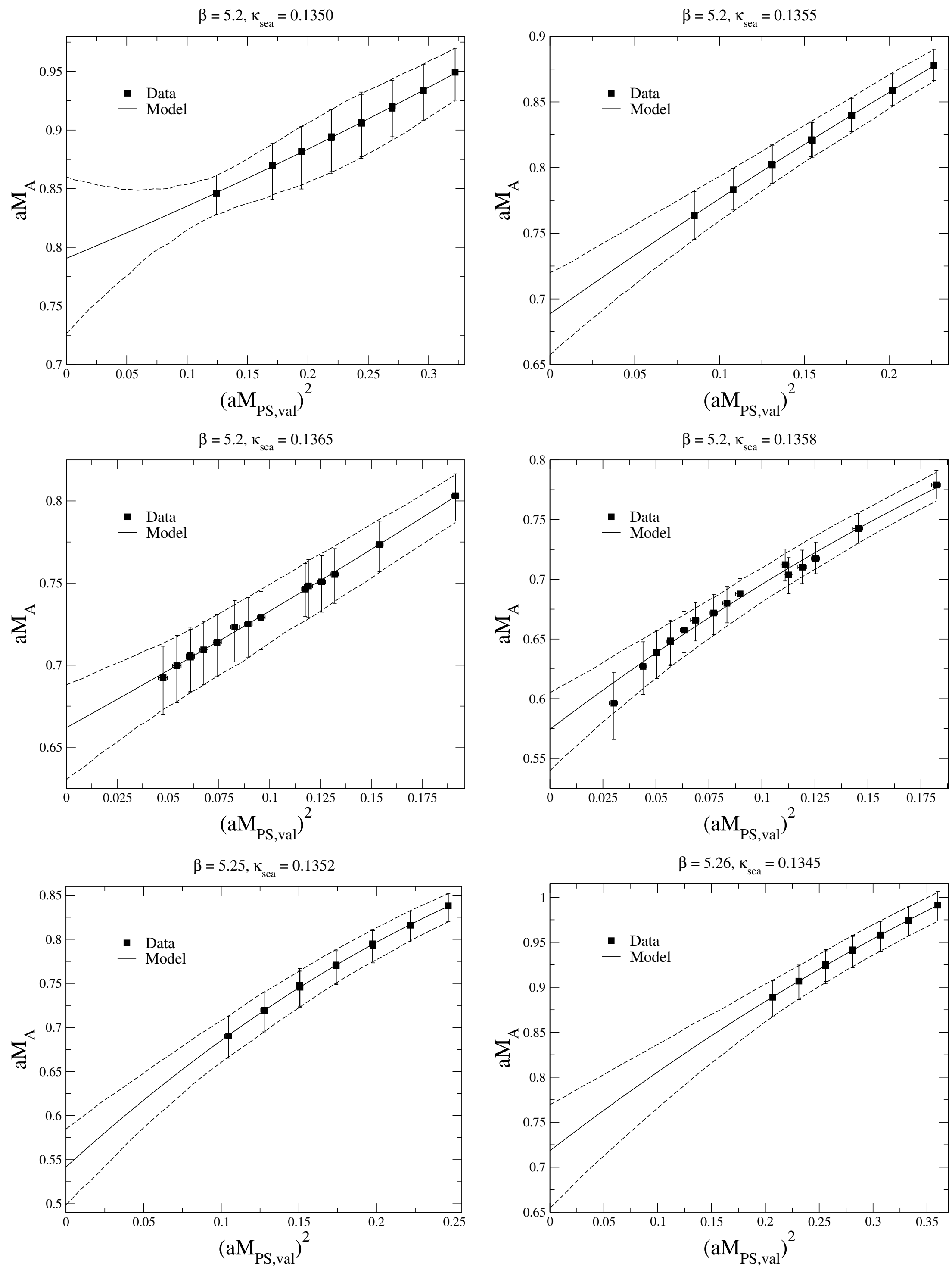

Figure B.9: Plot of fit results for partially quenched chiral extrapolations of aM_{A} versus $(aM_{\mathrm{PS}})^2$ using Equation (4.38) for the datasets at $\beta = 5.2$, $(5.25, 0.1352)$ and $(5.26, 0.1345)$.

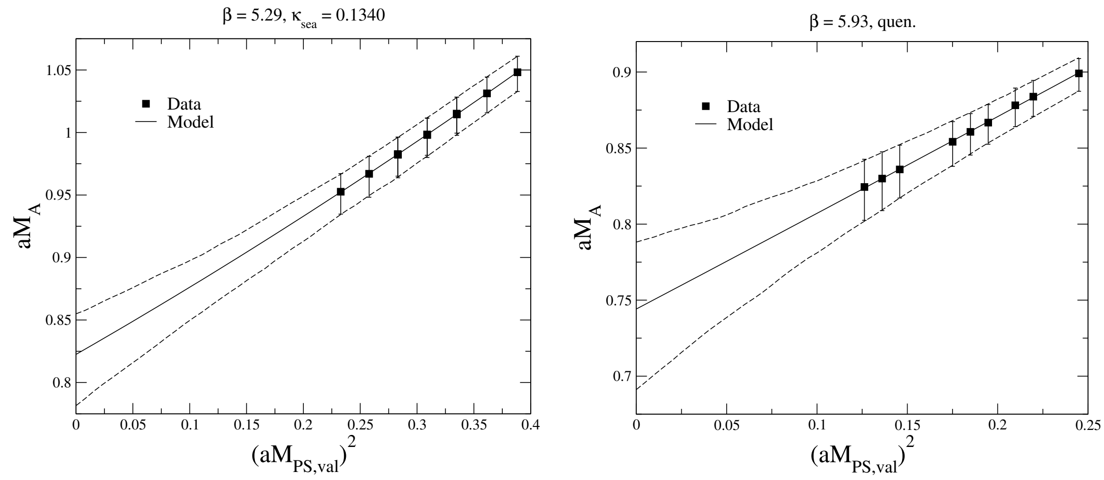

Figure B.10: Plot of fit results for partially quenched chiral extrapolations of $aM_{\rm A}$ versus $(aM_{\rm PS})^2$ using Equation (4.38) for the datasets at $(5.29, 0.1340)$ and $(5.93, \text{quen.})$

Dataset	A	B	C	χ^2/dof
$(5.2, 0.1350)$	$0.791\,^{+70}_{-64}$	$0.42\,^{+64}_{-73}$	$0.2\,^{+16}_{-13}$	0.00121
$(5.2, 0.1355)$	$0.689\,^{+31}_{-31}$	$0.91\,^{+27}_{-26}$	$-0.33\,^{+59}_{-75}$	0.000842
$(5.2, 0.13565)$	$0.662\,^{+26}_{-32}$	$0.68\,^{+35}_{-33}$	$0.3\,^{+12}_{-11}$	0.00558
$(5.2, 0.1358)$	$0.574\,^{+31}_{-35}$	$1.34\,^{+41}_{-37}$	$-1.2\,^{+14}_{-14}$	0.0992
$(5.25, 0.1352)$	$0.542\,^{+43}_{-43}$	$1.59\,^{+29}_{-36}$	$-1.59\,^{+81}_{-71}$	0.00327
$(5.26, 0.1345)$	$0.718\,^{+51}_{-64}$	$0.92\,^{+30}_{-25}$	$-0.45\,^{+36}_{-45}$	0.000615
$(5.29, 0.1340)$	$0.822\,^{+32}_{-41}$	$0.52\,^{+19}_{-17}$	$0.15\,^{+28}_{-27}$	0.000614
$(5.93, \text{quen.})$	$0.744\,^{+44}_{-53}$	$0.63\,^{+38}_{-28}$	$0.04\,^{+54}_{-73}$	0.00306

Table B.5: Summary of fit results for partially quenched chiral extrapolations of $aM_{\rm A}$ versus $(aM_{\rm PS})^2$ using Equation (4.38).

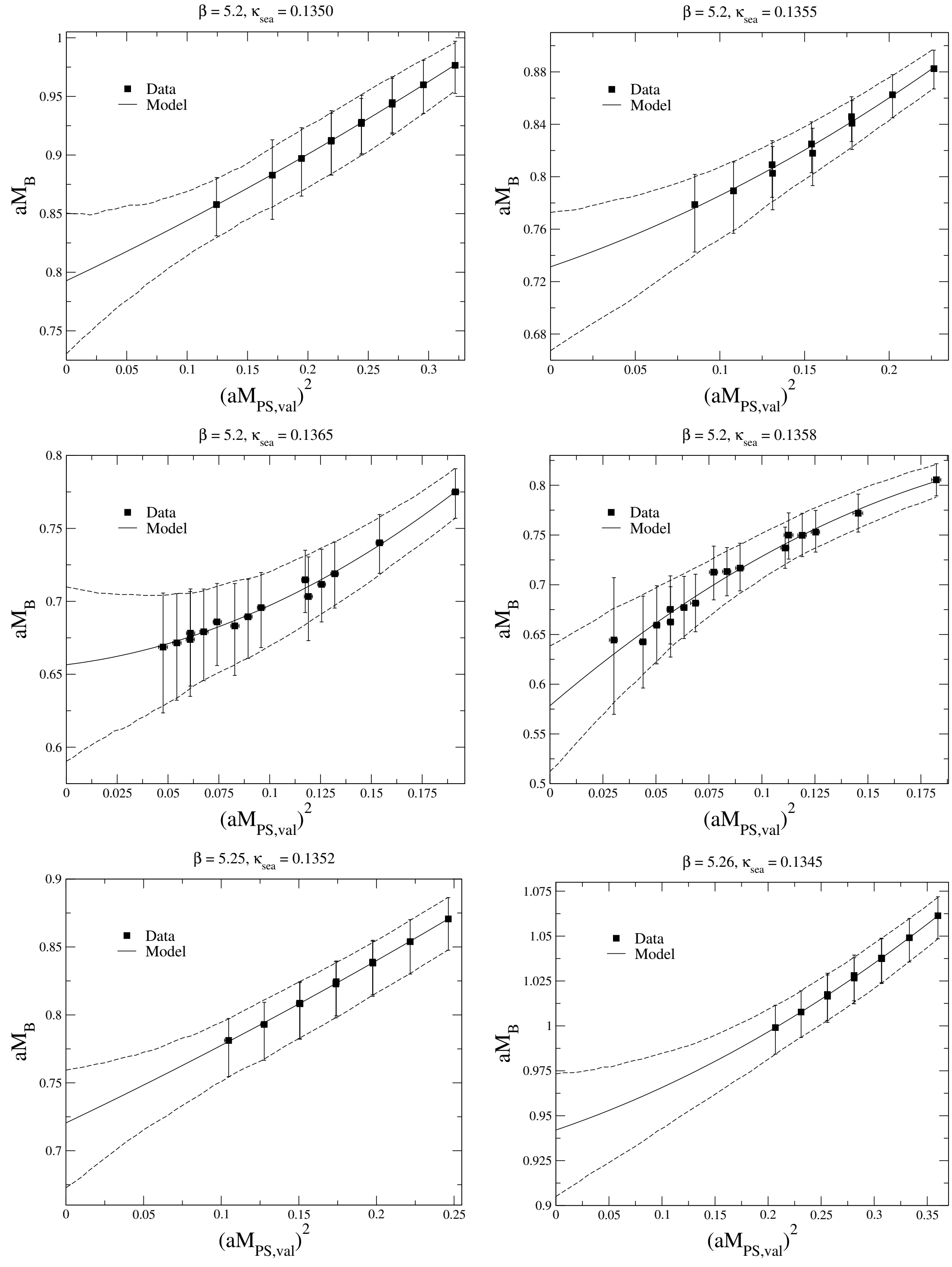

Figure B.11: Plot of fit results for partially quenched chiral extrapolations of aM_{B} versus $(aM_{\mathrm{PS}})^2$ using Equation (4.38) for the datasets at $\beta = 5.2$, $(5.25, 0.1352)$ and $(5.26, 0.1345)$.

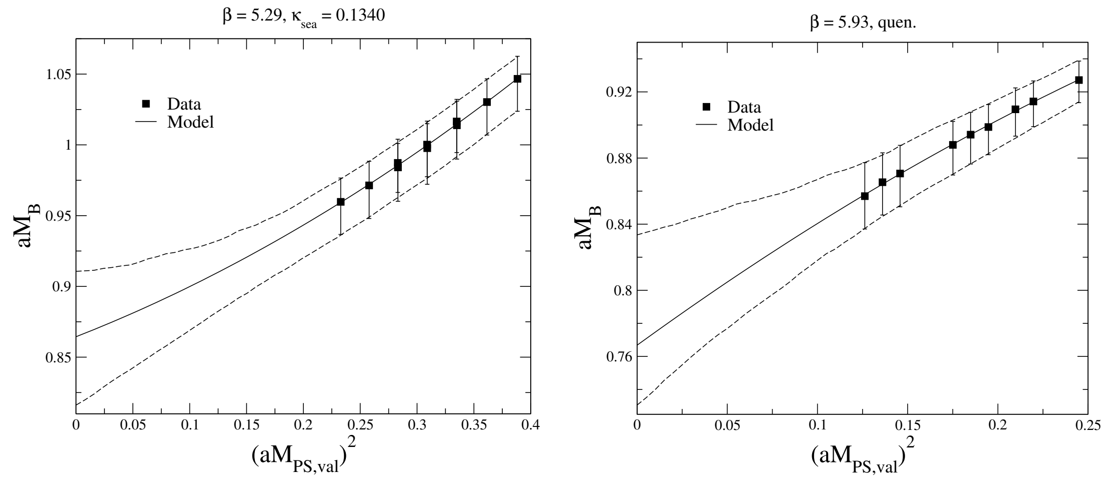

Figure B.12: Plot of fit results for partially quenched chiral extrapolations of aM_{B} versus $(aM_{\mathrm{PS}})^2$ using Equation (4.38) for the datasets at $(5.29, 0.1340)$ and $(5.93, \text{quen.})$

Dataset	A	B	C	χ^2/dof
$(5.2, 0.1350)$	$0.793\ ^{+58}_{-62}$	$0.49\ ^{+53}_{-58}$	$0.3\ ^{+12}_{-11}$	0.000633
$(5.2, 0.1355)$	$0.731\ ^{+41}_{-64}$	$0.44\ ^{+50}_{-30}$	$1.0\ ^{+\ 8}_{-11}$	0.0284
$(5.2, 0.13565)$	$0.657\ ^{+53}_{-66}$	$0.17\ ^{+83}_{-65}$	$2.3\ ^{+24}_{-27}$	0.0168
$(5.2, 0.1358)$	$0.578\ ^{+60}_{-66}$	$1.82\ ^{+79}_{-74}$	$-3.1\ ^{+25}_{-25}$	0.0543
$(5.25, 0.1352)$	$0.721\ ^{+39}_{-48}$	$0.54\ ^{+41}_{-42}$	$0.3\ ^{+11}_{-11}$	0.00149
$(5.26, 0.1345)$	$0.942\ ^{+31}_{-37}$	$0.20\ ^{+21}_{-19}$	$0.36\ ^{+32}_{-31}$	0.00182
$(5.29, 0.1340)$	$0.864\ ^{+46}_{-48}$	$0.31\ ^{+26}_{-26}$	$0.40\ ^{+39}_{-38}$	0.00547
$(5.93, \text{quen.})$	$0.767\ ^{+67}_{-36}$	$0.79\ ^{+22}_{-58}$	$-0.5\ ^{+13}_{-\ 5}$	0.00312

Table B.6: Summary of fit results for partially quenched chiral extrapolations of aM_{B} versus $(aM_{\mathrm{PS}})^2$ using Equation (4.38).

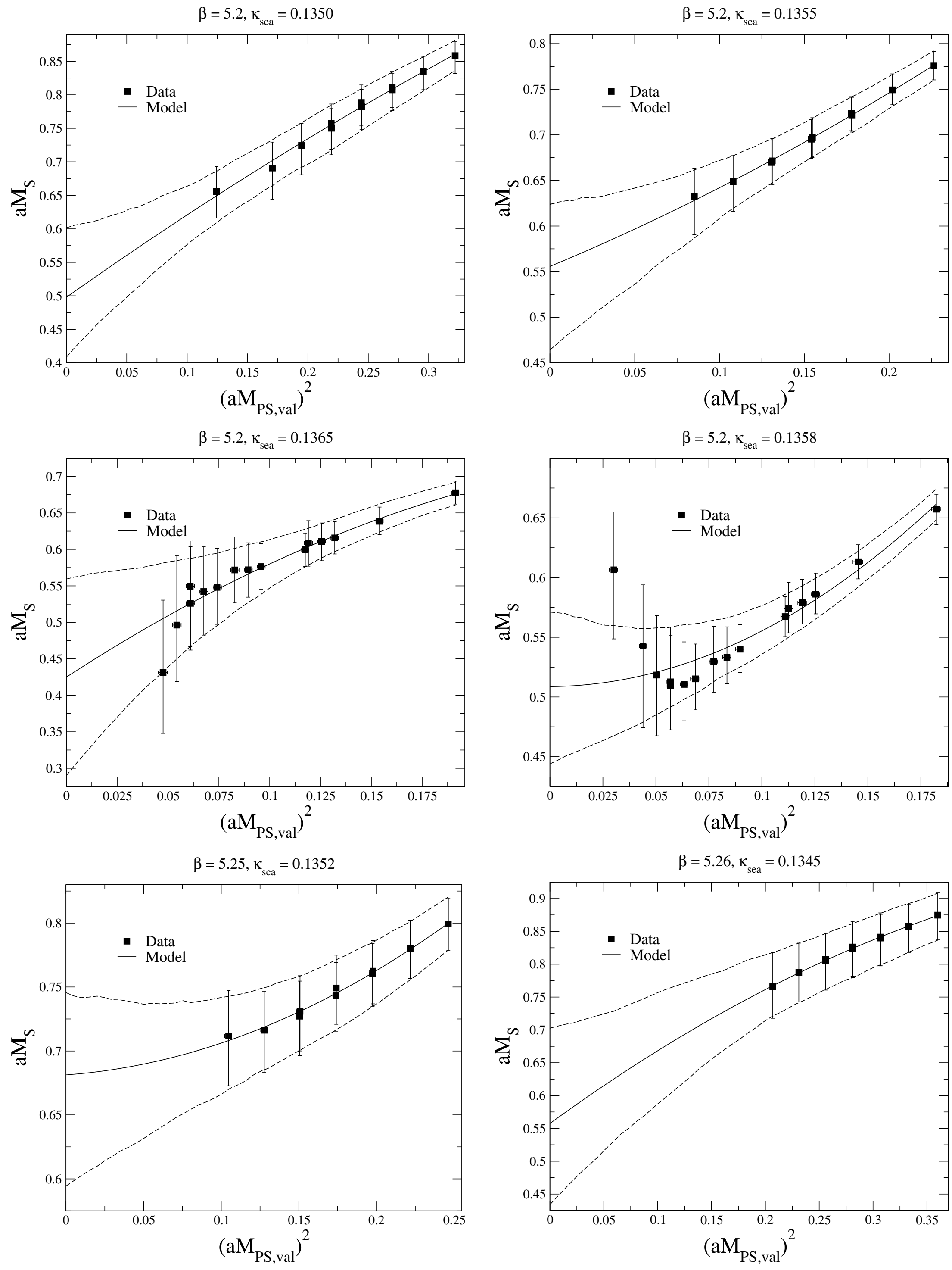

Figure B.13: Plot of fit results for partially quenched chiral extrapolations of $aM_{\rm S}$ versus $(aM_{\rm PS})^2$ using Equation (4.38) for the datasets at $\beta = 5.2$, $(5.25, 0.1352)$ and $(5.26, 0.1345)$.

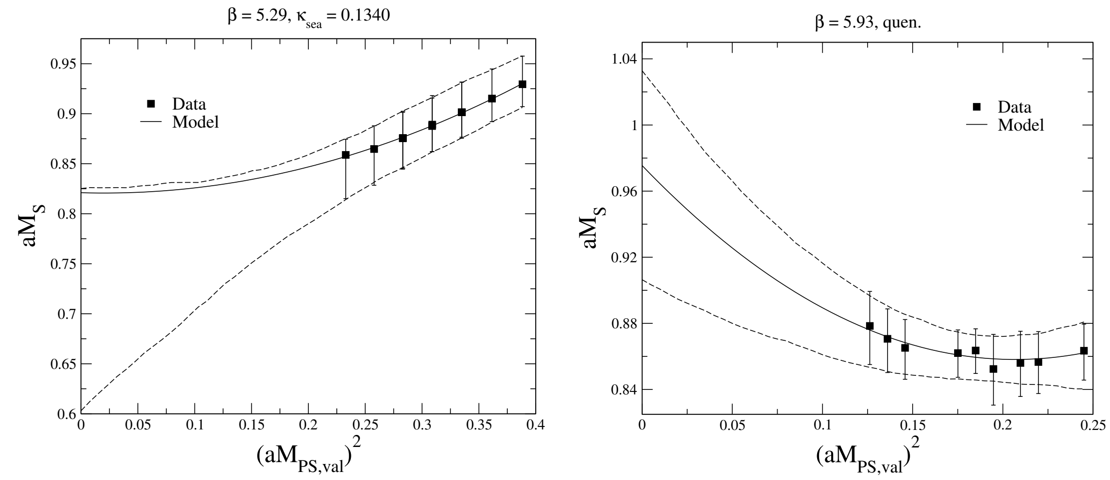

Figure B.14: Plot of fit results for partially quenched chiral extrapolations of aM_{S} versus $(aM_{\mathrm{PS}})^2$ using Equation (4.38) for the datasets at $(5.29, 0.1340)$ and $(5.93, \mathrm{quen.})$

Dataset	A	B	C	χ^2/dof
$(5.2, 0.1350)$	$0.50\ ^{+10}_{-\ 9}$	$1.27\ ^{+74}_{-88}$	$-0.4\ ^{+18}_{-15}$	0.0261
$(5.2, 0.1355)$	$0.556\ ^{+68}_{-92}$	$0.77\ ^{+79}_{-59}$	$0.9\ ^{+15}_{-21}$	0.00673
$(5.2, 0.13565)$	$0.42\ ^{+13}_{-13}$	$1.8\ ^{+16}_{-15}$	$-2.6\ ^{+45}_{-48}$	0.0885
$(5.2, 0.1358)$	$0.509\ ^{+62}_{-65}$	$0.01\ ^{+82}_{-73}$	$4.5\ ^{+25}_{-28}$	0.378
$(5.25, 0.1352)$	$0.681\ ^{+64}_{-87}$	$0.09\ ^{+72}_{-58}$	$1.6\ ^{+14}_{-17}$	0.00874
$(5.26, 0.1345)$	$0.56\ ^{+15}_{-12}$	$1.20\ ^{+58}_{-77}$	$-0.8\ ^{+11}_{-\ 8}$	0.00126
$(5.29, 0.1340)$	$0.82\ ^{+\ 0}_{-22}$	$0.0\ ^{+12}_{-\ 0}$	$0.8\ ^{+\ 0}_{-18}$	0.00171
$(5.93, \mathrm{quen.})$	$0.975\ ^{+57}_{-69}$	$-1.13\ ^{+57}_{-46}$	$2.7\ ^{+11}_{-14}$	0.0431

Table B.7: Summary of fit results for partially quenched chiral extrapolations of aM_{S} versus $(aM_{\mathrm{PS}})^2$ using Equation (4.38).

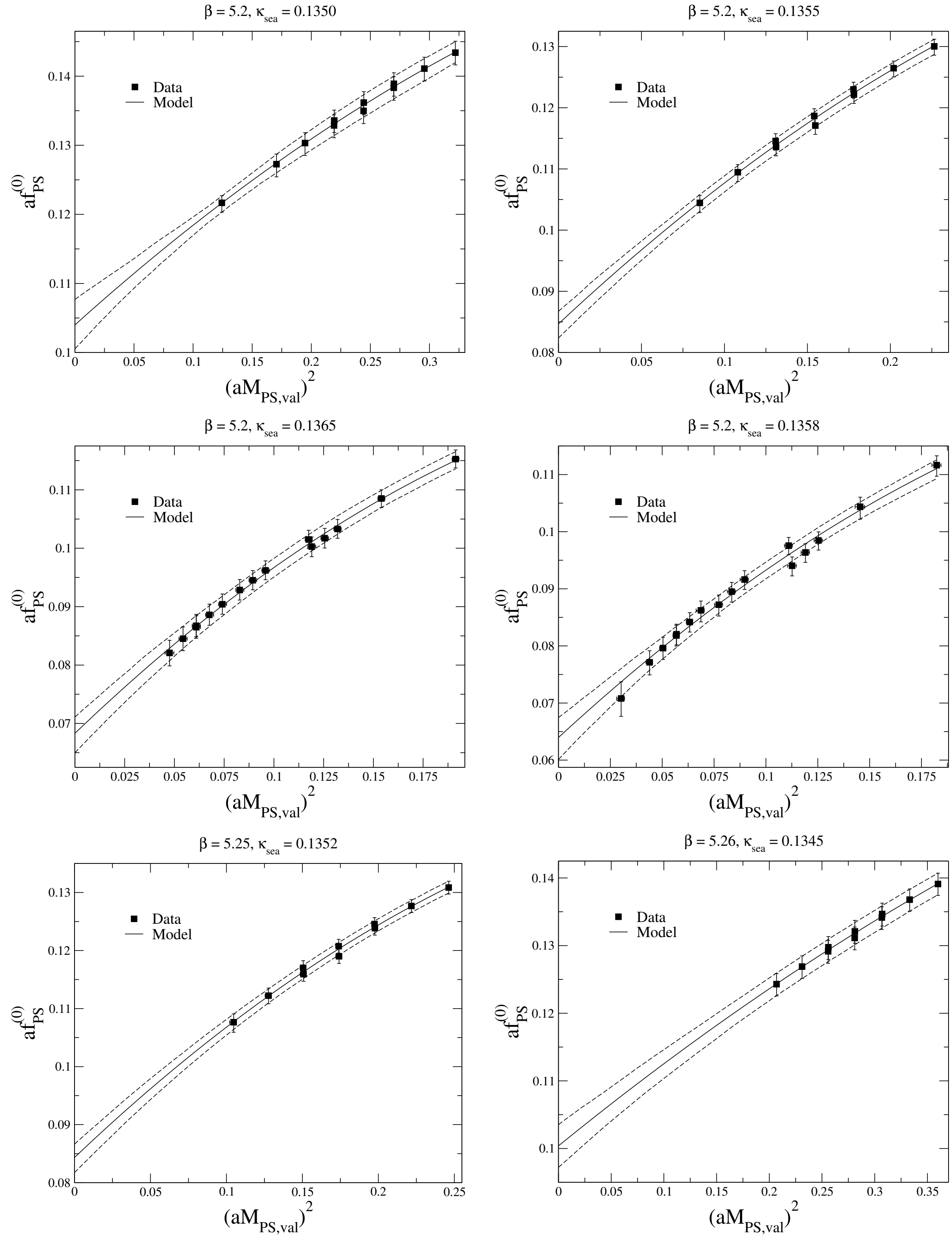

Figure B.15: Plot of fit results for partially quenched chiral extrapolations of $af_{\mathrm{PS}}^{(0)}$ versus $(aM_{\mathrm{PS}})^2$ using Equation (4.38) for the datasets at $\beta = 5.2$, $(5.25, 0.1352)$ and $(5.26, 0.1345)$.

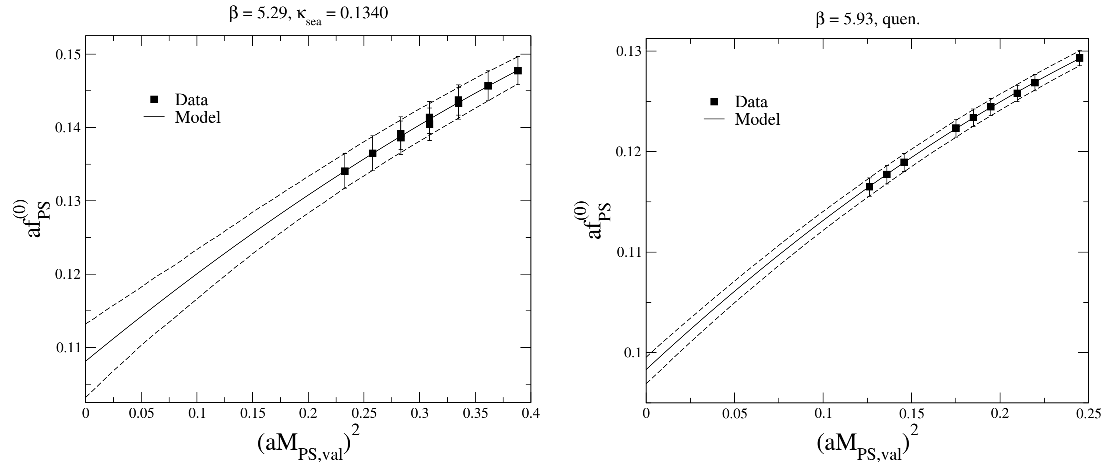

Figure B.16: Plot of fit results for partially quenched chiral extrapolations of $af_{\mathrm{PS}}^{(0)}$ versus $(aM_{\mathrm{PS}})^2$ using Equation (4.38) for the datasets at $(5.29, 0.1340)$ and $(5.93, \text{quen.})$

Dataset	A	B	C	χ^2/dof
$(5.2, 0.1350)$	$0.1040\ ^{+37}_{-35}$	$0.154\ ^{+32}_{-37}$	$-0.097\ ^{+71}_{-62}$	0.0582
$(5.2, 0.1355)$	$0.0847\ ^{+21}_{-23}$	$0.254\ ^{+22}_{-20}$	$-0.233\ ^{+56}_{-62}$	0.236
$(5.2, 0.13565)$	$0.0683\ ^{+28}_{-33}$	$0.327\ ^{+39}_{-32}$	$-0.43\ ^{+11}_{-13}$	0.111
$(5.2, 0.1358)$	$0.0640\ ^{+35}_{-39}$	$0.335\ ^{+52}_{-51}$	$-0.42\ ^{+19}_{-19}$	0.511
$(5.25, 0.1352)$	$0.0843\ ^{+23}_{-26}$	$0.249\ ^{+21}_{-16}$	$-0.241\ ^{+34}_{-54}$	0.283
$(5.26, 0.1345)$	$0.1004\ ^{+31}_{-32}$	$0.127\ ^{+17}_{-16}$	$-0.052\ ^{+24}_{-24}$	0.0451
$(5.29, 0.1340)$	$0.1081\ ^{+51}_{-49}$	$0.125\ ^{+23}_{-23}$	$-0.059\ ^{+33}_{-32}$	0.0252
$(5.93, \text{quen.})$	$0.0983\ ^{+12}_{-14}$	$0.1634\ ^{+92}_{-91}$	$-0.151\ ^{+20}_{-20}$	0.00809

Table B.8: Summary of fit results for partially quenched chiral extrapolations of $af_{\mathrm{PS}}^{(0)}$ versus $(aM_{\mathrm{PS}})^2$ using Equation (4.38).

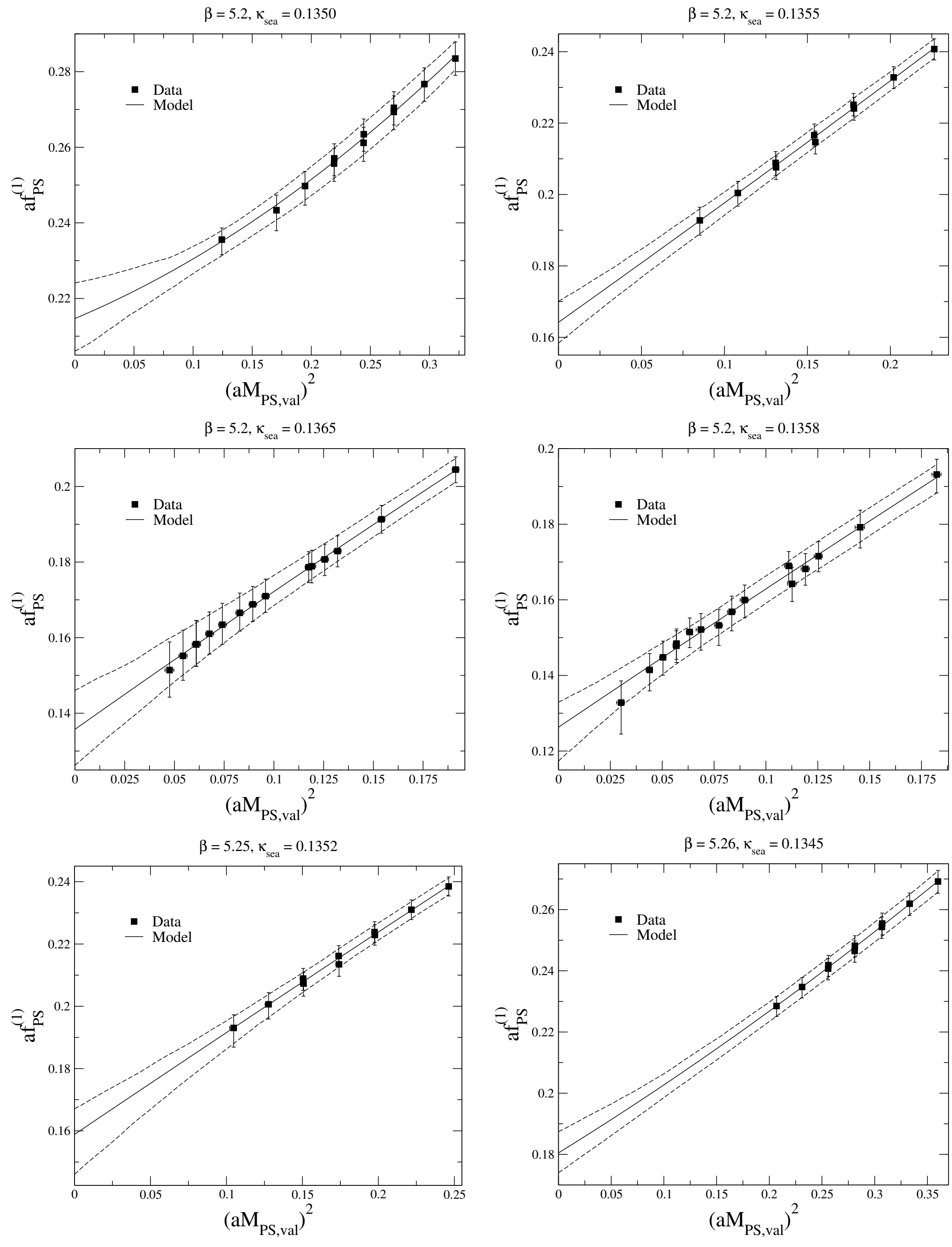

Figure B.17: Plot of fit results for partially quenched chiral extrapolations of $af_{\rm PS}^{(1)}$ versus $(aM_{\rm PS})^2$ using Equation (4.38) for the datasets at $\beta = 5.2$, $(5.25, 0.1352)$ and $(5.26, 0.1345)$.

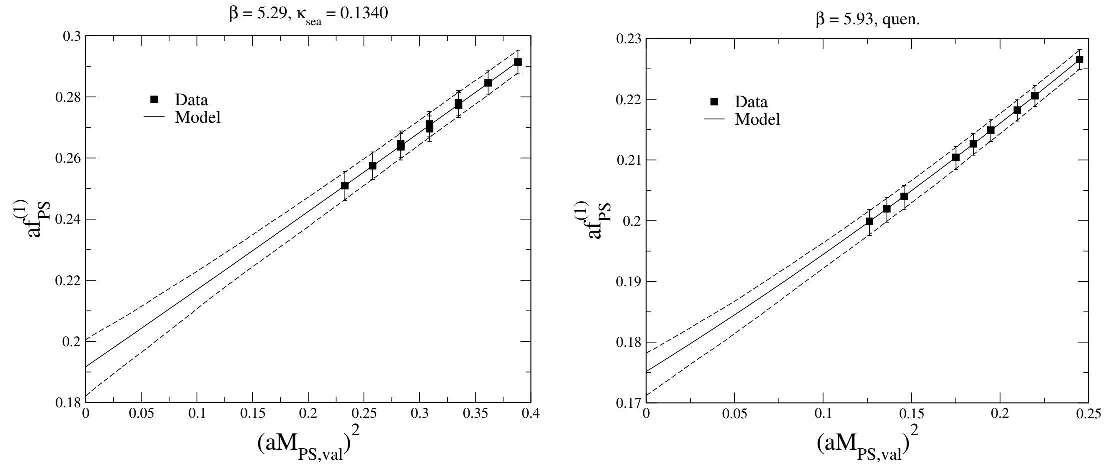

Figure B.18: Plot of fit results for partially quenched chiral extrapolations of $af_{\mathrm{PS}}^{(1)}$ versus $(aM_{\mathrm{PS}})^2$ using Equation (4.38) for the datasets at $(5.29, 0.1340)$ and $(5.93, \text{quen.})$

Dataset	A	B	C	χ^2/dof
$(5.2, 0.1350)$	$0.2147\ ^{+94}_{-87}$	$0.132\ ^{+85}_{-96}$	$0.26\ ^{+19}_{-16}$	0.0506
$(5.2, 0.1355)$	$0.1642\ ^{+58}_{-58}$	$0.331\ ^{+52}_{-52}$	$0.04\ ^{+13}_{-13}$	0.0679
$(5.2, 0.13565)$	$0.136\ ^{+10}_{-10}$	$0.37\ ^{+11}_{-12}$	$-0.07\ ^{+38}_{-36}$	0.0135
$(5.2, 0.1358)$	$0.1263\ ^{+66}_{-90}$	$0.37\ ^{+12}_{-10}$	$-0.04\ ^{+37}_{-49}$	0.150
$(5.25, 0.1352)$	$0.159\ ^{+\ 8}_{-13}$	$0.33\ ^{+11}_{-\ 7}$	$-0.01\ ^{+15}_{-24}$	0.0780
$(5.26, 0.1345)$	$0.1805\ ^{+69}_{-65}$	$0.213\ ^{+36}_{-42}$	$0.094\ ^{+61}_{-53}$	0.0354
$(5.29, 0.1340)$	$0.1917\ ^{+89}_{-95}$	$0.251\ ^{+45}_{-48}$	$0.016\ ^{+67}_{-63}$	0.0196
$(5.93, \text{quen.})$	$0.1752\ ^{+30}_{-40}$	$0.181\ ^{+26}_{-20}$	$0.116\ ^{+46}_{-53}$	0.000544

Table B.9: Summary of fit results for partially quenched chiral extrapolations of $af_{\mathrm{PS}}^{(1)}$ versus $(aM_{\mathrm{PS}})^2$ using Equation (4.38).

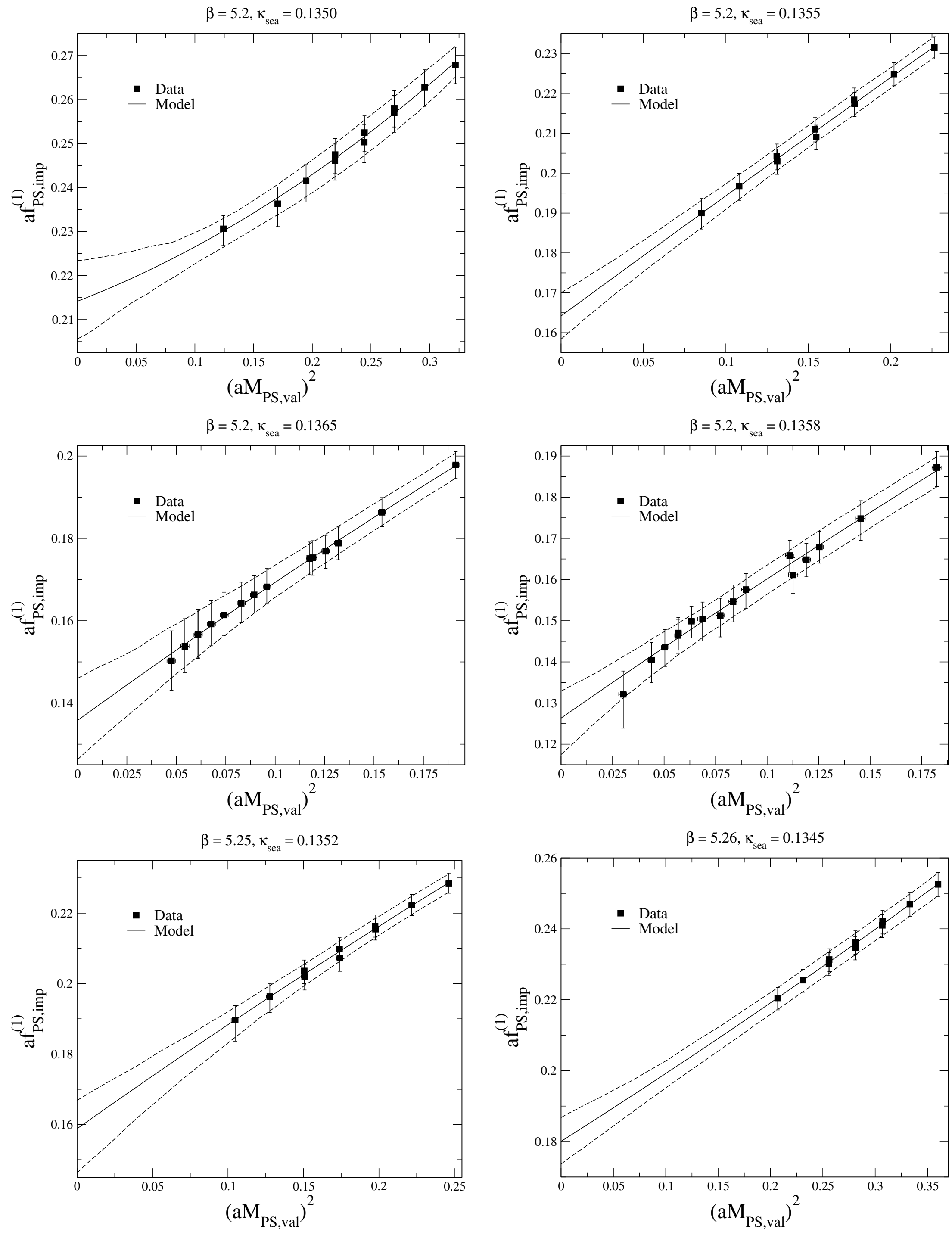

Figure B.19: Plot of fit results for partially quenched chiral extrapolations of $af^{(1)}_{\mathrm{PS,imp}}$ versus $(aM_{\mathrm{PS}})^2$ using Equation (4.38) for the datasets at $\beta = 5.2$, $(5.25, 0.1352)$ and $(5.26, 0.1345)$.

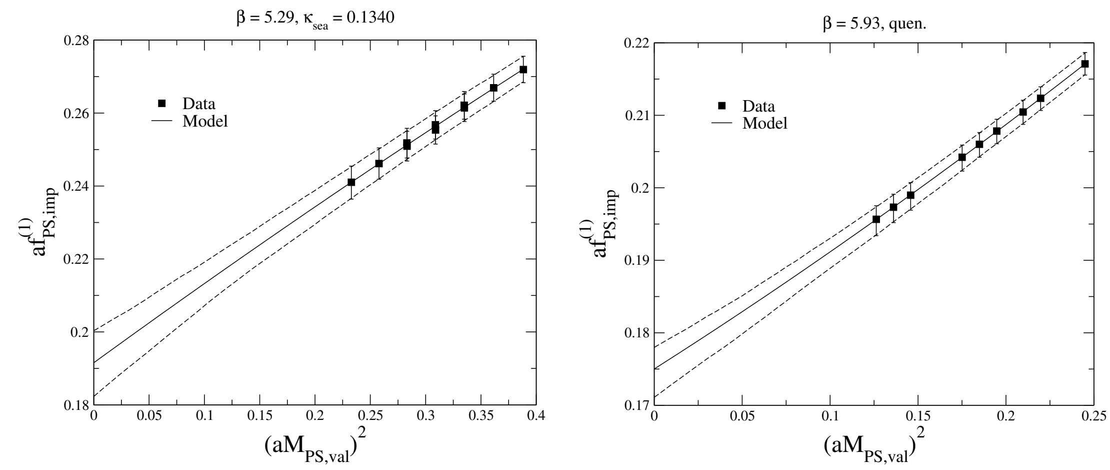

Figure B.20: Plot of fit results for partially quenched chiral extrapolations of $af^{(1)}_{\mathrm{PS,imp}}$ versus $(aM_{\mathrm{PS}})^2$ using Equation (4.38) for the datasets at $(5.29, 0.1340)$ and $(5.93, \mathrm{quen.})$

Dataset	A	B	C	χ^2/dof
$(5.2, 0.1350)$	$0.2142\ ^{+92}_{-85}$	$0.103\ ^{+81}_{-93}$	$0.20\ ^{+18}_{-15}$	0.0527
$(5.2, 0.1355)$	$0.1642\ ^{+58}_{-58}$	$0.304\ ^{+52}_{-50}$	$-0.02\ ^{+13}_{-13}$	0.0709
$(5.2, 0.13565)$	$0.136\ ^{+10}_{-10}$	$0.35\ ^{+11}_{-12}$	$-0.13\ ^{+38}_{-35}$	0.0138
$(5.2, 0.1358)$	$0.1263\ ^{+65}_{-88}$	$0.35\ ^{+12}_{-10}$	$-0.10\ ^{+36}_{-48}$	0.153
$(5.25, 0.1352)$	$0.159\ ^{+8}_{-13}$	$0.30\ ^{+10}_{-7}$	$-0.07\ ^{+14}_{-23}$	0.0797
$(5.26, 0.1345)$	$0.1800\ ^{+67}_{-64}$	$0.188\ ^{+34}_{-40}$	$0.039\ ^{+58}_{-52}$	0.0359
$(5.29, 0.1340)$	$0.1916\ ^{+88}_{-92}$	$0.220\ ^{+43}_{-46}$	$-0.033\ ^{+65}_{-59}$	0.0200
$(5.93, \mathrm{quen.})$	$0.1750\ ^{+30}_{-39}$	$0.154\ ^{+25}_{-20}$	$0.071\ ^{+45}_{-52}$	0.000562

Table B.10: Summary of fit results for partially quenched chiral extrapolations of $af^{(1)}_{\mathrm{PS,imp}}$ versus $(aM_{\mathrm{PS}})^2$ using Equation (4.38).

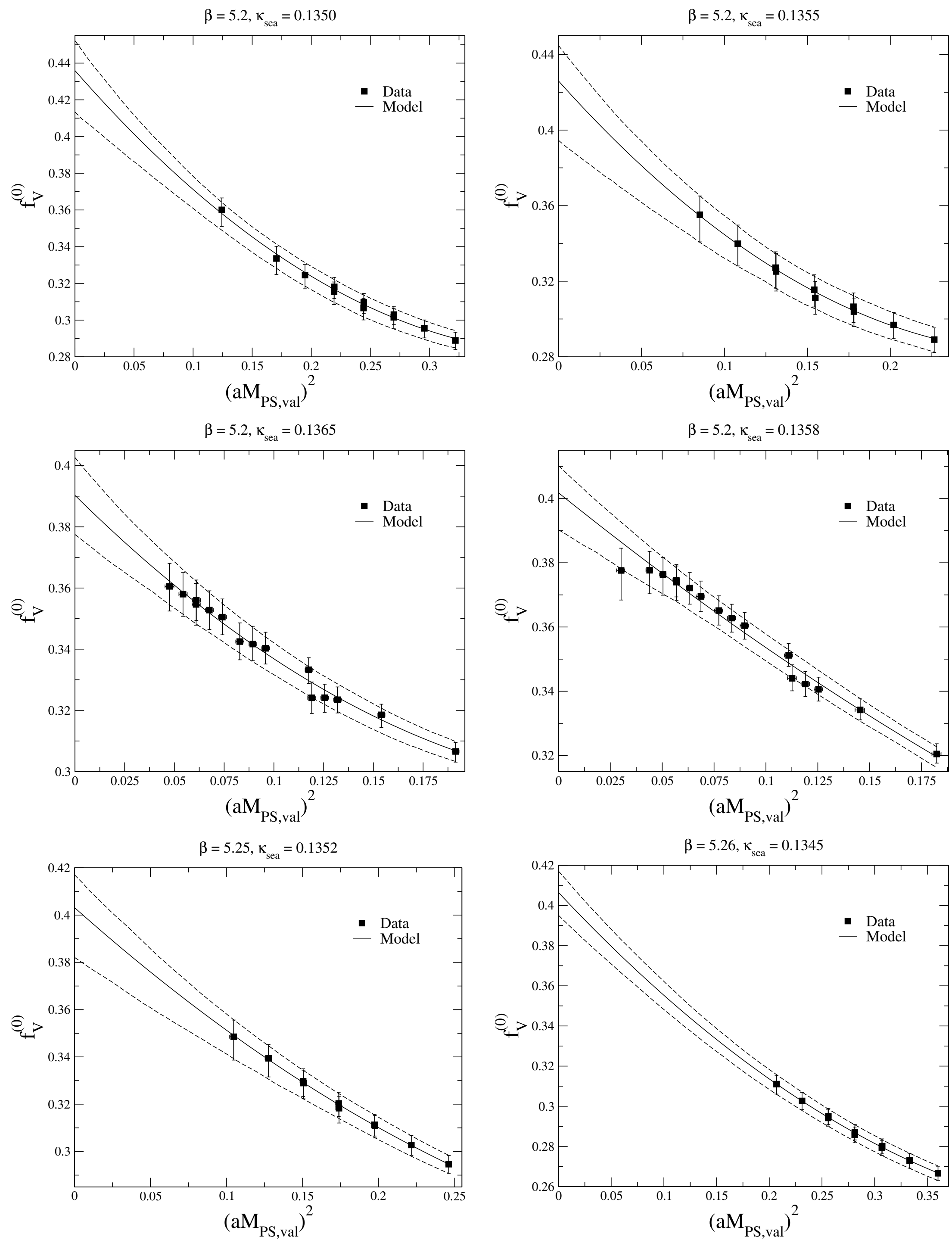

Figure B.21: Plot of fit results for partially quenched chiral extrapolations of $f_{\mathrm{V}}^{(0)}$ versus $(aM_{\mathrm{PS}})^2$ using Equation (4.38) for the datasets at $\beta = 5.2$, $(5.25, 0.1352)$ and $(5.26, 0.1345)$.

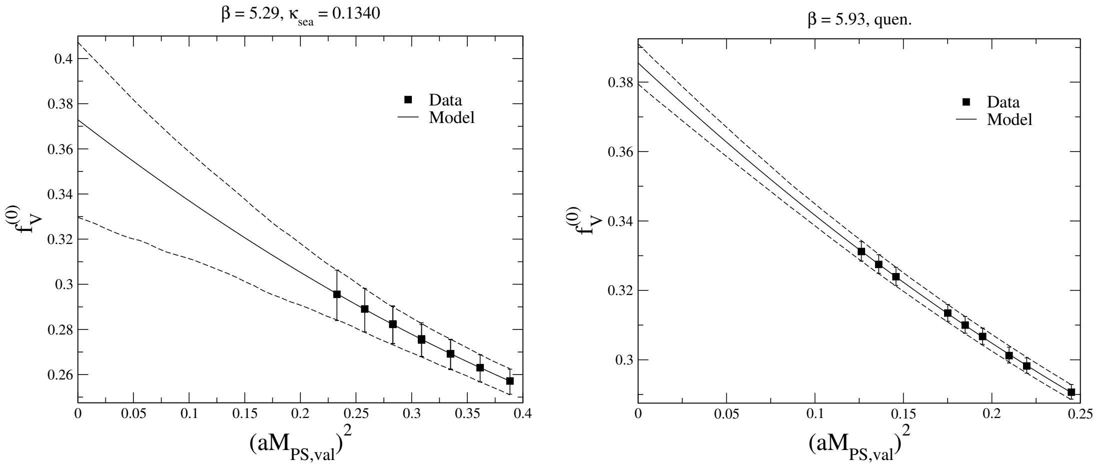

Figure B.22: Plot of fit results for partially quenched chiral extrapolations of $f_{\mathrm{V}}^{(0)}$ versus $(aM_{\mathrm{PS}})^2$ using Equation (4.38) for the datasets at $(5.29, 0.1340)$ and $(5.93, \mathrm{quen.})$

Dataset	A	B	C	χ^2/dof
$(5.2, 0.1350)$	0.436 $^{+16}_{-23}$	-0.73 $^{+17}_{-13}$	0.88 $^{+29}_{-33}$	0.0826
$(5.2, 0.1355)$	0.426 $^{+19}_{-31}$	-0.97 $^{+30}_{-19}$	1.67 $^{+50}_{-73}$	0.0353
$(5.2, 0.13565)$	0.390 $^{+12}_{-13}$	-0.64 $^{+14}_{-13}$	1.07 $^{+41}_{-48}$	0.217
$(5.2, 0.1358)$	0.402 $^{+\ 8}_{-12}$	-0.51 $^{+15}_{-11}$	0.38 $^{+39}_{-53}$	0.347
$(5.25, 0.1352)$	0.403 $^{+14}_{-21}$	-0.57 $^{+17}_{-11}$	0.53 $^{+24}_{-37}$	0.0145
$(5.26, 0.1345)$	0.406 $^{+11}_{-11}$	-0.559 $^{+60}_{-52}$	0.476 $^{+81}_{-84}$	0.0178
$(5.29, 0.1340)$	0.373 $^{+34}_{-43}$	-0.38 $^{+20}_{-16}$	0.21 $^{+22}_{-27}$	0.000565
$(5.93, \mathrm{quen.})$	0.3856 $^{+55}_{-61}$	-0.474 $^{+42}_{-38}$	0.353 $^{+79}_{-84}$	0.00805

Table B.11: Summary of fit results for partially quenched chiral extrapolations of $f_{\mathrm{V}}^{(0)}$ versus $(aM_{\mathrm{PS}})^2$ using Equation (4.38).

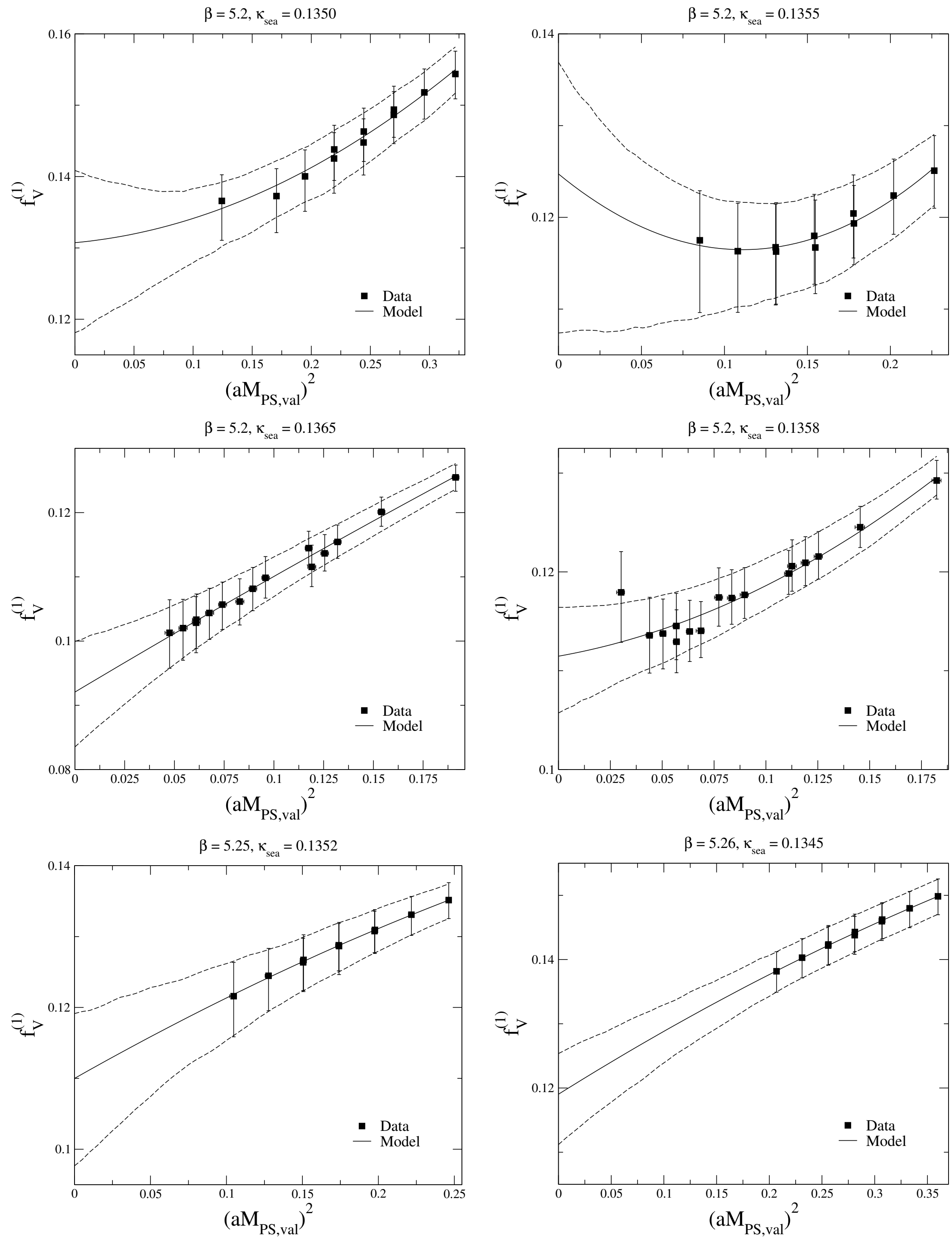

Figure B.23: Plot of fit results for partially quenched chiral extrapolations of $f_{\rm V}^{(1)}$ versus $(aM_{\rm PS})^2$ using Equation (4.38) for the datasets at $\beta = 5.2$, $(5.25, 0.1352)$ and $(5.26, 0.1345)$.

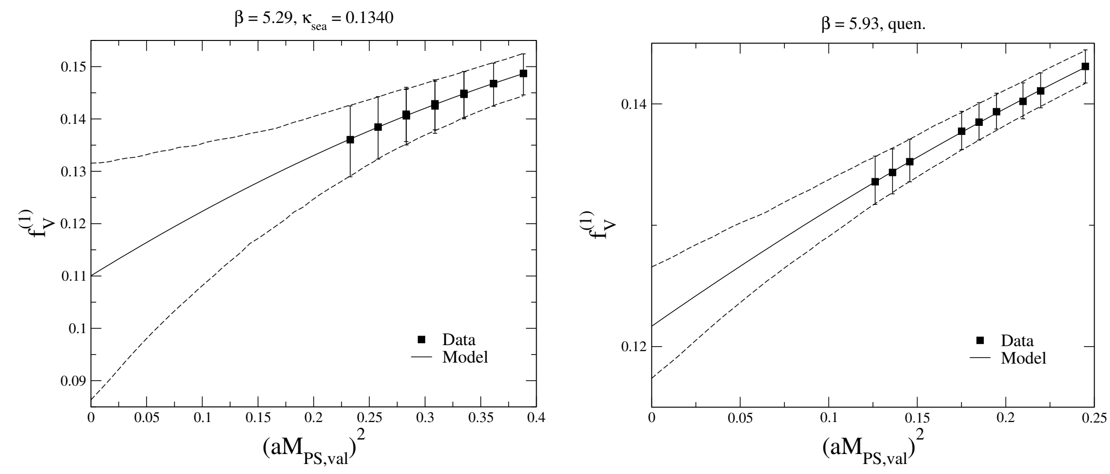

Figure B.24: Plot of fit results for partially quenched chiral extrapolations of $f_{\mathrm{V}}^{(1)}$ versus $(aM_{\mathrm{PS}})^2$ using Equation (4.38) for the datasets at $(5.29, 0.1340)$ and $(5.93, \text{quen.})$

Dataset	A	B	C	χ^2/dof
$(5.2, 0.1350)$	$0.131\ ^{+10}_{-13}$	$0.02\ ^{+10}_{-\ 9}$	$0.19\ ^{+17}_{-20}$	0.0545
$(5.2, 0.1355)$	$0.125\ ^{+12}_{-17}$	$-0.14\ ^{+17}_{-13}$	$0.67\ ^{+33}_{-43}$	0.0173
$(5.2, 0.13565)$	$0.0921\ ^{+79}_{-85}$	$0.185\ ^{+99}_{-90}$	$-0.04\ ^{+29}_{-33}$	0.0748
$(5.2, 0.1358)$	$0.1115\ ^{+49}_{-57}$	$0.037\ ^{+84}_{-61}$	$0.34\ ^{+25}_{-30}$	0.175
$(5.25, 0.1352)$	$0.110\ ^{+\ 9}_{-12}$	$0.121\ ^{+99}_{-72}$	$-0.07\ ^{+17}_{-21}$	0.00176
$(5.26, 0.1345)$	$0.1190\ ^{+63}_{-78}$	$0.103\ ^{+41}_{-35}$	$-0.047\ ^{+55}_{-61}$	0.00316
$(5.29, 0.1340)$	$0.110\ ^{+22}_{-24}$	$0.13\ ^{+12}_{-10}$	$-0.08\ ^{+13}_{-16}$	0.00116
$(5.93, \text{quen.})$	$0.1217\ ^{+49}_{-43}$	$0.102\ ^{+31}_{-32}$	$-0.060\ ^{+63}_{-63}$	0.00546

Table B.12: Summary of fit results for partially quenched chiral extrapolations of $f_{\mathrm{V}}^{(1)}$ versus $(aM_{\mathrm{PS}})^2$ using Equation (4.38).

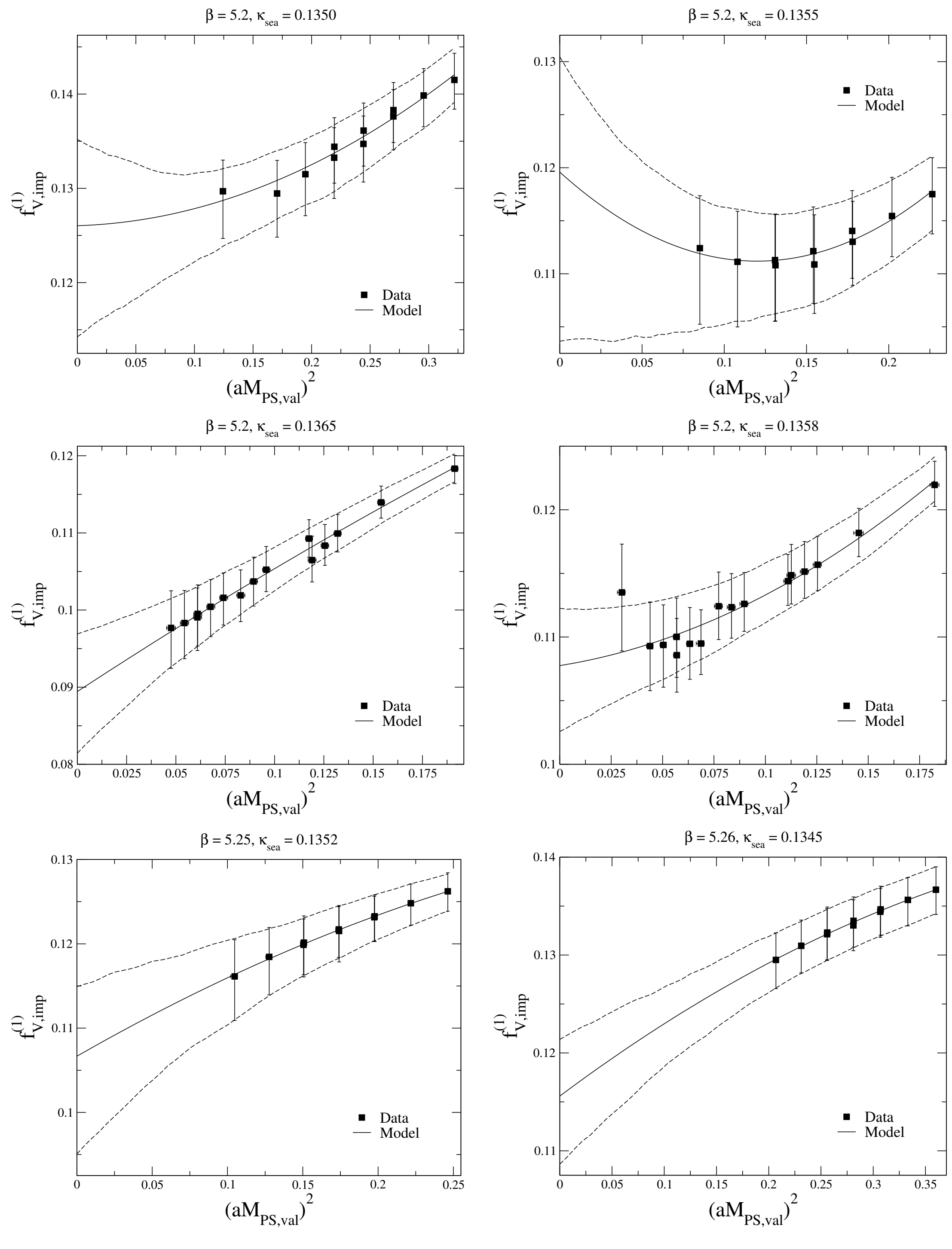

Figure B.25: Plot of fit results for partially quenched chiral extrapolations of $f^{(1)}_{\mathrm{V,imp}}$ versus $(aM_{\mathrm{PS}})^2$ using Equation (4.38) for the datasets at $\beta = 5.2$, $(5.25, 0.1352)$ and $(5.26, 0.1345)$.

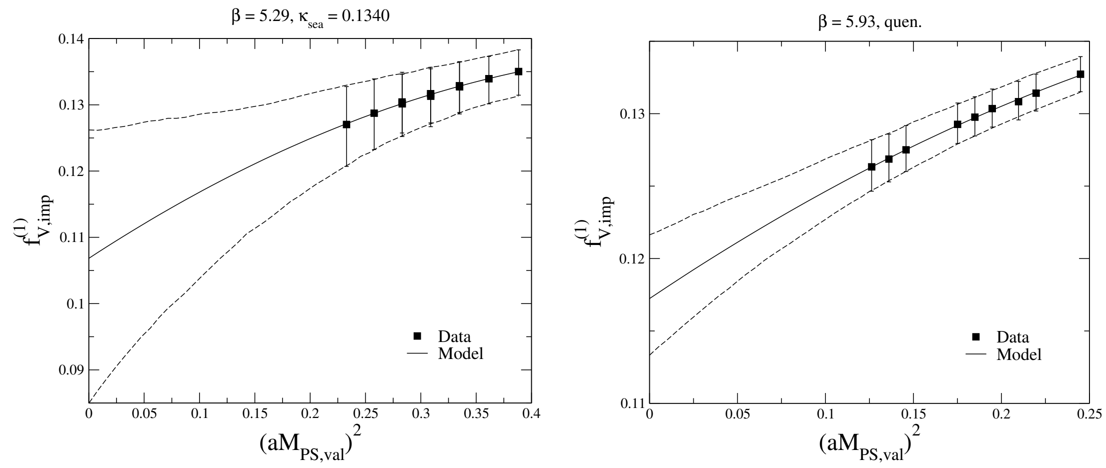

Figure B.26: Plot of fit results for partially quenched chiral extrapolations of $f^{(1)}_{\mathrm{V,imp}}$ versus $(aM_{\mathrm{PS}})^2$ using Equation (4.38) for the datasets at $(5.29, 0.1340)$ and $(5.93, \mathrm{quen.})$

Dataset	A	B	C	χ^2/dof
$(5.2, 0.1350)$	$0.126\,^{+\ 9}_{-12}$	$0.004\,^{+90}_{-80}$	$0.14\,^{+15}_{-18}$	0.0564
$(5.2, 0.1355)$	$0.120\,^{+11}_{-16}$	$-0.14\,^{+16}_{-11}$	$0.58\,^{+30}_{-40}$	0.0187
$(5.2, 0.13565)$	$0.0894\,^{+75}_{-80}$	$0.167\,^{+94}_{-83}$	$-0.08\,^{+27}_{-30}$	0.0785
$(5.2, 0.1358)$	$0.1078\,^{+45}_{-52}$	$0.026\,^{+76}_{-56}$	$0.29\,^{+22}_{-27}$	0.179
$(5.25, 0.1352)$	$0.107\,^{+\ 8}_{-12}$	$0.102\,^{+91}_{-66}$	$-0.09\,^{+16}_{-20}$	0.00169
$(5.26, 0.1345)$	$0.1156\,^{+58}_{-70}$	$0.080\,^{+37}_{-32}$	$-0.058\,^{+49}_{-55}$	0.00385
$(5.29, 0.1340)$	$0.107\,^{+19}_{-22}$	$0.11\,^{+11}_{-\ 9}$	$-0.09\,^{+12}_{-14}$	0.00125
$(5.93, \mathrm{quen.})$	$0.1172\,^{+44}_{-39}$	$0.082\,^{+28}_{-29}$	$-0.075\,^{+58}_{-57}$	0.00582

Table B.13: Summary of fit results for partially quenched chiral extrapolations of $f^{(1)}_{\mathrm{V,imp}}$ versus $(aM_{\mathrm{PS}})^2$ using Equation (4.38).

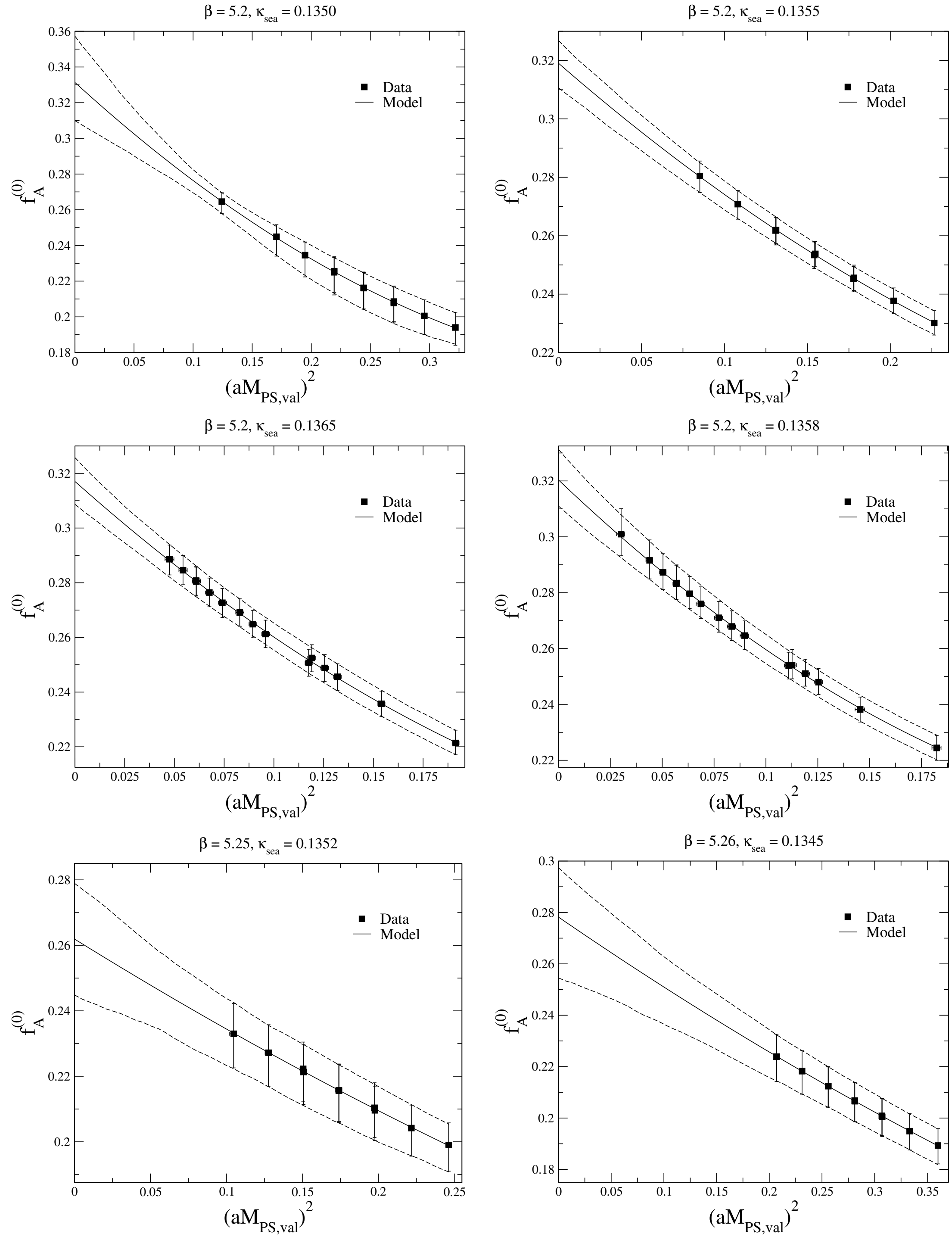

Figure B.27: Plot of fit results for partially quenched chiral extrapolations of $f_{\mathrm{A}}^{(0)}$ versus $(aM_{\mathrm{PS}})^2$ using Equation (4.38) for the datasets at $\beta = 5.2$, $(5.25, 0.1352)$ and $(5.26, 0.1345)$.

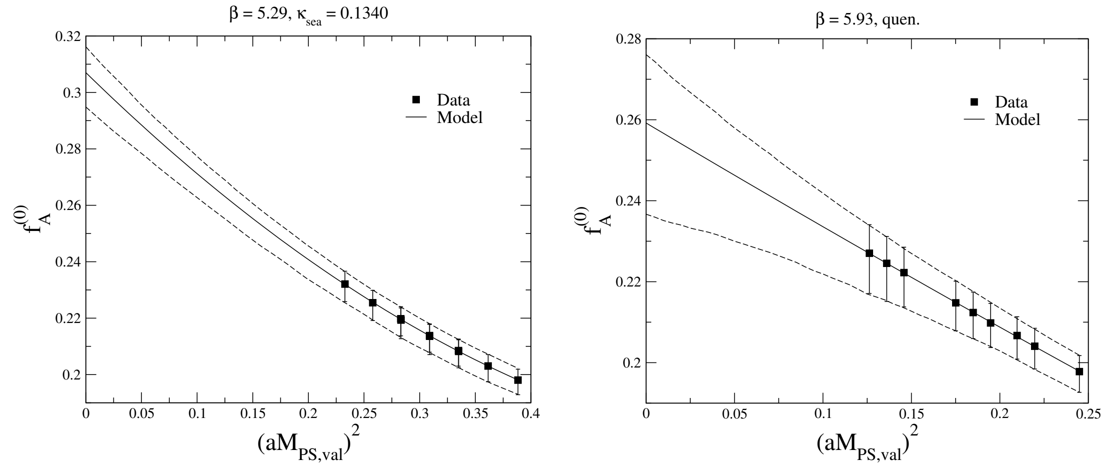

Figure B.28: Plot of fit results for partially quenched chiral extrapolations of $f_{\mathrm{A}}^{(0)}$ versus $(aM_{\mathrm{PS}})^2$ using Equation (4.38) for the datasets at $(5.29, 0.1340)$ and $(5.93, \text{quen.})$

Dataset	A	B	C	χ^2/dof
$(5.2, 0.1350)$	$0.331\ ^{+26}_{-21}$	$-0.60\ ^{+20}_{-31}$	$0.55\ ^{+64}_{-40}$	0.00190
$(5.2, 0.1355)$	$0.3191\ ^{+78}_{-84}$	$-0.494\ ^{+84}_{-72}$	$0.45\ ^{+21}_{-23}$	0.00338
$(5.2, 0.13565)$	$0.3171\ ^{+87}_{-83}$	$-0.64\ ^{+11}_{-10}$	$0.77\ ^{+35}_{-35}$	0.0219
$(5.2, 0.1358)$	$0.320\ ^{+11}_{-\ 9}$	$-0.70\ ^{+12}_{-13}$	$1.00\ ^{+45}_{-42}$	0.00913
$(5.25, 0.1352)$	$0.262\ ^{+17}_{-17}$	$-0.28\ ^{+13}_{-14}$	$0.13\ ^{+34}_{-32}$	0.00195
$(5.26, 0.1345)$	$0.278\ ^{+19}_{-24}$	$-0.28\ ^{+12}_{-10}$	$0.10\ ^{+16}_{-18}$	0.000382
$(5.29, 0.1340)$	$0.307\ ^{+\ 9}_{-12}$	$-0.385\ ^{+62}_{-54}$	$0.270\ ^{+85}_{-85}$	0.00130
$(5.93, \text{quen.})$	$0.259\ ^{+17}_{-23}$	$-0.26\ ^{+15}_{-11}$	$0.04\ ^{+21}_{-32}$	0.00111

Table B.14: Summary of fit results for partially quenched chiral extrapolations of $f_{\mathrm{A}}^{(0)}$ versus $(aM_{\mathrm{PS}})^2$ using Equation (4.38).

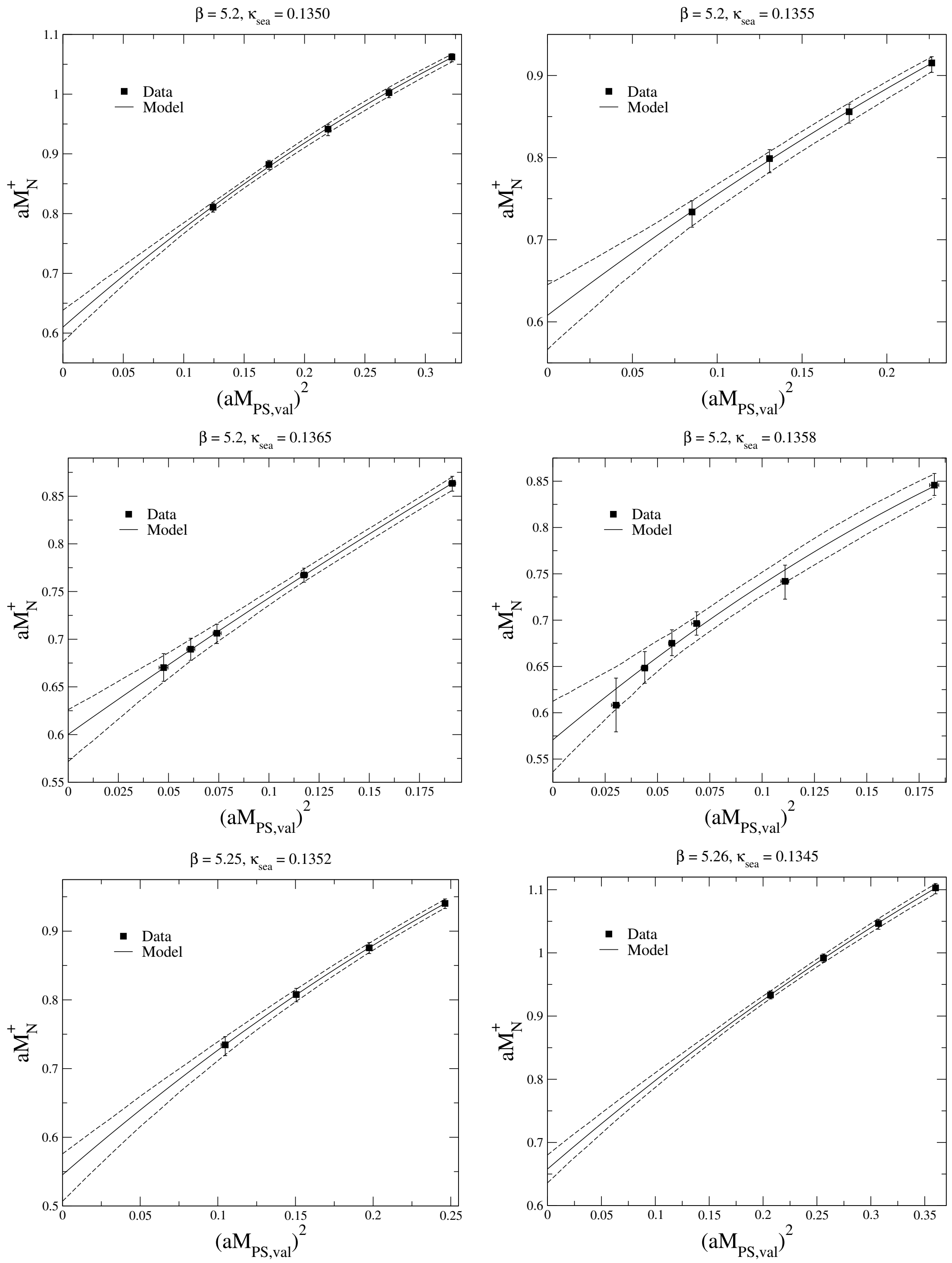

Figure B.29: Plot of fit results for partially quenched chiral extrapolations of aM_{N}^{+} versus $(aM_{\mathrm{PS}})^2$ using Equation (4.40) for the datasets at $\beta = 5.2$, $(5.25, 0.1352)$ and $(5.26, 0.1345)$.

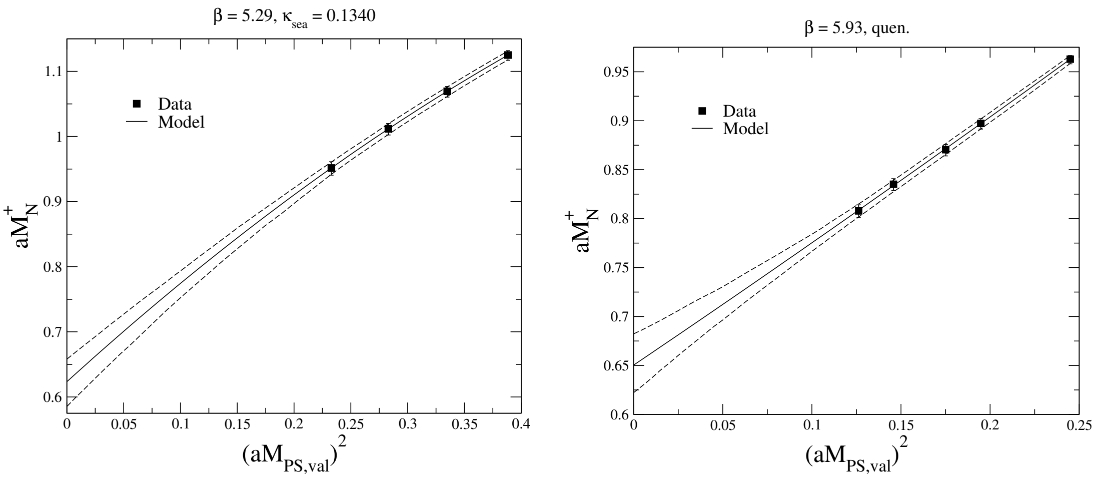

Figure B.30: Plot of fit results for partially quenched chiral extrapolations of aM_{N}^{+} versus $(aM_{\mathrm{PS}})^2$ using Equation (4.40) for the datasets at $(5.29, 0.1340)$ and $(5.93, \text{quen.})$

Dataset	A	B	C	χ^2/dof
$(5.2, 0.1350)$	$0.610\,^{+28}_{-24}$	$1.77\,^{+23}_{-30}$	$-1.14\,^{+57}_{-43}$	0.195
$(5.2, 0.1355)$	$0.608\,^{+37}_{-42}$	$1.57\,^{+43}_{-43}$	$-0.9\,^{+11}_{-12}$	0.0304
$(5.2, 0.13565)$	$0.600\,^{+26}_{-28}$	$1.49\,^{+37}_{-37}$	$-0.6\,^{+13}_{-13}$	0.00828
$(5.2, 0.1358)$	$0.571\,^{+42}_{-35}$	$1.89\,^{+60}_{-72}$	$-2.1\,^{+26}_{-23}$	0.377
$(5.25, 0.1352)$	$0.545\,^{+31}_{-38}$	$1.96\,^{+34}_{-26}$	$-1.43\,^{+58}_{-76}$	0.00126
$(5.26, 0.1345)$	$0.658\,^{+22}_{-22}$	$1.46\,^{+14}_{-15}$	$-0.63\,^{+21}_{-22}$	0.0365
$(5.29, 0.1340)$	$0.623\,^{+35}_{-38}$	$1.59\,^{+20}_{-19}$	$-0.75\,^{+27}_{-28}$	0.000940
$(5.93, \text{quen.})$	$0.650\,^{+32}_{-28}$	$1.23\,^{+27}_{-33}$	$0.19\,^{+77}_{-64}$	0.0512

Table B.15: Summary of fit results for partially quenched chiral extrapolations of aM_{N}^{+} versus $(aM_{\mathrm{PS}})^2$ using Equation (4.40).

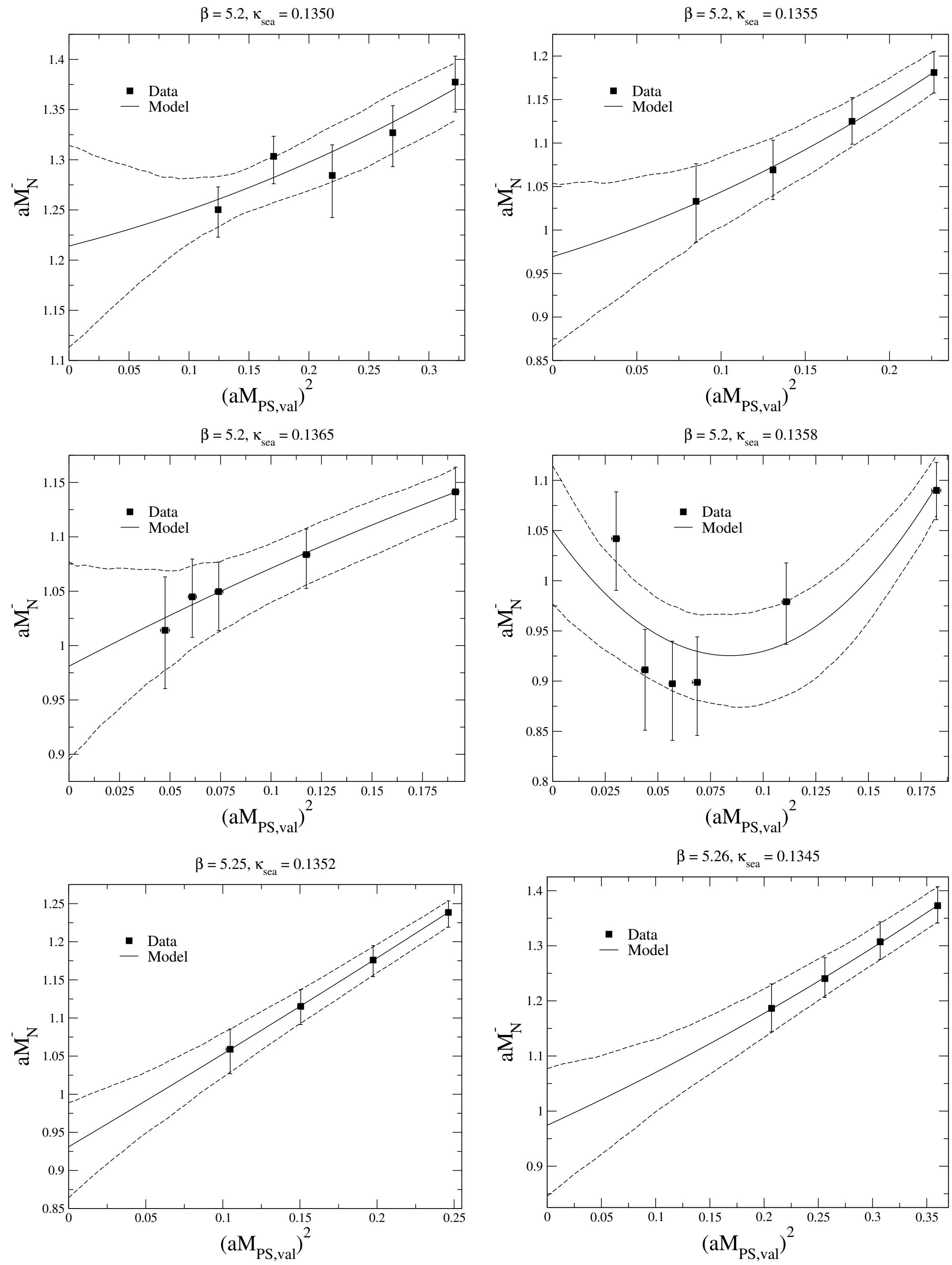

Figure B.31: Plot of fit results for partially quenched chiral extrapolations of aM_{N}^{-} versus $(aM_{\mathrm{PS}})^2$ using Equation (4.40) for the datasets at $\beta = 5.2$, $(5.25, 0.1352)$ and $(5.26, 0.1345)$.

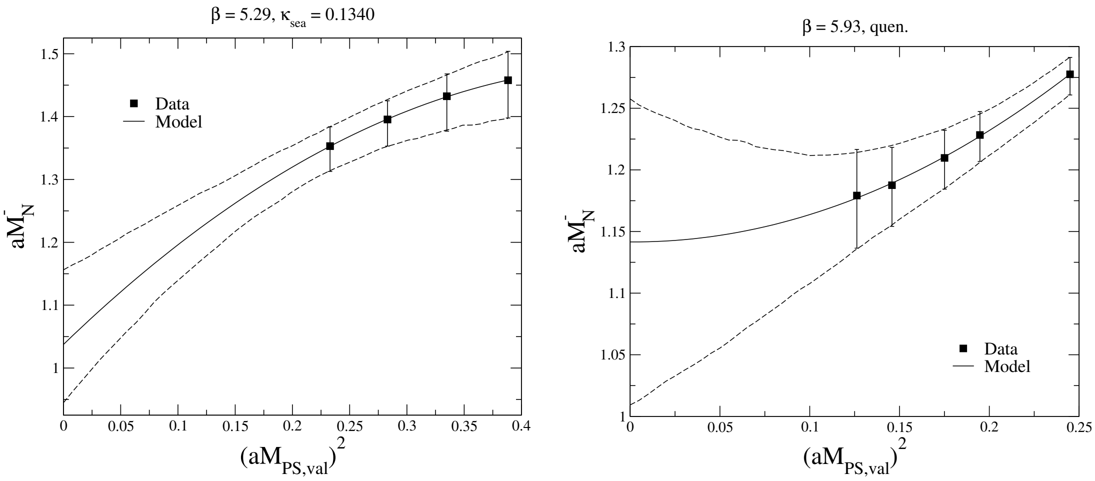

Figure B.32: Plot of fit results for partially quenched chiral extrapolations of aM_{N}^{-} versus $(aM_{\mathrm{PS}})^2$ using Equation (4.40) for the datasets at $(5.29, 0.1340)$ and $(5.93, \text{quen.})$

Dataset	A	B	C	χ^2/dof
$(5.2, 0.1350)$	$1.21\ ^{+10}_{-10}$	$0.30\ ^{+94}_{-97}$	$0.6\ ^{+19}_{-18}$	0.782
$(5.2, 0.1355)$	$0.97\ ^{+\ 8}_{-10}$	$0.6\ ^{+10}_{-\ 8}$	$1.5\ ^{+19}_{-26}$	0.0215
$(5.2, 0.13565)$	$0.981\ ^{+96}_{-86}$	$1.0\ ^{+11}_{-15}$	$-0.6\ ^{+51}_{-38}$	0.0475
$(5.2, 0.1358)$	$1.050\ ^{+64}_{-73}$	$-2.9\ ^{+15}_{-15}$	$17.6\ ^{+66}_{-60}$	1.543
$(5.25, 0.1352)$	$0.931\ ^{+58}_{-67}$	$1.19\ ^{+53}_{-50}$	$0.2\ ^{+11}_{-12}$	0.00137
$(5.26, 0.1345)$	$0.97\ ^{+10}_{-13}$	$0.90\ ^{+69}_{-55}$	$0.6\ ^{+\ 9}_{-11}$	0.00833
$(5.29, 0.1340)$	$1.04\ ^{+12}_{-\ 9}$	$1.76\ ^{+61}_{-84}$	$-1.7\ ^{+14}_{-11}$	0.000746
$(5.93, \text{quen.})$	$1.14\ ^{+12}_{-13}$	$0.0\ ^{+10}_{-\ 9}$	$2.3\ ^{+19}_{-22}$	0.00485

Table B.16: Summary of fit results for partially quenched chiral extrapolations of aM_{N}^{-} versus $(aM_{\mathrm{PS}})^2$ using Equation (4.40).

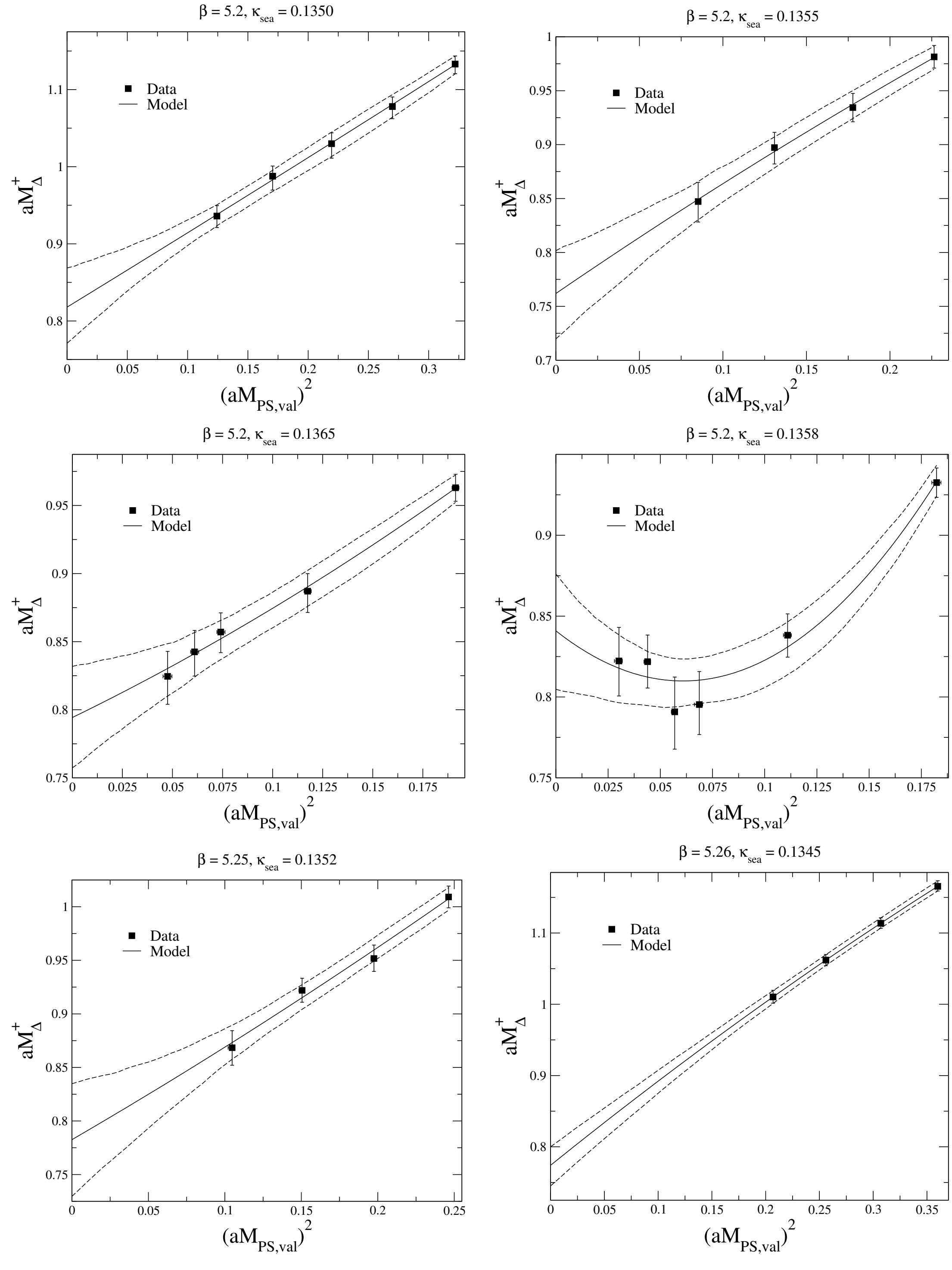

Figure B.33: Plot of fit results for partially quenched chiral extrapolations of aM_Δ^+ versus $(aM_{\rm PS})^2$ using Equation (4.40) for the datasets at $\beta = 5.2$, $(5.25, 0.1352)$ and $(5.26, 0.1345)$.

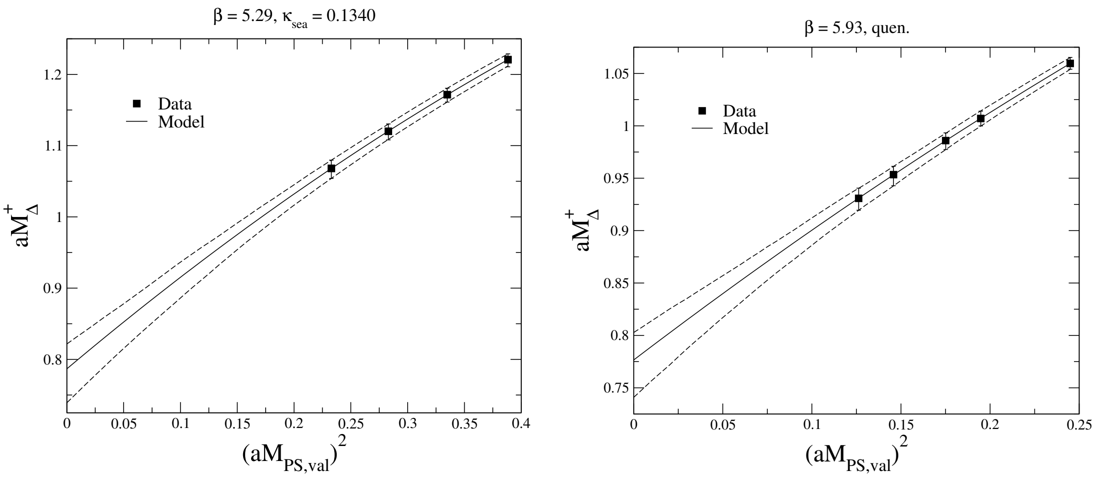

Figure B.34: Plot of fit results for partially quenched chiral extrapolations of aM_Δ^+ versus $(aM_{\mathrm{PS}})^2$ using Equation (4.40) for the datasets at $(5.29, 0.1340)$ and $(5.93, \text{quen.})$

Dataset	A	B	C	χ^2/dof
$(5.2, 0.1350)$	0.818^{+51}_{-47}	0.96^{+44}_{-48}	0.06^{+99}_{-88}	0.0769
$(5.2, 0.1355)$	0.762^{+40}_{-42}	1.06^{+46}_{-43}	-0.4^{+12}_{-13}	0.128
$(5.2, 0.13565)$	0.794^{+38}_{-37}	0.72^{+53}_{-58}	0.9^{+20}_{-18}	0.131
$(5.2, 0.1358)$	0.841^{+35}_{-36}	-1.01^{+72}_{-71}	8.4^{+28}_{-29}	0.676
$(5.25, 0.1352)$	0.783^{+52}_{-53}	0.83^{+49}_{-48}	0.3^{+10}_{-11}	0.899
$(5.26, 0.1345)$	0.774^{+26}_{-29}	1.22^{+16}_{-16}	-0.35^{+24}_{-25}	0.000192
$(5.29, 0.1340)$	0.787^{+35}_{-48}	1.34^{+23}_{-16}	-0.58^{+23}_{-31}	0.000574
$(5.93, \text{quen.})$	0.777^{+26}_{-36}	1.30^{+29}_{-22}	-0.57^{+49}_{-64}	0.000685

Table B.17: Summary of fit results for partially quenched chiral extrapolations of aM_Δ^+ versus $(aM_{\mathrm{PS}})^2$ using Equation (4.40).

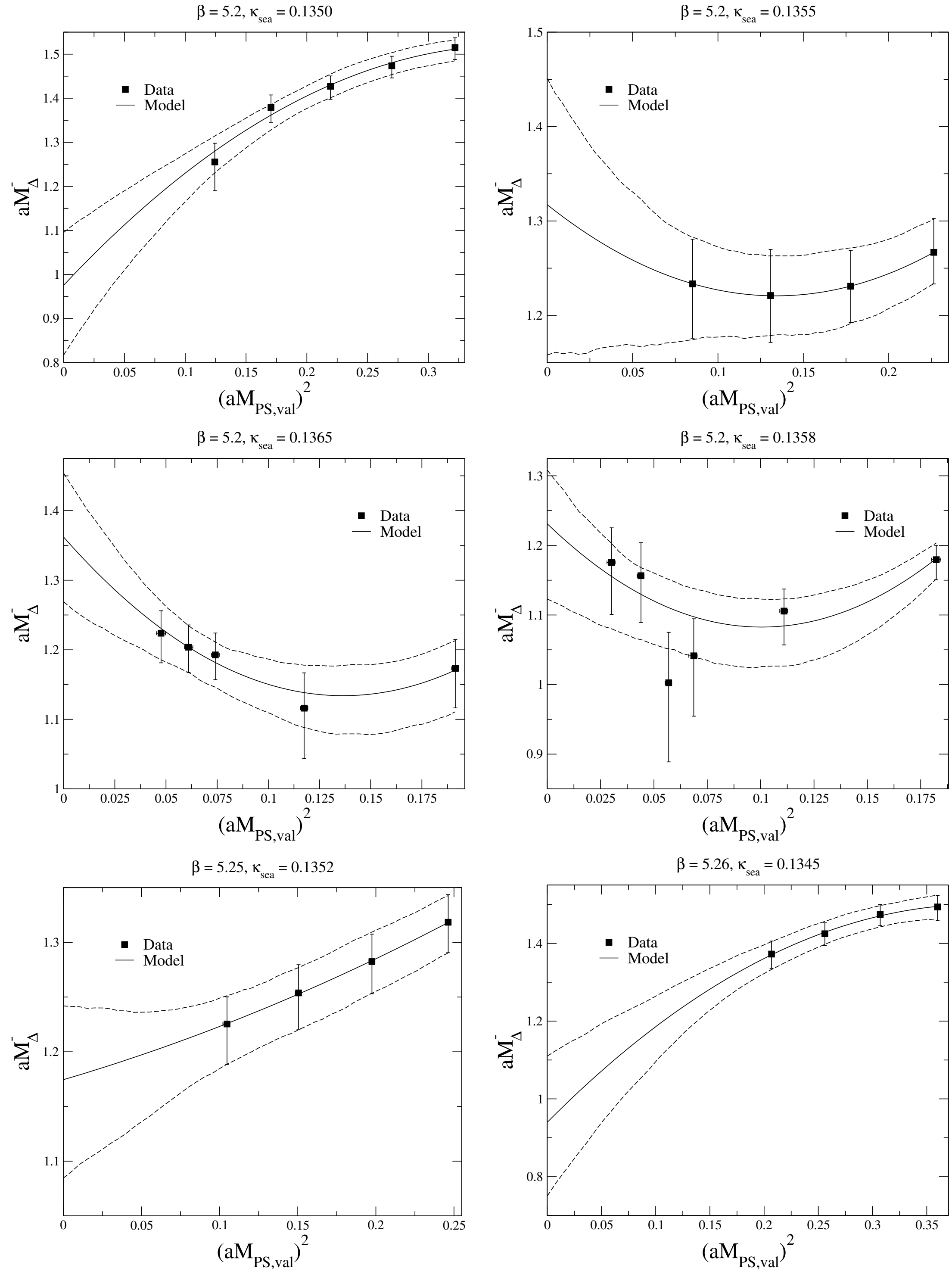

Figure B.35: Plot of fit results for partially quenched chiral extrapolations of aM_{Δ}^{-} versus $(aM_{\mathrm{PS}})^2$ using Equation (4.40) for the datasets at $\beta = 5.2$, $(5.25, 0.1352)$ and $(5.26, 0.1345)$.

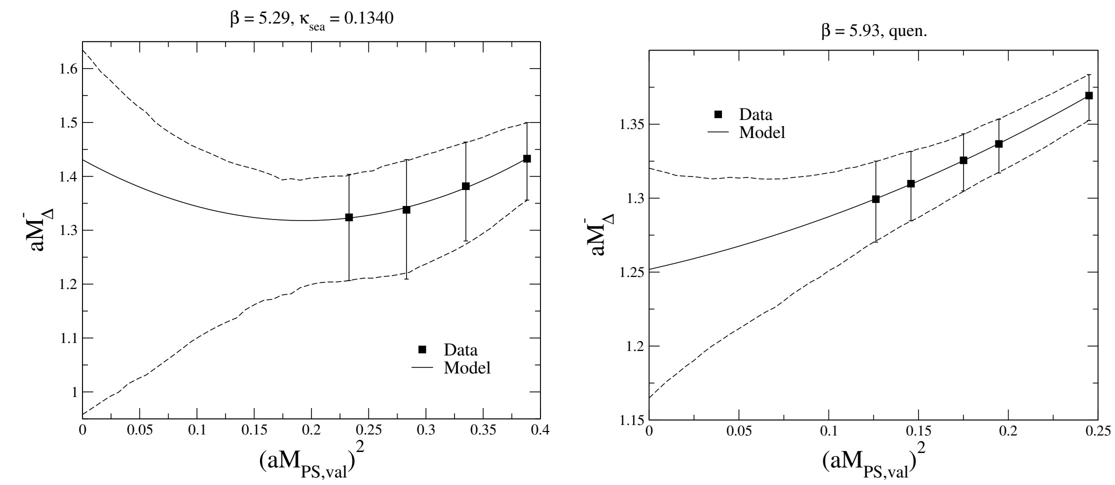

Figure B.36: Plot of fit results for partially quenched chiral extrapolations of aM^-_Δ versus $(aM_{\mathrm{PS}})^2$ using Equation (4.40) for the datasets at $(5.29, 0.1340)$ and $(5.93, \mathrm{quen.})$

Dataset	A	B	C	χ^2/dof
$(5.2, 0.1350)$	0.98^{+12}_{-16}	$2.9^{+12}_{-\ 9}$	-3.9^{+16}_{-23}	0.304
$(5.2, 0.1355)$	1.32^{+13}_{-16}	-1.4^{+17}_{-15}	5.4^{+39}_{-44}	0.0000428
$(5.2, 0.13565)$	1.362^{+92}_{-93}	-3.3^{+16}_{-17}	12.2^{+55}_{-51}	0.138
$(5.2, 0.1358)$	$1.23^{+\ 8}_{-11}$	-2.9^{+17}_{-16}	14.7^{+62}_{-62}	0.867
$(5.25, 0.1352)$	1.174^{+67}_{-90}	0.42^{+89}_{-64}	0.7^{+16}_{-20}	0.00244
$(5.26, 0.1345)$	0.94^{+17}_{-19}	2.8^{+12}_{-11}	-3.5^{+20}_{-21}	0.0357
$(5.29, 0.1340)$	1.43^{+20}_{-47}	-1.1^{+29}_{-16}	3.0^{+27}_{-42}	0.00288
$(5.93, \mathrm{quen.})$	1.252^{+68}_{-87}	0.27^{+68}_{-58}	0.9^{+13}_{-15}	0.000318

Table B.18: Summary of fit results for partially quenched chiral extrapolations of aM^-_Δ versus $(aM_{\mathrm{PS}})^2$ using Equation (4.40).

B.2 Full chiral extrapolations

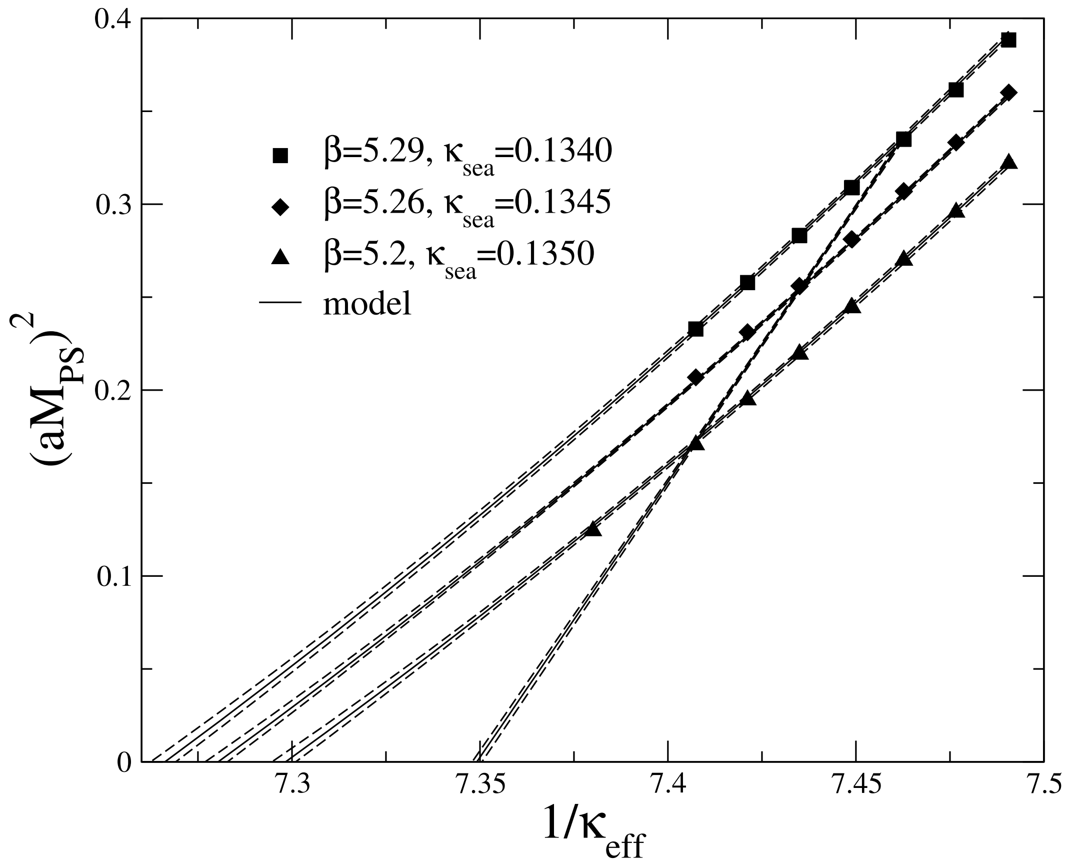

Figure B.37: Plot of fit results for a full chiral extrapolation to the matched datasets of $(aM_{\text{PS}})^2$ versus $1/\kappa_{\text{eff}}$ using Equation (4.44). Lines give unitary and partially quenched fit results.

κ_{crit}	B_{s}^{PS}	B_{v}^{PS}	$C_{\text{ss}}^{\text{PS}}$	$C_{\text{vv}}^{\text{PS}}$	$C_{\text{sv}}^{\text{PS}}$	$D_{\text{vv}}^{\text{PS}}$
$0.136070\ {}^{+23}_{-25}$	$3.00\ {}^{+19}_{-17}$	$1.462\ {}^{+72}_{-84}$	$-12.0\ {}^{+30}_{-33}$	$1.13\ {}^{+19}_{-14}$	$3.8\ {}^{+14}_{-13}$	0

Table B.19: Fit results for a full chiral extrapolation to the matched datasets of $(aM_{\text{PS}})^2$ versus the standard quark mass using Equation (4.41). Result gave $\chi^2/dof = 0.896$.

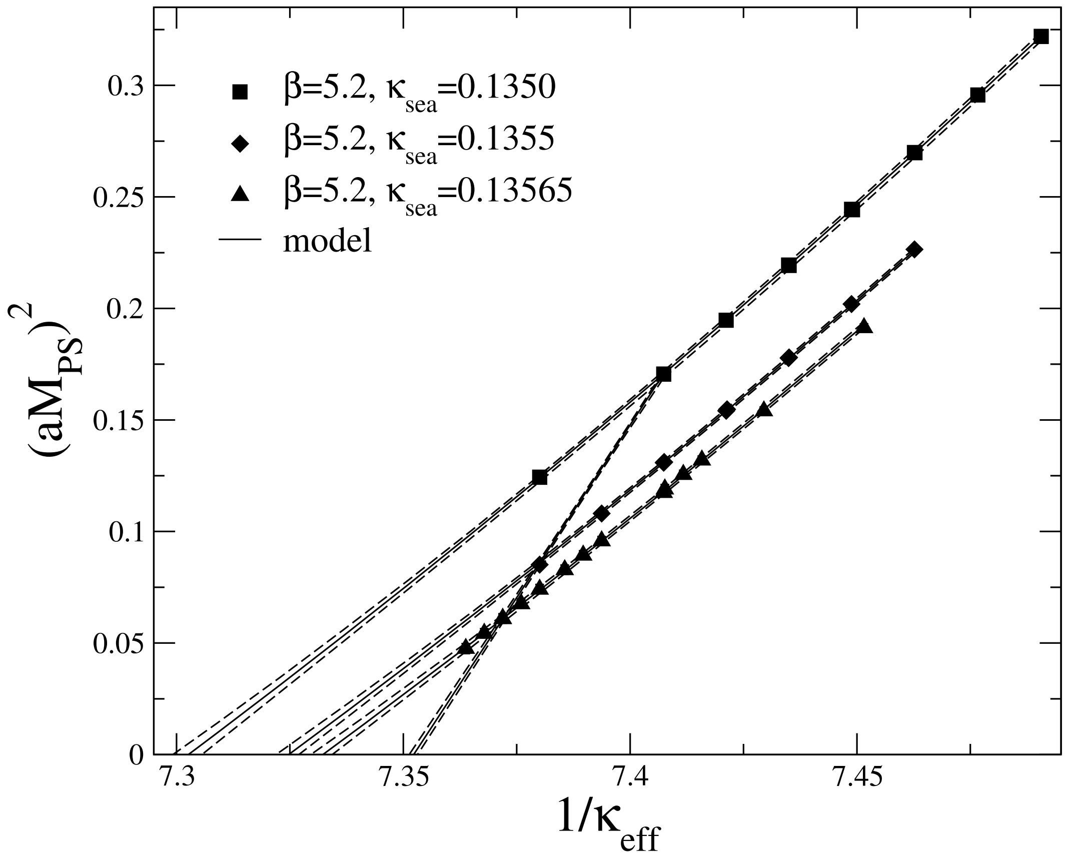

Figure B.38: Plot of fit results for a full chiral extrapolation to the datasets at $\beta = 5.2$ of $(aM_{\mathrm{PS}})^2$ versus $1/\kappa_{\mathrm{eff}}$ using Equation (4.44). Lines give unitary and partially quenched fit results.

κ_{crit}	$B_{\mathrm{s}}^{\mathrm{PS}}$	$B_{\mathrm{v}}^{\mathrm{PS}}$	$C_{\mathrm{ss}}^{\mathrm{PS}}$	$C_{\mathrm{vv}}^{\mathrm{PS}}$	$C_{\mathrm{sv}}^{\mathrm{PS}}$	$D_{\mathrm{vv}}^{\mathrm{PS}}$
$0.136012\ ^{+18}_{-16}$	$3.22\ ^{+10}_{-13}$	$1.485\ ^{+56}_{-64}$	$-14.1\ ^{+28}_{-27}$	$1.19\ ^{+65}_{-52}$	$5.0\ ^{+13}_{-14}$	$-0.7\ ^{+13}_{-15}$

Table B.20: Fit results for a full chiral extrapolation to the datasets at $\beta = 5.2$ of $(aM_{\mathrm{PS}})^2$ versus the standard quark mass using Equation (4.41). Result gave $\chi^2/dof = 0.0597$.

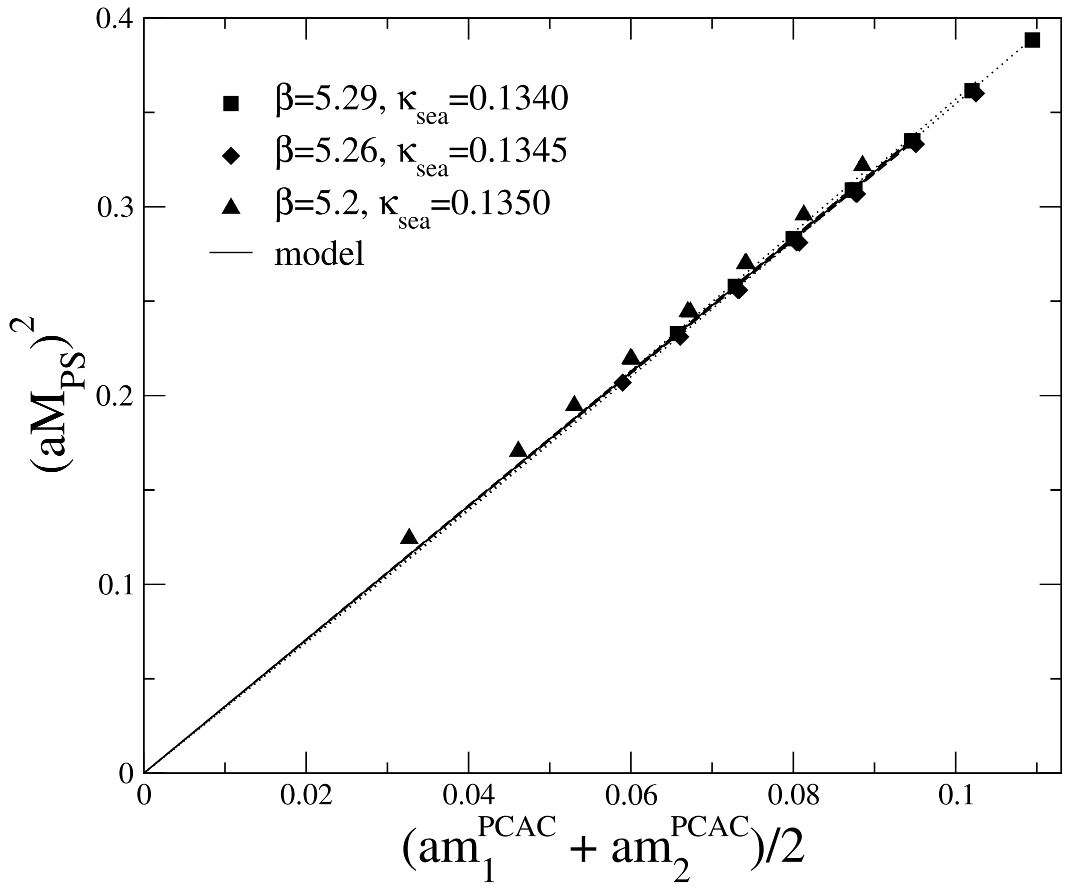

Figure B.39: Plot of fit results for a full chiral extrapolation to the matched datasets of $(aM_{\mathrm{PS}})^2$ versus a_{PCAC} using Equation (4.46). Lines give unitary and partially quenched fit results.

$B'^{\mathrm{PS}}_{\mathrm{v}}$	$C'^{\mathrm{PS}}_{\mathrm{vv}}$	$C'^{\mathrm{PS}}_{\mathrm{sv}}$	$D'^{\mathrm{PS}}_{\mathrm{vv}}$	χ^2/dof
$1.7696\ ^{+50}_{-56}$	$0.28\ ^{+10}_{-10}$	$-0.56\ ^{+21}_{-19}$	0	7.21

Table B.21: Fit results for a full chiral extrapolation to the matched datasets of $(aM_{\mathrm{PS}})^2$ versus am_{PCAC} using Equation (4.46).

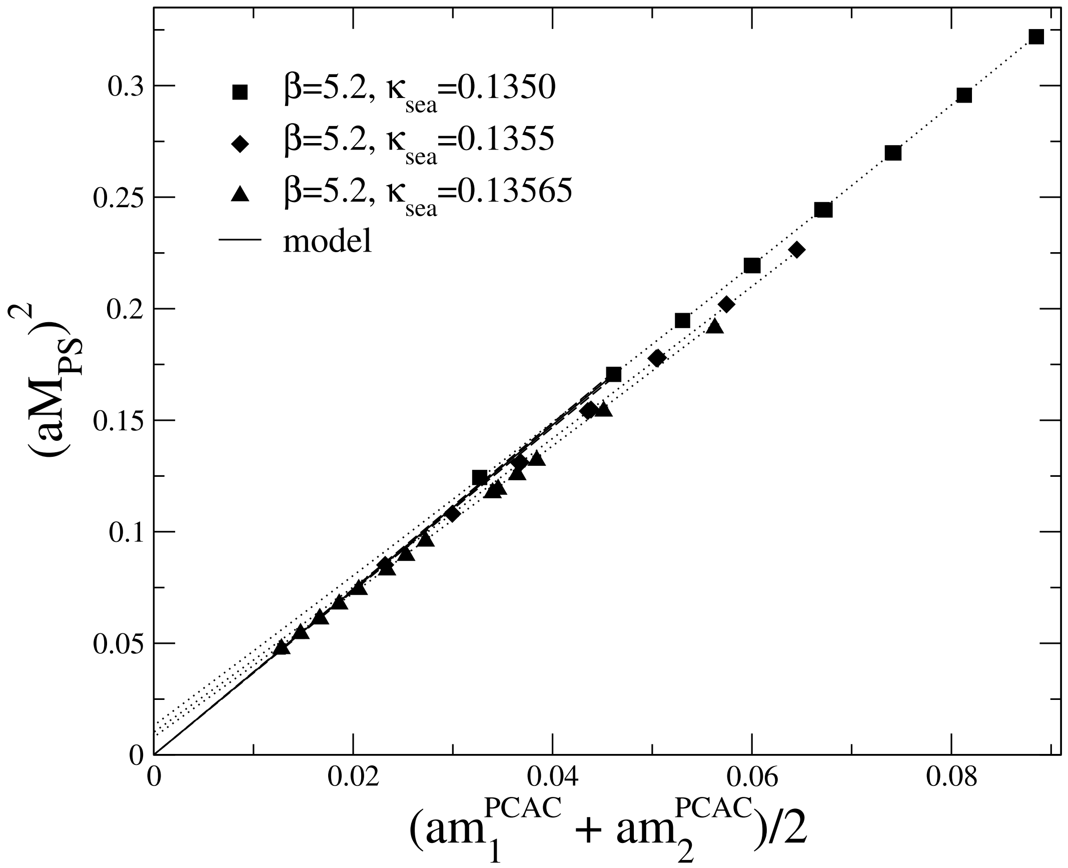

Figure B.40: Plot of fit results for a full chiral extrapolation to the datasets at $\beta = 5.2$ of $(aM_{\rm PS})^2$ versus $a_{\rm PCAC}$ using Equation (4.50). Lines give unitary and partially quenched fit results.

$B'^{\rm PS}_{\rm s}$	$B'^{\rm PS}_{\rm v}$	$C'^{\rm PS}_{\rm ss}$	$C'^{\rm PS}_{\rm vv}$	$C'^{\rm PS}_{\rm sv}$	$D'^{\rm PS}_{\rm vv}$	χ^2/dof
$0.59\ ^{+\ 9}_{-12}$	$1.553\ ^{+59}_{-41}$	$-6.5\ ^{+17}_{-14}$	$0.00\ ^{+36}_{-43}$	$2.32\ ^{+72}_{-78}$	$2.0\ ^{+11}_{-11}$	0.171

Table B.22: Fit results for a full chiral extrapolation to the datasets at $\beta = 5.2$ of $(aM_{\rm PS})^2$ versus $am_{\rm PCAC}$ using Equation (4.46).

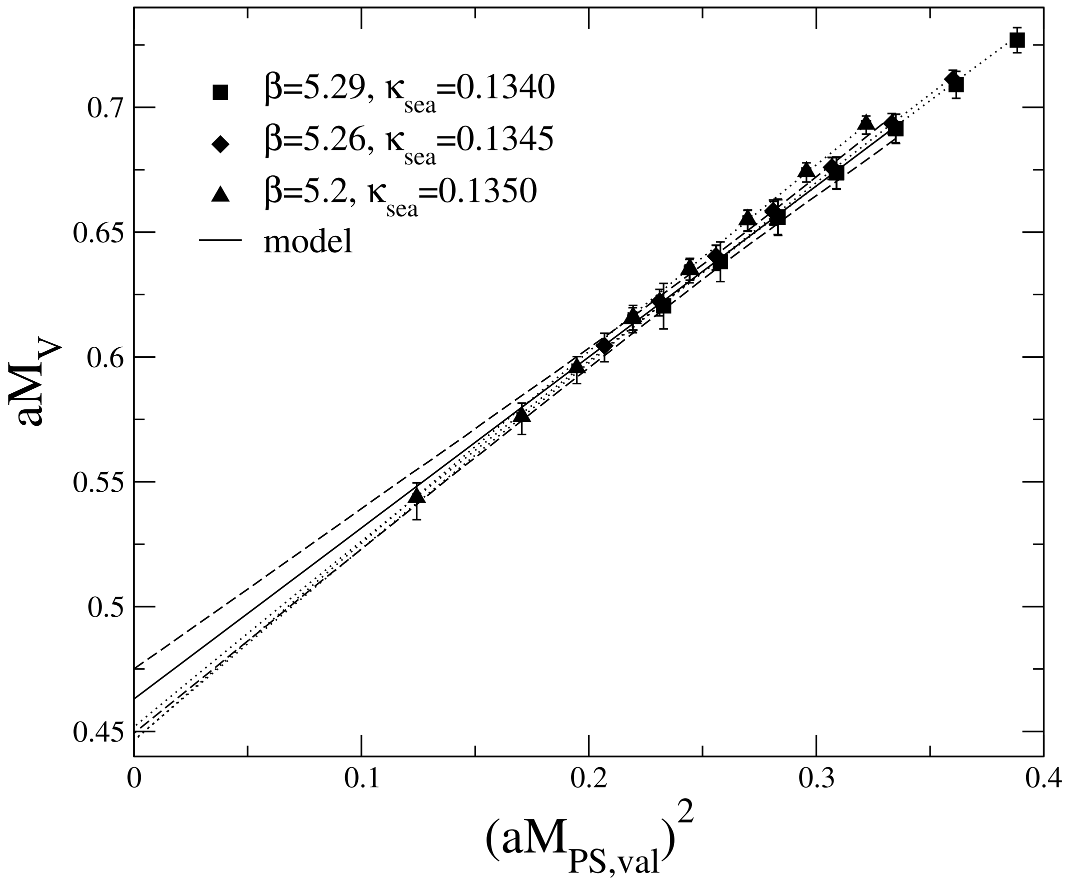

Figure B.41: Plot of fit results for a full chiral extrapolation to the matched datasets of aM_{V} versus $(aM_{\mathrm{PS}})^2$ using Equation (4.51). Solid and dashed lines give unitary fit results, dotted lines give partially quenched fit results.

A	B_{s}	B_{v}	C_{ss}	C_{vv}	C_{sv}	χ^2/dof
0.463 $^{+12}_{-14}$	-0.16 $^{+14}_{-16}$	0.85 $^{+17}_{-14}$	0.39 $^{+48}_{-46}$	-0.10 $^{+19}_{-24}$	-0.28 $^{+35}_{-35}$	0.0814

Table B.23: Fit results for a full chiral extrapolation to the matched datasets of aM_{V} versus $(aM_{\mathrm{PS}})^2$ using Equation (4.51).

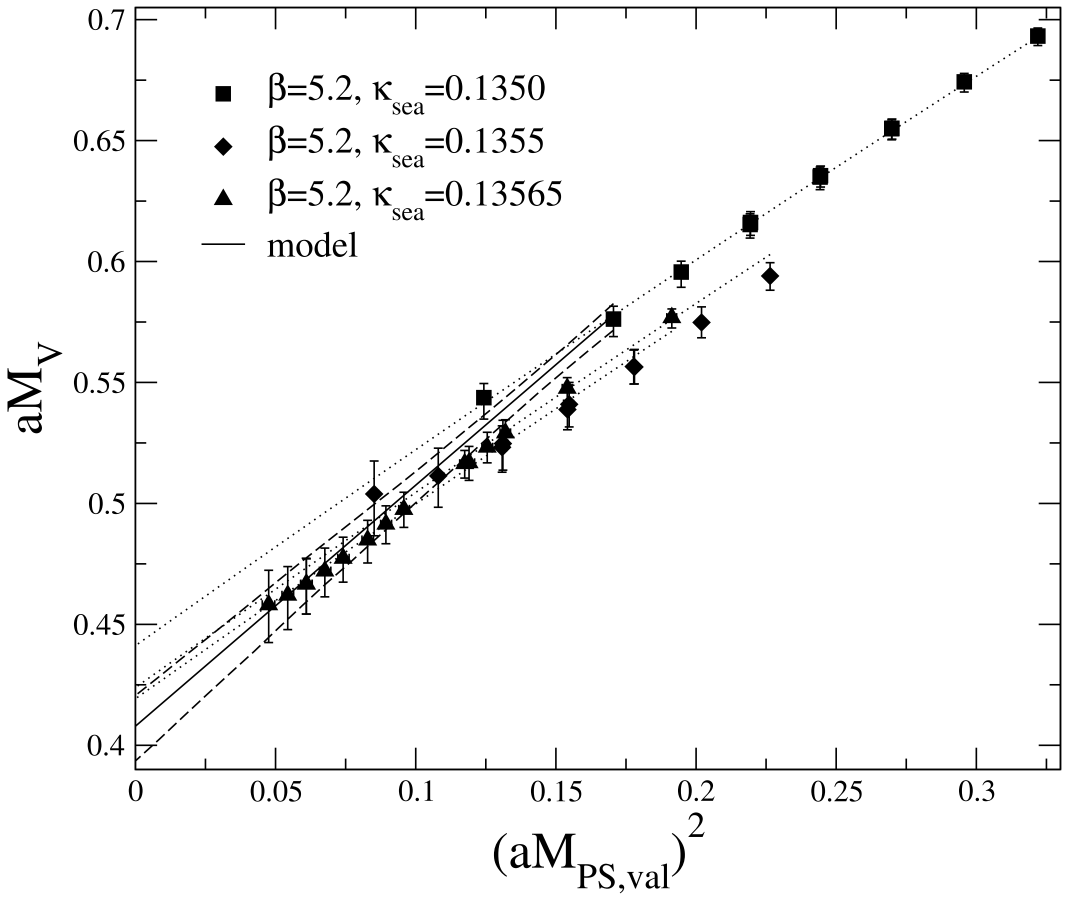

Figure B.42: Plot of fit results for a full chiral extrapolation to the datasets at $\beta = 5.2$ of aM_{V} versus $(aM_{\mathrm{PS}})^2$ using Equation (4.51). Solid and dashed lines give unitary fit results, dotted lines give partially quenched fit results.

A	B_{s}	B_{v}	C_{ss}	C_{vv}	C_{sv}	χ^2/dof
$0.408\,^{+13}_{-14}$	$0.180\,^{+73}_{-91}$	$0.82\,^{+13}_{-11}$	$0.09\,^{+63}_{-64}$	$-0.12\,^{+23}_{-28}$	$0.04\,^{+77}_{-67}$	0.504

Table B.24: Fit results for a full chiral extrapolation to the datasets at $\beta = 5.2$ of aM_{V} versus $(aM_{\mathrm{PS}})^2$ using Equation (4.51).

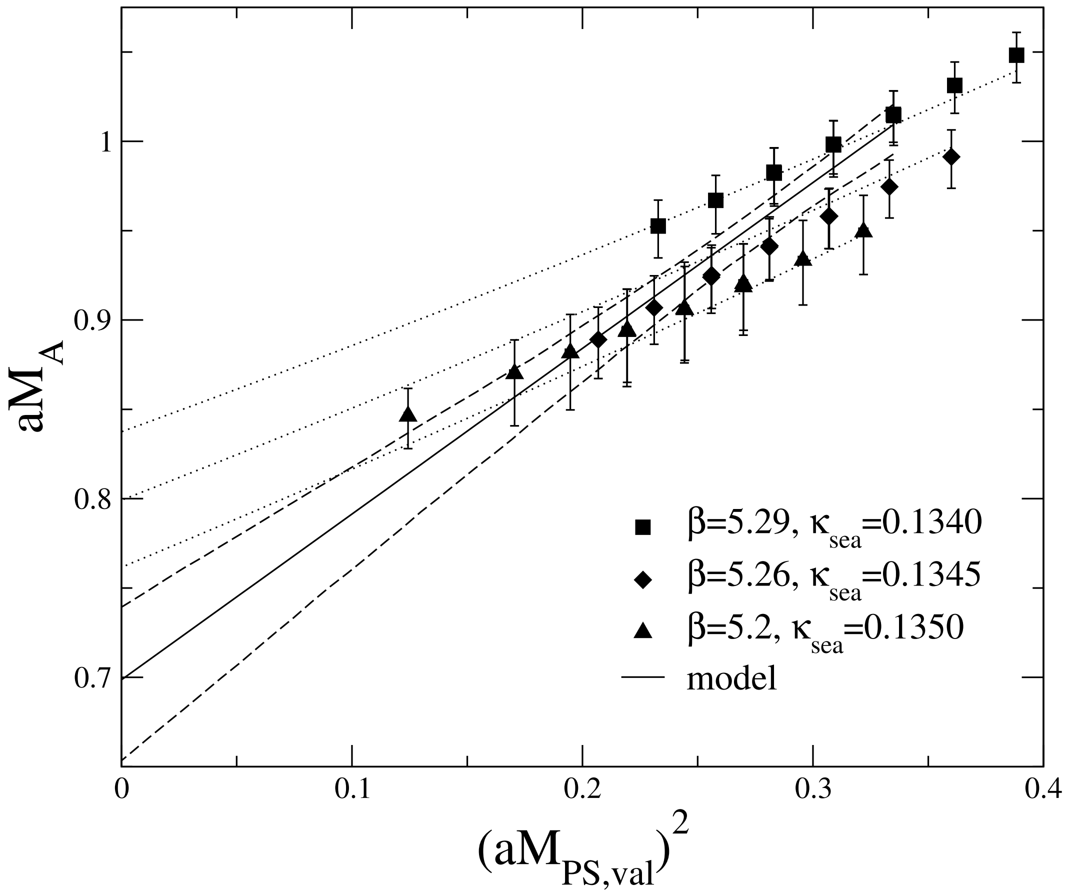

Figure B.43: Plot of fit results for a full chiral extrapolation to the matched datasets of aM_{A} versus $(aM_{\mathrm{PS}})^2$ using Equation (4.51). Solid and dashed lines give unitary fit results, dotted lines give partially quenched fit results.

A	B_{s}	B_{v}	C_{ss}	C_{vv}	C_{sv}	χ^2/dof
$0.699\ ^{+41}_{-45}$	$0.32\ ^{+57}_{-51}$	$0.61\ ^{+47}_{-58}$	$0.3\ ^{+13}_{-13}$	$0.13\ ^{+84}_{-63}$	$-0.4\ ^{+11}_{-12}$	0.243

Table B.25: Fit results for a full chiral extrapolation to the matched datasets of aM_{A} versus $(aM_{\mathrm{PS}})^2$ using Equation (4.51).

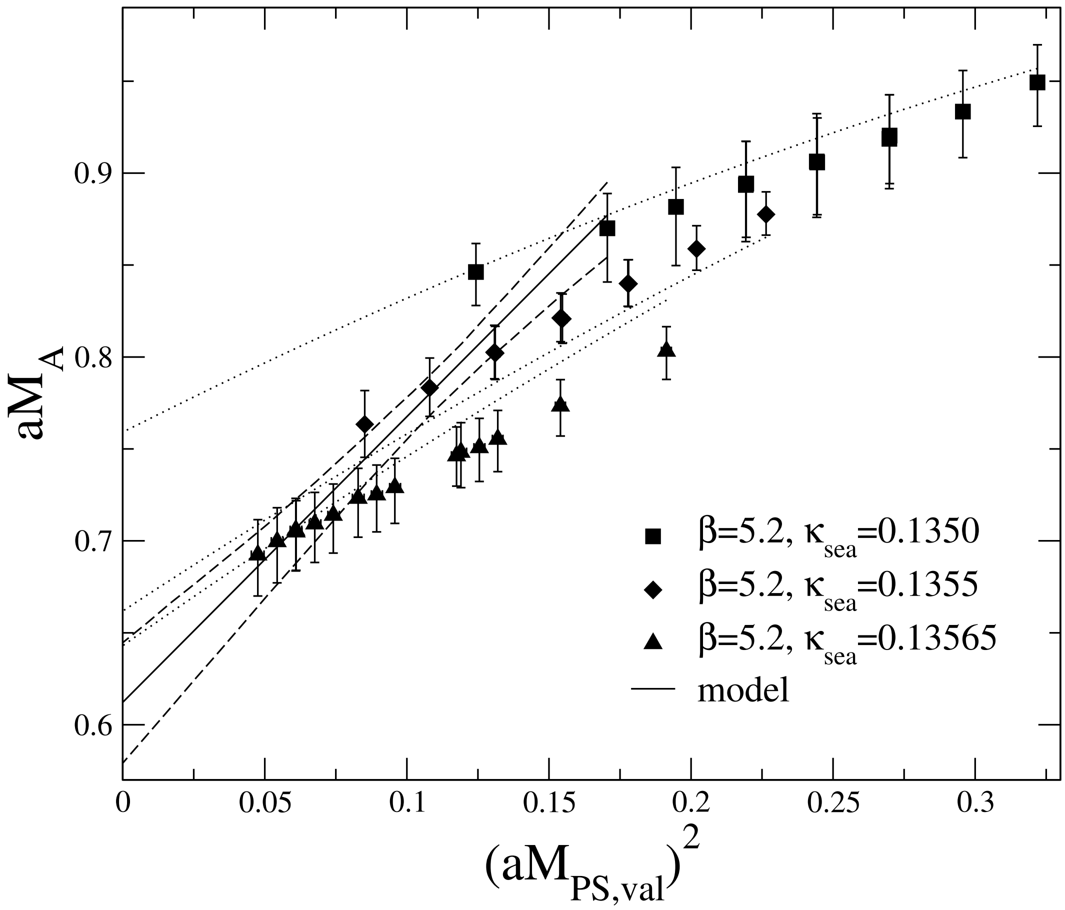

Figure B.44: Plot of fit results for a full chiral extrapolation to the datasets at $\beta = 5.2$ of aM_{A} versus $(aM_{\mathrm{PS}})^2$ using Equation (4.51). Solid and dashed lines give unitary fit results, dotted lines give partially quenched fit results.

A	B_{s}	B_{v}	C_{ss}	C_{vv}	C_{sv}	χ^2/dof
$0.612\ ^{+32}_{-33}$	$0.31\ ^{+26}_{-30}$	$1.25\ ^{+33}_{-29}$	$3.3\ ^{+19}_{-16}$	$-0.51\ ^{+86}_{-97}$	$-2.7\ ^{+20}_{-22}$	0.841

Table B.26: Fit results for a full chiral extrapolation to the datasets at $\beta = 5.2$ of aM_{A} versus $(aM_{\mathrm{PS}})^2$ using Equation (4.51).

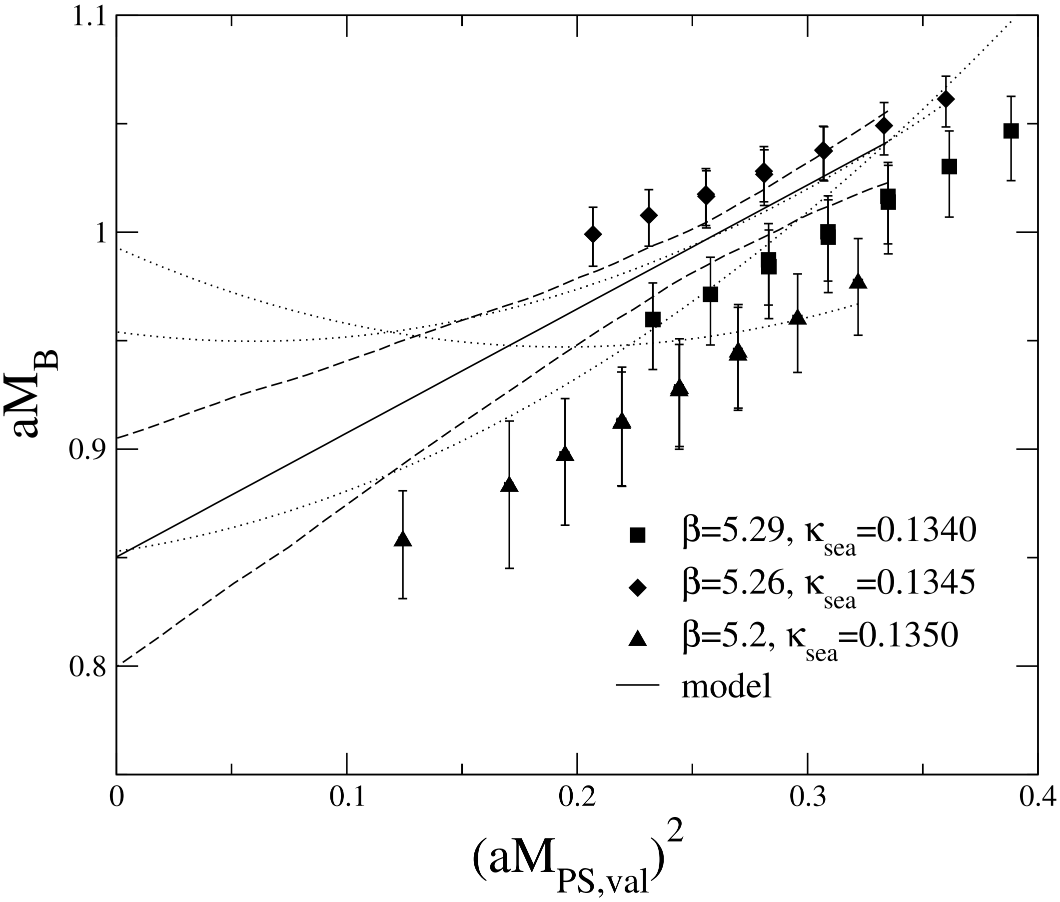

Figure B.45: Plot of fit results for a full chiral extrapolation to the matched datasets of aM_{B} versus $(aM_{\mathrm{PS}})^2$ using Equation (4.51). Solid and dashed lines give unitary fit results, dotted lines give partially quenched fit results.

A	B_{s}	B_{v}	C_{ss}	C_{vv}	C_{sv}	χ^2/dof
$0.850\ ^{+55}_{-51}$	$1.70\ ^{+64}_{-51}$	$-1.12\ ^{+56}_{-65}$	$-5.0\ ^{+16}_{-19}$	$1.21\ ^{+70}_{-56}$	$3.8\ ^{+13}_{-12}$	2.337

Table B.27: Fit results for a full chiral extrapolation to the matched datasets of aM_{B} versus $(aM_{\mathrm{PS}})^2$ using Equation (4.51).

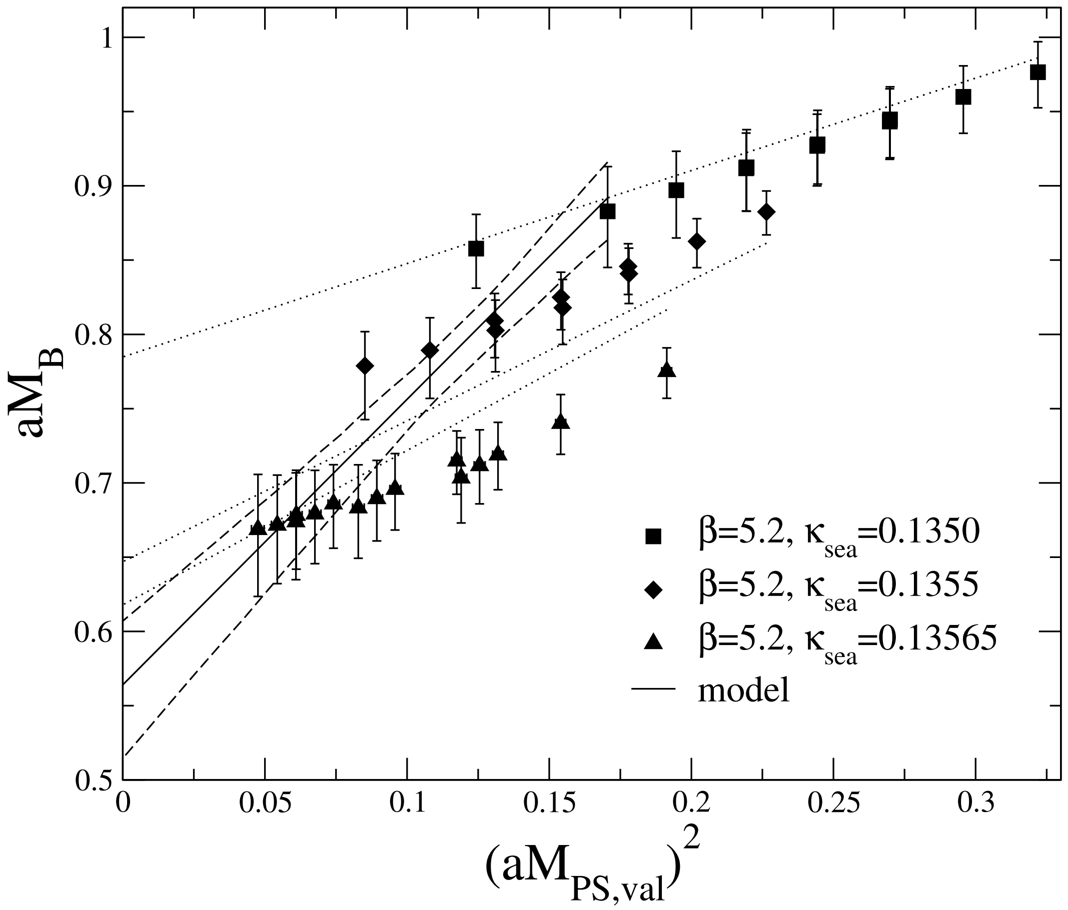

Figure B.46: Plot of fit results for a full chiral extrapolation to the datasets at $\beta = 5.2$ of aM_{B} versus $(aM_{\mathrm{PS}})^2$ using Equation (4.51). Solid and dashed lines give unitary fit results, dotted lines give partially quenched fit results.

A	B_{s}	B_{v}	C_{ss}	C_{vv}	C_{sv}	χ^2/dof
$0.564\ ^{+43}_{-50}$	$0.65\ ^{+31}_{-34}$	$1.27\ ^{+44}_{-43}$	$3.8\ ^{+22}_{-20}$	$0.0\ ^{+11}_{-11}$	$-3.7\ ^{+22}_{-23}$	1.422

Table B.28: Fit results for a full chiral extrapolation to the datasets at $\beta = 5.2$ of aM_{B} versus $(aM_{\mathrm{PS}})^2$ using Equation (4.51).

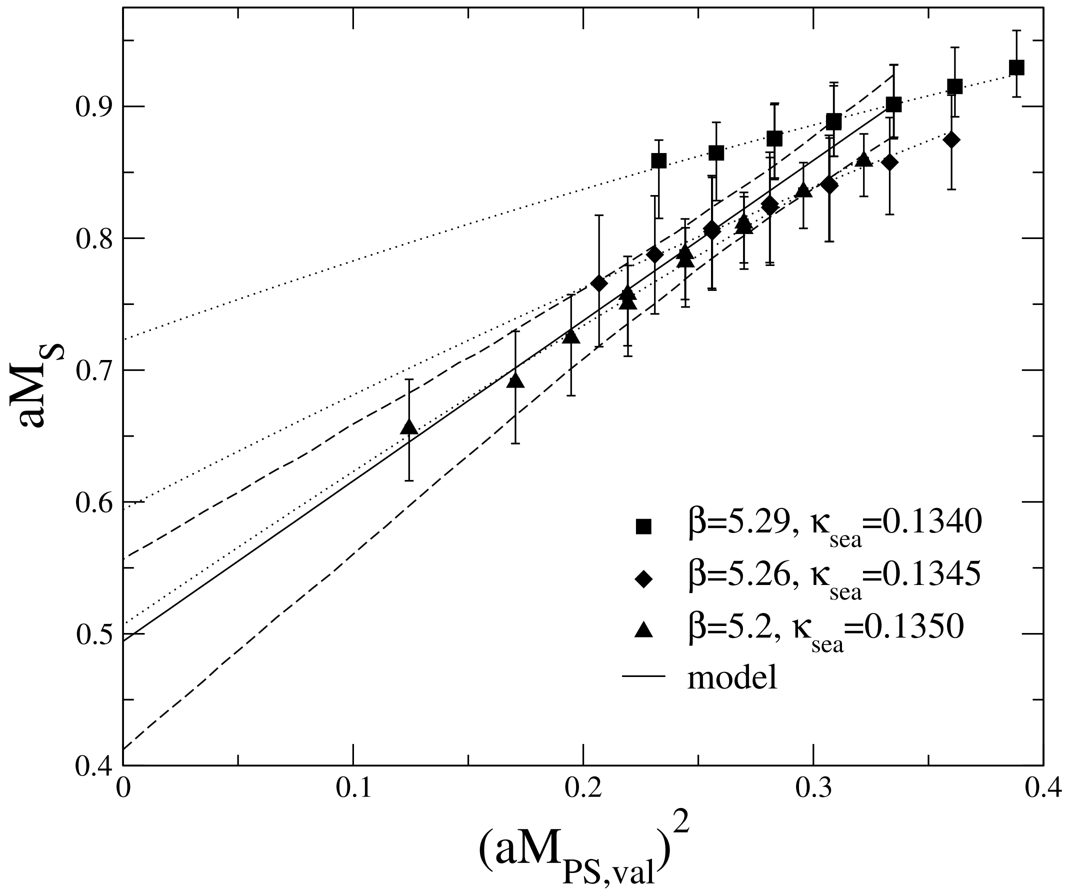

Figure B.47: Plot of fit results for a full chiral extrapolation to the matched datasets of aM_{S} versus $(aM_{\mathrm{PS}})^2$ using Equation (4.51). Solid and dashed lines give unitary fit results, dotted lines give partially quenched fit results.

A	B_{s}	B_{v}	C_{ss}	C_{vv}	C_{sv}	χ^2/dof
$0.494\ ^{+62}_{-82}$	$-0.55\ ^{+81}_{-78}$	$1.78\ ^{+88}_{-82}$	$3.7\ ^{+16}_{-23}$	$-0.2\ ^{+13}_{-17}$	$-3.4\ ^{+21}_{-12}$	0.0147

Table B.29: Fit results for a full chiral extrapolation to the matched datasets of aM_{S} versus $(aM_{\mathrm{PS}})^2$ using Equation (4.51).

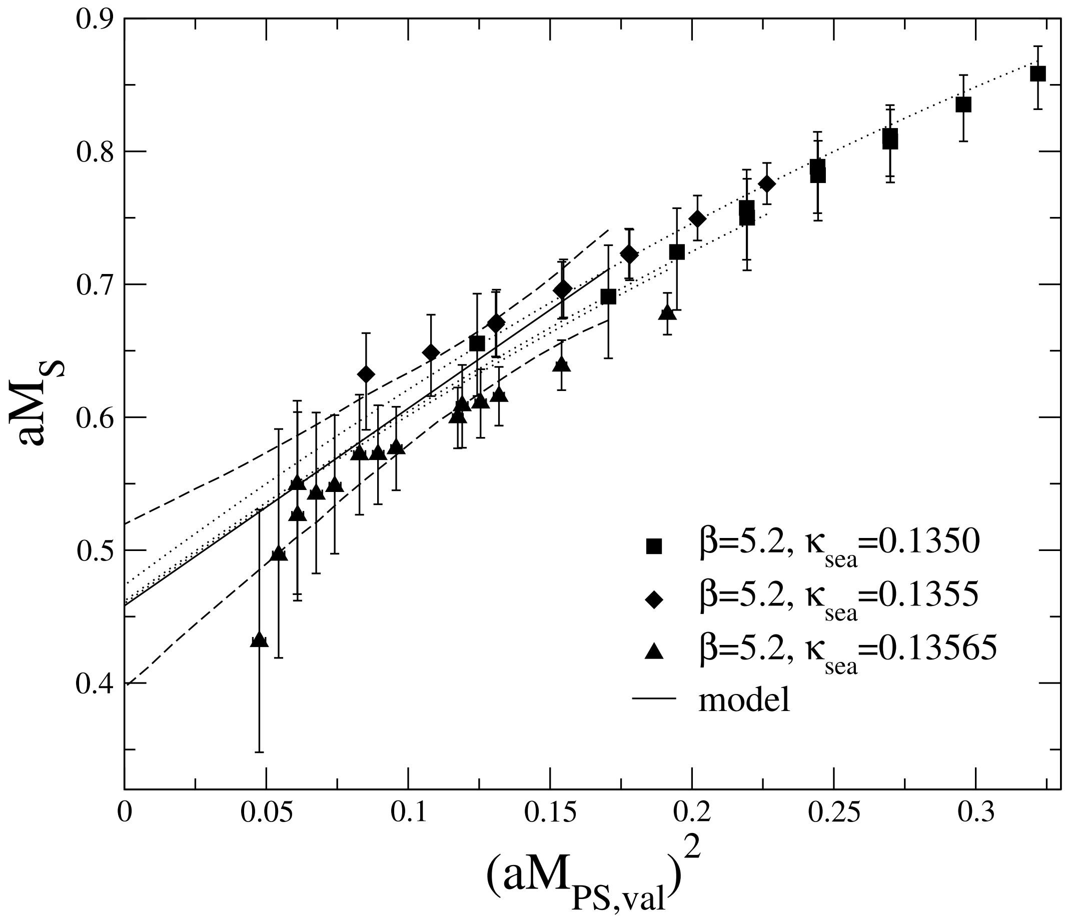

Figure B.48: Plot of fit results for a full chiral extrapolation to the datasets at $\beta = 5.2$ of $aM_{\rm S}$ versus $(aM_{\rm PS})^2$ using Equation (4.51). Solid and dashed lines give unitary fit results, dotted lines give partially quenched fit results.

A	$B_{\rm s}$	$B_{\rm v}$	$C_{\rm ss}$	$C_{\rm vv}$	$C_{\rm sv}$	χ^2/dof
$0.458\ ^{+61}_{-62}$	$0.00\ ^{+40}_{-45}$	$1.49\ ^{+63}_{-58}$	$0.6\ ^{+25}_{-24}$	$-1.1\ ^{+17}_{-16}$	$0.5\ ^{+29}_{-30}$	0.927

Table B.30: Fit results for a full chiral extrapolation to the datasets at $\beta = 5.2$ of $aM_{\rm S}$ versus $(aM_{\rm PS})^2$ using Equation (4.51).

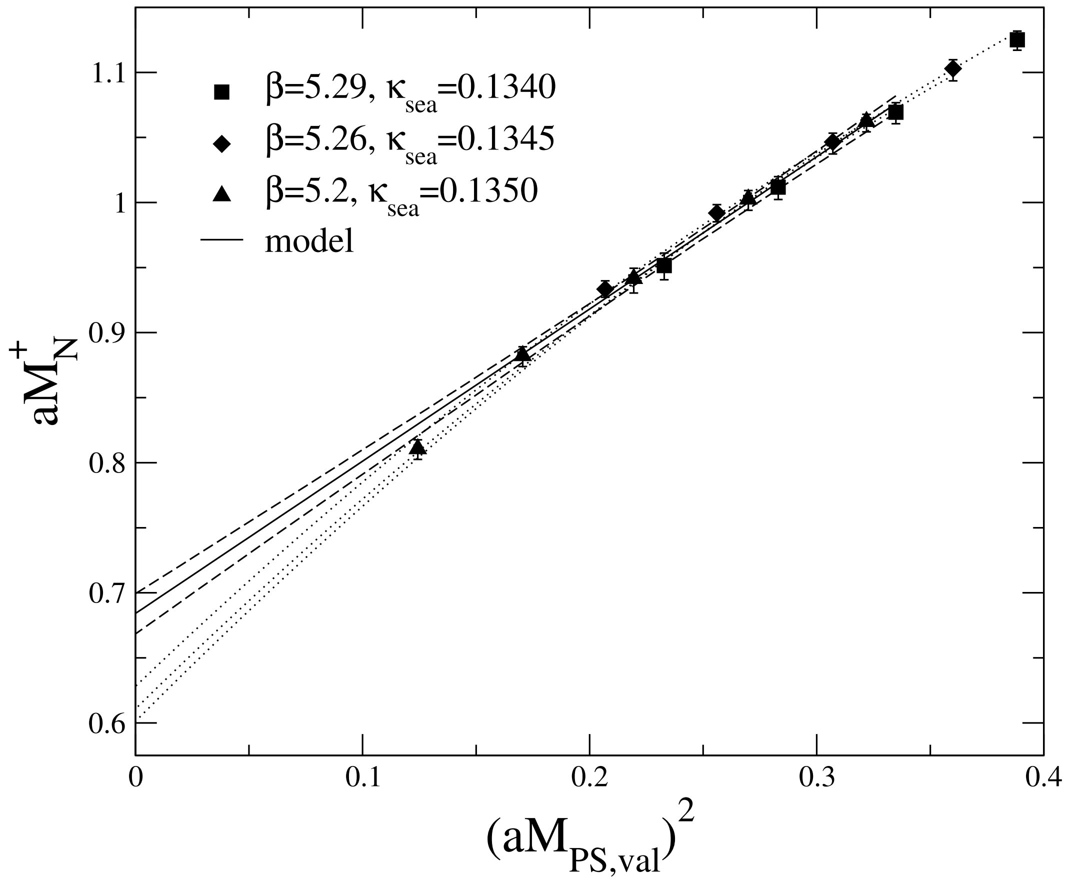

Figure B.49: Plot of fit results for a full chiral extrapolation to the matched datasets of aM_{N}^{+} versus $(aM_{\mathrm{PS}})^2$ using Equation (4.51). Solid and dashed lines give unitary fit results, dotted lines give partially quenched fit results.

A	B_{s}	B_{v}	C_{ss}	C_{vv}	C_{sv}	χ^2/dof
$0.684\,^{+15}_{-16}$	$-0.41\,^{+19}_{-16}$	$1.58\,^{+15}_{-18}$	$0.49\,^{+43}_{-48}$	$-0.99\,^{+36}_{-30}$	$0.51\,^{+45}_{-51}$	1.142

Table B.31: Fit results for a full chiral extrapolation to the matched datasets of aM_{N}^{+} versus $(aM_{\mathrm{PS}})^2$ using Equation (4.51).

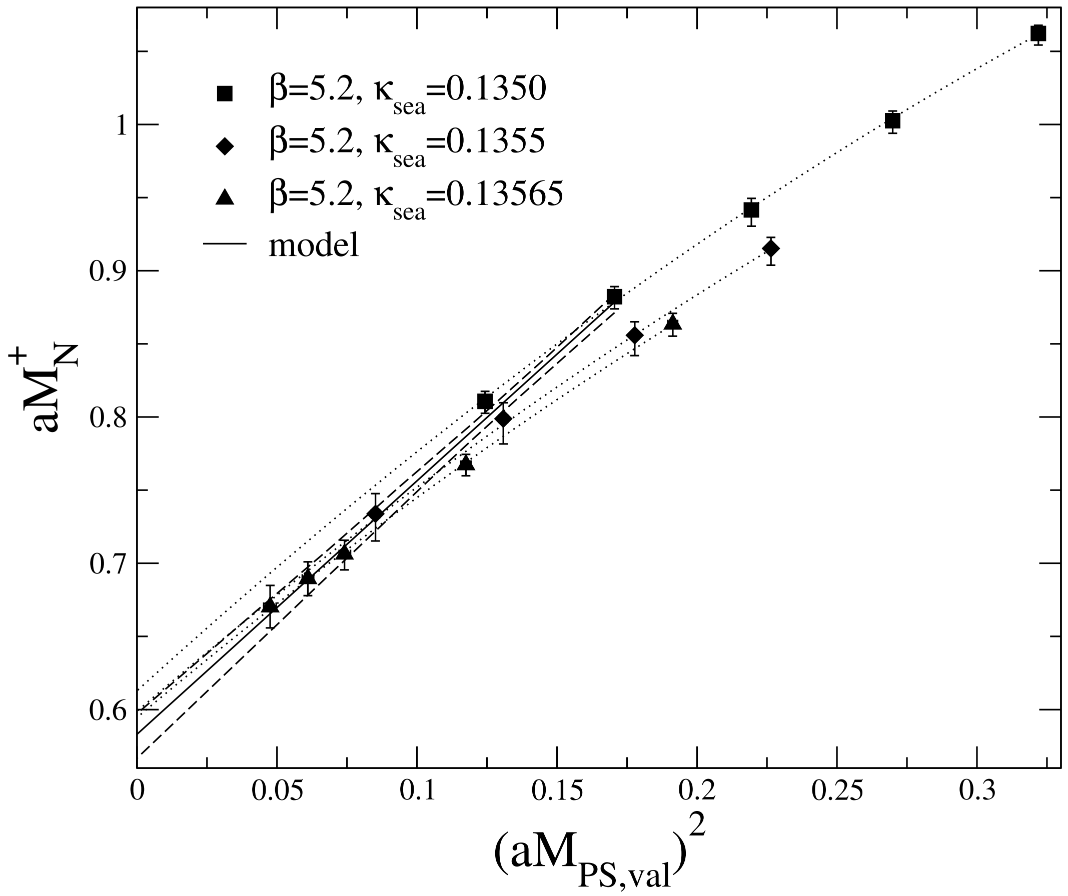

Figure B.50: Plot of fit results for a full chiral extrapolation to the datasets at $\beta = 5.2$ of aM_{N}^{+} versus $(aM_{\mathrm{PS}})^2$ using Equation (4.51). Solid and dashed lines give unitary fit results, dotted lines give partially quenched fit results.

A	B_{s}	B_{v}	C_{ss}	C_{vv}	C_{sv}	χ^2/dof
$0.583\,^{+14}_{-16}$	$0.19\,^{+11}_{-10}$	$1.54\,^{+15}_{-17}$	$-0.12\,^{+95}_{-89}$	$-1.08\,^{+54}_{-40}$	$1.2\,^{+11}_{-12}$	0.0673

Table B.32: Fit results for a full chiral extrapolation to the datasets at $\beta = 5.2$ of aM_{N}^{+} versus $(aM_{\mathrm{PS}})^2$ using Equation (4.51).

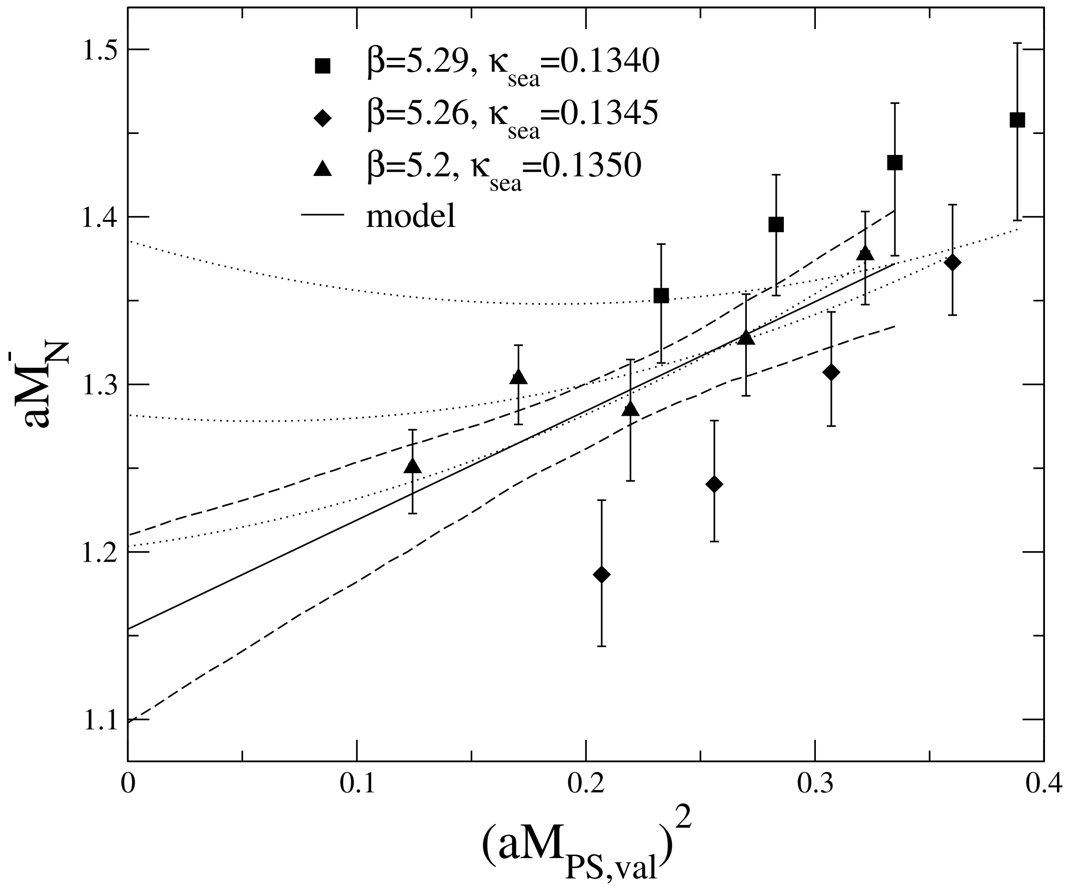

Figure B.51: Plot of fit results for a full chiral extrapolation to the matched datasets of aM_{N}^{-} versus $(aM_{\mathrm{PS}})^2$ using Equation (4.51). Solid and dashed lines give unitary fit results, dotted lines give partially quenched fit results.

A	B_{s}	B_{v}	C_{ss}	C_{vv}	C_{sv}	χ^2/dof
$1.154\ ^{+56}_{-56}$	$-0.12\ ^{+90}_{-86}$	$0.78\ ^{+77}_{-84}$	$2.4\ ^{+24}_{-25}$	$1.1\ ^{+14}_{-13}$	$-3.5\ ^{+23}_{-23}$	2.560

Table B.33: Fit results for a full chiral extrapolation to the matched datasets of aM_{N}^{-} versus $(aM_{\mathrm{PS}})^2$ using Equation (4.51).

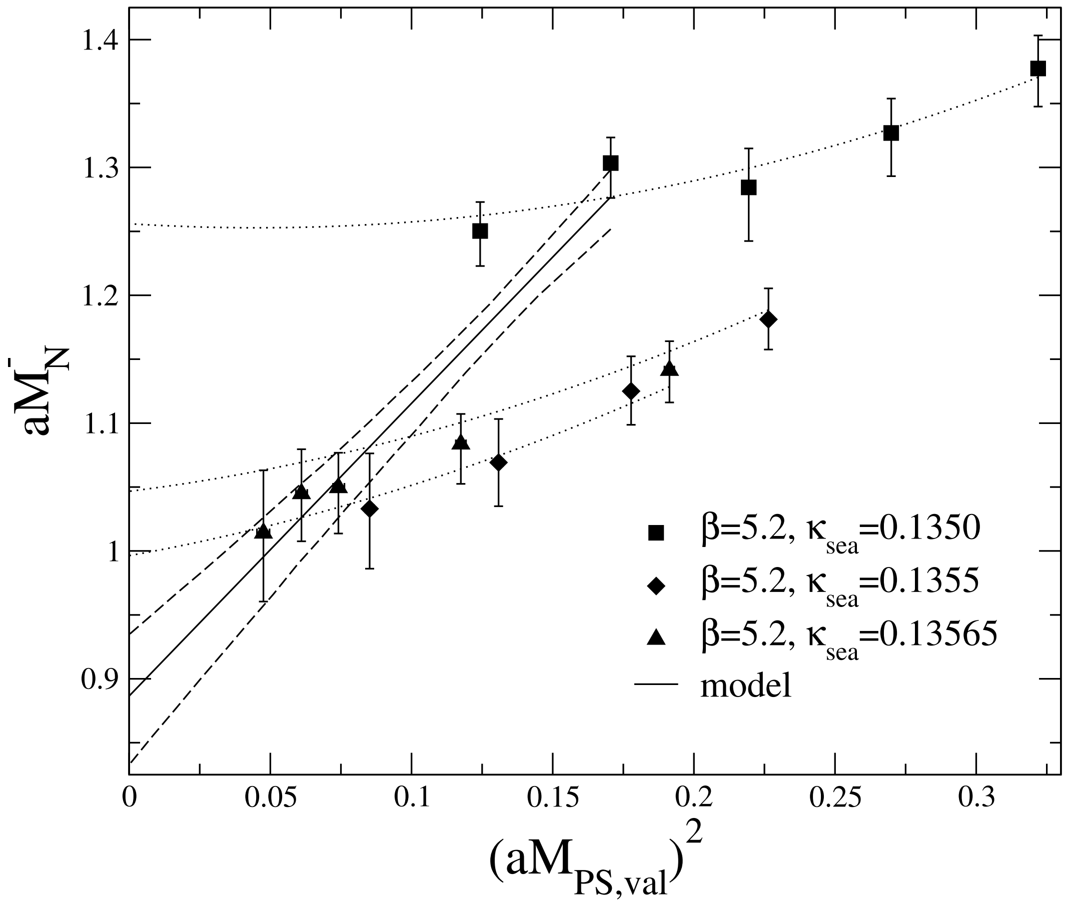

Figure B.52: Plot of fit results for a full chiral extrapolation to the datasets at $\beta = 5.2$ of $aM_{\rm N}^-$ versus $(aM_{\rm PS})^2$ using Equation (4.51). Solid and dashed lines give unitary fit results, dotted lines give partially quenched fit results.

A	$B_{\rm s}$	$B_{\rm v}$	$C_{\rm ss}$	$C_{\rm vv}$	$C_{\rm sv}$	χ^2/dof
$0.887\,^{+48}_{-54}$	$1.59\,^{+38}_{-40}$	$0.69\,^{+52}_{-50}$	$3.4\,^{+30}_{-27}$	$1.5\,^{+19}_{-16}$	$-4.9\,^{+40}_{-40}$	0.692

Table B.34: Fit results for a full chiral extrapolation to the datasets at $\beta = 5.2$ of $aM_{\rm N}^-$ versus $(aM_{\rm PS})^2$ using Equation (4.51).

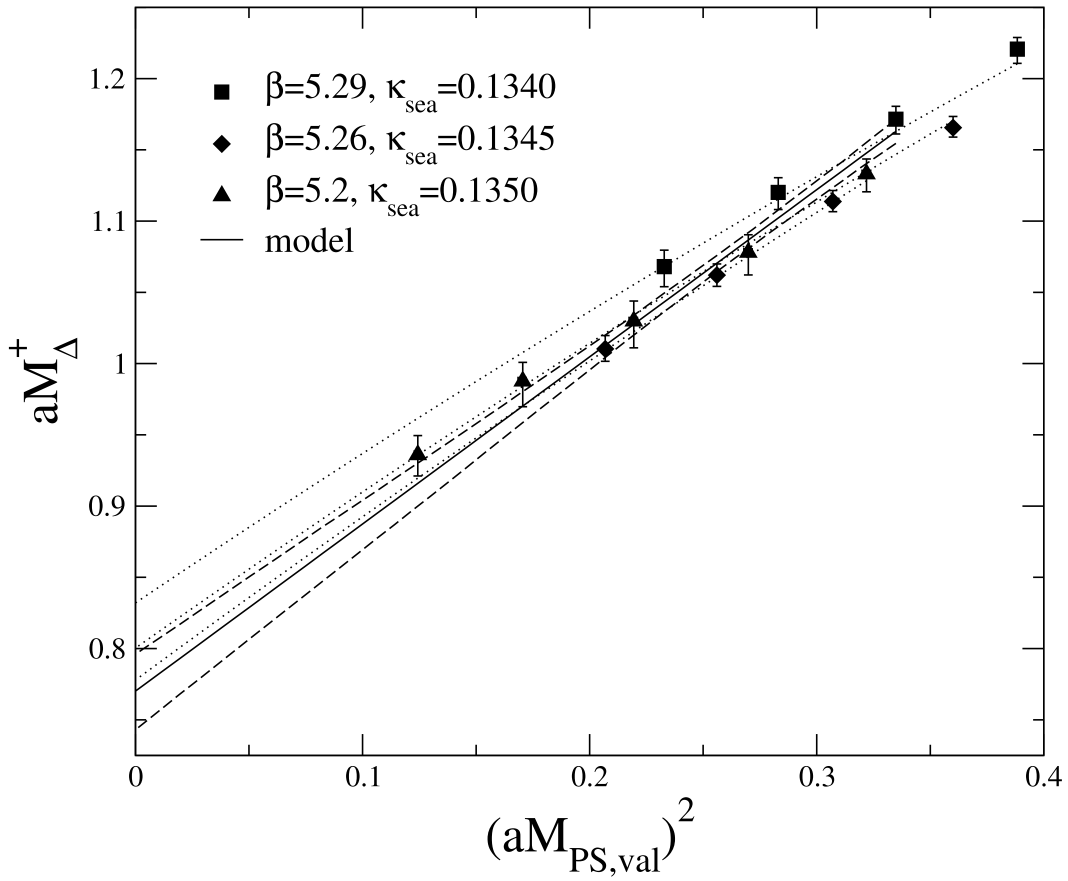

Figure B.53: Plot of fit results for a full chiral extrapolation to the matched datasets of aM_{Δ}^{+} versus $(aM_{\rm PS})^2$ using Equation (4.51). Solid and dashed lines give unitary fit results, dotted lines give partially quenched fit results.

A	$B_{\rm s}$	$B_{\rm v}$	$C_{\rm ss}$	$C_{\rm vv}$	$C_{\rm sv}$	χ^2/dof
0.770 $^{+26}_{-27}$	-0.10 $^{+26}_{-24}$	1.27 $^{+23}_{-25}$	0.85 $^{+66}_{-69}$	-0.26 $^{+43}_{-42}$	-0.59 $^{+71}_{-63}$	1.142

Table B.35: Fit results for a full chiral extrapolation to the matched datasets of aM_{Δ}^{+} versus $(aM_{\rm PS})^2$ using Equation (4.51).

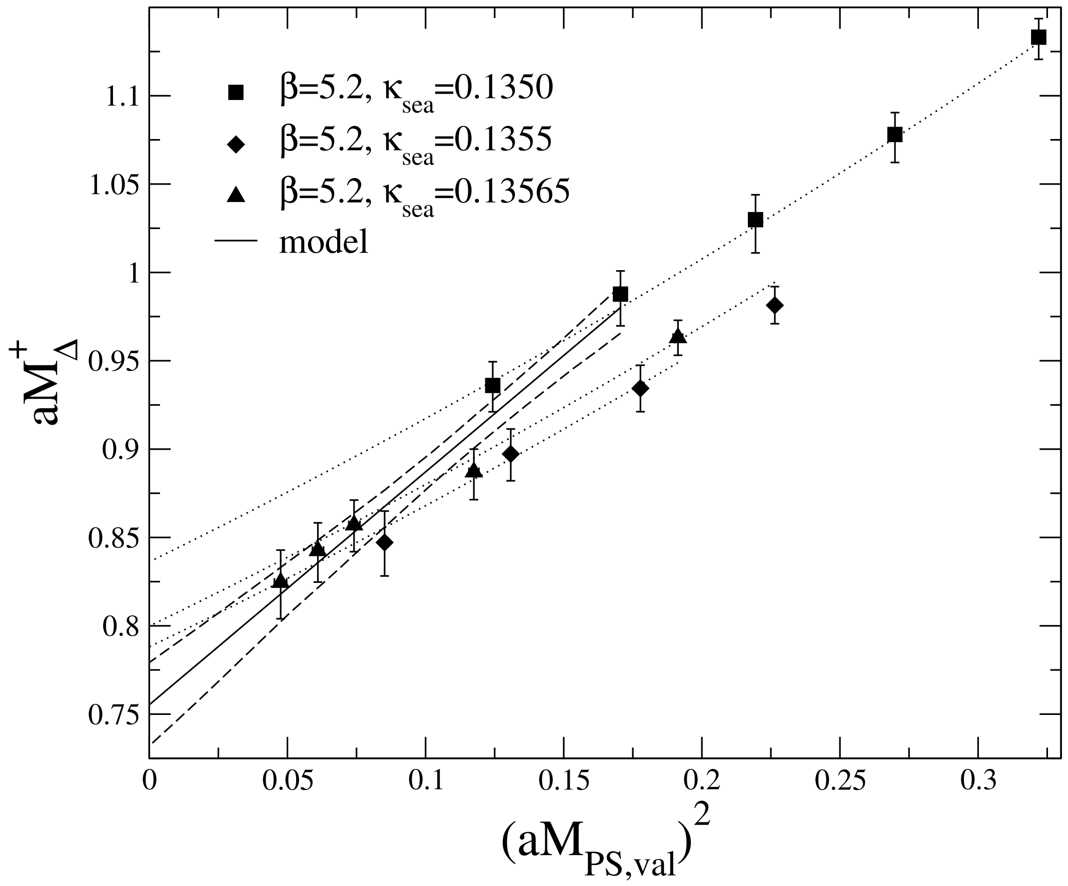

Figure B.54: Plot of fit results for a full chiral extrapolation to the datasets at $\beta = 5.2$ of aM_{Δ}^{+} versus $(aM_{\rm PS})^2$ using Equation (4.51). Solid and dashed lines give unitary fit results, dotted lines give partially quenched fit results.

A	$B_{\rm s}$	$B_{\rm v}$	$C_{\rm ss}$	$C_{\rm vv}$	$C_{\rm sv}$	χ^2/dof
$0.755\ ^{+24}_{-23}$	$0.57\ ^{+17}_{-18}$	$0.75\ ^{+22}_{-24}$	$-0.6\ ^{+12}_{-11}$	$0.46\ ^{+93}_{-79}$	$0.1\ ^{+16}_{-17}$	0.842

Table B.36: Fit results for a full chiral extrapolation to the datasets at $\beta = 5.2$ of aM_{Δ}^{+} versus $(aM_{\rm PS})^2$ using Equation (4.51).

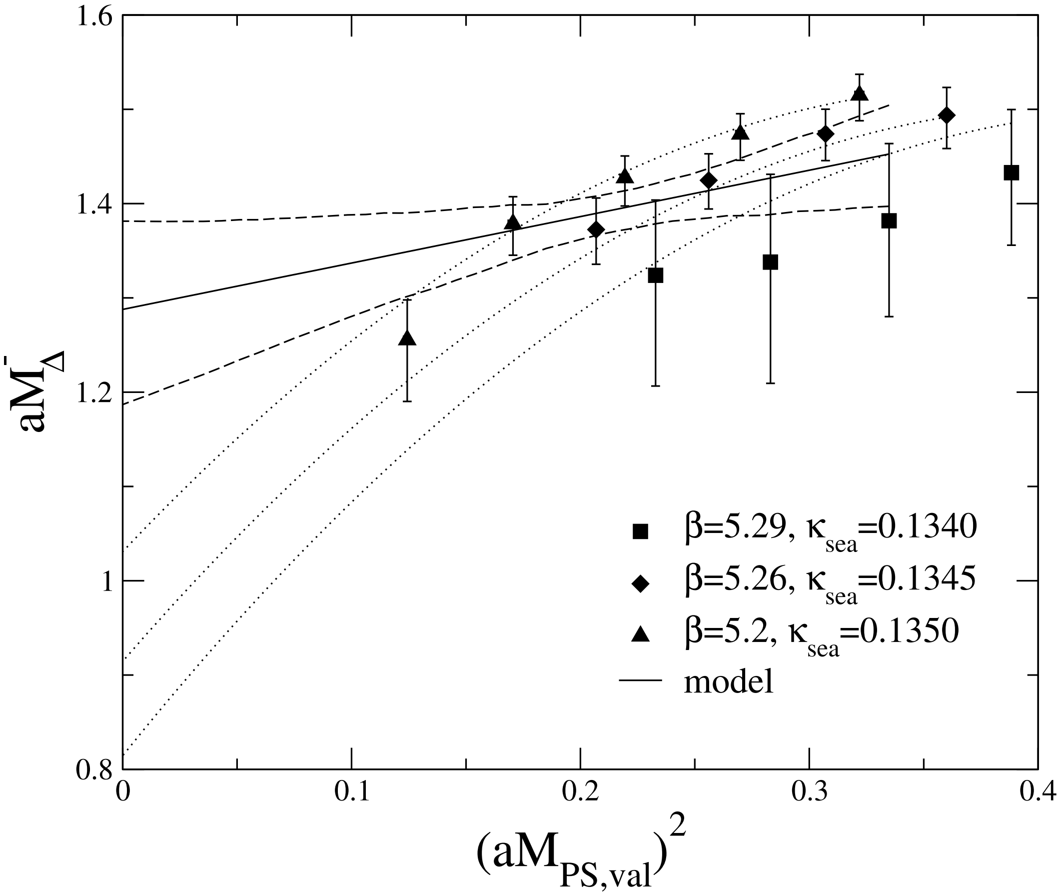

Figure B.55: Plot of fit results for a full chiral extrapolation to the matched datasets of aM_Δ^- versus $(aM_{\mathrm{PS}})^2$ using Equation (4.51). Solid and dashed lines give unitary fit results, dotted lines give partially quenched fit results.

A	B_{s}	B_{v}	C_{ss}	C_{vv}	C_{sv}	χ^2/dof
$1.29\,^{+\,9}_{-10}$	$-1.60\,^{+75}_{-90}$	$2.09\,^{+93}_{-85}$	$0.6\,^{+24}_{-29}$	$-3.3\,^{+12}_{-17}$	$2.8\,^{+31}_{-20}$	0.381

Table B.37: Fit results for a full chiral extrapolation to the matched datasets of aM_Δ^- versus $(aM_{\mathrm{PS}})^2$ using Equation (4.51).

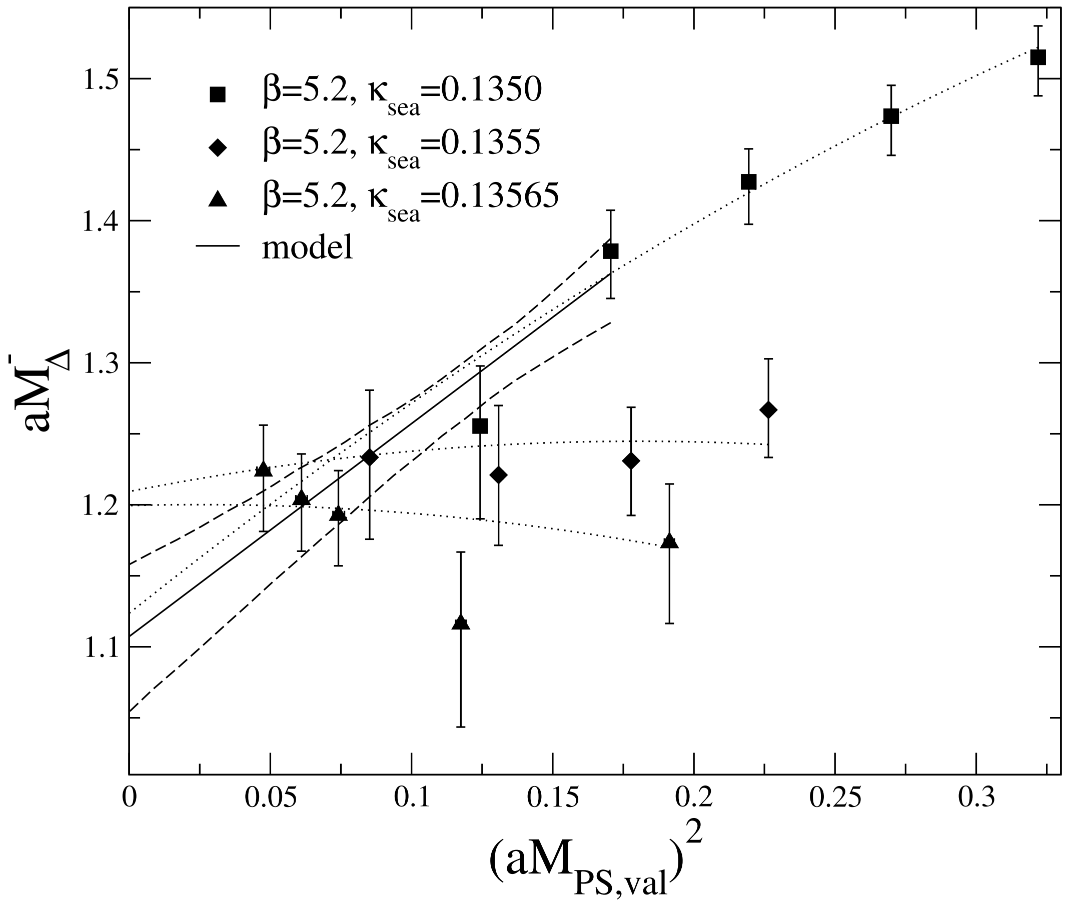

Figure B.56: Plot of fit results for a full chiral extrapolation to the datasets at $\beta = 5.2$ of aM_{Δ}^{-} versus $(aM_{\mathrm{PS}})^2$ using Equation (4.51). Solid and dashed lines give unitary fit results, dotted lines give partially quenched fit results.

A	B_{s}	B_{v}	C_{ss}	C_{vv}	C_{sv}	χ^2/dof
1.107 $^{+51}_{-53}$	2.30 $^{+56}_{-65}$	-0.80 $^{+68}_{-63}$	-12.9 $^{+35}_{-43}$	-1.1 $^{+16}_{-21}$	14.0 $^{+56}_{-42}$	0.443

Table B.38: Fit results for a full chiral extrapolation to the datasets at $\beta = 5.2$ of aM_{Δ}^{-} versus $(aM_{\mathrm{PS}})^2$ using Equation (4.51).

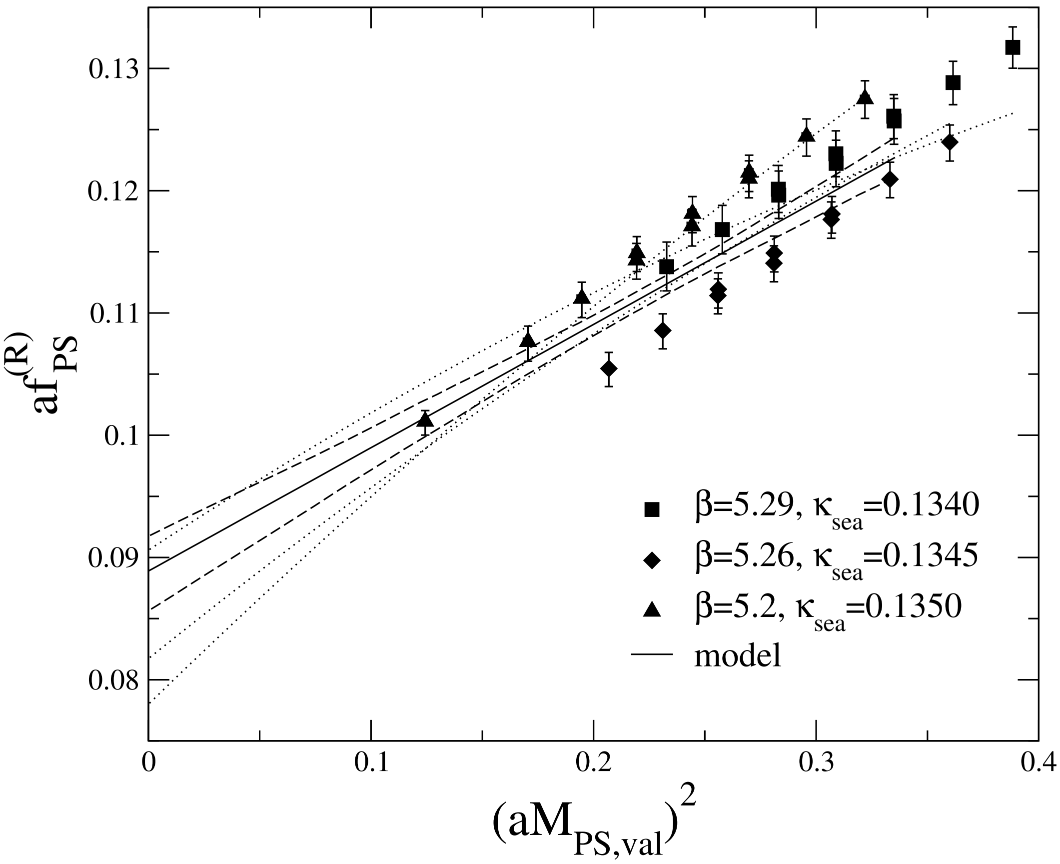

Figure B.57: Plot of fit results for a full chiral extrapolation to the matched datasets of $af_{\rm PS}^{(\rm R)}$ versus $(aM_{\rm PS})^2$ using Equation (4.51). Solid and dashed lines give unitary fit results, dotted lines give partially quenched fit results.

A	$B_{\rm s}$	$B_{\rm v}$	$C_{\rm ss}$	$C_{\rm vv}$	$C_{\rm sv}$	χ^2/dof
0.0889 $^{+28}_{-32}$	-0.135 $^{+37}_{-35}$	0.236 $^{+31}_{-31}$	0.42 $^{+11}_{-11}$	-0.070 $^{+41}_{-35}$	-0.35 $^{+10}_{-10}$	= 2.779

Table B.39: Fit results for a full chiral extrapolation to the matched datasets of $af_{\rm PS}^{(\rm R)}$ versus $(aM_{\rm PS})^2$ using Equation (4.51).

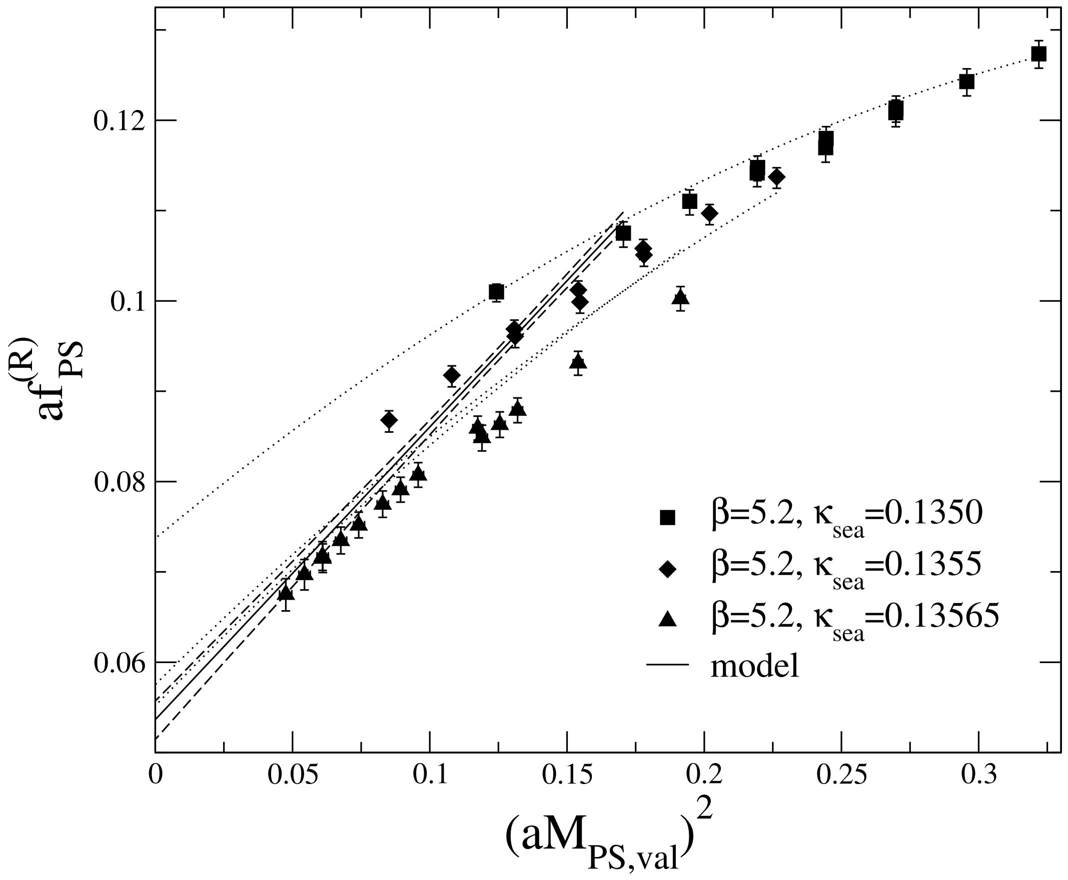

Figure B.58: Plot of fit results for a full chiral extrapolation to the datasets at $\beta = 5.2$ of $af^{(\mathrm{R})}_{\mathrm{PS}}$ versus $(aM_{\mathrm{PS}})^2$ using Equation (4.51). Solid and dashed lines give unitary fit results, dotted lines give partially quenched fit results.

A	B_{s}	B_{v}	C_{ss}	C_{vv}	C_{sv}	χ^2/dof
0.0536 $^{+21}_{-22}$	-0.026 $^{+17}_{-17}$	0.350 $^{+21}_{-20}$	0.84 $^{+11}_{-11}$	-0.268 $^{+50}_{-46}$	-0.57 $^{+13}_{-14}$	5.889

Table B.40: Fit results for a full chiral extrapolation to the datasets at $\beta = 5.2$ of $af^{(\mathrm{R})}_{\mathrm{PS}}$ versus $(aM_{\mathrm{PS}})^2$ using Equation (4.51).

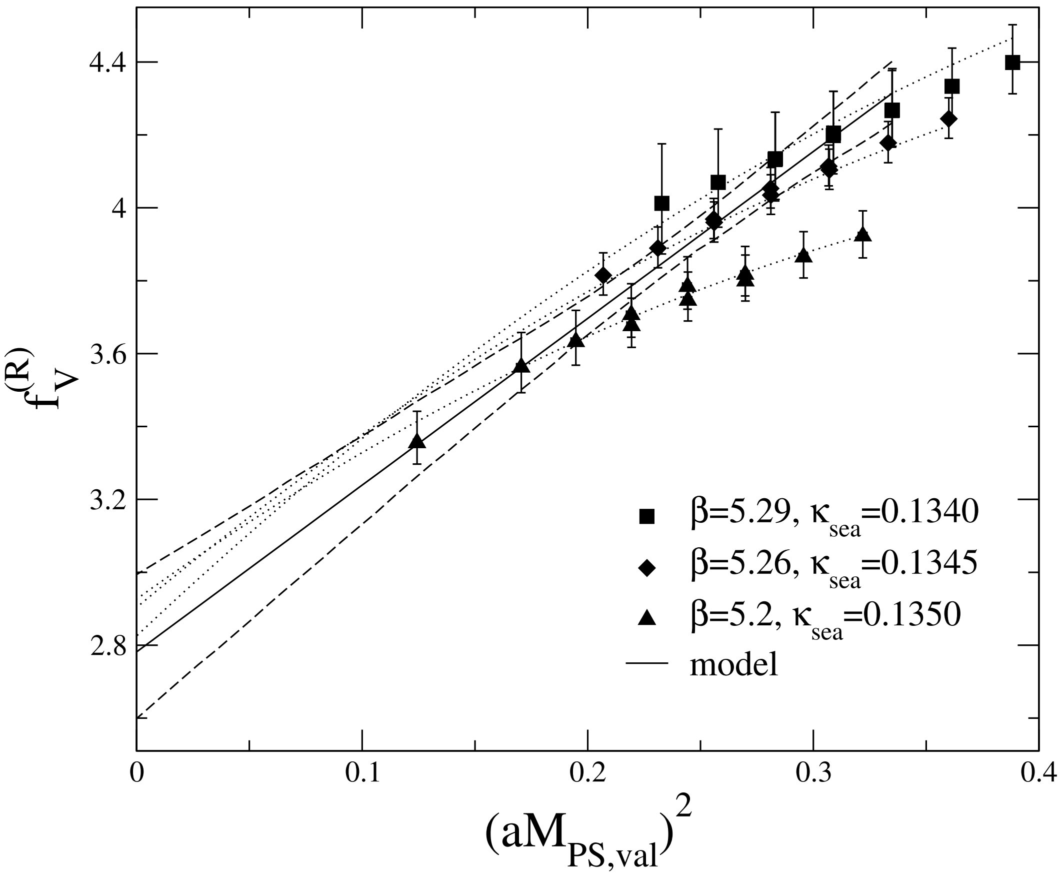

Figure B.59: Plot of fit results for a full chiral extrapolation to the matched datasets of $f_V^{(R)}$ versus $(aM_{PS})^2$ using Equation (4.51). Solid and dashed lines give unitary fit results, dotted lines give partially quenched fit results.

A	B_s	B_v	C_{ss}	C_{vv}	C_{sv}	χ^2/dof
2.78^{+21}_{-18}	1.6^{+22}_{-22}	3.0^{+23}_{-21}	-4.4^{+86}_{-73}	-4.1^{+25}_{-23}	8.5^{+67}_{-79}	0.134

Table B.41: Fit results for a full chiral extrapolation to the matched datasets of $f_V^{(R)}$ versus $(aM_{PS})^2$ using Equation (4.51).

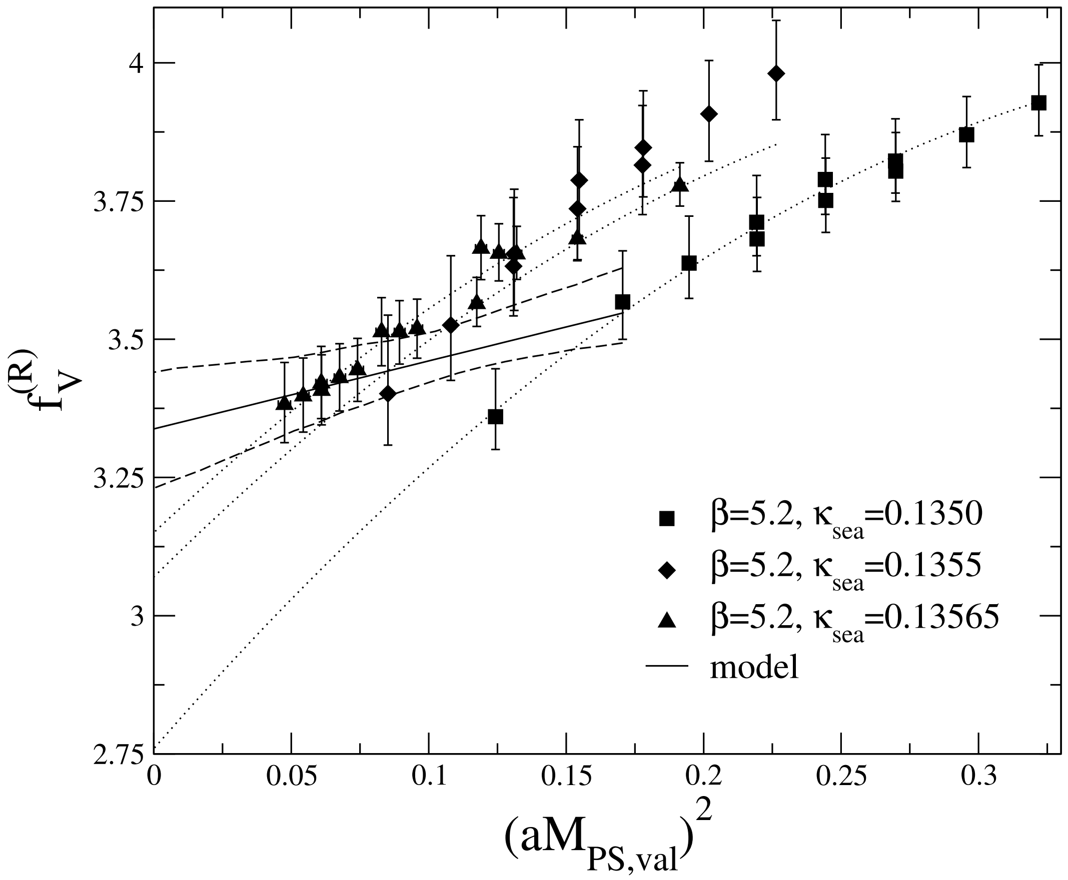

Figure B.60: Plot of fit results for a full chiral extrapolation to the datasets at $\beta = 5.2$ of $f_{\mathrm{V}}^{(\mathrm{R})}$ versus $(aM_{\mathrm{PS}})^2$ using Equation (4.51). Solid and dashed lines give unitary fit results, dotted lines give partially quenched fit results.

A	B_{s}	B_{v}	C_{ss}	C_{vv}	C_{sv}	χ^2/dof
$3.34\,^{+10}_{-11}$	$-2.90\,^{+89}_{-71}$	$4.13\,^{+88}_{-84}$	$-2.9\,^{+59}_{-52}$	$-6.5\,^{+28}_{-25}$	$9.4\,^{+59}_{-72}$	0.380

Table B.42: Fit results for a full chiral extrapolation to the datasets at $\beta = 5.2$ of $f_{\mathrm{V}}^{(\mathrm{R})}$ versus $(aM_{\mathrm{PS}})^2$ using Equation (4.51).

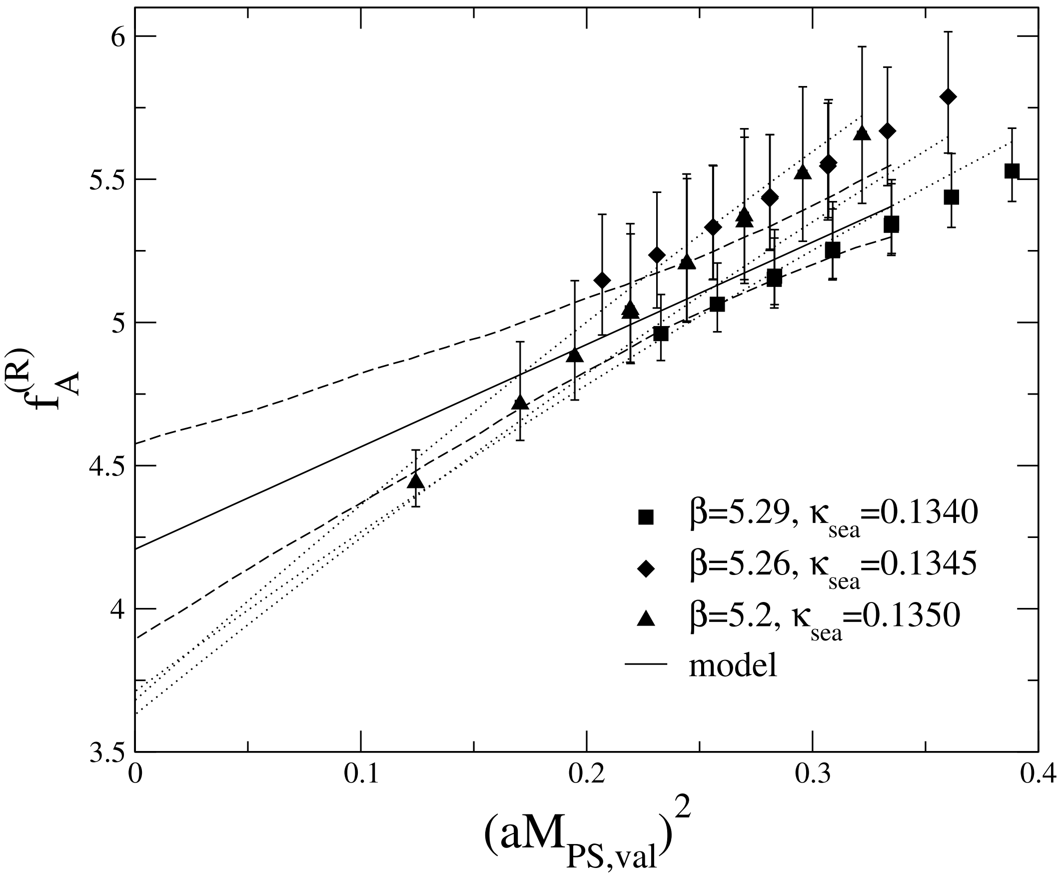

Figure B.61: Plot of fit results for a full chiral extrapolation to the matched datasets of $f_{\mathrm{A}}^{(\mathrm{R})}$ versus $(aM_{\mathrm{PS}})^2$ using Equation (4.51). Solid and dashed lines give unitary fit results, dotted lines give partially quenched fit results.

A	B_{s}	B_{v}	C_{ss}	C_{vv}	C_{sv}	χ^2/dof
$4.21\ ^{+37}_{-31}$	$-4.8\ ^{+40}_{-54}$	$8.3\ ^{+46}_{-34}$	$10\ ^{+11}_{-\ 9}$	$-2.2\ ^{+44}_{-73}$	$-7.6\ ^{+90}_{-81}$	0.503

Table B.43: Fit results for a full chiral extrapolation to the matched datasets of $f_{\mathrm{A}}^{(\mathrm{R})}$ versus $(aM_{\mathrm{PS}})^2$ using Equation (4.51).

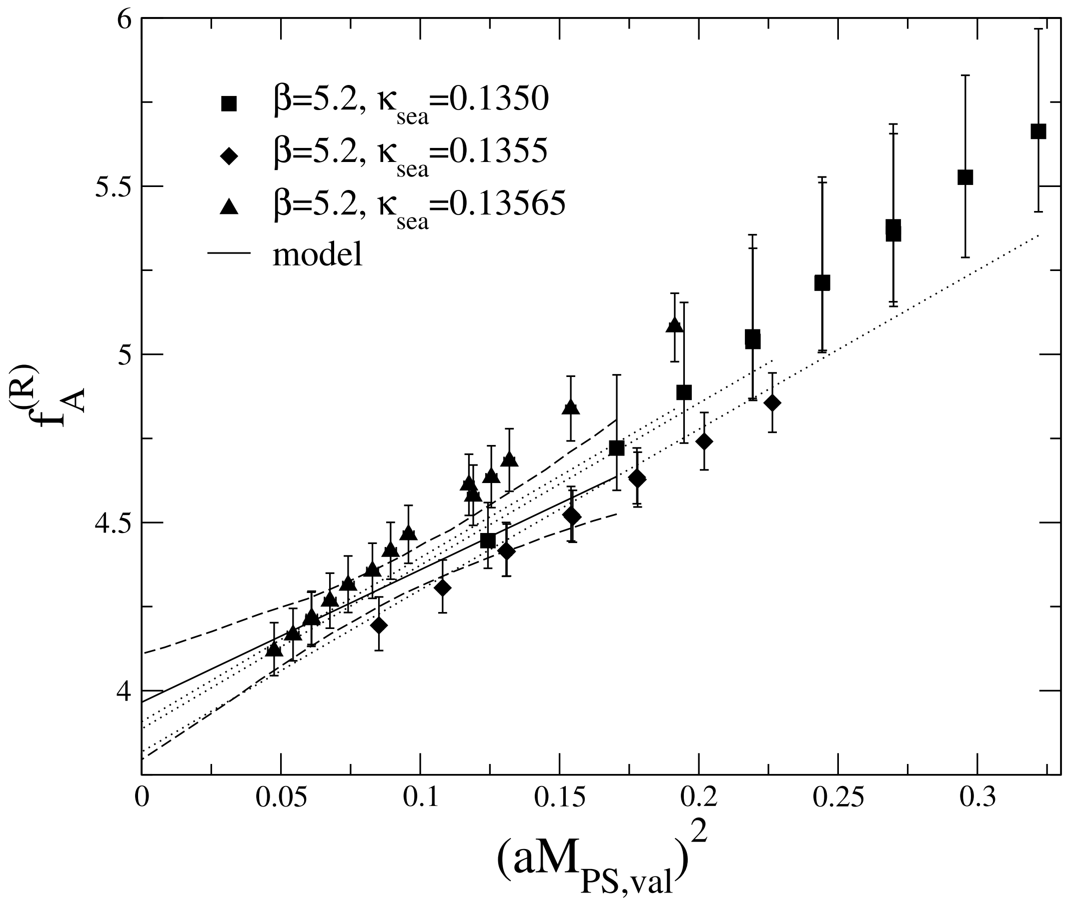

Figure B.62: Plot of fit results for a full chiral extrapolation to the datasets at $\beta = 5.2$ of $f_{\mathrm{A}}^{(\mathrm{R})}$ versus $(aM_{\mathrm{PS}})^2$ using Equation (4.51). Solid and dashed lines give unitary fit results, dotted lines give partially quenched fit results.

A	B_{s}	B_{v}	C_{ss}	C_{vv}	C_{sv}	χ^2/dof
3.97 $^{+14}_{-17}$	-1.0 $^{+27}_{-21}$	4.9 $^{+14}_{-18}$	1 $^{+14}_{-18}$	-0.2 $^{+48}_{-51}$	0 $^{+19}_{-17}$	1.495

Table B.44: Fit results for a full chiral extrapolation to the datasets at $\beta = 5.2$ of $f_{\mathrm{A}}^{(\mathrm{R})}$ versus $(aM_{\mathrm{PS}})^2$ using Equation (4.51).

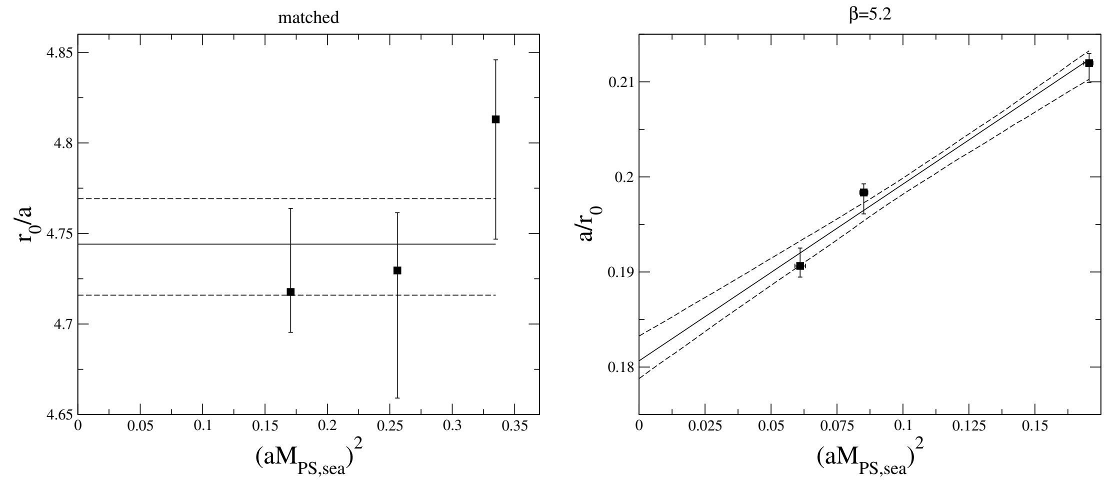

Figure B.63: Fit results for r_0/a and a/r_0 versus $(aM_{\mathrm{PS,sea}})^2$ for the matched and $\beta = 5.2$ datasets respectively.

Dataset	r_0/a	A_{r_0}	B_{r_0}	χ^2/dof	Q
matched	$4.744\ ^{+25}_{-28}$			1.307	0.271
$\beta = 5.2$		$0.1807\ ^{+26}_{-19}$	$0.186\ ^{+14}_{-24}$	2.280	0.131

Table B.45: Fit coefficients for r_0/a and a/r_0 versus $(aM_{\mathrm{PS,sea}})^2$ for the matched and $\beta = 5.2$ datasets respectively.

Appendix C

Physical results

C.1 Meson spectrum

Dataset	M_{a_0}	M_{a_1}	M_{b_1}
$(5.2, 0.1350)$	$872\ ^{+170}_{-147}$	$1368\ ^{+140}_{-102}$	$1372\ ^{+124}_{-106}$
$(5.2, 0.1355)$	$915\ ^{+122}_{-143}$	$1132\ ^{+110}_{-\ 82}$	$1197\ ^{+122}_{-125}$
$(5.2, 0.13565)$	$807\ ^{+256}_{-231}$	$1237\ ^{+\ 82}_{-\ 73}$	$1222\ ^{+120}_{-130}$
$(5.2, 0.1358)$	$885\ ^{+106}_{-104}$	$1013\ ^{+\ 60}_{-\ 70}$	$1025\ ^{+102}_{-108}$
$(5.25, 0.1352)$	$1213\ ^{+139}_{-149}$	$980\ ^{+\ 98}_{-\ 86}$	$1287\ ^{+100}_{-\ 97}$
$(5.26, 0.1345)$	$987\ ^{+250}_{-207}$	$1266\ ^{+103}_{-110}$	$1650\ ^{+\ 84}_{-\ 70}$
$(5.29, 0.1340)$	$1415\ ^{+\ 65}_{-409}$	$1424\ ^{+134}_{-110}$	$1494\ ^{+127}_{-115}$
$(5.93, \text{quen.})$	$1581\ ^{+\ 91}_{-114}$	$1223\ ^{+\ 68}_{-\ 94}$	$1262\ ^{+107}_{-\ 63}$
matched	$829\ ^{+112}_{-130}$	$1162\ ^{+\ 75}_{-\ 76}$	
$\beta = 5.2$	$870\ ^{+127}_{-109}$	$1158\ ^{+\ 73}_{-\ 71}$	$1072\ ^{+\ 96}_{-\ 89}$

Table C.1: Results for the non-strange meson masses (in MeV) from partially quenched and full chiral extrapolations with the scale set by M_ρ.

Dataset	M_{K^*}	$M_{\eta_{ss}}$	M_ϕ
$(5.2, 0.1350)$	$878\,^{+11}_{-9}$	$703.8\,^{+36}_{-27}$	$991\,^{+19}_{-14}$
$(5.2, 0.1355)$	$823\,^{+30}_{-25}$	$697.6\,^{+27}_{-30}$	$913\,^{+36}_{-24}$
$(5.2, 0.13565)$	$885\,^{+20}_{-18}$	$693.7\,^{+37}_{-35}$	$994\,^{+29}_{-24}$
$(5.2, 0.1358)$	$868\,^{+16}_{-15}$	$692.1\,^{+63}_{-64}$	$967\,^{+22}_{-17}$
$(5.25, 0.1352)$	$877\,^{+13}_{-12}$	$698.5\,^{+25}_{-32}$	$982\,^{+21}_{-18}$
$(5.26, 0.1345)$	$883.3\,^{+59}_{-49}$	$705.8\,^{+23}_{-20}$	$998\,^{+10}_{-8}$
$(5.29, 0.1340)$	$877\,^{+10}_{-12}$	$699.9\,^{+16}_{-17}$	$984\,^{+18}_{-20}$
$(5.93, \text{quen.})$	$879.6\,^{+60}_{-66}$	$698.4\,^{+15}_{-17}$	$987\,^{+9}_{-10}$
matched	$888\,^{+19}_{-16}$	$704.1\,^{+35}_{-26}$	$1011\,^{+34}_{-29}$
$\beta = 5.2$	$870\,^{+11}_{-11}$	$698.2\,^{+25}_{-23}$	$972\,^{+21}_{-20}$

Table C.2: Results for the strange meson masses (in MeV) from partially quenched and full chiral extrapolations with the scale set by M_ρ and am_{s} fixed by M_{K}.

Dataset	M_{K}	$M_{\eta_{ss}}$	M_{ϕ}
$(5.2, 0.1350)$	535^{+22}_{-24}	761^{+35}_{-37}	1029^{+10}_{-7}
$(5.2, 0.1355)$	670^{+39}_{-71}	955^{+58}_{-109}	1164^{+159}_{-112}
$(5.2, 0.13565)$	520^{+42}_{-39}	727^{+59}_{-59}	1015^{+18}_{-8}
$(5.2, 0.1358)$	561^{+35}_{-37}	783^{+50}_{-57}	1026^{+31}_{-19}
$(5.25, 0.1352)$	539^{+29}_{-29}	760^{+42}_{-43}	1020^{+10}_{-6}
$(5.26, 0.1345)$	524^{+11}_{-13}	747^{+18}_{-20}	1024.5^{+28}_{-26}
$(5.29, 0.1340)$	539^{+30}_{-23}	761^{+44}_{-35}	1022.6^{+74}_{-35}
$(5.93, \text{quen.})$	533^{+15}_{-13}	751^{+23}_{-20}	1020.0^{+53}_{-37}
matched	514^{+35}_{-36}	730^{+57}_{-54}	1028.6^{+93}_{-62}
$\beta = 5.2$	555^{+30}_{-28}	784^{+45}_{-41}	1024.5^{+68}_{-67}

Table C.3: Results for the strange meson masses (in MeV) from partially quenched and full chiral extrapolations with the scale set by M_ρ and am_{s} fixed by M_{K^*}.

Dataset	M_{K}	M_{K^*}	$M_{\eta_{ss}}$
$(5.2, 0.1350)$	$526\,^{+14}_{-19}$	$891.4\,^{+31}_{-42}$	$747\,^{+22}_{-28}$
$(5.2, 0.1355)$	$588\,^{+5}_{-20}$	$855\,^{+28}_{-27}$	$832\,^{+6}_{-30}$
$(5.2, 0.13565)$	$525\,^{+25}_{-32}$	$898.6\,^{+45}_{-86}$	$734\,^{+34}_{-46}$
$(5.2, 0.1358)$	$554\,^{+14}_{-22}$	$893\,^{+10}_{-12}$	$774\,^{+19}_{-31}$
$(5.25, 0.1352)$	$539\,^{+19}_{-24}$	$896.0\,^{+34}_{-48}$	$760\,^{+28}_{-35}$
$(5.26, 0.1345)$	$519\,^{+9}_{-11}$	$893.6\,^{+12}_{-13}$	$739\,^{+14}_{-17}$
$(5.29, 0.1340)$	$535\,^{+22}_{-20}$	$894.6\,^{+17}_{-34}$	$757\,^{+34}_{-30}$
$(5.93, \text{quen.})$	$532\,^{+11}_{-10}$	$895.8\,^{+19}_{-25}$	$750\,^{+16}_{-15}$
matched	$506\,^{+30}_{-30}$	$891.8\,^{+29}_{-39}$	$717\,^{+46}_{-45}$
$\beta = 5.2$	$550\,^{+25}_{-24}$	$893.6\,^{+33}_{-30}$	$776\,^{+40}_{-35}$

Table C.4: Results for the strange meson masses (in MeV) from partially quenched and full chiral extrapolations with the scale set by M_ρ and am_{s} fixed by M_ϕ.

Dataset	M_ρ	M_{a_0}	M_{a_1}	M_{b_1}
$(5.2, 0.1350)$	$831\ ^{+29}_{-34}$	$939\ ^{+183}_{-157}$	$1476\ ^{+129}_{-108}$	$1481\ ^{+111}_{-110}$
$(5.2, 0.1355)$	$940\ ^{+62}_{-74}$	$1113\ ^{+133}_{-170}$	$1378\ ^{+67}_{-54}$	$1459\ ^{+87}_{-123}$
$(5.2, 0.13565)$	$857\ ^{+41}_{-50}$	$896\ ^{+266}_{-267}$	$1376\ ^{+51}_{-64}$	$1361\ ^{+107}_{-132}$
$(5.2, 0.1358)$	$929\ ^{+29}_{-44}$	$1069\ ^{+121}_{-133}$	$1218\ ^{+51}_{-79}$	$1230\ ^{+115}_{-145}$
$(5.25, 0.1352)$	$875\ ^{+39}_{-48}$	$1379\ ^{+127}_{-168}$	$1110\ ^{+81}_{-87}$	$1463\ ^{+75}_{-99}$
$(5.26, 0.1345)$	$822\ ^{+21}_{-33}$	$1052\ ^{+261}_{-233}$	$1350\ ^{+78}_{-118}$	$1760\ ^{+54}_{-76}$
$(5.29, 0.1340)$	$848\ ^{+56}_{-67}$	$1559\ ^{+7}_{-409}$	$1567\ ^{+61}_{-82}$	$1645\ ^{+86}_{-99}$
$(5.93, \text{quen.})$	$876\ ^{+19}_{-18}$	$1804\ ^{+103}_{-123}$	$1390\ ^{+78}_{-93}$	$1434\ ^{+120}_{-67}$
matched	$874\ ^{+22}_{-26}$	$937\ ^{+114}_{-152}$	$1317\ ^{+74}_{-84}$	
$\beta = 5.2$	$896\ ^{+27}_{-34}$	$1009\ ^{+128}_{-134}$	$1345\ ^{+66}_{-73}$	$1243\ ^{+90}_{-111}$

Table C.5: Results for the non-strange meson masses (in MeV) from partially quenched and full chiral extrapolations with the scale set by r_0.

Dataset	M_{K^*}	$M_{\eta_{ss}}$	M_ϕ
$(5.2, 0.1350)$	$930\ ^{+18}_{-22}$	$702.0\ ^{+34}_{-22}$	$1035\ ^{+13}_{-12}$
$(5.2, 0.1355)$	$977\ ^{+37}_{-40}$	$695.5\ ^{+18}_{-20}$	$1035\ ^{+23}_{-21}$
$(5.2, 0.13565)$	$960\ ^{+22}_{-27}$	$693.2\ ^{+32}_{-28}$	$1059\ ^{+12}_{-15}$
$(5.2, 0.1358)$	$1008\ ^{+18}_{-28}$	$691.7\ ^{+43}_{-44}$	$1089\ ^{+12}_{-20}$
$(5.25, 0.1352)$	$969\ ^{+27}_{-31}$	$696.8\ ^{+20}_{-24}$	$1062\ ^{+17}_{-21}$
$(5.26, 0.1345)$	$927\ ^{+15}_{-25}$	$704.1\ ^{+22}_{-16}$	$1036\ ^{+12}_{-19}$
$(5.29, 0.1340)$	$944\ ^{+39}_{-48}$	$698.3\ ^{+13}_{-12}$	$1042\ ^{+27}_{-33}$
$(5.93, \text{quen.})$	$972\ ^{+12}_{-11}$	$696.6\ ^{+13}_{-13}$	$1067.0\ ^{+71}_{-70}$
matched	$977\ ^{+18}_{-22}$	$701.3\ ^{+28}_{-19}$	$1084\ ^{+29}_{-29}$
$\beta = 5.2$	$981\ ^{+19}_{-23}$	$696.4\ ^{+18}_{-17}$	$1068\ ^{+14}_{-18}$

Table C.6: Results for the strange meson masses (in MeV) from partially quenched and full chiral extrapolations with the scale set by r_0 and am_{s} fixed by M_{K}.

C.2 Baryon spectrum

Dataset	M_N^+	M_N^-	M_Δ^+	M_Δ^-
$(5.2, 0.1350)$	$1071\ ^{+75}_{-51}$	$2097\ ^{+209}_{-172}$	$1421\ ^{+102}_{-72}$	$1713\ ^{+214}_{-279}$
$(5.2, 0.1355)$	$1009\ ^{+102}_{-91}$	$1587\ ^{+168}_{-158}$	$1254\ ^{+116}_{-89}$	$2131\ ^{+299}_{-290}$
$(5.2, 0.13565)$	$1130\ ^{+79}_{-66}$	$1832\ ^{+230}_{-189}$	$1483\ ^{+104}_{-85}$	$2498\ ^{+221}_{-210}$
$(5.2, 0.1358)$	$1012\ ^{+76}_{-60}$	$1796\ ^{+130}_{-140}$	$1452\ ^{+85}_{-75}$	$2111\ ^{+141}_{-176}$
$(5.25, 0.1352)$	$990\ ^{+68}_{-71}$	$1669\ ^{+119}_{-111}$	$1401\ ^{+118}_{-100}$	$2093\ ^{+162}_{-187}$
$(5.26, 0.1345)$	$1166\ ^{+58}_{-40}$	$1713\ ^{+192}_{-214}$	$1366\ ^{+64}_{-53}$	$1672\ ^{+297}_{-318}$
$(5.29, 0.1340)$	$1091\ ^{+118}_{-94}$	$1807\ ^{+244}_{-188}$	$1371\ ^{+117}_{-112}$	$2455\ ^{+425}_{-795}$
$(5.93, \text{quen.})$	$1077\ ^{+51}_{-48}$	$1865\ ^{+177}_{-213}$	$1283\ ^{+44}_{-61}$	$2049\ ^{+111}_{-141}$
matched	$1141\ ^{+37}_{-33}$		$1283\ ^{+50}_{-46}$	
$\beta = 5.2$	$1105\ ^{+45}_{-43}$	$1677\ ^{+130}_{-132}$	$1423\ ^{+57}_{-49}$	

Table C.7: Results for the baryon masses (in MeV) from partially quenched and full chiral extrapolations with the scale set by M_ρ.

Dataset	M_N^+	M_N^-	M_Δ^+	M_Δ^-
$(5.2, 0.1350)$	$1153\,^{+56}_{-43}$	$2264\,^{+192}_{-183}$	$1532\,^{+91}_{-79}$	$1845\,^{+224}_{-278}$
$(5.2, 0.1355)$	$1224\,^{+75}_{-78}$	$1934\,^{+169}_{-192}$	$1526\,^{+83}_{-79}$	$2608\,^{+251}_{-293}$
$(5.2, 0.13565)$	$1256\,^{+54}_{-59}$	$2040\,^{+175}_{-172}$	$1651\,^{+74}_{-80}$	$2791\,^{+168}_{-192}$
$(5.2, 0.1358)$	$1215\,^{+77}_{-78}$	$2181\,^{+114}_{-164}$	$1757\,^{+59}_{-83}$	$2561\,^{+137}_{-229}$
$(5.25, 0.1352)$	$1121\,^{+59}_{-75}$	$1895\,^{+112}_{-136}$	$1591\,^{+101}_{-102}$	$2380\,^{+134}_{-183}$
$(5.26, 0.1345)$	$1242\,^{+39}_{-47}$	$1827\,^{+185}_{-244}$	$1457\,^{+47}_{-60}$	$1781\,^{+299}_{-341}$
$(5.29, 0.1340)$	$1199\,^{+60}_{-77}$	$1987\,^{+217}_{-183}$	$1507\,^{+64}_{-94}$	$2707\,^{+355}_{-883}$
$(5.93, \text{quen.})$	$1222\,^{+57}_{-52}$	$2124\,^{+206}_{-237}$	$1457\,^{+46}_{-66}$	$2332\,^{+120}_{-156}$
matched	$1292\,^{+27}_{-28}$		$1453\,^{+44}_{-50}$	
$\beta = 5.2$	$1283\,^{+32}_{-39}$	$1948\,^{+101}_{-120}$	$1655\,^{+51}_{-54}$	

Table C.8: Results for the baryon masses (in MeV) from partially quenched and full chiral extrapolations with the scale set by r_0.

C.3 Decay constants

.

Dataset	f_π	f_ρ	f_{a_1}
$(5.2, 0.1350)$	$146.3\ ^{+90}_{-63}$	$2.87\ ^{+15}_{-10}$	$3.68\ ^{+24}_{-26}$
$(5.2, 0.1355)$	$114.6\ ^{+93}_{-67}$	$2.94\ ^{+22}_{-11}$	$3.800\ ^{+96}_{-89}$
$(5.2, 0.13565)$	$105.9\ ^{+72}_{-69}$	$3.18\ ^{+10}_{-\ 9}$	$3.822\ ^{+96}_{-95}$
$(5.2, 0.1358)$	$93.4\ ^{+64}_{-58}$	$3.083\ ^{+86}_{-60}$	$3.79\ ^{+11}_{-12}$
$(5.25, 0.1352)$	$123.8\ ^{+73}_{-65}$	$3.09\ ^{+17}_{-10}$	$4.62\ ^{+32}_{-28}$
$(5.26, 0.1345)$	$143.2\ ^{+67}_{-54}$	$3.075\ ^{+84}_{-76}$	$4.37\ ^{+40}_{-28}$
$(5.29, 0.1340)$	$152\ ^{+14}_{-12}$	$3.35\ ^{+42}_{-27}$	$3.97\ ^{+16}_{-11}$
$(5.93, \text{quen.})$	$136.4\ ^{+35}_{-36}$	$3.125\ ^{+47}_{-41}$	$4.54\ ^{+42}_{-27}$
matched		$2.81\ ^{+21}_{-18}$	$4.23\ ^{+36}_{-31}$
$\beta = 5.2$			$3.99\ ^{+13}_{-16}$

Table C.9: Results for the non-strange meson decay constants from partially quenched and full chiral extrapolations with the scale set by M_ρ. f_π is given in MeV.

Dataset	f_{K}	f_{K^*}	f_ϕ
$(5.2, 0.1350)$	$162.1\,^{+66}_{-44}$	$3.254\,^{+78}_{-44}$	$3.675\,^{+86}_{-60}$
$(5.2, 0.1355)$	$141.1\,^{+73}_{-49}$	$3.53\,^{+11}_{-\ 6}$	$4.08\,^{+13}_{-13}$
$(5.2, 0.13565)$	$135.7\,^{+51}_{-46}$	$3.519\,^{+57}_{-52}$	$3.833\,^{+66}_{-66}$
$(5.2, 0.1358)$	$125.8\,^{+34}_{-31}$	$3.402\,^{+41}_{-38}$	$3.747\,^{+56}_{-61}$
$(5.25, 0.1352)$	$147.9\,^{+59}_{-45}$	$3.417\,^{+95}_{-53}$	$3.778\,^{+69}_{-53}$
$(5.26, 0.1345)$	$156.1\,^{+59}_{-44}$	$3.408\,^{+58}_{-58}$	$3.792\,^{+55}_{-54}$
$(5.29, 0.1340)$	$165\,^{+12}_{-10}$	$3.63\,^{+30}_{-19}$	$3.94\,^{+19}_{-\ 9}$
$(5.93, \mathrm{quen.})$	$154.0\,^{+27}_{-29}$	$3.472\,^{+28}_{-24}$	$3.857\,^{+37}_{-32}$
matched		$3.03\,^{+21}_{-18}$	$3.21\,^{+34}_{-28}$

Table C.10: Results for the strange meson decay constants from partially quenched and full chiral extrapolations with the scale set by M_ρ and am_{s} fixed by M_{K}. f_{K} is given in MeV.

Dataset	f_{K}	f_{K^*}	f_ϕ
$(5.2, 0.1350)$	$164.6\,^{+51}_{-27}$	$3.321\,^{+92}_{-48}$	$3.81\,^{+16}_{-13}$
$(5.2, 0.1355)$	$160.5\,^{+19}_{-37}$	$4.01\,^{+22}_{-25}$	$4.33\,^{+14}_{-59}$
$(5.2, 0.13565)$	$138.3\,^{+45}_{-27}$	$3.55\,^{+11}_{-\ 7}$	$3.89\,^{+15}_{-15}$
$(5.2, 0.1358)$	$133.9\,^{+36}_{-37}$	$3.500\,^{+99}_{-83}$	$3.96\,^{+19}_{-20}$
$(5.25, 0.1352)$	$152.0\,^{+39}_{-24}$	$3.48\,^{+11}_{-\ 5}$	$3.91\,^{+17}_{-13}$
$(5.26, 0.1345)$	$157.6\,^{+54}_{-41}$	$3.449\,^{+58}_{-51}$	$3.884\,^{+89}_{-86}$
$(5.29, 0.1340)$	$167\,^{+11}_{-\ 8}$	$3.68\,^{+26}_{-12}$	$4.06\,^{+25}_{-\ 7}$
$(5.93, \mathrm{quen.})$	$156.5\,^{+21}_{-19}$	$3.529\,^{+44}_{-32}$	$3.980\,^{+97}_{-77}$
matched		$3.05\,^{+27}_{-18}$	$3.23\,^{+43}_{-30}$

Table C.11: Results for the strange meson decay constants from partially quenched and full chiral extrapolations with the scale set by M_ρ and am_{s} fixed by M_{K^*}. f_{K} is given in MeV.

Dataset	f_{K}	f_{K^*}	f_ϕ
$(5.2, 0.1350)$	$164.0\,^{+55}_{-32}$	$3.304\,^{+78}_{-43}$	$3.78\,^{+12}_{-11}$
$(5.2, 0.1355)$	$151.0\,^{+54}_{-47}$	$3.77\,^{+12}_{-11}$	$4.36\,^{+\ 9}_{-19}$
$(5.2, 0.13565)$	$138.9\,^{+32}_{-30}$	$3.560\,^{+79}_{-66}$	$3.90\,^{+12}_{-14}$
$(5.2, 0.1358)$	$133.0\,^{+22}_{-28}$	$3.489\,^{+62}_{-59}$	$3.93\,^{+12}_{-14}$
$(5.25, 0.1352)$	$152.0\,^{+40}_{-28}$	$3.480\,^{+91}_{-43}$	$3.91\,^{+13}_{-12}$
$(5.26, 0.1345)$	$157.3\,^{+54}_{-40}$	$3.441\,^{+56}_{-53}$	$3.866\,^{+83}_{-79}$
$(5.29, 0.1340)$	$167\,^{+12}_{-\ 9}$	$3.68\,^{+27}_{-13}$	$4.05\,^{+23}_{-\ 7}$
$(5.93, \text{quen.})$	$156.5\,^{+22}_{-22}$	$3.528\,^{+37}_{-28}$	$3.978\,^{+75}_{-65}$
matched		$3.04\,^{+26}_{-17}$	$3.22\,^{+40}_{-29}$

Table C.12: Results for the strange meson decay constants from partially quenched and full chiral extrapolations with the scale set by M_ρ and am_{s} fixed by M_ϕ. f_{K} is given in MeV.

Dataset	f_π	f_ρ	f_{a_1}
$(5.2, 0.1350)$	$157.7\ ^{+56}_{-46}$	$2.87\ ^{+15}_{-10}$	$3.67\ ^{+24}_{-26}$
$(5.2, 0.1355)$	$138.8\ ^{+43}_{-35}$	$2.92\ ^{+22}_{-12}$	$3.79\ ^{+10}_{-9}$
$(5.2, 0.13565)$	$117.4\ ^{+44}_{-58}$	$3.17\ ^{+10}_{-9}$	$3.82\ ^{+10}_{-10}$
$(5.2, 0.1358)$	$111.7\ ^{+48}_{-69}$	$3.078\ ^{+88}_{-61}$	$3.78\ ^{+11}_{-12}$
$(5.25, 0.1352)$	$140.3\ ^{+35}_{-45}$	$3.08\ ^{+17}_{-10}$	$4.62\ ^{+32}_{-28}$
$(5.26, 0.1345)$	$152.6\ ^{+44}_{-56}$	$3.073\ ^{+86}_{-77}$	$4.36\ ^{+40}_{-28}$
$(5.29, 0.1340)$	$167.0\ ^{+72}_{-80}$	$3.35\ ^{+43}_{-28}$	$3.96\ ^{+16}_{-11}$
$(5.93, \text{quen.})$	$154.8\ ^{+18}_{-24}$	$3.121\ ^{+48}_{-42}$	$4.53\ ^{+42}_{-27}$
matched		$2.81\ ^{+21}_{-18}$	$4.23\ ^{+36}_{-31}$
$\beta = 5.2$			$3.98\ ^{+14}_{-16}$

Table C.13: Results for the non-strange meson decay constants from partially quenched and full chiral extrapolations with the scale set by r_0. f_π is given in MeV.

Dataset	f_{K}	f_{K^*}	f_ϕ
$(5.2, 0.1350)$	$172.5\ ^{+34}_{-26}$	$3.20\ ^{+11}_{-\ 7}$	$3.555\ ^{+86}_{-62}$
$(5.2, 0.1355)$	$161.3\ ^{+28}_{-25}$	$3.32\ ^{+16}_{-11}$	$3.73\ ^{+11}_{-10}$
$(5.2, 0.13565)$	$144.7\ ^{+32}_{-35}$	$3.450\ ^{+69}_{-67}$	$3.715\ ^{+58}_{-50}$
$(5.2, 0.1358)$	$139.5\ ^{+24}_{-38}$	$3.294\ ^{+55}_{-37}$	$3.522\ ^{+47}_{-34}$
$(5.25, 0.1352)$	$161.8\ ^{+26}_{-31}$	$3.34\ ^{+13}_{-\ 8}$	$3.610\ ^{+98}_{-62}$
$(5.26, 0.1345)$	$164.8\ ^{+31}_{-46}$	$3.364\ ^{+76}_{-67}$	$3.695\ ^{+77}_{-57}$
$(5.29, 0.1340)$	$178.8\ ^{+57}_{-66}$	$3.57\ ^{+35}_{-24}$	$3.82\ ^{+27}_{-20}$
$(5.93, \text{quen.})$	$170.7\ ^{+14}_{-18}$	$3.386\ ^{+35}_{-35}$	$3.675\ ^{+32}_{-33}$
matched		$2.98\ ^{+22}_{-17}$	$3.13\ ^{+28}_{-25}$

Table C.14: Results for the strange meson decay constants from partially quenched and full chiral extrapolations with the scale set by r_0 and am_{s} fixed by M_{K}. f_{K} is given in MeV.

C.4 Quark masses

C.4.1 Standard quark masses

Dataset	$m_{\mathrm{n}}^{\overline{MS}}$	$m_{\mathrm{s}}^{\overline{MS}}(M_{\mathrm{K}})$	$m_{\mathrm{s}}^{\overline{MS}}(M_{\mathrm{K}^*})$	$m_{\mathrm{s}}^{\overline{MS}}(M_\phi)$
$(5.2, 0.1350)$	$4.64\ ^{+28}_{-25}$	$114.5\ ^{+54}_{-52}$	$132\ ^{+15}_{-16}$	$127\ ^{+11}_{-13}$
$(5.2, 0.1355)$	$4.75\ ^{+29}_{-38}$	$116.0\ ^{+61}_{-82}$	$202\ ^{+30}_{-48}$	$159\ ^{+\ 7}_{-19}$
$(5.2, 0.13565)$	$4.34\ ^{+33}_{-35}$	$106.8\ ^{+67}_{-65}$	$116\ ^{+22}_{-22}$	$119\ ^{+16}_{-19}$
$(5.2, 0.1358)$	$4.67\ ^{+28}_{-29}$	$114.8\ ^{+47}_{-52}$	$144\ ^{+22}_{-22}$	$141\ ^{+11}_{-14}$
$(5.25, 0.1352)$	$4.42\ ^{+24}_{-32}$	$109.5\ ^{+50}_{-68}$	$128\ ^{+16}_{-18}$	$128\ ^{+13}_{-16}$
$(5.26, 0.1345)$	$4.64\ ^{+15}_{-17}$	$115.0\ ^{+34}_{-37}$	$127.2\ ^{+79}_{-92}$	$124.8\ ^{+69}_{-82}$
$(5.29, 0.1340)$	$4.44\ ^{+28}_{-33}$	$110.1\ ^{+63}_{-72}$	$128\ ^{+20}_{-16}$	$127\ ^{+17}_{-15}$
$(5.93, \text{quen.})$	$4.21\ ^{+10}_{-\ 9}$	$106.4\ ^{+24}_{-21}$	$121.8\ ^{+92}_{-80}$	$121.6\ ^{+67}_{-65}$
$\beta = 5.2$	$2.093\ ^{+89}_{-82}$	$104.7\ ^{+40}_{-40}$	$130\ ^{+18}_{-15}$	$127\ ^{+16}_{-13}$

Table C.15: Standard renormalised quark masses at a reference scale of 2 GeV with mass scale set by M_ρ and matching scale, $\mu = 1/a$.

Dataset	$m_{\rm n}^{\overline{MS}}$	$m_{\rm s}^{\overline{MS}}(M_{\rm K})$	$m_{\rm s}^{\overline{MS}}(M_{\rm K^*})$	$m_{\rm s}^{\overline{MS}}(M_{\phi})$
$(5.2, 0.1350)$	$4.88\ ^{+30}_{-26}$	$120.4\ ^{+57}_{-55}$	$139\ ^{+16}_{-16}$	$134\ ^{+11}_{-13}$
$(5.2, 0.1355)$	$4.98\ ^{+30}_{-40}$	$121.6\ ^{+64}_{-86}$	$212\ ^{+31}_{-50}$	$167\ ^{+\ 7}_{-20}$
$(5.2, 0.13565)$	$4.57\ ^{+35}_{-36}$	$112.5\ ^{+70}_{-68}$	$123\ ^{+23}_{-23}$	$125\ ^{+17}_{-20}$
$(5.2, 0.1358)$	$4.91\ ^{+29}_{-30}$	$120.6\ ^{+50}_{-54}$	$152\ ^{+23}_{-23}$	$148\ ^{+11}_{-15}$
$(5.25, 0.1352)$	$4.65\ ^{+25}_{-34}$	$115.2\ ^{+53}_{-71}$	$134\ ^{+17}_{-19}$	$134\ ^{+14}_{-17}$
$(5.26, 0.1345)$	$4.88\ ^{+16}_{-18}$	$121.0\ ^{+35}_{-39}$	$133.8\ ^{+83}_{-97}$	$131.3\ ^{+72}_{-86}$
$(5.29, 0.1340)$	$4.66\ ^{+30}_{-35}$	$115.7\ ^{+66}_{-76}$	$135\ ^{+21}_{-17}$	$133\ ^{+18}_{-16}$
$(5.93, \text{quen.})$	$4.35\ ^{+11}_{-\ 9}$	$109.9\ ^{+25}_{-21}$	$125.8\ ^{+95}_{-83}$	$125.5\ ^{+69}_{-67}$
$\beta = 5.2$	$2.194\ ^{+93}_{-86}$	$109.8\ ^{+41}_{-42}$	$136\ ^{+18}_{-16}$	$134\ ^{+17}_{-14}$

Table C.16: Standard renormalised quark masses at a reference scale of 2 GeV with mass scale set by M_ρ and matching scale, $\mu = \pi/a$.

Dataset	$m_{\rm n}^{\overline{MS}}$	$m_{\rm s}^{\overline{MS}}(M_{\rm K})$
$(5.2, 0.1350)$	$4.34\ ^{+25}_{-18}$	$107.8\ ^{+46}_{-34}$
$(5.2, 0.1355)$	$3.97\ ^{+10}_{-13}$	$99.2\ ^{+19}_{-26}$
$(5.2, 0.13565)$	$3.94\ ^{+27}_{-20}$	$98.0\ ^{+45}_{-36}$
$(5.2, 0.1358)$	$3.94\ ^{+22}_{-18}$	$98.8\ ^{+43}_{-31}$
$(5.25, 0.1352)$	$3.94\ ^{+16}_{-19}$	$98.8\ ^{+32}_{-39}$
$(5.26, 0.1345)$	$4.38\ ^{+15}_{-\ 8}$	$109.2\ ^{+32}_{-19}$
$(5.29, 0.1340)$	$4.07\ ^{+10}_{-\ 7}$	$101.9\ ^{+22}_{-15}$
$(5.93, \mathrm{quen.})$	$3.737\ ^{+51}_{-48}$	$95.3\ ^{+12}_{-12}$
$\beta = 5.2$	$1.841\ ^{+56}_{-36}$	$93.7\ ^{+30}_{-23}$

Table C.17: Standard renormalised quark masses at a reference scale of 2 GeV with mass scale set by r_0 and matching scale, $\mu = 1/a$.

Dataset	$m_{\mathrm{n}}^{\overline{MS}}$	$m_{\mathrm{s}}^{\overline{MS}}(M_{\mathrm{K}})$
$(5.2, 0.1350)$	$4.58\ ^{+26}_{-19}$	$113.8\ ^{+48}_{-36}$
$(5.2, 0.1355)$	$4.20\ ^{+11}_{-14}$	$104.8\ ^{+20}_{-27}$
$(5.2, 0.13565)$	$4.16\ ^{+28}_{-21}$	$103.8\ ^{+48}_{-38}$
$(5.2, 0.1358)$	$4.17\ ^{+23}_{-19}$	$104.6\ ^{+45}_{-33}$
$(5.25, 0.1352)$	$4.17\ ^{+17}_{-20}$	$104.5\ ^{+34}_{-41}$
$(5.26, 0.1345)$	$4.62\ ^{+15}_{-9}$	$115.2\ ^{+34}_{-20}$
$(5.29, 0.1340)$	$4.29\ ^{+11}_{-7}$	$107.5\ ^{+23}_{-15}$
$(5.93, \text{quen.})$	$3.870\ ^{+52}_{-49}$	$98.7\ ^{+13}_{-12}$
$\beta = 5.2$	$1.950\ ^{+59}_{-38}$	$99.3\ ^{+32}_{-24}$

Table C.18: Standard renormalised quark masses at a reference scale of 2 GeV with mass scale set by r_0 and matching scale, $\mu = \pi/a$.

C.4.2 PCAC quark masses

Dataset	$m_{\rm n}^{\overline{MS}}$	$m_{\rm s}^{\overline{MS}}(M_{\rm K})$	$m_{\rm s}^{\overline{MS}}(M_{\rm K^*})$	$m_{\rm s}^{\overline{MS}}(M_\phi)$
$(5.2, 0.1350)$	$3.43\ ^{+12}_{-15}$	$94.3\ ^{+34}_{-46}$	$111\ ^{+14}_{-15}$	$108\ ^{+10}_{-13}$
$(5.2, 0.1355)$	$3.73\ ^{+22}_{-30}$	$102.0\ ^{+67}_{-85}$	$196\ ^{+42}_{-58}$	$150\ ^{+10}_{-23}$
$(5.2, 0.13565)$	$3.30\ ^{+20}_{-21}$	$91.6\ ^{+53}_{-60}$	$101\ ^{+24}_{-22}$	$105\ ^{+17}_{-20}$
$(5.2, 0.1358)$	$3.51\ ^{+17}_{-15}$	$100.6\ ^{+50}_{-53}$	$133\ ^{+27}_{-27}$	$131\ ^{+15}_{-18}$
$(5.25, 0.1352)$	$3.53\ ^{+20}_{-20}$	$95.3\ ^{+50}_{-58}$	$113\ ^{+20}_{-18}$	$115\ ^{+15}_{-17}$
$(5.26, 0.1345)$	$3.64\ ^{+11}_{-14}$	$97.8\ ^{+30}_{-38}$	$109.3\ ^{+76}_{-88}$	$108.8\ ^{+65}_{-82}$
$(5.29, 0.1340)$	$3.63\ ^{+25}_{-26}$	$96.5\ ^{+67}_{-74}$	$114\ ^{+22}_{-17}$	$114\ ^{+18}_{-16}$
$(5.93, \text{quen.})$	$3.826\ ^{+98}_{-79}$	$101.4\ ^{+25}_{-21}$	$117\ ^{+10}_{-\ 8}$	$121.3\ ^{+79}_{-71}$
$\beta = 5.2$	$3.25\ ^{+11}_{-12}$	$100.4\ ^{+42}_{-47}$	$126\ ^{+19}_{-16}$	$123\ ^{+17}_{-14}$

Table C.19: Renormalised PCAC quark masses at a reference scale of 2 GeV with mass scale set by M_ρ and matching scale, $\mu = 1/a$.

Dataset	$m_{\mathrm{n}}^{\overline{MS}}$	$m_{\mathrm{s}}^{\overline{MS}}(M_{\mathrm{K}})$	$m_{\mathrm{s}}^{\overline{MS}}(M_{\mathrm{K}^*})$	$m_{\mathrm{s}}^{\overline{MS}}(M_{\phi})$
$(5.2, 0.1350)$	$3.46\ ^{+12}_{-15}$	$95.0\ ^{+34}_{-47}$	$111\ ^{+14}_{-15}$	$109\ ^{+10}_{-13}$
$(5.2, 0.1355)$	$3.74\ ^{+23}_{-30}$	$102.3\ ^{+67}_{-85}$	$197\ ^{+42}_{-58}$	$151\ ^{+10}_{-23}$
$(5.2, 0.13565)$	$3.33\ ^{+20}_{-21}$	$92.4\ ^{+54}_{-61}$	$102\ ^{+24}_{-22}$	$106\ ^{+17}_{-20}$
$(5.2, 0.1358)$	$3.53\ ^{+17}_{-16}$	$101.2\ ^{+50}_{-53}$	$134\ ^{+27}_{-27}$	$132\ ^{+15}_{-19}$
$(5.25, 0.1352)$	$3.56\ ^{+20}_{-21}$	$96.1\ ^{+51}_{-58}$	$114\ ^{+20}_{-18}$	$116\ ^{+15}_{-17}$
$(5.26, 0.1345)$	$3.67\ ^{+11}_{-14}$	$98.7\ ^{+30}_{-38}$	$110.2\ ^{+76}_{-89}$	$109.8\ ^{+66}_{-82}$
$(5.29, 0.1340)$	$3.66\ ^{+25}_{-26}$	$97.4\ ^{+68}_{-75}$	$115\ ^{+22}_{-17}$	$115\ ^{+18}_{-16}$
$(5.93, \text{quen.})$	$3.841\ ^{+98}_{-80}$	$101.8\ ^{+25}_{-22}$	$117\ ^{+10}_{-\ 8}$	$121.8\ ^{+79}_{-72}$
$\beta = 5.2$	$3.27\ ^{+11}_{-12}$	$100.8\ ^{+42}_{-47}$	$127\ ^{+19}_{-16}$	$123\ ^{+17}_{-14}$

Table C.20: Renormalised PCAC quark masses at a reference scale of 2 GeV with mass scale set by M_ρ and matching scale, $\mu = \pi/a$.

Dataset	$m_{\rm n}^{\overline{MS}}$	$m_{\rm s}^{\overline{MS}}(M_{\rm K})$
$(5.2, 0.1350)$	$3.205\,^{+39}_{-46}$	$87.4\,^{+11}_{-14}$
$(5.2, 0.1355)$	$3.115\,^{+45}_{-68}$	$83.9\,^{+10}_{-17}$
$(5.2, 0.13565)$	$2.99\,^{+11}_{-10}$	$82.0\,^{+22}_{-20}$
$(5.2, 0.1358)$	$2.96\,^{+12}_{-\ 7}$	$82.1\,^{+28}_{-15}$
$(5.25, 0.1352)$	$3.141\,^{+86}_{-50}$	$84.2\,^{+17}_{-12}$
$(5.26, 0.1345)$	$3.434\,^{+69}_{-35}$	$92.0\,^{+20}_{-10}$
$(5.29, 0.1340)$	$3.325\,^{+60}_{-34}$	$88.2\,^{+15}_{-\ 9}$
$(5.93, \text{quen.})$	$3.394\,^{+37}_{-27}$	$89.69\,^{+80}_{-58}$
$\beta = 5.2$	$2.860\,^{+48}_{-33}$	$88.4\,^{+26}_{-27}$

Table C.21: Renormalised PCAC quark masses at a reference scale of 2 GeV with mass scale set by r_0 and matching scale, $\mu = 1/a$.

Dataset	$m_{\rm n}^{\overline{MS}}$	$m_{\rm s}^{\overline{MS}}(M_{\rm K})$
$(5.2, 0.1350)$	$3.236\ ^{+39}_{-48}$	$88.3\ ^{+11}_{-14}$
$(5.2, 0.1355)$	$3.151\ ^{+46}_{-69}$	$84.9\ ^{+10}_{-17}$
$(5.2, 0.13565)$	$3.03\ ^{+11}_{-10}$	$83.1\ ^{+22}_{-20}$
$(5.2, 0.1358)$	$3.00\ ^{+13}_{-\ 7}$	$83.2\ ^{+29}_{-15}$
$(5.25, 0.1352)$	$3.185\ ^{+87}_{-51}$	$85.4\ ^{+17}_{-12}$
$(5.26, 0.1345)$	$3.474\ ^{+70}_{-36}$	$93.0\ ^{+20}_{-10}$
$(5.29, 0.1340)$	$3.369\ ^{+61}_{-35}$	$89.4\ ^{+15}_{-\ 9}$
$(5.93, \text{quen.})$	$3.419\ ^{+37}_{-27}$	$90.33\ ^{+81}_{-59}$
$\beta = 5.2$	$2.902\ ^{+48}_{-34}$	$89.7\ ^{+26}_{-28}$

Table C.22: Renormalised PCAC quark masses at a reference scale of 2 GeV with mass scale set by r_0 and matching scale, $\mu = \pi/a$.

Bibliography

[1] S. Weinberg, *The Quantum Theory of Fields* (Cambridge University Press, Cambridge, 1995).

[2] M. E. Peskin and D. V. Schroeder, *An Introduction to Quantum Field Theory* (Addison-Wesley Publishing Company, Reading, Massachusetts, 1995).

[3] I. Montvay and G. Munster, *Quantum Fields on a Lattice* (Cambridge University Press, Cambridge, 1994).

[4] H. J. Rothe, *Lattice Gauge Theories An Introduction* (World Scientific, Singapore - New Jersey - London - Hong Kong, 1992).

[5] K. G. Wilson, Phys. Rev. **D10**, 2445 (1974).

[6] K. Symanzik, Nucl. Phys. **B226**, 187 (1983).

[7] K. Symanzik, Nucl. Phys. **B226**, 205 (1983).

[8] M. Lüscher and P. Weisz, Commun. Math. Phys. **97**, 59 (1985).

[9] M. Lüscher *et al.*, Nucl. Phys. **B478**, 365 (1996), hep-lat/9605038.

[10] B. Sheikholeslami and R. Wohlert, Nucl. Phys. **B259**, 572 (1985).

[11] M. Bochicchio *et al.*, Nucl. Phys. **B262**, 331 (1985).

[12] M. Lüscher *et al.*, Nucl. Phys. **B491**, 323 (1997), hep-lat/9609035.

[13] M. Lüscher *et al.*, Nucl. Phys. **B491**, 344 (1997), hep-lat/9611015.

[14] M. Guagnelli and R. Sommer, Nucl. Phys. Proc. Suppl. **63**, 886 (1998), hep-lat/9709088.

[15] M. Guagnelli *et al.*, Nucl. Phys. **B595**, 44 (2001), hep-lat/0009021.

[16] K. Jansen and R. Sommer, Nucl. Phys. **B530**, 185 (1998), hep-lat/9803017.

[17] G. M. deDivitiis and R. Petronzio, Phys. Lett. **B419**, 311 (1998), hep-lat/9710071.

[18] T. Bhattacharya *et al.*, Nucl. Phys. Proc. Suppl. **106**, 789 (2002), hep-lat/0111001.

[19] T. Bakeyev *et al.*, hep-lat/0209148.

[20] K. Jansen *et al.*, Phys. Lett. **B372**, 275 (1996), hep-lat/9512009.

[21] S. Capitani *et al.*, Nucl. Phys. **B544**, 669 (1999), hep-lat/9810063.

[22] F. Knechtli *et al.*, hep-lat/0209025.

[23] D. Bericevic *et al.*, hep-lat/0209168.

[24] S. Sint and R. Sommer, Nucl. Phys. **B465**, 71 (1996), hep-lat/9508012.

[25] M. Lüscher and P. Weisz, Nucl. Phys. **B479**, 429 (1996), hep-lat/9606016.

[26] S. Sint and P. Weisz, Nucl. Phys. **B502**, 251 (1997), hep-lat/9704001.

[27] S. Sint and P. Weisz, Nucl. Phys. Proc. Suppl. **63**, 856 (1998), hep-lat/9709096.

[28] S. Capitani *et al.*, Nucl. Phys. Proc. Suppl. **63**, 874 (1998), hep-lat/9709049.

[29] S. Capitani *et al.*, hep-lat/9711007.

[30] G. P. Lepage and P. B. Mackenzie, Phys. Rev. **D48**, 2250 (1993), hep-lat/9209022.

[31] A. D. Kennedy *et al.*, J. Comp. Phys. **64**, 133 (1986).

[32] S. Aoki *et al.*, Nucl. Phys. Proc. Suppl. **73**, 189 (1999), hep-lat/9809146.

[33] S. Duane *et al.*, Phys. Lett. **B195**, 216 (1987).

[34] Y. Chung *et al.*, Nucl. Phys. **B197**, 55 (1982).

[35] T. Bhattacharya *et al.*, Phys. Rev. **D53**, 6486 (1996), hep-lat/9512021.

[36] W. Rarita and J. Schwinger, Phys. Rev. **60**, 61 (1941).

[37] M. Benmerrouche, R. M. Davidson, and N. C. Mukhopadhyay, Phys. Rev. **C39**, 2339 (1989).

[38] D. B. Leinweber, T. Draper, and R. M. Woloshyn, Phys. Rev. **D46**, 3067 (1992), hep-lat/9208025.

[39] P. Lacock *et al.*, Phys. Rev. **D51**, 6403 (1995), hep-lat/9412079.

[40] R. Gupta, D. Daniel, and J. Grandy, Phys. Rev. **D48**, 3330 (1993), hep-lat/9304009.

[41] B. R. Martin, *Statistics for Physicists* (Academic Press, London and New York, 1971).

[42] B. Efron and R. J. Tibshirani, *An Introduction to the Bootstrap* (Chapman and Hall, New York, 1993).

[43] W. H. Press, B. P. Flannery, S. A. Teukolsky, and W. T. Vetterling, *Numerical recipes in C* (Cambridge University Press, Cambridge, 1988).

[44] C. Michael and A. McKerrell, Phys. Rev. **D51**, 3745 (1995), hep-lat/9412087.

[45] C. R. Allton *et al.*, Phys. Rev. **D65**, 054502 (2002), hep-lat/0107021.

[46] D. J. Hepburn, Nucl. Phys. Proc. Suppl. **106**, 278 (2002), hep-lat/0110029.

[47] C. Michael *et al.*, Nucl. Phys. Proc. Suppl. **106**, 293 (2002), hep-lat/0109028.

[48] D. J. Hepburn, Nucl. Phys. Proc. Suppl. **119**, 338 (2003), hep-lat/0209036.

[49] A. C. Irving *et al.*, Phys. Rev. **D58**, 114504 (1998), hep-lat/9807015.

[50] R. Sommer, Nucl. Phys. **B411**, 839 (1994), hep-lat/9310022.

[51] R. G. Edwards, U. M. Heller, and T. R. Klassen, Nucl. Phys. **B517**, 377 (1998), hep-lat/9711003.

[52] C. R. Allton *et al.*, Phys. Rev. **D60**, 034507 (1999), hep-lat/9808016.

[53] S. Aoki *et al.*, hep-lat/0212039.

[54] A. C. Irving, hep-lat/0208065.

[55] S. Collins *et al.*, Phys. Rev. **D67**, 014504 (2003), hep-lat/0110159.

[56] J. Gasser and H. Leutwyler, Nucl. Phys. **B250**, 465 (1985).

[57] C. W. Bernard and M. F. L. Golterman, Phys. Rev. **D49**, 486 (1994), hep-lat/9306005.

[58] S. Sharpe and N. Shoresh, Phys. Rev. **D62**, 094503 (2000), hep-lat/0006017.

[59] C. W. Bernard and M. F. L. Golterman, Phys. Rev. **D46**, 853 (1992), hep-lat/9204007.

[60] G. Rupak and N. Shoresh, Phys. Rev. **D66**, 054503 (2002), hep-lat/0201019.

[61] O. Bär, G. Rupak, and N. Shoresh, hep-lat/0306021.

[62] F. Farchioni *et al.*, Phys. Lett. **B561**, 102 (2003), hep-lat/0307002.

[63] F. Farchioni *et al.*, hep-lat/0307002.

[64] F. Farchioni *et al.*, hep-lat/0309094.

[65] A. A. Khan *et al.*, Phys.Rev. **D65**, 054505 (2002), hep-lat/0105015.

[66] S. R. Sharpe, Phys.Rev. **D56**, 7052 (1997), hep-lat/9707018.

[67] K. G. Chetyrkin *et al.*, Comput. Phys. Commun. **133**, 43 (2000), hep-ph/0004189.

[68] K. Hagiwara and others (Particle data group, Phys. Rev. **D66**, 010001 (2002).

[69] H. Leutwyler, Phys. Lett. **B378**, 313 (1996), hep-ph/9602366.

[70] K. C. Bowler *et al.*, Phys.Lett. **B162**, 354 (1985).

[71] S. Ono, Phys.Rev. **D17**, 888 (1978).

[72] P. Lacock and C. Michael, Phys.Rev. **D52**, 5213 (1995), hep-lat/9506009.